

Space vehicle radiation pressure modelling: A demonstration on Galileo satellites in GNSS

Zhen Li

Department of Civil, Environmental and Geomatic Engineering
University College London

A thesis submitted for the degree of

Doctor of Philosophy

December 2018

I, *Zhen Li* confirm that the work presented in this thesis is my own. Where information has been derived from other sources, I confirm that this has been indicated in the thesis.

.....

The text of Chapter 4 and Section 7.2.6 is, in part, a reformatted version of material appearing in: Li, Z., Ziebart, M., Bhattacharai, S., Harrison, D., 2018. A shadow function model based on perspective projection and atmospheric effect for satellites in eclipse. *Adv. Sp. Res.* doi: 10.1016/j.asr.2018.10.027. The dissertation author was the primary researcher and author, whilst the co-authors listed in this publication directed and supervised the research which forms the basis for these sections.

The text of Sections 5.1, 5.3 is, in part, a reformatted version of material appearing in: Li, Z., Ziebart, M., Bhattacharai, S., Harrison, D., Grey, S., 2018. Fast solar radiation pressure modelling with ray tracing and multiple reflections. *Adv. Sp. Res.* 61, 2352-2365. doi: 10.1016/j.asr.2018.02.019. The dissertation author was the primary researcher and author, whilst the co-authors listed in this publication directed and supervised the research which forms the basis for these sections.

Abstract

In an operational sense, orbit prediction is a fundamental requirement in generating the broadcast ephemeris for Global Navigation Satellite System (GNSS) satellites. Galileo as the European GNSS is now under construction and will be fully operational in 2020. Orbit prediction error is a significant component of the error budget of broadcast ephemeris of Galileo satellites. In short, orbit prediction is intrinsically linked to broadcast ephemeris quality. The quality of orbit prediction relies on accurate force models and initial state (position and velocity). The initial state is usually obtained from precise orbit determination. This research focuses on aspects of force modelling.

For the Galileo satellites, the largest force not well modelled is radiation pressure. Using the physics of radiation pressure as an entry point, this thesis is organised according to the technical elements (radiation flux, interaction between radiation flux and surfaces) of radiation pressure modelling. In terms of radiation flux modelling, a runtime and accuracy configurable Earth radiation flux model is developed based on the longwave and shortwave Earth flux observations from Clouds and Earth's Radiant Energy System (CERES), a shadow function that considers both the Earth's oblateness and atmospheric effect is developed to scale the solar radiation flux at a satellite's location when the satellite is in eclipse. In terms of the interaction between radiation flux and satellite's surfaces, a fast ray tracing algorithm is implemented and gets a speedup by a factor of 30–50 compared with the classical modelling method. In addition, an empirical solar radiation pressure model (the DREMT) is developed based on box-wing satellite model to cope with the un-modelled residuals of physical models. Finally, both the physical models and empirical models are validated in the orbit prediction test.

The orbit contribution of Signal in Space Ranging Error (SISRE) is used as an indicator to assess the quality of a 7-day predicted orbit. The newly developed DREMT improved the orbit by around 50% compared with the widely used empirical models (ECOM-1 and ECOM-2) when satellites are not in eclipse. After applying the physical models as *a priori* models in orbit prediction, DREMT, EOCM-1, and ECOM-2 get identical prediction performance. The DREMT does not get significant improvements using *a priori* models because it already contains box-wing satellite information implicitly. It is generally the case that the prediction performance is better in non-eclipse seasons than that in eclipse seasons due to a lack of knowledge regarding satellite attitude in eclipse.

Impact Statement

This research addresses the radiation force modelling for the Galileo satellites. The modelling improvements from this research allow the positions of satellites in space be determined more accurately. Satellites with accurate orbit provide more precise data for various applications, including precise positioning in GNSS and monitoring of the changes on Earth's surface.

In terms of academic impact, the modelling methods applied to Galileo satellites in this research act as a demonstration to prove that refined force models improve orbit quality. The philosophy on empirically modelling radiation pressure is a contribution to knowledge due to the fact that it avoids estimating empirical parameters blindly, which allows the analyses of physical processes on satellites go deeper. As one of the outcomes of this research, a modelling software package is made public to the community. In addition, two papers about the research methods have been published on high quality journals in this area. As one of direct applications at the scientific end, the orbit of Galileo satellites calculated using the models developed in this research is used to determine the terrestrial reference frame (a system of coordinates used for monitoring the shape of the Earth), which lies a fundamental basis for many investigations in earth sciences. The modelling methods used in this research can be further extended and applied to other satellites in Earth observation missions such as measuring sea level change and monitoring terrain deformation, which can provide more accurate data for research in global climate change and hazard reduction.

This research has a more day-to-day application as well. By changing the way in which the orbits of GNSS satellites are calculated, the performance of GNSS has been improved. Billions of people around the world are benefited in routine navigation applications with electronic devices such as smart phones. Commercial companies in the industry of autonomous driving vehicles are able to improve their product performance using more accurate positioning signals from the Galileo satellites. In addition, using more accurate positioning techniques to control farm machinery in precision agriculture helps to improve the working efficiency and thus improving food production.

In conclusion, the outcomes in this research make contribute to force modelling of GNSS satellites and thus benefit science communities that need high precision GNSS orbit.

Acknowledgements

This research is jointly funded by China Scholarship Council and University College London (UCL). This work is also linked to a project “SRP modelling for long-term orbit prediction” funded by European Space Agency.

First and foremost, I would like to thank my supervisors, Professor Marek Ziebart and Dr. Paul Groves, for their creative guidance, constructive criticism and constant encouragement over the course of my research, and for their careful review and comments on earlier versions of this thesis.

I would like to express special thanks to a few individuals who have given comments and contributed to technical discussions in this project. Dr. Santosh Bhattacharai (now a lecturer at UCL) has helped with several technical problems in force modelling, as well as professional proofreading for several of my papers. I would like to thank Dr. Stuart Grey (now at University of Strathclyde) for the visualization tools of space-craft and solving some technical problems in javascript. Dr. Christopher Atkins has helped with several discussions on the error propagation of random variables. Mr David Harrison helped with some problems in C++ programming and software design. I would like to thank Dr. Tim Springer from European Space Operations Centre who has contributed to the validation of force models in precise orbit determination. I would like to thank all the people who have made my time in UCL enjoyable and memorable.

Thanks to Professor Chuang Shi from Beihang University of China and Professor Zhenhong Li from Newcastle University, associate Professor Jingsong Huang and associate Professor Bingying Li from Wuhan University for their recommendations in the application of PhD and the scholarship.

Finally, I would like to say thank you to my parents. Their constant encourage and love have made it possible my study in London. Every word in this thesis is also irrigated with their love.

Contents

1	Introduction	29
1.1	Background	29
1.1.1	Introduction to GNSS	29
1.1.2	Satellites' orbit and forces acting on a satellite	31
1.2	An overview of the relevant aspects in radiation pressure modelling	32
1.2.1	The attitude of the Galileo satellites	32
1.2.2	The elements of radiation pressure modelling	33
1.3	Objectives and methodology	35
1.3.1	Statement of the general objective	35
1.3.2	Statement of the detailed objectives	35
1.3.3	Methodology	35
1.4	Thesis outline	38
2	A literature review of radiation pressure modelling	39
2.1	A review of radiation pressure modelling	39
2.1.1	The history of radiation pressure modelling	39
2.1.2	The modelling methodology of radiation pressure in precise orbit determination	41
2.2	Modelling methods on solar radiation pressure	42
2.2.1	The empirical approaches	42
2.2.2	The semi-analytical approaches	46
2.2.3	The analytical approaches	48
2.3	Modelling method of Earth radiation pressure	50
2.3.1	Knocke's model	51
2.3.2	The TUM model	51
2.4	Modelling method on shadow function	52
2.4.1	The cylinder model	52
2.4.2	The spherical Earth conical model	52
2.4.3	Adjustments to the spherical Earth conical model	53
2.5	Inspirations from the literature review	54
2.5.1	Maximise the utilisation of <i>a priori</i> information	55
2.5.2	Revisit the empirical representation	55

CONTENTS

3 Radiation flux modelling	57
3.1 Solar radiation flux	57
3.1.1 Total Solar Irradiance	58
3.1.2 Solar radiation flux at a satellite's location	59
3.2 Earth radiation flux	60
3.2.1 CERES Earth radiation flux data	61
3.2.2 Divide the TOA surface with a quad-tree structure	61
3.2.3 Fill each triangle with Earth radiation flux	65
3.2.4 The Earth radiation flux at a satellite's location	69
3.2.5 Results on Earth radiation flux modelling	70
3.3 Thermal radiation flux	75
3.3.1 Absorption from the Earth and solar radiation	76
3.3.2 The thermal radiation at radiators	77
3.4 Antenna radiation power	78
3.5 Summary	79
4 Solar radiation flux modelling during eclipses	81
4.1 What is a shadow function?	81
4.2 The geometrical problem	82
4.2.1 Definition of Image Space Frame	83
4.2.2 Existence of the Earth's image on the projection plane	85
4.2.3 Perspective projection of the Earth and the Sun onto the image plane	87
4.2.4 Solve the intersections between the projections of the Earth and the Sun	90
4.2.5 Calculate the overlapping area	91
4.3 The physical problem	93
4.4 The calculation of shadow function	95
4.5 Algorithm implementation of the shadow function modelling	98
4.6 Results	102
4.6.1 The GRACE accelerometer observations and shadow function . .	102
4.6.2 GRACE results	104
4.6.3 Galileo results	104
4.7 Summary	108
5 Interactions between radiation flux and satellite surface	111
5.1 Physical foundation of radiation pressure	111
5.1.1 The active case	112
5.1.2 The passive case	112
5.2 Galileo satellites information description	114
5.2.1 General structures of the Galileo IOV and FOC satellites	114
5.2.2 The satellite geometry and optical properties	117

CONTENTS

5.2.3	Satellite mass information	117
5.3	The ray tracing technique	119
5.3.1	State of the art in ray tracing	119
5.3.2	The representation of the satellite's geometry	120
5.3.3	Simulation of radiation flux in ray tracing	123
5.3.4	The ray-primitive intersection	126
5.3.5	Applying BVH in radiation pressure modelling	128
5.3.6	Parameters choice in ray tracing and improvement in computation efficiency	131
5.3.7	Uncertainty analysis of the ray tracing approach	135
5.4	Radiation pressure modelling for the solar panels	137
5.4.1	Direct solar radiation pressure modelling	138
5.4.2	Direct Earth radiation pressure modelling	139
5.5	Radiation pressure modelling for the satellite bus	140
5.5.1	Grid files generation	140
5.5.2	User algorithm of the grid files	142
5.6	The other force effects	143
5.6.1	Antenna thrust	143
5.6.2	Lorentz force	143
5.7	Summary	145
6	Empirical representation of solar radiation pressure	147
6.1	Assumptions in the satellite's geometry and attitude	147
6.1.1	Box-wing geometry and radiation pressure computation	148
6.1.2	Nominal attitude and angular parameters	148
6.2	Modelling method of the DREMT	152
6.2.1	Apply the Box-wing geometry	152
6.2.2	Parameterization of the box-wing model	154
6.2.3	Empirical representation of box-wing model	156
6.3	Accuracy loss of the DREMT	158
6.4	Can the DREMT absorb other forces on the satellite bus?	161
6.5	Consistency with the ray tracing solar radiation pressure model	162
6.6	Summary	163
7	Validation of force models in orbit prediction	167
7.1	Precise orbit data and orbit prediction	167
7.1.1	Precise orbit data	167
7.1.2	Orbit prediction	169
7.1.3	Orbit dynamic fitting	170
7.1.4	Indicators to assess the accuracy of predicted orbit	171
7.2	The impacts on the Galileo satellites' orbit	171
7.2.1	The direct solar radiation pressure	172

CONTENTS

7.2.2	The thermal re-radiation pressure	173
7.2.3	The direct Earth radiation pressure	174
7.2.4	The multiple reflections in ray tracing	176
7.2.5	The antenna thrust	177
7.2.6	The impacts of shadow function on the orbit	178
7.2.7	Orbit prediction with the physical models	180
7.2.8	Why the along track orbit error is larger than that in radial	182
7.3	Long-term orbit prediction with empirical models	183
7.3.1	Empirical models only	183
7.3.2	Empirical models + <i>a priori</i> force models	187
7.3.3	Findings	191
7.4	Reconstruction of acceleration from empirical models	191
7.5	Summary	195
8	Conclusions and discussion	197
8.1	Overview of the thesis	197
8.2	Summary in relation to the general objective	197
8.3	Conclusions and achievement of detailed objectives	198
8.3.1	Modelling Earth radiation pressure	199
8.3.2	Development of shadow function during eclipse	199
8.3.3	Fast ray tracing approach to model flux–surface interactions	200
8.3.4	Development of an empirical solar radiation pressure model	201
8.3.5	Performance assessment of force models in orbit prediction	202
8.4	Research contributions	202
8.5	Future work	203
A	Calculation on spherical surface	205
A.1	The Great-circle distance	205
A.2	Intersection between great circle arcs	205
A.3	The area of polygon on spherical surface	207
B	The mathematics of orbit fitting	211

List of Figures

1.1	The description of a satellite's position using Keplerian elements (the semi-major axis and eccentricity are not shown)	31
1.2	The description of a Galileo satellite's attitude. φ is the yaw angle and β is the sun elevation over orbital plane.	33
2.1	The definition of DYB system to describe the ECOM. The D component is from the satellite to the Sun, the Y is along the solar panel rotation axis and B component completes a right hand system. The angular argument u in the ECOM is the argument of latitude of the satellite. Angle ε is the angle between the Earth, the satellite and the Sun. Angle Δu is the difference between the argument of latitude of the sun in orbital plane and the argument of latitude of the satellite.	43
2.2	The Earth's shadow is in a shape of cylinder, what shows in this figure is the projection of the cylinder onto the plane composed of the centre of the Sun, the centre of the Earth and the satellite centre of mass. In CYM, the space is divided into 2 parts, the space inside the cylinder is in umbra while the space outside the cylinder is in full phase.	53
2.3	The projection of the cones onto the plane composed of the centre of the Sun, the centre of the Earth and the satellite centre of mass. The SECM can distinguish the full phase, penumbra and umbra state. In the calculation of the shadow function values, a fundamental plane is defined to be perpendicular to the shadow axis and goes through the satellite. .	53
2.4	The projections of the Earth and the Sun on the fundamental plane. It also shows the how the area of blocked solar disk is calculated.	54
3.1	The solar radiation spectrum for direct light at both the top of the Earth's atmosphere and at sea level [Nick, 2008].	57
3.2	The 3D model of SORCE satellite sourced from Laboratory for Atmospheric and Space Physics at the University of Colorado [2018]	58
3.3	The plot of all the TSI measurements from SORCE since March 2003 [Kopp, 2018]	59
3.4	The monthly averaged SW flux from CERES grid files.	62
3.5	The monthly averaged LW flux from CERES grid files.	63

LIST OF FIGURES

3.6	The initial regular octahedron for the division of the TOA.	64
3.7	A triangle with vertices 1,2, and 3 are divided into 4 small triangles by choosing the middle point of each side as a new vertex. A, B, and C are the middle points of each side.	65
3.8	The subdivision of the spherical TOA from level 0 to level 5. The x, y, and z axis are represented by the red, green and blue arrows separately.	66
3.9	The triangles of level 2 under equidistant cylindrical projection	66
3.10	One level 4 triangle ABC is above the UK. It contains several cells of 1° by 1° . The short wave Earth radiation flux in June is shown. The boundaries of the triangle is shown in blue while the grid lines are shown in red.	67
3.11	The TOA surface is divided into level 2 triangular network. For the k^{th} triangle that is visible to the satellite, the angle between the normal to that triangle and the Sun's direction is $\theta_{s,k}$, the angle between the viewing direction (from the centre of the triangle to the satellite) and the triangle's normal is θ_k	69
3.12	The variation of monthly averaged global mean Earth flux (on the TOA) derived from the CERES data. The SW has been offset by $245 \text{ W} \cdot \text{m}^{-2}$ and the LW has been offset by $90 \text{ W} \cdot \text{m}^{-2}$	72
3.13	The variation of the LW and SW Earth radiation flux at a Galileo satellite's location derived from the CERES grid data	73
3.14	The difference in Earth radiation flux (SW+LW) between CERES grid and different level subdivision for Galileo E11 satellite during one orbit	74
3.15	The visible triangles of E11 satellite at UTC 2015/03/11/19:59:44 with the level 4 subdivision triangular mesh. The blue triangles are showing the visible area.	75
3.16	30-m dish antenna of the German Space Operation Centre (GSOC) at its ground station near Weilheim [Steigenberger et al., 2018]	78
4.1	The basic geometrical relations among the Sun, the Earth and the satellite. The definition of the ISF (Image Space Frame) is also shown.	84
4.2	The geometrical relation among the PEC, PSC and the satellite. Based on this, the unit vector \mathbf{u} (normalization of vector from PSC to PEC) can be worked out.	85
4.3	The relative positions of the satellite, the Earth, and the Sun. Point S_1 and S_2 split line S_1S_2 into three segments. The dashed circles are the possible positions of the satellite on the line. S_1P_1 and S_2P_2 are tangent planes that touch the Earth at points P_1 and P_2	86

LIST OF FIGURES

4.4	The situation where the Earth's image is an ellipse. Figure 4.4a is for that the centre of the solar disk is inside the Earth's image and Fig. 4.4b is for that the centre of the solar disk is outside the Earth's image. Q_1 and Q_2 are the two intersections between the ellipse and the circle. O_e and O_s are the projections of the centres of the Earth and the Sun separately.	92
4.5	The situation where the Earth's image is a hyperbola. Figure 4.5a is for that the centre of the solar disk is inside the Earth's image and Fig. 4.5b is for that the centre of the solar disk is outside the Earth's image. Q_1 and Q_2 are the two intersections between the hyperbola and the circle. O_e and O_s are the projections of the centres of the Earth and the Sun separately.	93
4.6	The projection (the ellipse case) of the solid Earth, the TOA and the Sun on the image. In this figure, the Sun's image is totally inside the atmosphere. O_e is the centre of the Earth's image, O_s is the centre of the Sun's image. The point that for the calculation of the radiation reduction lies exactly at the centre of the Sun in this figure, but it could be anywhere (inside the atmosphere's image) on the line O_eO_s	95
4.7	The 5 possible situations of the relative positions among the projections of the TOA, the Earth and the Sun. The circles represent the possible positions of the Sun's projection. Case a means the Sun is fully outside the TOA. Case b means part of the Sun's projection has entered Earth's atmosphere. Case c means the Sun's projection is fully in the projection of the atmosphere while case d means part of the Sun's projection is blocked by the solid Earth. Case e means the solar disk is fully blocked by the solid Earth.	96
4.8	The cases b, c, and d in details. G_1 and G_2 are the lower boundary and upper boundary for the overlapping part between the Sun's image and the TOA's image.	97
4.9	The algorithm flow of the shadow function modelling	99
4.10	The algorithm flow of the perspective projection	101
4.11	The two GRACE satellites on a polar orbit.	103
4.12	The z component of accelerometer observations in satellite frame of GRACE-A satellite. The epochs are in GPS time [H:M:S].	103
4.13	The changes of shadow function during one eclipse event for GRACE-A satellite on Jan 20th, 2007	106
4.14	The variations of shadow function during one eclipse event for Galileo E11 on Jan 11th, 2015	107

LIST OF FIGURES

5.1	The force effects due to incident rays (incident angle θ) on a plane. The incident rays are in \mathbf{s} direction, the normal to the plane is \mathbf{n} and the specular reflection direction is \mathbf{r} . The diffusely reflected radiation is distributed in a semi-sphere but the force \mathbf{F}_3 is in $-\mathbf{n}$ direction. The direct hit of the incident rays generate force \mathbf{F}_1 and the specularly reflected rays generate force \mathbf{F}_2 .	113
5.2	The artists' view of Galileo IOV (left) and FOC (right) satellites [ESA, 2015].	115
5.3	The structures of the Galileo IOV and FOC satellite bus	116
5.4	The rendered geometry of the Galileo IOV and FOC satellite based on the primitives in Table 5.4.	122
5.5	The definition of PAS (Pixel Array System) for one Galileo IOV satellite bus. The radiation flux direction is represented by latitude φ and longitude λ in BFS. The boundary of the AABB of the spacecraft is shown in black.	125
5.6	The differences in magnitude of acceleration between 0.1 mm pixel spacing and the other 4 pixel spacings. Red dots represent FOC satellite while blue dots stand for IOV satellite.	133
5.7	The rate of intersection number between different reflections and the 10th reflection. Red dots represent FOC satellite while blue dots stand for IOV satellite.	133
5.8	The differences in magnitude of acceleration between 10 reflections and the other number of reflections. Red dots represent FOC satellite while blue dots stand for IOV satellite.	134
5.9	The Sun-facing side of the stowed solar panels for two Galileo FOC satellites. credit: space in images [ESA, 2015].	138
5.10	The rear side of the solar panels for one Galileo FOC satellite. credit: space in images [ESA, 2015].	139
5.11	The accelerations (the grid files) of the Galileo IOV and FOC satellite bus derived from the ray tracing.	141
5.12	The user algorithm for the calculation of the radiation pressure acceleration due to any radiation flux using the grid files	142
5.13	The histograms of the differences in x, y, and z component for Galileo IOV and FOC satellites. The dash line is the PDF of normal distribution with corresponding mean μ and standard deviation σ .	144
6.1	The solar radiation illumination of the box-wing geometry with respect to φ . “+p” represents the sun-facing side of solar panels, “-p” represents the rear side of solar panels.	150
6.2	The geometry among angle β , Δu and ϵ . ‘E’ represents the Earth, ‘P’ represents the satellite and ‘S’ stands for the Sun.	151
6.3	This shows the relation between ε and φ is $\varepsilon = \frac{\pi}{2} - \varphi$	151

LIST OF FIGURES

6.4	The variation of the function for each term in Eq. 6.21	157
6.5	The box-wing accelerations in the D and B components for the IOV and FOC satellites.	159
6.6	The fitting RMS in D and B components for the 3 empirical models: ECOM-1, ECOM-2 and the DREMT.	160
6.7	The fitting RMS in D and B components with constant accelerations a_x and a_z for the 3 empirical models: ECOM-1, ECOM-2 and the DREMT.	162
6.8	The RMS in D and B components of fitting the 3 empirical models to the ray tracing model.	164
6.9	The acceleration differences between the ray tracing derived model and the box-wing model for IOV and FOC satellites.	165
7.1	The distribution of the MGEX stations that track Galileo satellites.	168
7.2	The relations amongst reference orbit, fitted orbit and predicted orbit.	170
7.3	The illumination of the solar radiation and Earth radiation on the solar panels and the satellite bus. The red bar and blue bar represent solar radiation and Earth radiation separately. “+p” and “-p” stands for the sun-facing side and rear side of solar panels.	172
7.4	The variation of direct solar radiation pressure with respect to the orbital angle Δu for one Galileo IOV satellite.	173
7.5	The RMS of orbit errors in radial, along, cross and 3D caused by the direct solar radiation pressure in 24 hours	173
7.6	The variation of TRR acceleration with respect to the orbital angle Δu for one Galileo IOV satellite.	174
7.7	The RMS of orbit errors in radial, along, cross and 3D caused by the TRR within 24 hours	174
7.8	The variations of shortwave and longwave Earth radiation flux at a IOV satellite’s position.	175
7.9	The variation of direct Earth radiation pressure with respect to the orbital angle Δu for one Galileo IOV satellite.	175
7.10	The RMS of orbit errors in radial, along, cross and 3D caused by the direct Earth radiation pressure within 24 hours.	176
7.11	The difference in accelerations caused by the 3 reflections and 1 reflection models in the ray tracing for IOV and FOC satellites.	177
7.12	The RMS of orbit errors of IOV and FOC satellites in radial, along, cross and 3D within 24 hours caused by the 3rd reflections in the ray tracing derived model.	177
7.13	The RMS of orbit errors of IOV and FOC satellites in radial, along, cross and 3D within 24 hours caused by antenna thrust.	178
7.14	The difference in orbit error RMS amongst shadow function models PPM, SECM and PPM_atm.	179

LIST OF FIGURES

7.15 The RMS of 3D orbit errors in 24 hours for the various combinations of non-gravitational force models for the Galileo IOV satellites (average of E11, E12 and E19).	181
7.16 The RMS of 3D orbit errors in 24 hours for the various combinations of non-gravitational force models for the Galileo FOC satellites (average of E14, E22, E24, E26 and E30).	181
7.17 The average RMS of 2-day orbit fitting for IOV and FOC satellites using ECOM-1, ECOM-2 and the DREMT.	184
7.18 The average RMS in radial, along track, cross track and the SISRE _{orb} of a 7-day orbit prediction without <i>a priori</i> models during non-eclipse seasons.	185
7.19 The average RMS in radial, along track, cross track and the SISRE _{orb} of 7 days orbit prediction without <i>a priori</i> models during eclipse seasons.	186
7.20 This figure shows the SISRE of 1 to 7 day's orbit prediction for IOV satellites using ECOM-1, ECOM-2 and the DREMT.	186
7.21 The average RMS of 2-day orbit fitting for the Galileo satellites using ECOM-1, ECOM-2 and the DREMT with the augmentation of the <i>a priori</i> force models.	188
7.22 The average RMS in radial, along track, cross track and the SISRE _{orb} of 7 days orbit prediction with <i>a priori</i> models during non-eclipse seasons.	189
7.23 The average RMS in radial, along track, cross track and the SISRE _{orb} of 7 days orbit prediction with <i>a priori</i> models during eclipse seasons.	190
7.24 This figure shows the SISRE of 1 to 7 day's orbit prediction for IOV satellites using ECOM-1, ECOM-2 and the DREMT.	190
7.25 The empirical parameters of ECOM-1, ECOM-2, DREMT for E11 and E22 over non-eclipse seasons.	192
7.26 The reconstructed accelerations in the D and B components of E11 (IOV) for the ECOM-1, ECOM-2, DREMT, and the physical models.	193
7.27 The reconstructed accelerations in the D and B components of E22 (FOC) for ECOM-1, ECOM-2, DREMT, and the physical models.	194
A.1 The intersection between two great circle arcs.	206
A.2 A spherical polygon with 4 vertices (sides are Great-circle arcs). The interior angle are α_1 , α_2 , α_3 , and α_4	208
A.3 The interior angle and path from A to B	208

List of Tables

3.1	The variation of solar flux at Earth's perihelion and aphelion	60
3.2	The coordinates of the vertices of the regular octahedron	64
3.3	The list of faces for the regular octahedron	64
3.4	The relative error in area of TOA's surface for different levels of subdivision	71
3.5	The errors of global mean Earth radiation flux (both the SW and the LW) for different levels of subdivision. unit: $[10^{-6} \text{ W} \cdot \text{m}^{-2}]$	72
3.6	The standard deviation and average of the difference between the CERES grid and different levels of subdivision in the Earth radiation flux (SW+LW), unit $[\text{W} \cdot \text{m}^{-2}]$	73
3.7	The runtime of the different levels of subdivision [unit: ms]	75
3.8	The average transmit power of navigation antenna for different Galileo satellites [Steigenberger et al., 2018]	78
4.1	The value of a shadow function	82
4.2	The conditions for the 5 cases	100
4.3	The penumbra entry/exit time (in GPS time) for GRACE-A satellite on 20th January, 2007 (time format: H:M:S).	105
4.4	The error statistics of different shadow function models based on the comparison with $F_{s,acc}$ for GRACE-A satellite (over 30 penumbra transitions)	105
4.5	The error statistics of the differences between the PPM_atm and the other shadow function models for Galileo E11 (over 34 penumbra transitions)	105
4.6	The penumbra entry/exit time (in GPS time, time format: Y/M/D:h:m:s) for Galileo E11 from 6th to 15th January, 2015.	108
5.1	The basic geometry and optical parameters for Galileo IOV satellite [ν : reflectivity, μ : specularity]	118
5.2	The basic geometry and optical parameters for Galileo FOC satellite [ν : reflectivity, μ : specularity]	118
5.3	The mass and COM of Galileo IOV and FOC satellites	119
5.4	The definition of local body frame and AABB for all the primitives	121
5.5	The error statistics for different pixel spacings. unit: $[\text{nm} \cdot \text{s}^{-2}]$	132

LIST OF TABLES

5.6	The speedup test for Galileo IOV and FOC satellite bus	135
5.7	The covariances of resultant force for the Galileo IOV and FOC satellites ($\delta = 0.1$), unit: $\text{nm} \cdot \text{m}^{-2}$	137
5.8	The covariances of resultant force for the Galileo IOV and FOC satellites (pixel size: 1 cm). unit: $\text{nm} \cdot \text{m}^{-2}$	137
5.9	The parameters in generating the grid files	140
5.10	The statistics of the differences for 10,000 samples, unit: $[\text{nm} \cdot \text{s}^{-2}]$. . .	143
6.1	The parameters used for the box-wing model	152
6.2	The parameters for the first try of parameterization of the box-wing model	154
6.3	The parameters for the second try of parameterization of the box-wing model	154
6.4	This definitions of parameters “Q”	155
6.5	The values of “Q” parameters in Eq. 6.21 for Galileo satellites. unit: $[\text{m}^2]$	156
6.6	The statistics of the fitting RMS of ECOM-1, ECOM-2 and DREMT for IOV and FOC satellites over all the Sun elevations. unit: $[\text{nm} \cdot \text{s}^{-2}]$. . .	160
6.7	The statistics of the fitting RMS of ECOM-1, ECOM-2 and DREMT for IOV and FOC satellites over all the Sun elevations with additional acceleration in x and z axes. unit: $[\text{nm} \cdot \text{s}^{-2}]$	161
6.8	The statistics of the fitting RMS of ECOM-1, ECOM-2 and DREMT with the ray tracing model for Galileo satellites over all the Sun elevations. unit: $[\text{nm} \cdot \text{s}^{-2}]$	163
7.1	The strategy of CODE MGEX orbit solution	168
7.2	The list of the IOV and FOC satellites available in 2016	169
7.3	The satellite information in shadow function tests	179
7.4	The average RMS in radial orbit error over 7 days’ orbit prediction with the SECM, the PPM and the PPM_atm [m]	179
7.5	The average RMS of 24-hour orbit prediction with the force models (SRP+TRR+ERP+ANT) for the year 2016 [m]	181
7.6	The average RMS (non-eclipse) in radial, along, cross track and the SISRE_orb of all the chosen satellites for a 7-day orbit prediction. unit: [m]	184
7.7	The average RMS (during eclipses) in radial, along, cross track and the SISRE_orb of all the chosen satellites for a 7-day orbit prediction. unit: [m]	185
7.8	The information on <i>a priori</i> models used in this section	187
7.9	The average RMS (during non-eclipses) in radial, along, cross track and the SISRE_orb of all the chosen satellites for a 7-day orbit prediction with <i>a priori</i> models. unit: [m]	188
7.10	The average RMS (during eclipses) in radial, along, cross track and the SISRE_orb of all the chosen satellites for a 7-day orbit prediction with <i>a priori</i> models. unit: [m]	189

LIST OF TABLES

7.11 The average and standard deviation of each parameter in ECOM-1, ECOM-2 and DREMT. unit: [nm · s ⁻²]	192
7.12 The magnitude of each physical effect and their RMS in 24-hour orbit prediction.	195

Nomenclature

List of acronyms and abbreviations

AABB	Axis aligned Bounding Box
AC	Analysis Centre
ANT	Antenna Thrust
BDS	Beidou satellite navigation system
BFS	Body Fixed System
BVH	Bounding Volume Hierarchy
CODE	Centre for Orbit Determination in Europe
CPU	Central Processing Unit
ECEF	Earth-Centred Earth-Fixed
ECI	Earth-Centred Inertial
ECOM	Extended CODE Orbit Model
EGM08	Earth Gravity Model 2008
EOP	Earth Orientation Parameter
ERP	Earth Radiation Pressure
ESA	European Space Agency
ESOC	European Space Operations Centre
FOC	Galileo Full Operation Capability
GEO	Geosynchronous Orbit
GFZ	German Research Centre for Geosciences
GLONASS	GLObalnaya NAvigatsionnaya Sputnikovaya Sistema
GNSS	Global Navigation Satellite System
GPS	Global Positioning System
GPST	GPS Time
GPU	Graphics Processing Unit
GR	General Relativity
GRACE	Gravity Recovery and Climate Experiment
GSPM	GPS Solar Pressure Model
IERS	International Earth Rotation Service
IGR	IGS Rapid
IGS	International GNSS Service
IGSO	Inclined Geosynchronous Orbit

Nomenclature

IGU	IGS Ultra-rapid
IOV	Galileo In-Orbit Validation
JPL	Jet Propulsion Laboratory
LBS	Local Body System for each primitive
LLA	Laser Retroreflector Array
LW	Longwave Earth radiation flux
MEO	Medium Earth Orbit
MGEX	Multi-GNSS experiment and Pilot Project
MIT	Massachusetts Institute of Technology
MJD	Modified Julian Date
NASA	National Aeronautics and Space Administration (USA)
NGS	National Geodetic Survey
PPM	Perspective Projection Based shadow function model
PPM_atm	Perspective Projection Based shadow function model with atmospheric effect
PPP	Precise Point Positioning
PRN	Pseudo-Random Noise
QZSS	Quasi-Zenith Satellite System
RMS	Root Mean Square
SADM	Solar Array Drive Mechanism
SECM	Spherical Earth Conical shadow function Model
SISRE	Signal In Space Ranging Error
SLR	Satellite Laser Ranging
SP3	Standard Product (Orbits and Clocks) 3
SP3c	Extended Standard Product 3
SRP	Solar Radiation Pressure
SVN	Space Vehicle Number
SW	Shortwave Earth radiation flux
TAI	International Atomic Time
TOA	Top Of Atmosphere
TRR	Thermal Re-radiation Pressure
TSI	Total Solar Irradiance
TT	Terrestrial Time
TTFF	Time-To-First-Fix
UCL	University College London
UERE	User Equivalent Range Error
USN/USNO	United State Naval Observatory
UTC	Coordinated Universal Time
WGS84	World Geodetic System 1984
WHU	Wuhan University

List of symbols

AU	Astronomical Unit, 149597870.700 km
c	The light speed, 299792458 m · s ⁻¹
E_s	The Total Solar Irradiance, 1361 W · m ⁻²
\mathbf{W}_s	The solar radiation flux at a satellite's location
\mathbf{W}_e	The Earth radiation flux at a satellite's location
F_s	The shadow function
$F_{s,\text{acc}}$	The shadow function derived from GRACE accelerometer observations
\mathbf{r}	The position of the satellite
\mathbf{r}_\odot	The position of the Sun
φ	The latitude of Sun in satellite Body Fixed Frame
λ	The longitude of Sun in satellite Body Fixed Frame
ε	The angle between Earth, satellite and the Sun
Δu	The orbital angle of the satellite in the orbital plane
β	The Sun elevation over orbital plane
$\mathbf{F}_{p,s}$	The direct solar radiation pressure on solar panels
$\mathbf{F}_{p,e}$	The direct Earth radiation pressure on solar panels
\mathbf{W}_a	The transmit power of navigation antenna
$\text{SISRE}_{\text{orb}}$	The orbit contribution to SISRE

Chapter 1

Introduction

The work presented in this thesis addresses aspects of radiation pressure modelling in the field of GNSS (Global Navigation Satellite System). Radiation pressure modelling for GNSS satellites is broken down into radiation flux modelling and the interaction between the satellite surface and the radiation flux. For GNSS applications that need high accuracy in the satellites' orbit, the forces acting on the satellite need to be known accurately. Radiation pressure as the largest non-gravitational force acting on GNSS satellites is a major issue in orbit modelling.

In this chapter, first, the development of GNSS and its applications are introduced to address how radiation pressure modelling can fit in the context of its applications. Then, a general concept of radiation pressure modelling is formed by introducing its elements. The objectives and the methodology are presented to tackle the issues in radiation pressure modelling for GNSS satellites. An outline of the following chapters of the thesis follows.

1.1 Background

1.1.1 Introduction to GNSS

GNSS is a system that can provide positioning and timing services through ranging from a receiver to the satellites [Teunissen and Montenbruck, 2017]. Generally, a GNSS has three segments: the space segment, the ground segment and the user segment. The space segment mainly refers to a constellation of satellites. Each of the satellites can transmit signals that contain the range measurements information. The ground segment includes the globally distributed monitoring stations to monitor the working status of each satellite. One of the monitoring stations is acted as the master station, which will compute the positions and clock errors (offset of its local clock from the GNSS system time) of each satellite, then inject these information into the satellites. The user segment is composed of the receivers. The end users can get their positions and time by receiving the signals from the satellites.

Currently, there are four GNSSs: American GPS, European Galileo, Russian GLONASS and Chinese BeiDou. American GPS and Russian GLONASS were devel-

1. INTRODUCTION

oped and became fully operational contemporaneously in the 1990s. BeiDou and Galileo will both become fully operational in 2020. The constellation of GPS is composed of 24 satellites that are evenly distributed in 6 orbital planes [National Coordination Office for Space-Based Positioning Navigation And Timing, 2018]. GLONASS constellation is composed of 24 satellites that are evenly distributed in 3 orbital planes [Information and Analysis Center for Positioning Naviagation and Timing, 2018]. Galileo system contains 30 satellites (24 in full service and 6 spares) which are distributed in 3 orbital planes [European Global Navigation Satellite Systems Agency, 2018]. All the satellites of these 3 systems are in MEO (Medium Earth Orbit). BeiDou is the only one among these 4 GNSSs that has 3 types of orbit. Currently, the second generation of BeiDou has 5 GEO (Geosynchronous Orbit) satellites, 5 IGSO (Inclined Geosynchronous orbit) satellites and 4 MEO satellites. In 2020, it will evolve into the third generation, which contains 5 GEO satellites, 3 IGSO satellite and 27 MEO satellites [China Satellite Navigation Office, 2018]. Along with the regional navigation satellite system such as the Japanese QZSS (Quasi-Zenith Satellite System) and Indian IRNSS (Indian Regional Navigation Satellite System), the total number of navigation satellites is over 100.

Satellite navigation plays more and more important roles in the development of economic and social applications. GNSS has very wide applications in many fields. It has been used in supporting critical infrastructures such as telecommunications and the power supply of many countries. European Global Navigation Satellite Systems Agency [2017b] publishes the GNSS market report every two years, with the latest edition released in 2017. It's reported that the global installed base is forecasted to increase from 5.8 bln GNSS devices in use in 2017 to almost 8 bln (an estimate of more than one device per person on the planet) in 2020 , where smartphones account for almost 80% of the global installed base of GNSS devices. In 2017's report, the applications are mainly listed in the field of LBS (Location Based Services), road, aviation, maritime, agriculture, and surveying. The fact that smartphones are the most popular platform to support mobile LBS makes the LBS applications have the largest percentage of the global installed base. Road applications follow LBS as distant second, with 380 mln devices in use in 2017. Especially, GNSS receivers as one type of sensors in autonomous driving can provide reliable and accurate positioning. The development of autonomous driving will evidently bring more users to the GNSS.

Except for the engineering applications in mass markets, GNSS also has a wide range of applications in science. In geodesy, GNSS technology is used to maintain the ITRF (International Terrestrial Reference Frame), which provides a set of coordinates of some points located on the Earth's surface. The ITRF is extensively used in the research of plate tectonics, regional subsidence or loading [Altamimi et al., 2001]. In the recent years, on-board GNSS receivers on LEO (Low Earth Orbit) spacecraft is used to precisely determine the positions of LEO satellites [Jaeggi et al., 2010; Kang et al., 2006; Peter et al., 2017]. GNSS observations are also used to monitor and model the distribution of TEC (Total Electron Content) in the ionosphere [Ren et al., 2016; Schaer, 1996]. Specifically, two Galileo satellites were launched into highly eccentric

1. INTRODUCTION

orbit due to a technical issue, however, these two satellites in eccentric orbit provide good platform to test the gravitational red-shift [Delva and Puchades, 2017] using its high-performance atomic clocks.

However, all the GNSS applications require the GNSS itself to be stable and of high accuracy both in its orbit and clock errors. This study addresses the orbit part and take the Galileo satellites as a demonstration. The improved force modelling techniques will help to improve the quality of the Galileo satellites' orbit, which will benefit all the applications.

1.1.2 Satellites' orbit and forces acting on a satellite

The state of motion (position and velocity) of a satellite in space can be described by a set of Cartesian coordinates or 6 Keplerian elements. These two forms can be converted to each other. The conversion between the Cartesian coordinates and the 6 Keplerian elements can be found in Montenbruck and Gill [2005].

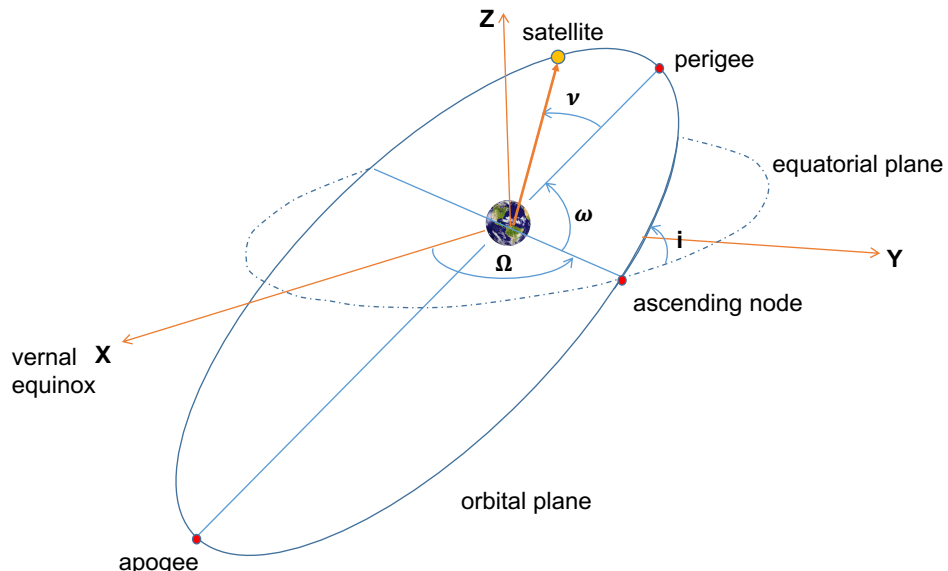


Figure 1.1: The description of a satellite's position using Keplerian elements (the semi-major axis and eccentricity are not shown)

Figure 1.1 shows the definition of the Keplerian elements. The size and shape of a satellite's orbit are determined by the semi-major axis a and eccentricity e . The orientation of the orbital plane is determined by the inclination i and the longitude of the ascending node Ω . The argument of perigee ω defines the orientation of the ellipse in the orbital plane. The true anomaly ν describes the position of the satellite in orbital plane. The sum of true anomaly and the argument of perigee is also called argument of latitude, i.e. $u = \nu + \omega$.

When a GNSS satellite is moving in space, the largest force acting on the satellite is the Earth gravitational force. At an altitude of around 22,000 km (in MEO), the acceleration due to Earth gravitational force is around $0.5 \text{ m} \cdot \text{s}^{-2}$. Also, the gravitational forces from some celestial bodies such as the moon, and the Sun are considerable and

1. INTRODUCTION

are at a magnitude of $10^{-5} \text{ m} \cdot \text{s}^{-2}$. In addition, the gravitational forces from the moon and the Sun are also acting on the body of the Earth and thus cause a time-varying deformation on the Earth (including the solid Earth tide and ocean tide). As a consequence, the gravitational force on a satellite exhibits small periodic variations, which can affect the motion of satellite. The amplitude of the ocean tides are about one order of magnitude smaller than that of solid Earth tides [Montenbruck and Gill, 2005]. A rigorous description of a satellite's motion should be using the theory of general relativity. In practice, Newtonian equations with relativistic corrections (in magnitude of $10^{-10} \text{ m} \cdot \text{s}^{-2}$) are used to describe the satellites' motion.

Except for the above gravitational forces, there are also non-gravitational forces acting on GNSS satellites. Most GNSS satellites are in MEO or higher orbit, the atmospheric drag is negligible. Thus, the largest non-gravitational force is the radiation force, which is the focus of this study. The modelling of radiation pressure forces includes the modelling of radiation flux and how the radiation flux interacts with the satellite surface. The concepts of radiation pressure modelling in context are explained in the following sections.

1.2 An overview of the relevant aspects in radiation pressure modelling

1.2.1 The attitude of the Galileo satellites

The attitude of a GNSS satellite is the pointing of BFS (Body Fixed System) in space. GNSS satellites are designed for navigation mission. Thus, they have a specific attitude law to control the satellites' attitude in space. The principles are as follows:

- The solar panels are perpendicular to the Sun to collect as much energy as possible.
- The navigation antenna boresight has to point to the Earth in order to transmit navigation signals.

The navigation antenna of Galileo satellites are mounted at their $+z$ panel of the satellite body. Thus, the positive z-axis of the satellite body fixed frame is pointing from the satellite to the centre of Earth. The solar panels are mounted at the y panel of the satellite body. The solar panels have to be perpendicular to the Sun and the y -axis is perpendicular to the z -axis. The pointing of the y -axis is computed by cross product of the z pointing vector and the satellite-sun vector. The above description is the definition of the so-called nominal attitude as shown in Fig. 1.2. The unit vectors

1. INTRODUCTION

of the three axes of the body fixed frame are computed:

$$\begin{aligned}\mathbf{e}_z &= -\frac{\mathbf{r}}{\|\mathbf{r}\|} \\ \mathbf{e}_y &= \frac{\mathbf{e}_s \times \mathbf{e}_z}{\|\mathbf{e}_s \times \mathbf{e}_z\|} \\ \mathbf{e}_x &= \mathbf{e}_y \times \mathbf{e}_z\end{aligned}\quad (1.1)$$

where \mathbf{r} is the position of the satellite, \mathbf{r}_\odot is the position of the Sun, $\mathbf{e}_s = \mathbf{r}_\odot - \mathbf{r}$.

Under the nominal attitude, the satellite-sun vector always lie in the xz plane of the BFS. This statement is important and will be used in the development of the new empirical model in chapter 6. A brief proof is given as follows:

$$\because \mathbf{e}_s \cdot \mathbf{e}_y = 0 \text{ and } \mathbf{e}_x \cdot \mathbf{e}_y = 0$$

$$\therefore \mathbf{e}_y \perp \text{plane A which is composed by } \mathbf{e}_s \text{ and } \mathbf{e}_x.$$

$$\because \mathbf{e}_s \cdot \mathbf{e}_y = 0 \text{ and } \mathbf{e}_z \cdot \mathbf{e}_y = 0$$

$$\therefore \mathbf{e}_y \perp \text{plane B which is composed by } \mathbf{e}_s \text{ and } \mathbf{e}_z.$$

\therefore plane A and plane B are exactly the same, which means \mathbf{e}_s is in the plane xz.

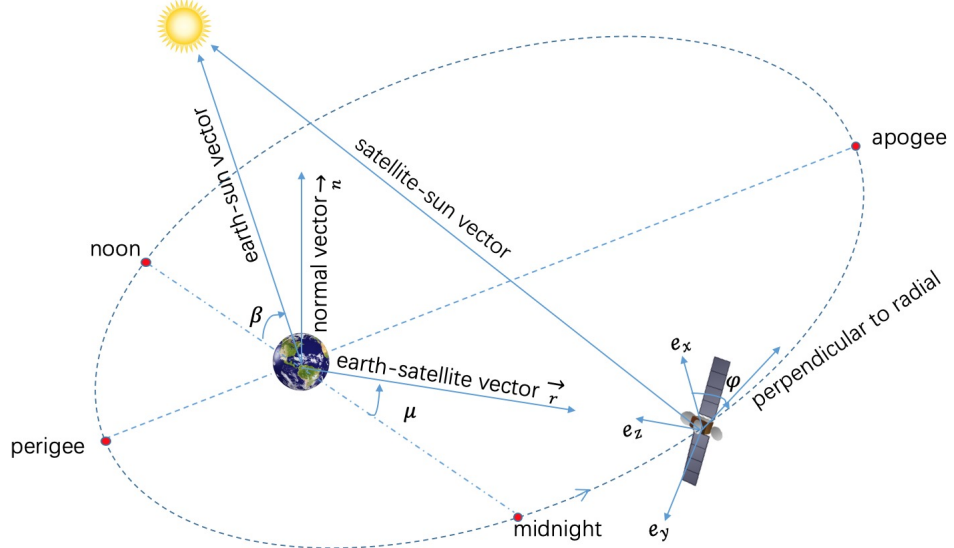


Figure 1.2: The description of a Galileo satellite's attitude. φ is the yaw angle and β is the sun elevation over orbital plane.

However, when the Galileo satellites are in eclipse seasons, the nominal attitude can not be kept due to the limits of hardware (the maximum angular velocity of momentum wheels). The details about the attitude of Galileo satellites in eclipse are not made public. Thus, in this study, all the data processing is under the nominal attitude assumption.

1.2.2 The elements of radiation pressure modelling

Broadly speaking, the elements of radiation pressure modelling mainly include the radiation flux modelling, and how the radiation flux interacts with the satellite surface.

1. INTRODUCTION

Radiation flux is a measure of the amount of radiant energy an object receives from a given source. It is described in the unit of $\text{W} \cdot \text{m}^{-2}$.

In terms of the radiation flux modelling, there are four radiation flux sources for the GNSS satellites: the solar radiation flux, the Earth radiation flux and the thermal radiation flux and the antenna transmit power. The thermal radiation flux is in two parts: one is from the re-radiation of the absorbed solar radiation and Earth radiation, the second part is from the heat generated inside the satellite bus and dumped as thermal energy through radiators on the surface of the satellite bus. In addition, when the satellite goes into eclipse, the solar radiation at the satellite's location will be reduced due to part or all of the solar disk is blocked by the Earth. There is a shadow function to describe the ratio of the solar radiation flux at eclipse to that outside of the eclipse. The radiation flux modelling is discussed in chapter 3. The shadow function modelling is discussed in chapter 4.

In terms of the interactions between the radiation flux and the satellite surface, the calculation for the solar panels and the satellite bus are separated. The solar panels are in a relatively simple shape and they are perpendicular to the Sun under nominal attitude. These two characteristics will make the radiation pressure modelling of the solar panels much simpler than that of the satellite bus. Due to the complex shape of the satellite bus, a ray tracing approach is adopted to deal with the interactions between the radiation flux and the surface of the satellite bus. In this process, the incident radiation flux is simulated by a pixel array, where each ray starts from the pixel. Once the intersections between the incident rays and the satellite bus are computed, the radiation force at each intersection can be computed. The total radiation force is the sum of all the forces at each intersection. In addition, the specular reflected rays are treated as new incident rays but with a reduced intensity to deal with the multiple reflections. The details of this approach will be discussed in chapter 5.

Radiation forces are usually separated according to the radiation sources in the past research. As a consequence, the solar radiation can directly generate the direct solar radiation pressure (SRP), the Earth radiation can directly produce the direct Earth radiation pressure (ERP), the re-radiation of the absorbed solar radiation and Earth radiation will generate the Thermal Re-radiation pressure (TRR), the recoil of the transmitted radiation of the navigation antenna can produce the so-called Antenna Thrust (AT). However, this thesis is organised naturally according to the elements of radiation pressure (i.e. the radiation flux modelling and the interaction between radiation flux and the satellite surface). In this way, it not only provides a better way to understand the physics naturally but also pave a way to integrate all the possible radiation force modelling into one.

However, the above physics based modelling approaches need the inputs to be of high accuracy. The inaccurate inputs such as the surface optical properties, the satellite geometry model and the incident radiation flux will result in errors in the radiation force models. There is a need for an empirical model to absorb the un-modelled radiation forces. The development of the empirical model is discussed in chapter 6.

1. INTRODUCTION

1.3 Objectives and methodology

A statement of the general objective of this research is presented in Subsection 1.3.1. It is broken down into detailed objectives which are described in the following subsection.

1.3.1 Statement of the general objective

The main task of this study is to improve the quality of predicted orbit of Galileo satellites. This task requires to develop a package of force models that accurately describe the motion of Galileo satellites in space. These force models can be used both in the precise orbit determination and orbit prediction of Galileo satellites, and will contribute to improving the accuracy of broadcast ephemeris.

In a general sense, for Galileo satellites, a perturbation acceleration in the radial direction at a magnitude of $0.1 \text{ nm} \cdot \text{s}^{-2}$ can lead to orbit errors of 8 cm after 24 hours, while a radial acceleration at a magnitude of $0.01 \text{ nm} \cdot \text{s}^{-2}$ can only lead to 1 cm orbit error after 24 hours. Therefore, in the force modelling, any force effects larger than $0.01 \text{ nm} \cdot \text{s}^{-2}$ should be accounted for in this study.

The general objective of this study is to improve the orbit prediction of Galileo satellites. This includes physically modelling radiation forces acting on the satellite and an empirical model to absorb the residual force effects.

1.3.2 Statement of the detailed objectives

In this section, the detailed objectives of this research are outlined. These are research tasks, designed with the general objective in mind, and these include:

- Earth radiation flux modelling based on the CERES Earth flux measurements.
- Shadow function modelling to scale the solar radiation flux when a satellite is in eclipse
- A fast ray tracing approach to deal with the interactions between radiation flux and the satellite surfaces
- An empirical model to absorb the un-modelled radiation force effects
- Orbit prediction performance tests of the empirical models and the developed physical models

1.3.3 Methodology

In this section, the methodology for the implementation of each detailed objective in Subsection 1.3.2 are presented.

- **Earth radiation flux modelling**

1. INTRODUCTION

The distribution of Earth radiation flux has both temporal and spatial variations [Knocke, 1989]. The Earth radiation flux as a very important parameter in the research of weather and the Earth's energy balance has been monitored for many years. These monitoring data are a good source for Earth radiation flux modelling. In this study, the measurements of Earth radiation flux at TOA ¹ (Top Of Atmosphere) from the CERES (Cloud and Earth's Radiant Energy System) are used. These data are in grid files including both the longwave (LW) and shortwave (SW) components. The spatial resolution of the grid files is 1 ° in both latitude and longitude.

To calculate the Earth radiation flux at a satellite's location, the visible area for that satellite has to be worked out. Thus, each of the cell in the grid has to be checked to see if it is visible to the satellite. It is a slow process to check 64800 (360 in longitude and 180 in latitude) cells for one grid file. In this study, the spherical surface of the TOA is divided into different levels of triangles where each side of the triangle is a great circle arc. The level 0 subdivision is made of 8 triangles, as the level goes higher, the number of the triangles gets larger. The number of the triangles at level n is 8×4^n . Then, the Earth radiation flux for each of the triangle is calculated according to the CERES grid files. Lower level division has lower accuracy but runs faster. Higher level division has higher accuracy but runs slower. In this way, the Earth radiation flux model becomes configurable both in accuracy and runtime for different satellites.

- **Shadow function modelling during eclipse**

When a satellite goes into eclipse caused by the ellipsoidal Earth, the solar radiation at the satellite's location is reduced according to how much of the solar disk is blocked (a geometrical problem). In addition, when the solar radiation goes through the Earth's atmosphere, the solar radiation can be scattered, refracted and absorbed by the Earth's atmosphere, which makes the solar radiation intensity reduced (a physical problem).

In this study, let the viewpoint be satellite's centre of mass and make the satellite look at the centre of the Sun, perspective projection is applied to get images of the Earth and the Sun, which enable the calculation of the overlapping area between the Sun's image and the Earth's image. In this way, the geometrical problem is solved. In terms of the physical problem, an assumption that the solar radiation reduction (due to the atmospheric effects) is reduced linearly from the TOA to the boundary of the solid Earth is used to construct a radiation reduction coefficient within the Earth's atmosphere. A shadow function model (PPM_atm) is constructed by considering both the geometrical problem and the physical problem. In addition, the impact of the shadow function to the satellite's orbit is shown in the orbit prediction.

- **Fast ray tracing approach to deal with the interactions between radiation flux and the satellite surface**

¹According to CERES, the TOA is defined to be 30 km high above the Earth's surface in Earth radiation flux observing.

1. INTRODUCTION

In radiation pressure modelling, one important element is the interaction between radiation flux and the surface of the satellite. It is difficult to model the interaction with an analytical approach due to the complex shape of satellites. The ray tracing approach in radiation pressure modelling proposed by [Ziebart \[2001\]](#) has been successfully applied to many spacecraft. However, this approach is slow in computation to model satellites with complex shape.

Thus, a ray tracing approach using BVH (Bounding Volume Hierarchy) to organise the primitives of satellite 3D geometry is proposed in this study. This application of BVH in ray tracing includes two parts: one is the construction of the BVH with the primitives, the other is the traversal of the BVH to find the intersection between the ray and the satellite surface. Although the BVH structure is widely used in computer graphics, this is the first time to use it in radiation pressure modelling. It can greatly speed the computation of radiation pressure modelling for satellites with complex shape.

Based on the faster ray tracing approach, the magnitude of radiation force due to multiple reflection and the uncertainty in the resultant forces are also analysed.

- Empirical model to absorb the residual force effects**

The physical models developed in this study can not accurately describe all the non-gravitational forces acting on a satellite. There are two reasons: one is that the inputs of physical models maybe inaccurate, the other is that there exist un-modelled force effects. In practice, there need an empirical model to absorb the residual force effects in orbit estimation. Previous approaches such as the GSPM (GPS Solar Pressure Model) for GPS satellites and the widely used ECOM (Extended CODE Orbit Model) are developed using trial-and-error method. Generally, a low degree Fourier's series is used in the orbit estimation, terms are kept if they are good for the estimation and remove the terms that degrade the estimation.

In this study, a new way of developing empirical models is put forward. An analytical formula is deduced based on the box-wing assumption of the satellite's geometry. Then, the parameters in the analytical formula to be estimated are designed by considering both the accuracy of the model and the correlations between parameters. The final form of the empirical model is a compromise between the accuracy and correlation (the correlation between estimated parameters weaken the estimation).

- Orbit prediction performance of the existing empirical models and the physical models**

The empirical models and physical models are tested in orbit fitting and orbit prediction. The magnitude of physical force models are computed for both the Galileo IOV (In Orbit Validation) and FOC (Full Operation Capacity) satellites. Also, the impacts of individual force on the satellites' orbit are assessed in a 24-hour orbit prediction. In terms of the empirical models, a 2-day orbit fitting is carried out and the fit RMS is used as an indicator to assess the quality of the models. The test is in two

1. INTRODUCTION

configurations, i.e. with or without the *a priori* physical models. Then, a 7-day orbit prediction is carried out and the orbit contribution of Signal In Space Ranging Error is used as the principal indicator to assess the quality of orbit prediction.

1.4 Thesis outline

This section gives a brief description of the following chapters of this thesis. Chapter 2 describes the radiation pressure modelling methods in the literature. Chapter 3 presents the radiation flux modelling – which is an important element of radiation pressure modelling. Chapter 4 introduces a shadow function to scale the solar radiation flux during penumbra of the Earth’s eclipse (it is a supplement of solar radiation flux modelling presented in Chapter 3). Chapter 5 describes the interaction between radiation flux and the satellite’s surface which is another important element of radiation pressure modelling. Chapter 6 presents a new physics based empirical modelling approach which is used to construct a new empirical model for the Galileo satellites. Chapter 7 presents the impacts of individual force effects on the orbit of Galileo satellites and the orbit prediction test results with the developed force models (including both the physical models and the empirical models).

Chapter 2

A literature review of radiation pressure modelling

The purpose of this chapter is to provide a literature review of radiation pressure modelling. The history of radiation pressure and the modelling techniques in precise orbit determination is introduced in the first place. A detailed description in the literature of solar radiation pressure modelling, Earth radiation pressure modelling and the shadow function modelling is presented. Some inspirations are generated by reviewing the previous work.

2.1 A review of radiation pressure modelling

2.1.1 The history of radiation pressure modelling

In 1862, James Clerk Maxwell made an assertion that light has the property of momentum and thus it exerts a pressure upon any surface it is exposed to according to his theory of electromagnetism [Maxwell, 1891]. Shortly after Maxwell's prediction, the experiments done by Lebedev [1901], Nichols and Hull [1903; 1902] on measurements of mirror deflection due to incident radiation from a vacuum confirmed the existence of radiation pressure. From then on, radiation pressure had been verified and thus opened a door for many applications and research. It has many applications in physics and biology, such as using radiation pressure to measure high-power laser emission [Williams et al., 2013], using laser radiation pressure to make an optical tweezer [Ashkin, 1980; Moffitt et al., 2008], using laser radiation pressure to cool atoms [Tan et al., 2004; Wineland et al., 1978].

In the field of astrodynamics and geodesy, the radiation pressure from the Sun, the Earth and even satellites themselves is considered as a perturbation force on the satellites' orbit. The first theory on the effects of solar radiation pressure to asteroids's orbit was revealed by an Russian civil engineer Ivan Osipovich Yarkovsky in the year 1901 [Beekman, 2006; Yarkovsky, 1901], which was called "Yarkovsky's effect". This effect describes a tiny thrust on small asteroids caused by the heating of solar radiation

2. A LITERATURE REVIEW OF RADIATION PRESSURE MODELLING

that significantly affects the orbital motion of asteroids [Andrés et al., 2006; Chen et al., 2014; Eugster, 2012; Guo, 2014]. “Yarkovsky’s effect” was first observed by radar ranging at asteroid 6489 Golevka [Chesley et al., 2003].

Humankind entered space age when the first artificial satellite was launched in 1957. The radiation force on artificial satellites was revealed on Echo I (launched in 1960), which was a balloon-based satellite that had a high area-to-mass ratio. Researchers found that the drag force alone could not explain observed variations in the orbital eccentricity [Kozai, 1961; Muhleman et al., 1960; Parkinson et al., 1960; Shapiro and Jones, 1960]. At that time, though radiation pressure was discovered and applied to the motion of artificial satellites, the accuracy of the radiation pressure models were not as high as it is now. The modelling of solar radiation pressure was limited by the orbit accuracy and observation techniques.

The LAGEOS (LAser GEodynamics Satellite) mission launched in 1976 was the first spacecraft dedicated exclusively to high-precision laser ranging and acquired laser-ranging data that were not degraded by errors originating in the satellite orbit [NASA, 1976]. The requirements for the accuracy of radiation pressure models became higher than before. This also stimulate more research on the radiation pressure modelling [Aksnes, 1976; Boulton, 1984; Poliakhova, 1963]. During this period, researchers not only focused on solar radiation pressure modelling, they also did work on Earth radiation pressure modelling [Anselmo et al., 1983; Lautman, 1977; Sehnal, 1969; 1981], atmospheric drag modelling [De Moraes, 1981], and thermal radiation effects [Rubincam, 1988]. Those force models had the ability to compute trajectories of meter level accuracy for an arc length of 30 days for LAGEOS [Smith and Dunn, 1980]. A difference from decades ago was that the accuracy of the radiation pressure models can be validated by the SLR (Satellite Laser Ranging) measurements.

The first launch of GPS (Global Positioning System, originally Navstar GPS) satellite in 1973 opened a new era of satellite navigation. The OCS (Operational Control System) of GPS used radiation pressure models to produce broadcast ephemeris (with an accuracy of several meters) for all GPS satellites. With the development of the Russian GLONASS, Chinese Beidou, and European Galileo, the applications of the GNSS (Global Navigation Satellite System) have been largely extended. The applications such as PPP (Precise Point Positioning), the establishment of the ITRF (International Terrestrial Reference Frame), monitoring of the volcanoes and crustal deformation need high accuracy of the satellites’ orbit. The requirements in highly accurate orbit are met by highly accurate radiation pressure models. The development of the radiation pressure modelling is tightly linked to the process of orbit determination and prediction. Fliegel et al. [1992] was one of the earliest in the work of GPS satellites radiation pressure modelling [Beutler, 2014]. He mainly worked on GPS Block IIA, Block IIR satellites [Fliegel and Gallini, 1996; Fliegel et al., 2001]. During the 1990s, the modelling technique got improved and there appeared different philosophy on modelling methodology.

2. A LITERATURE REVIEW OF RADIATION PRESSURE MODELLING

2.1.2 The modelling methodology of radiation pressure in precise orbit determination

The orbit accuracy of artificial satellites have been improved from tens of meters at 1950s to cm level today [Vetter, 2007] due to the development in observation techniques and force modelling. As for the radiation pressure modelling for GPS satellites, the dimensions and optical properties of Block I and Block II were used to form the solar radiation pressure models (ROCK42) in [Fliegel et al., 1992]. In the modelling of ROCK42, Fliegel considered the physics of how radiation interacts with the surfaces of the satellite. The methods that consider the physics of radiation pressure are classified to “analytical approach”. The output of the ROCK42 was in the form of Fourier’s series with respect to ε angle (the angle between the satellite, the Earth and the Sun). The ROCK42 model starts from the physical process of radiation pressure but the output was an empirical formula. The “analytical part” of the ROCK42 was mainly extended by [Ziebart, 1998] and the “empirical part” was extended by researchers such as Arnold et al. [2015]; Bar-Sever and Kuang [2004]; Bar-Sever and Russ [1997]; Springer et al. [1999a;b]. In addition, there are also models trying to combine the advantages of both the purely empirical and purely analytical models, which produced the so-called “semi-analytical” models like the adjustable box-wing model [Rodriguez-Solano et al., 2012b] and the cuboid model for Galileo satellites [Montenbruck et al., 2015b]. Thus, the modelling methods diverge into “purely analytical”, “semi-analytical”, and “purely empirical”.

Purely empirical approaches use no *a priori* physical information about the satellite dimensions or the surface material properties. The empirical models are assumed to absorb all the other un-modelled forces in the process of orbit determination. These models usually appear in the form of Fourier’s series truncated at a certain degree (typically consisting of some combination of constant, once-per-revolution and twice-per-revolution trigonometric functions). In those models, the empirical parameters are estimated from the tracking data with varying arc lengths (from a single pass to several years). These models played important roles in the precise orbit determination of GNSS satellites. Generally speaking, the methodology of building empirical models is like this: Construct the initial form of the model using Fourier’s series. Then try the model in orbit determination process. New terms were added when the fit quality was deemed poor and when the post-fit residuals show the presence of missing harmonics. Terms were removed when they appear to be poorly determined or highly correlated with other terms. After some trial and error, the final form of the empirical model can be fixed [Arnold et al., 2015; Bar-Sever and Kuang, 2004; Liu et al., 2016; McMahon and Scheeres, 2014].

The semi-analytical approaches use some knowledge on the shape of satellites. For GNSS satellites, most of them have a pair of “wings” (the solar panels) and a “box” (the satellite bus that contains all the payload). Thus, the current “semi-analytical” models adjust some parameters based on the “box-wing” geometry. However, in the earlier

2. A LITERATURE REVIEW OF RADIATION PRESSURE MODELLING

years, the shape of the satellites was also modelled as a “cannon-ball”. It assumed that the satellite is a sphere and has no attitude characteristics [Kubo-oka and Sengoku, 1999; List et al., 2015]. The “box-wing” model uses 6 rectangular facets and the solar panels to represent the geometry of the satellite. The physics of the radiation pressure is applied to the “box-wing” geometry under certain attitude. The adjustable “box-wing” model estimates some optical properties of the facets through the tracking data [Montenbruck et al., 2015b]. A typical one is the model developed by Rodriguez-Solano et al. [2012b]. What distinguishes the “semi-analytical” from the “empirical” models is that the “semi-analytical” considers some *a priori* information (both satellite geometry and the attitude) in the modelling.

Analytical approaches are characterised by the exploitation of all available data on the satellite, such as the detailed geometry, highly accurate optical properties of the surface materials, accurate attitude, and the telemetry data such as surface temperatures during operating. The analytical approaches rely more upon *a priori* information and less or no tracking data in the modelling process. These approaches give more information on how the photon fluxes interact with the surface physically. However, in the modelling practice, they are also limited by the fidelity of the data sources. In the orbit prediction process, the analytical models are usually used as *a priori* models and some parameters (such as scaling factors) are still to be estimated [Doornbos et al., 2002; García et al., 2016; Tobias and Garcia, 2016].

This section gives a brief description on the radiation pressure methods in the precise orbit determination of GNSS satellites. The details on each of the methods are described in the following sections.

2.2 Modelling methods on solar radiation pressure

2.2.1 The empirical approaches

Empirical approaches for solar radiation pressure are assumed to represent all the unmodelled non-gravitational forces. Solar radiation pressure is the largest among all the other non-gravitational forces acting on GNSS satellites (This is the reason why these models are still called solar radiation pressure modelling). The widely used empirical models in the orbit determination of GNSS satellites are the Extended CODE Orbit Model (ECOM) and the JPL GPS Solar Pressure Model (GSPM).

2.2.1.1 The Extended CODE Orbit Model

The ECOM was originally developed and tested at Centre for Orbit Determination in Europe (CODE), a consortium of Astronomical Institute at the University of Berne (AIUB), the Federal Office of Topography (Switzerland), Institute Géographique National (France) and the Institute für Angewandte Geodäsie (Germany). The first validation of the ECOM was carried by Rothacher et al. [1996]; Springer et al. [1999a].

The ECOM used the ROCK model as *a priori* model and estimate the un-modelled

2. A LITERATURE REVIEW OF RADIATION PRESSURE MODELLING

part. The ECOM was expressed in a new frame DYZ. The D component is from the satellite to the Sun (positive towards to the Sun), Y component is along the satellite's solar panel rotation axis. The Z component¹ completes the right-hand system. The angular quantity in the model is the argument of latitude of the satellite. The definition of the DYZ system is shown in Fig. 2.1.

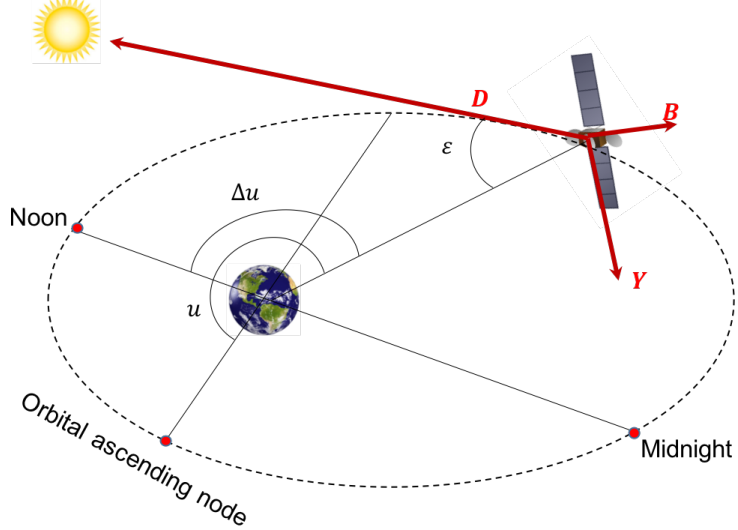


Figure 2.1: The definition of DYZ system to describe the ECOM. The D component is from the satellite to the Sun, the Y is along the solar panel rotation axis and Z component completes a right hand system. The angular argument u in the ECOM is the argument of latitude of the satellite. Angle ε is the angle between the Earth, the satellite and the Sun. Angle Δu is the difference between the argument of latitude of the sun in orbital plane and the argument of latitude of the satellite.

The ECOM has 9 parameters to be estimated from the tracking data. The SRP acceleration \mathbf{a}_{srp} is

$$\mathbf{a}_{srp} = \mathbf{a}_{ROCK} + D(u) \cdot \mathbf{e}_D + Y(u) \cdot \mathbf{e}_Y + B(u) \cdot \mathbf{e}_B \quad (2.1)$$

where

$$D(u) = D_0 + D_c \cdot \cos u + D_s \cdot \sin u$$

$$Y(u) = Y_0 + Y_c \cdot \cos u + Y_s \cdot \sin u$$

$$B(u) = B_0 + B_c \cdot \cos u + B_s \cdot \sin u$$

\mathbf{e}_D is a unit vector in sun-satellite direction.

\mathbf{e}_Y is a unit vector along the satellite's solar panel rotation axis.

$\mathbf{e}_B = \mathbf{e}_Y \times \mathbf{e}_D$.

u is the argument of latitude of the satellite.

\mathbf{a}_{ROCK} is the acceleration computed from the ROCK42 model.

$D_0, D_c, D_s, Y_0, Y_c, Y_s, B_0, B_c$, and B_s are the 9 parameters.

¹In [Beutler et al., 1994], it was described as X. The following development of the ECOM changed it to B. In order to be consistent with the subsequent study, it is described as B.

2. A LITERATURE REVIEW OF RADIATION PRESSURE MODELLING

The full ECOM model (with 9 parameters) was implemented into the Bernese GPS Software. After extensive tests in the orbit determination, a small set of optimal orbit parametrizations was found. In the subsequent developments from Springer et al. [1999b], the number of the parameters to be estimated had been reduced to 5. This is also the so-called reduced ECOM or the “ECOM-1”¹ [Arnold et al., 2015]. The expression of ECOM-1 is

$$\mathbf{a}_{srp} = D_0 \cdot \mathbf{e}_D + Y_0 \cdot \mathbf{e}_Y + B(\Delta u) \cdot \mathbf{e}_B \quad (2.2)$$

where

D_0 is a constant parameter at D component.

Y_0 is a constant parameter at Y component.

$B(\Delta u) = B_0 + B_c \cdot \cos \Delta u + B_s \cdot \sin \Delta u$

D_0, Y_0, B_0, B_c, B_s are the 5 parameters to be estimated.

The ECOM-1 has been used in many IGS analysis centres since 1996. Furthermore, no *a priori* model has been used for the CODE IGS contribution since July 2013. There are two main differences between this ECOM-1 and the ECOM with full parameters.

- **angular parameter**

The 9-parameter ECOM uses the argument of latitude u while ECOM-1 uses Δu (the difference between argument of latitude of the Sun in orbital plane and the argument of latitude of the satellite).

- ***a priori* model**

The 9-parameter ECOM uses *a priori* model while the ECOM-1 can be applied without any *a priori* model with tests on GPS satellites [Springer et al., 1999b].

In 2015, a new solar radiation pressure model (known as “ECOM-2”) for GNSS orbit determination at CODE was put forward [Arnold et al., 2015]. During a rather long time, spurious spectral lines are known to exist in geophysical parameters, in particular in the Earth Orientation Parameters (EOPs) and in the estimated geocentre coordinates, which could be attributed to the ECOM [Arnold et al., 2015]. Under this background, the CODE updated its solar radiation pressure model to cope with the issues. By analysing the orbit determination results and illumination of the Sun on the satellite bus under nominal attitude, Arnold et al. [2015] demonstrated that only even-order short-period harmonic perturbations acting along the D component occur for GPS and GLONASS satellites, and only odd-order perturbation acting along the B component. Based on the above demonstrations, the ECOM-2 is expressed

$$\mathbf{a}_{srp} = D(\Delta u) \cdot \mathbf{e}_D + Y_0 \cdot \mathbf{e}_Y + B(\Delta u) \cdot \mathbf{e}_B \quad (2.3)$$

¹In [Arnold et al., 2015], the ECOM-2 was put forward, thus the previous reduced ECOM is renamed to ECOM-1.

2. A LITERATURE REVIEW OF RADIATION PRESSURE MODELLING

where

$$D(\Delta u) = D_0 + \sum_{i=1}^{n_D} \{D_{2i,c} \cos 2i\Delta u + D_{2i,s} \sin 2i\Delta u\}$$

$$B(\Delta u) = B_0 + \sum_{i=1}^{n_B} \{B_{2i-1,c} \cos(2i-1)\Delta u + B_{2i-1,s} \sin(2i-1)\Delta u\}$$

n_D and n_B are the user-defined upper limits for the degree of the Fourier's series. D_0 , $D_{2i,c}$, $D_{2i,s}$, B_0 , $B_{2i,c}$, and $B_{2i,s}$ are the parameters to be estimated.

The ECOM-2 naturally includes ECOM-1 (it is equivalent to ECOM-1 when $n_D = 0$ and $n_B = 1$). The ECOM-2 considers the variation in the D direction, which is mostly caused by the variation of cross-sectional area between the solar flux and the satellite surface. The test results on Galileo satellites show that ECOM-2 is superior to ECOM-1 in both the solutions of orbit and clocks [Dach et al., 2015].

2.2.1.2 The JPL GSPM model

The JPL GSPM was firstly developed at Jet Propulsion Laboratory, California Institute of Technology. It is an *a priori* empirical model obtained from several years of tracking data [Bar-Sever and Russ, 1997]. The GSPM uses ε (see Fig. 2.1) as the angular parameter in the expansion of truncated Fourier's series. In the orbit determination process, one scaling factor along the satellite to Sun direction and a Y bias (it is similar as Y_0 parameter in the ECOM) are estimated [Bar-Sever and Kuang, 2004; Sibthorpe et al., 2011]. This model has been used operationally at the Jet Propulsion Laboratory's IGS analysis centre.

The JPL GSPM was developed for different Blocks of GPS satellites at different years, thus, it had different versions. The first version of the GSPM was developed for GPS Block IIA satellites and was named GSPM.II.97. This model was expressed in a coordinate system called UVW. It is described as follows [Bar-Sever and Russ, 1997]:

- \mathbf{U} is pointing along the Sun-satellite direction.
- \mathbf{V} is pointing along the y-axis of the BFS.
- \mathbf{W} completes the right-hand system.

The above definition of the UVW system is consistent with the DYB system used in the ECOM. It is still described as UVW in order to distinguish it from the ECOM. The GSPM.II.97 is expressed as follows:

$$F_u = f(m, r_\odot) s (C_{U_0} + C_{U_1} \cos \varepsilon + S_{U_1} \sin \varepsilon + C_{U_2} \cos 2\varepsilon + S_{U_2} \sin 2\varepsilon)$$

$$F_v = C_{V_0} + C_{V_1} \cos \varepsilon + S_{V_1} \sin \varepsilon \quad (2.4)$$

$$F_w = f(m, r_\odot) s (C_{W_1} \cos \varepsilon + S_{W_1} \sin \varepsilon + C_{W_2} \cos 2\varepsilon + S_{W_2} \sin 2\varepsilon)$$

where

$f(m, r_\odot) = \frac{\text{AU}^2}{mr_\odot^2}$ is a function of the satellite's mass m and distance from the Sun to

2. A LITERATURE REVIEW OF RADIATION PRESSURE MODELLING

the satellite r_{\odot} .

s is an overall scale factor that is set to 1 during the estimation of the model parameters. C_{U_0} , C_{U_1} , S_{U_1} , C_{U_2} , S_{U_2} , C_{V_0} , C_{V_1} , S_{V_1} , C_{W_1} , S_{W_1} , C_{W_2} , and S_{W_2} are the parameters to be estimated from the tracking data.

[Bar-Sever and Kuang \[2004\]](#) came up with a new version of the GSPM (GSPM.04). GSPM.04 is expressed in the satellite Body Fixed Frame, which is different from the GSPM.II.97. The GSPM.04 still uses ε as the angular parameter and is obtained based on 4.5 years of tracking data (from Jan 1998 to June 2002) [[Bar-Sever and Kuang, 2004; 2005](#)]. The GSPM.04 is expressed as follows:

$$\begin{aligned} F_x &= 10^{-5} s \frac{\text{AU}^2}{mr_{\odot}^2} (S_{X_1} \sin \varepsilon + S_{X_2} \sin 2\varepsilon + S_{X_3} \sin 3\varepsilon + S_{X_5} \sin 5\varepsilon + S_{X_7} \sin 7\varepsilon) \\ F_y &= C_{Y_0} + 10^{-5} \frac{\text{AU}^2}{mr_{\odot}^2} (C_{Y_1} \cos \varepsilon + C_{Y_2} \cos 2\varepsilon) \\ F_z &= 10^{-5} s \frac{\text{AU}^2}{mr_{\odot}^2} (C_{Z_1} \cos \varepsilon + C_{Z_3} \cos 3\varepsilon + C_{Z_5} \cos 5\varepsilon) \end{aligned} \quad (2.5)$$

where F_x , F_y , and F_z are the modelled accelerations along BFS x, y, and z axes respectively.

r_{\odot} is the distance from the Sun to the satellite.

m is the mass of the satellite.

s is a overall scaling factor.

S_{X_1} , S_{X_2} , S_{X_3} , S_{X_5} , S_{X_7} , C_{Y_0} , C_{Y_1} , C_{Y_2} , C_{Z_1} , C_{Z_3} , and C_{Z_5} are the parameters to be estimated.

The GSPM is still being updated. [Sibthorpe et al. \[2010\]](#) used 13.5 years (Jan 1997 - May 2010) of precise orbits to generate the GSPM for Block IIA, IIR, IIR-M. This version of the GSPM is called GSPM10. Tests results from [Sibthorpe et al. \[2010\]](#) showed that the GSPM10 is superior over GSPM04 in the fix rate of ambiguities in carrier phase data, the orbit overlaps, and orbit prediction. [Sibois et al. \[2014\]](#) came up with the GSPM13 based on over 20 years of orbit solutions. This GSPM13 is used as a priori model in JPL's IGS analysis centre contribution to the IGS 2nd reprocessing effort. Although the GSPM evolves and more data is used to build the model, the basic formula still keeps the same as that in [[Bar-Sever and Kuang, 2004](#)].

2.2.2 The semi-analytical approaches

The semi-analytical approaches consider some knowledge of the satellites' *a priori* information and estimate several parameters (the number of the estimated parameters is as small as possible) in the model. The typical methods applied to GNSS satellites are the adjustable box-wing model in [Rodriguez-Solano et al. \[2012b\]](#) and the cuboid box model for Galileo satellites in [Montenbruck et al. \[2015b\]](#). Both adjustable box-wing model and the cuboid box model applied simple geometry of the satellite, the differences lie in the parameterization of the model (i.e. how to design the parameters estimated from the tracking data).

2. A LITERATURE REVIEW OF RADIATION PRESSURE MODELLING

2.2.2.1 The adjustable box-wing model

The adjustable box-wing model is built based on the physics of radiation pressure and the box-wing geometry of the satellite. Firstly, an analytical box-wing model has been derived based on the physical interaction between the direct solar radiation and a satellite consisting of a bus (box shape) and solar panels. Then, some optical properties of the corresponding satellite surfaces are adjusted to fit the GNSS tracking data [Rodriguez-Solano et al., 2012b].

This is an intermediate approach between the purely analytical and the purely empirical. In the physics aspect, the adjustable box-wing model assumed that the absorbed radiation is re-radiated immediately back to the space, also the heating and cooling effects are not considered (this assumption is reasonable for materials like Multi-Layer Insulation (MLI) on the satellite bus). Also the self-shadowing effects between the satellite's components are ignored.

Once the formula based on the physics of radiation pressure is built for the box-wing geometry, 9 parameters are estimated including 7 parameters about the optical properties, 1 Y bias parameter and 1 solar panel rotation lag. The 9 parameters are listed as follows:

- SP : solar panel scaling factor ($1 + \rho + \frac{2}{3}\delta$)
- SB : solar panel rotation lag
- Y_0 : Y bias acceleration
- $+XAD$: absorption plus diffusion of $+X$ bus ($\alpha + \delta$)
- $+ZAD$: absorption plus diffusion of $+Z$ bus ($\alpha + \delta$)
- $-ZAD$: absorption plus diffusion of $-Z$ bus ($\alpha + \delta$)
- $+XR$: reflection coefficient of $+X$ bus (ρ)
- $+ZR$: reflection coefficient of $+Z$ bus (ρ)
- $-ZR$: reflection coefficient of $-Z$ bus (ρ)

where α is the fraction of absorbed photons, ρ is the fraction of reflected photons and δ is the specularly fraction of diffusely reflected photons.

The adjustable box-wing model is developed under the nominal attitude. The sun illuminates $+Z$ and $-Z$ panel of the satellite bus alternately. The $+X$ panel of the satellite bus is always illuminated because this model was built for the GPS II/IIA satellites. For Galileo satellites, the $-X$ panel of the satellite is always illuminated. In the orbit estimation process, the 9 parameters were estimated once per day with different constraints: (1) SP , SB , and Y_0 unconstrained; (2) $+XAD$, $+ZAD$, and $-ZAD$ tightly constrained to 0.01 (around 1% of the *a priori* value); and (3) $+XR$, $+ZR$, and $-ZR$ loosely constrained to 0.1 (similar to the *a priori* values). In addition, the

2. A LITERATURE REVIEW OF RADIATION PRESSURE MODELLING

pseudo-stochastic pulses (in velocity) were estimated once per day in the radial, along and cross-track directions with constraints of 10^{-6} , 10^{-6} , and 10^{-9} m/s respectively [Rodriguez-Solano et al., 2012b].

2.2.2.2 The cuboid box model for Galileo satellites

The cuboid box model considers the total solar radiation pressure as the sum of satellite box radiation pressure \mathbf{a}_{box} and the ECOM-1 \mathbf{a}_{emp} [Montenbruck et al., 2015b], i.e.

$$\mathbf{a}_{srp} = \frac{AU^2}{\|\mathbf{r}_\odot\|^2} (\mathbf{a}_{box} + \mathbf{a}_{emp}) \quad (2.6)$$

where \mathbf{r}_\odot is the vector from the satellite to the Sun.

The cuboid box model was built based on the analysis of partials of the clock residuals w.r.t the parameters in ECOM-1 (D_0 , B_0 , B_c , B_s). Based on the analysis, the adopted *a priori* cuboid model was confined to contributions from absorption plus diffuse reflection and ignoring a possible asymmetry of the $\pm z$ faces. The final cuboid model was simplified to only 2 parameters ($a_C^{\alpha\delta}$ and $a_S^{\alpha\delta}$). The D and B component of \mathbf{a}_{box} are expressed:

$$\begin{aligned} a_{box,D} &= -a_C^{\alpha\delta} \left(|\cos \varepsilon| + \sin \varepsilon + \frac{2}{3} \right) - a_S^{\alpha\delta} \left(|\cos \varepsilon| - \sin \varepsilon - \frac{4}{3} \sin^2 \varepsilon + \frac{2}{3} \right) \\ a_{box,B} &= -\frac{4}{3} a_S^{\alpha\delta} \cos \varepsilon \sin \varepsilon \end{aligned} \quad (2.7)$$

where ε is the angle between the Earth, the satellite and the Sun. $a_C^{\alpha\delta}$ is a parameter that is related to the impact of the stretched body of the satellite box, $a_S^{\alpha\delta}$ is a parameter that is related to the impact of the cube part of the satellite box.

The difference between the cuboid model and the adjustable box-wing model is that the cuboid model starts from the analysis of the impacts of solar radiation pressure on the clock residuals, then a simplification (only 2 parameters need to be estimated) of the box model has been made based on the analysis, while the adjustable box-wing model applied the full box-wing model and estimated 9 parameters. The advantage of the cuboid model is that less parameters to estimate may reduce the correlation between the parameters and the orbit state vector (position and velocity).

2.2.3 The analytical approaches

The analytical approaches were the earliest to be developed among the empirical and semi-analytical approaches. This is due to the nature of analytical approaches (they provide a chance to explore the essence of the problem because they are purely physics based). One difference between the analytical and the empirical approaches is that the analytical approaches distinguish solar radiation pressure from Earth radiation pressure, thermal radiation pressure and other indirect radiation pressure.

In the early ages, the analytical approaches are developed for satellites with simple shape (such as the LAGEOS) [Farinella and Vokrouhlicky, 1996; Vokrouhlicky and

2. A LITERATURE REVIEW OF RADIATION PRESSURE MODELLING

Farinella, 1995a; Vokrouhlicky et al., 1993; Vokrouhlický, 1989]. This is due to that simple shape can be integrated analytically for the calculation of solar radiation pressure. With the improvement in the accuracy of the satellite's orbit, the complex shape of the satellites have to be account for in the modelling.

One early research that considered the complex shape of satellites in solar radiation pressure modelling can be found in Chan [1981]. In this paper, the theoretical reasoning for the finite element division of the satellite's surfaces was proposed. However, the practical use of the finite element approach in solar radiation pressure modelling was difficult at that time due to the limitation of computation. In order to cope with the limitation, researchers represented the satellite's geometry with facets, among which, the work from Fliegel et al. [1992] on GPS solar radiation pressure modelling was a case. Later, with the development of computers, researchers started to consider more detailed geometry of the satellite and the approach based on finite element was put into practice. There were two main approaches in the solar radiation pressure modelling using finite element, one is the so called Test Particle Monte Carlo (TPMC) [Fritzsche et al., 1998; Klinkrad and Fritzsche, 1998; Klinkrad et al., 1990; 1991], the other is the ray tracing with a pixel array to simulate the radiation source [Ziebart, 1998; 2001; 2004].

2.2.3.1 The Test Particle Monte Carlo approach

The method from Klinkrad et al. [1990] was implemented into a software system called Analysis of Non-Gravitational Accelerations due to Radiation and Aerodynamics (ANGARA) by Fritzsche et al. [1998]; Klinkrad and Fritzsche [1998]. The ANGARA used the TPMC approach to model aerodynamic drag and lift, direct solar radiation pressure, Earth albedo radiation pressure, and Earth infra-red radiation pressure [Tuer and Springer, 1973].

In ANGARA, the satellite geometry is described by means of a definition language which is compatible with software ESABASE¹. The components of the satellite are described by discretised planar surface elements [Klinkrad et al., 1991]. For a given satellite geometry, the algorithm calculate an appropriate control volume composed of a large number of equal-sized elements (voxels). The space of the satellite's geometry is divided into cells. For each of the voxels, a list of the surfaces with at least one vertex inside the voxel is stored.

The ray is initially launched randomly from a window which is automatically determined according to the satellite geometry. Each voxel is checked for a possible intersection of the ray with an inside surface along its direction of motion. Once a hit is detected, the ray is reflected according to the surface normal, and the ray is traced further till the next hit or the bounding control volume is left [Klinkrad et al.,

¹ESABASE is a software application (and framework) for space environment analyses, which play a vital role in spacecraft mission planning [ESA, 2018]

2. A LITERATURE REVIEW OF RADIATION PRESSURE MODELLING

1991]. The ANGARA has been used to build force models for SEASAT ¹, ERS ² and ENVISAT ³ [Doornbos et al., 2002; Klinkrad et al., 1991].

2.2.3.2 The ray tracing approach

A ray tracing based solar radiation pressure modelling approach was put forward by Ziebart [1998; 2001; 2004] from UCL (University College London). In this approach, the geometry of the satellite is represented by different primitives such as planes, cylinders, spheres, and cones. The radiation source is simulated by a pixel array where rays are launched from the centre of the pixels. The ray tracing approach was used to model direct solar radiation pressure and thermal re-radiation pressure. The output of the model is a lookup table of accelerations with respect to the direction of the radiation source (in the UCL solar radiation pressure software, the direction of the solar radiation source is represented by a pair of latitude and longitude in the body fixed frame of the satellite).

Currently, the ray tracing modelling method has been applied to the solar radiation pressure modelling of GPS Block IIR [Adhya, 2005; Ziebart et al., 2005], JASON ⁴ [Cerri et al., 2010], and the radiation torque modelling of ENVISAT [Virdee, 2016]. The good performance of the UCL model made it one of the standards in precise orbit determination for the Jason series of altimeter missions [Cerri et al., 2010].

The ray tracing approach for solar radiation pressure modelling from Ziebart [1998; 2001; 2004] is different from the Test Particle Monte Carlo approach described in 2.2.3.1 in the representation of the satellite's geometry and the generation of rays. In terms of the representation of the satellite's geometry, the primitive approach can capture the details of curved surfaces better than the tessellation approach in the TPMC, which means the coordinates of the intersections between the rays and the surfaces can have better accuracy. In terms of the generation of the simulated rays, the ray tracing approach uses a pixel array to simulate the radiation source which means the start of each ray is deterministic. The TPMC approach generates the rays randomly from a window which means it is less efficient than the pixel array approach in computation.

2.3 Modelling method of Earth radiation pressure

During the 1980s, almost at the same time when researchers started considering analytical modelling of solar radiation pressure, the work on Earth radiation pressure

¹SEASAT was the first Earth-orbiting satellite designed for remote sensing of the Earth's oceans and had on board the first spaceborne SAR (Synthetic Aperture Radar)

²ESA's two European Remote Sensing (ERS) satellites, ERS-1 and ERS-2, were launched into the same orbit in 1991 and 1995 respectively. Their payloads included a synthetic aperture imaging radar, radar altimeter and instruments to measure ocean surface temperature and wind fields.

³ENVISAT ("Environmental Satellite") is a large inactive Earth-observing satellite which is still in orbit. Operated by the European Space Agency (ESA), it was the world's largest civilian Earth observation satellite.

⁴JASON is a satellite oceanography mission to monitor global ocean circulation, study the ties between the ocean and the atmosphere, improve global climate forecasts and predictions.

2. A LITERATURE REVIEW OF RADIATION PRESSURE MODELLING

modelling was started. Because the magnitude of solar radiation pressure is much larger than that of Earth radiation pressure and the empirical solar radiation pressure models are assumed to absorb all the unmodelled forces, the research on empirical modelling of Earth radiation pressure was rare. For the analytical Earth radiation models, most of the work were tested on the LAGEOS because of its simple shape [Anselmo et al., 1983; Knocke and Ries, 1987; Knocke et al., 1988; Knocke, 1989; Lála, 1990; Lautman, 1977; Rodriguez-Solano et al., 2012a; Sosnica et al., 2013; Vokrouhlicky and Farinella, 1995b].

The two widely used Earth radiation pressure models (both are analytical) are Knocke's model [Knocke and Ries, 1987; Knocke et al., 1988; Knocke, 1989] and the model developed at TUM (Technical University of Munich) by Rodriguez-Solano et al. [2011; 2012a]. The modelling methods of the two models are described in this section.

2.3.1 Knocke's model

Knocke's model was developed and implemented in the UTOPIA (University of Texas Orbit Determination Program). It has been applied to the precise orbit determination of missions like LAGEOS, GEOS-1 and GEOS-2. The mathematical foundation of the Earth radiation pressure modelling was revealed in the PhD thesis of Knocke [1989].

In terms of the Earth radiation flux calculation, the TOA (Top Of Atmosphere) surface is divided into rings which have equal projected attenuated areas [Knocke, 1989]. This can enable the Earth flux calculation for the visible area of the satellite. In the UTOPIA, the number of divided elements for the visible area is 19. Tests indicated that increasing the total number of elements beyond this point does not significantly affect the resulting magnitude [Knocke, 1989]. A latitudinally varying representation of the shortwave and longwave radiation ¹ of the terrestrial sphere was included in Knocke's model. The actual representation of the Earth radiation flux was a 4×4 spherical harmonic expansion in the UTOPIA.

In terms of the satellite's geometry, the calculation formula for sphere-like satellites was used [Knocke, 1989]. As for the satellite in other shapes, an augmentation factor was introduced to deal with the varying cross-section area of the satellite [Knocke, 1989; Lochry, 1966].

Both the Earth radiation flux model and the satellite's geometry model can be improved in the future study.

2.3.2 The TUM model

The TUM model was developed by Rodriguez-Solano et al. [2011; 2012a;c] mainly for GNSS satellites. This model introduced the box-wing geometry of the satellites in the

¹In some literature, the earth radiation is also called albedo radiation, see Rodriguez-Solano et al. [2012a]. To deliver a clear concept, the Earth radiation is divided into longwave part and shortwave part, the longwave part is mainly caused by the thermal emission of the Earth while the shortwave part is mainly caused by reflection of the Earth's atmosphere (the reflection part is the same meaning as the albedo).

2. A LITERATURE REVIEW OF RADIATION PRESSURE MODELLING

modelling. The reflectivity and emissivity coefficients of surface elements of the TOA were obtained from monthly satellite data of NASA's CERES project [CERES, 2017] to construct a sophisticated model of the Earth radiation flux.

Comparing with the Knocke's model, the TUM model is superior both in the satellite's geometry model and the Earth radiation model. The box-wing geometry is more accurate than the cannon-ball geometry in the Knock's model. Due to the introduction of the reflectivity and emissivity data from CERES project, the Earth radiation flux was calculated with two main assumptions [Rodriguez-Solano et al., 2012a]:

- The Earth behaves like a Lambertian sphere. Both the reflection and emission are considered diffusely.
- The global energy is conservative which means all the energy received by the Earth from the Sun must also be totally reflected or emitted.

The TUM model has been used within the IGS in the operation processing as well as for reprocessing.

2.4 Modelling method on shadow function

A shadow function is a ratio in the solar radiation flux at the satellite's location between the penumbra and full phase. When the satellite goes into eclipse seasons, the shadow function has impacts upon the solar radiation pressure acting on the satellites. Conventional approaches to shadow function modelling use a spherical Earth assumption. There are currently two approaches that are widely used: the SECM (Spherical Earth Conical Model) and the CYM (Cylinder Model) Longo and Rickman [1995]; Montenbruck and Gill [2005]; Neta and Vallado [1997]; Vallado [2007]. Their algorithm can be found in textbooks. The most widely used within GNSS community is the SECM. There are also some adjustments on the SECM to make it more accurate. This section will describe both of the CYM and the SECM.

2.4.1 The cylinder model

Cylinder model assumes the Earth is a sphere and the shadow of the Earth in space is a cylinder [Montenbruck and Gill, 2005; Vallado, 2007]. The CYM can not describe the transient state (penumbra) between the full phase and the umbra as shown in Fig. 2.2. In this case, the shadow function becomes a two-valued function, i.e, it is 0 for umbra and 1 for full phase. The simplicity of CYM makes it unable to model the penumbra case. Thus, it is not suitable in the solar radiation pressure modelling during penumbra.

2.4.2 The spherical Earth conical model

The SECM assumes the Earth is a sphere but the shadow of the Earth is a bicone in space. Figure 2.3 shows the projection of the two cones (the two boundaries of the full

2. A LITERATURE REVIEW OF RADIATION PRESSURE MODELLING

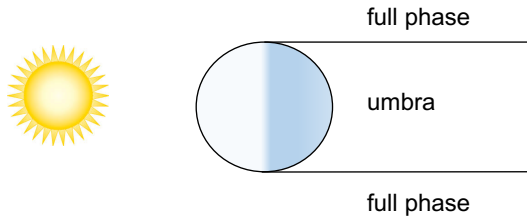


Figure 2.2: The Earth's shadow is in a shape of cylinder, what shows in this figure is the projection of the cylinder onto the plane composed of the centre of the Sun, the centre of the Earth and the satellite centre of mass. In CYM, the space is divided into 2 parts, the space inside the cylinder is in umbra while the space outside the cylinder is in full phase.

phase make one cone and the two boundaries of the penumbra make another cone) on the plane composed of the centre of the Sun, the centre of the Earth and the satellite centre of mass.

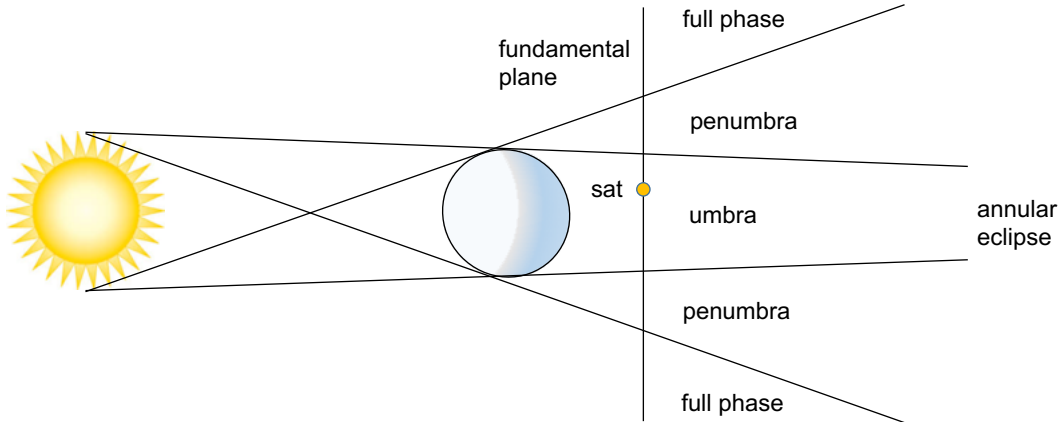


Figure 2.3: The projection of the cones onto the plane composed of the centre of the Sun, the centre of the Earth and the satellite centre of mass. The SECM can distinguish the full phase, penumbra and umbra state. In the calculation of the shadow function values, a fundamental plane is defined to be perpendicular to the shadow axis and goes through the satellite.

The details of modelling approach of the SECM can be found in [Montenbruck and Gill \[2005\]](#). In the method, a fundamental plane is defined to be perpendicular to the shadow axis and passes through the centre of the satellite (see Fig. 2.3). What appear on the fundamental plane are the projections of the Sun and the Earth. If the Earth's oblateness is ignored, their projections are two circles as shown in Fig. 2.4. The overlapping area between the Sun's image and the Earth's image can be computed according to the two circles. The amount of unblocked area of the solar disk is a measure of the shadow function. The shadow function can be calculated by the ratio between the unblocked area of the solar disk over its whole area.

2.4.3 Adjustments to the spherical Earth conical model

The accuracy of the above models can not meet the requirements in applications like long term orbit prediction (long term evolution of the space debris) [[Hubaux et al., 2012](#)] and the non-conservative force modelling in the Earth's gravity field recovery

2. A LITERATURE REVIEW OF RADIATION PRESSURE MODELLING

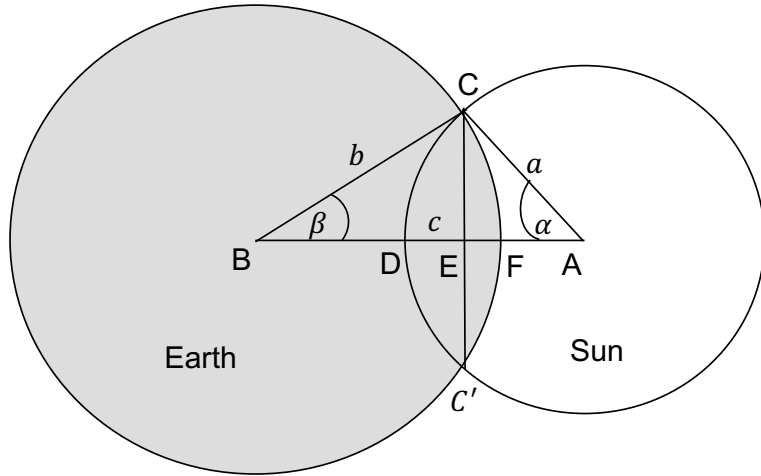


Figure 2.4: The projections of the Earth and the Sun on the fundamental plane. It also shows the how the area of blocked solar disk is calculated.

[Robertson, 2015]. Some adjustments can be applied to the SECM to achieve higher accuracy. The main adjustments are in two aspects: one is to consider the Earth's oblateness; the other is to consider the Earth's atmosphere.

In terms of the Earth's oblateness, there are two ways to deal with. One is to adjust the radius of the sphere according to the position of the satellite so that the spherical surface fits the ellipsoidal Earth locally [Robertson, 2015]. The other is to use an ellipsoidal Earth model in calculation. Adhya et al. [2004] provided an elegant way to test the eclipse state of a satellite (i.e. full phase, penumbra and umbra) using an ellipsoidal Earth. But Adhya et al. [2004] did not provide a way to calculate the shadow function.

In terms of the atmospheric effects to the shadow function, one theory on the shadow function modelling can be found from [Vokrouhlicky et al., 1993; 1994a;b]. In this theory, the atmospheric effects such as atmospheric refraction, absorption and scattering are considered. The atmospheric refraction bends the solar rays and results in a deformation of the solar image as seen from the satellite. The absorption and scattering processes attenuate the radiative intensity of each solar ray crossing the Earth's atmosphere. This model accounts for atmospheric effects using complex physics. However, both the shape of the solid Earth and Earth's atmosphere were modelled as spheres in the model.

2.5 Inspirations from the literature review

The above sections described the principal literature related to the research topics in this study. The literature review not only makes clear of how investigators dealt with the problems in the past but also provides with clues of how to solve the problems in the future. With the development of the orbit determination and the observation techniques, the requirements to accuracy of solar radiation pressure is more and more demanding.

2. A LITERATURE REVIEW OF RADIATION PRESSURE MODELLING

A statement that the analytical approaches will be playing more and more important roles in solar radiation pressure modelling can be given as more reliable information contributes more to the improvements of the modelling. But, the analytical approach has errors due to the un-modelled physical effects and the inaccuracy in the input parameters. Thus, the strategy in this study is trying the best to utilise the available *a priori* information in the analytical approaches, then the residual un-modelled radiation pressure force can be absorbed by the empirical parameters. The details of the above two aspects will be discussed in the following sections.

2.5.1 Maximise the utilisation of *a priori* information

The radiation pressure acting on satellites are mainly the solar radiation pressure, thermal radiation pressure, antenna thrust, and the Earth radiation pressure. Analytical modelling of these forces will need the geometry of the satellites, the optical properties of the surface materials, the radiation flux, and the attitude of the satellites. In addition, during the eclipse seasons, the solar flux will be reduced during penumbra transitions. Thus, an accurate shadow function model is needed to describe the solar flux reduction during penumbra transitions.

In this study, a detailed satellite's geometry model is introduced. The geometry is used both in the solar radiation pressure and Earth radiation pressure modelling with the ray tracing technique. In this process, *a priori* information such as the satellite's geometry, optical properties, attitude are utilised.

In terms of the shadow function modelling, the previous approach either considers the Earth's oblateness or the detailed atmospheric effect in the modelling. None of the literatures considers both the atmospheric effect and the Earth's oblateness in the shadow function. Thus a rigorous modelling approach using perspective projection to account for the Earth's oblateness is put forward in this study. Meanwhile, a simplified atmospheric effect in the solar radiation reduction is applied.

2.5.2 Revisit the empirical representation

Looking over the modelling process of the current purely empirical radiation pressure models, the main characteristic is trial and error. An empirical model is achieved by adding or removing terms in a truncated Fourier's series according to the orbit determination results. The above modelling process is done under the condition that little *a priori* information about the satellite is known.

A question is triggered that how to empirically represent the un-modelled residual after applying the *a priori* radiation pressure models. In this study, some explorations will be done to partly answer the question. The previous experiment and trial approach of building empirical models does not have a clear target, thus a different way of building empirical models is explored. The methodology of the new way is to work out the analytical expressions (all the parameters in these expressions have clear physical meanings) of the radiation pressure forces under some assumptions, then, efforts are

2. A LITERATURE REVIEW OF RADIATION PRESSURE MODELLING

made to reduce the number of parameters and the correlations between the parameters. The final expressions appear to have an empirical looking but every parameter has clear physical meaning.

Chapter 3

Radiation flux modelling

Radiation flux is the amount of power radiated through a given area (in the unit of $\text{W} \cdot \text{m}^{-2}$). Radiation flux is a very important element in radiation pressure modelling because it is strongly related to the magnitude of radiation force. For GNSS satellites, the radiation sources are mainly the Sun, the Earth and the satellite itself (the thermal dump from the satellite's payloads and the absorbed radiation re-radiated as thermal energy). The task of radiation flux modelling is to calculate the radiation flux for the satellite surfaces due to possible radiation sources.

3.1 Solar radiation flux

Solar radiation is the main energy source for Earth orbiters and it also causes the largest radiation force among all the other radiation sources. The intensity of the solar radiation over all wavelengths is represented by the Total Solar Irradiance (TSI), which is the spatially and spectrally integrated radiant power from the Sun at a distance of one Astronomical Unit (AU) [Kopp, 2018]. Figure 3.1 shows the spectrum of solar radiation.

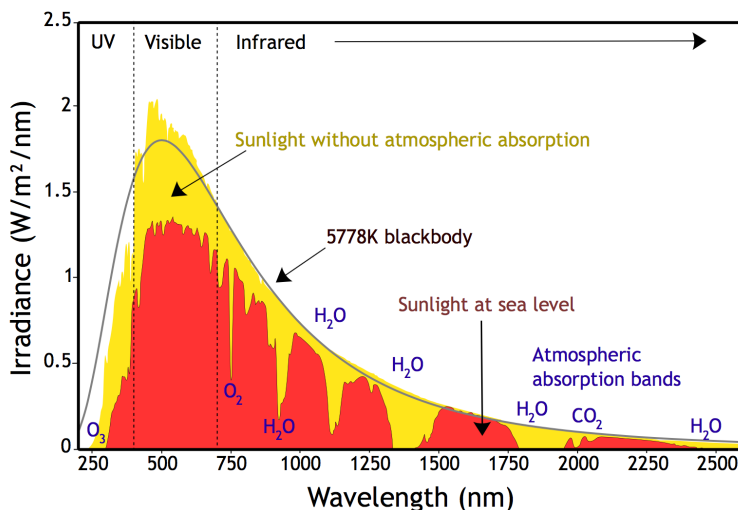


Figure 3.1: The solar radiation spectrum for direct light at both the top of the Earth's atmosphere and at sea level [Nick, 2008].

3. RADIATION FLUX MODELLING

The solar radiation flux modelling includes two parts: one is the modelling of the TSI; the other is the solar radiation flux at a satellite's location. The following sections will discuss both of them.

3.1.1 Total Solar Irradiance

The TSI is a key parameter in the climate research because it is a component of the Earth radiation budget [Mendoza, 2005]. Thus, it has been measured by a mature community of scientists over many years. The primary contribution in TSI measurement is from the Solar Radiation and Climate Experiment (SORCE) project. The SORCE spacecraft (see Fig. 3.2) with radiometers to measure the precise solar radiation was launched into an orbit with inclination 40° , altitude 645 km on January 25, 2003 and is operated by the Laboratory for Atmospheric and Space Physics at the University of Colorado. The spacecraft carries four instruments including the Spectrum Irradiance Monitor (SIM), Solar Stellar Irradiance Comparison Experiment (SOLSTICE), Total Irradiance Monitor (TIM), and the XUV Photometer System (XPS), among which, only TIM provides the data we need in this study.

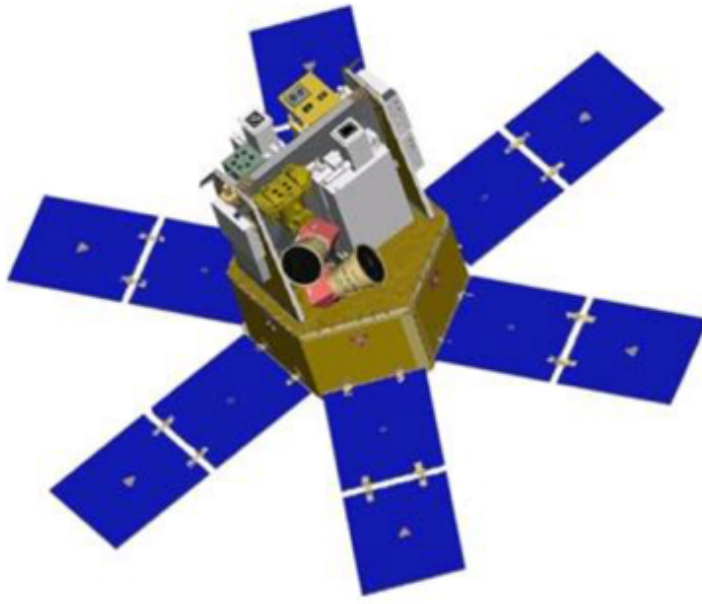


Figure 3.2: The 3D model of SORCE satellite sourced from [Laboratory for Atmospheric and Space Physics at the University of Colorado \[2018\]](#)

The SORCE project kept TSI datasets of more than 14 years. All the TSI data records are plotted in Fig. 3.3. The most accurate value of TSI is $1360.8 \pm 0.5 \text{W} \cdot \text{m}^{-2}$ according to measurements from the Total Irradiance Monitor (TIM) on SORCE satellite and a series of new radiometric laboratory tests [Kopp, 2018; Kopp and Lean, 2011]. The uncertainty of the current TSI value is less than 0.04%. The TSI is varying with time due to solar activities. In the modelling of solar radiation pressure, the TSI E_s is treated to be a constant with a value of $1361 \text{W} \cdot \text{m}^{-2}$.

3. RADIATION FLUX MODELLING

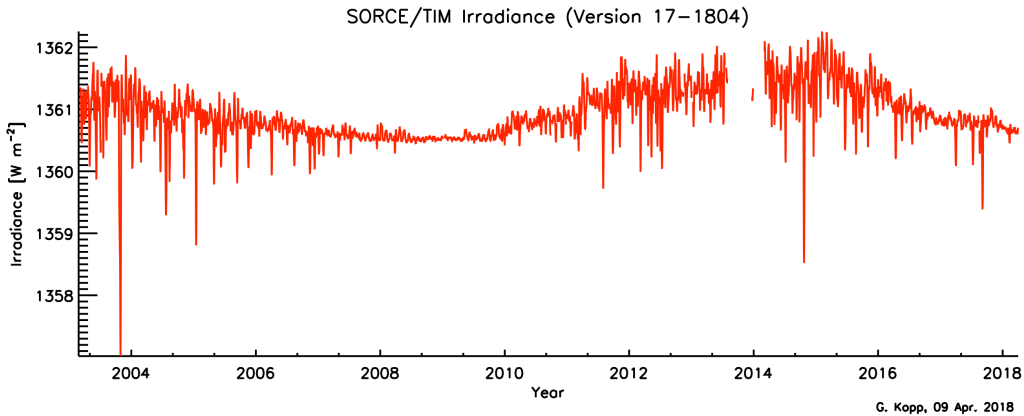


Figure 3.3: The plot of all the TSI measurements from SORCE since March 2003 [Kopp, 2018]

3.1.2 Solar radiation flux at a satellite's location

The solar radiation flux at a satellite's location depends on the distance from the satellite to the Sun (the distance from the Earth's satellites to the Sun is varying due to the fact that the Earth is orbiting the Sun) and the eclipse state. The solar radiation can be blocked by the Earth during eclipses for Earth orbiting satellites. This causes a reduction in the solar radiation flux at the satellite's location. The scaling factor to describe the reduction is called a shadow function which is complex in modelling, thus, the details of shadow function modelling will be discussed in a separated chapter (see chapter 4). In this section, we only discuss the variation of the solar flux at the satellite's location due to the variations of the distance from the satellite to the Sun. The solar radiation flux at any point in space is inversely proportional to the square of the distance from the Sun to that point. Thus, the solar radiation flux at the satellite's location \mathbf{W}_s is given

$$\mathbf{W}_s = F_s \cdot E_s \cdot AU^2 \frac{\mathbf{r} - \mathbf{r}_\odot}{\|\mathbf{r} - \mathbf{r}_\odot\|^3} \quad (3.1)$$

where E_s is the TSI, \mathbf{r} and \mathbf{r}_\odot are the positions of the satellite and the Sun in Earth Centred Inertial system, F_s is the shadow function which varies between 0 and 1.

If a satellite is not in eclipse (i.e. $F_s = 1$), the variation of the solar flux at its location is mainly driven by the satellite–Sun distance. In order to work out the relation between the variation in the solar flux magnitude and the variation in satellite–Sun distance, the differential of the magnitude of solar radiation flux W_s with respect to satellite–Sun distance x is calculated.

$$\frac{\partial W_s(x)}{\partial x} = -2E_s \cdot \frac{AU^2}{x^3} \quad (3.2)$$

Because the satellite–Sun distance is varying around 1 AU, $W_s(x)$ can be approximated to first order at 1 AU:

$$W_s(x) = E_s + \left. \frac{\partial W_s(x)}{\partial x} \right|_{x=1AU} \cdot \Delta x \quad (3.3)$$

3. RADIATION FLUX MODELLING

where Δx is the difference between the satellite-Sun distance and 1 AU.

The relation between the variation in solar radiation flux $\Delta W_s(x)$ and the variation in the distance Δx is given

$$\Delta W_s(x) = -2E_s \cdot \frac{\Delta x}{AU} \quad (3.4)$$

The eccentricity of the Earth's orbit around the Sun makes the solar radiation flux vary between -3.34% and $+3.34\%$. This gives a variation (between the perihelion and aphelion) of circa $90.9 \text{ W} \cdot \text{m}^{-2}$. The details are showing in the following table 3.1.

Table 3.1: The variation of solar flux at Earth's perihelion and aphelion

Item	Distance (AU)	Variation
Perihelion	0.98329	+3.34%
Aphelion	1.0167	-3.34%

3.2 Earth radiation flux

Earth radiation energy is mainly from the Sun. When the solar radiation reaches the Earth, part of the solar radiation is reflected into the space, the other part of the solar radiation is absorbed. The absorbed radiation is assumed to be emitted into space as thermal energy. The reflected radiation is dominated by the Shortwave radiation (SW) while the emitted radiation is dominated by the longwave radiation (LW). Both the LW and the SW have strong geographical and temporal variations. According to the research in Knocke [1989], both the emission and the reflection can be regarded diffuse, which means the reflected or emitted radiation intensity follow Lambert's cosine law ¹.

The main purpose of Earth radiation flux modelling is to calculate the Earth radiation flux at a satellite's location. Usually, only part of the Earth's surface is visible to the satellite. The Earth radiation from the Earth's surface that is invisible to the satellite can not illuminate on the satellite, which means it has no impacts on the Earth radiation flux modelling. Thus, one important part in Earth radiation flux modelling is to figure out the visible part of the Earth's surface to the satellite. The LW Earth radiation can reach the satellite for the visible part. However, the situation is more complex for the SW Earth radiation flux. For the Earth surface that is visible to the satellite, if it is also visible to the Sun, the SW radiation from the Sun can be reflected and reach the satellite, if it is only visible to the satellite but invisible to the Sun, there is no SW radiation reaching the satellite.

As a component of the Earth's energy balance system, the Earth radiation has been studied and monitored over many years. The Cloud and Earth's Radiant Energy System (CERES) experiment is one of the main projects to provide Earth radiation measurements. The CERES can provide the Earth radiation flux observations in both

¹The radiant intensity observed from an ideal diffusely reflecting or ideal diffuse radiator is directly proportional to the cosine of the angle between the direction of the incident radiation and the surface normal

3. RADIATION FLUX MODELLING

the longwave and shortwave. The following sections will give a brief introduction to the observations of the CERES project, then, followed by the method of how to utilise the CERES observations in Earth radiation flux modelling for radiation pressure modelling purpose.

3.2.1 CERES Earth radiation flux data

CERES is one of the highest priority scientific satellite instruments developed for NASA's Earth Observing System. CERES products include both solar-reflected (the SW) and Earth-emitted (the LW) radiation on the Top Of Atmosphere (TOA). In the definition from the CERES, the wavelength range for the LW is from $8 \mu\text{m}$ to $12 \mu\text{m}$, the wavelength range for the SW is from $0.3 \mu\text{m}$ to $5 \mu\text{m}$ [Wielicki et al., 1996]. CERES provides monthly grid files for the SW and LW which have a space resolution of 1° on the TOA. In this study, we take 10 years (2008–2018) monthly averaged grid data from the CERES datasets. The Fig. 3.4 and Fig. 3.5 show the monthly averaged LW and the SW from January to December.

According to the definition from CERES, the TOA is defined to be a spheroid with equatorial radius 6408.137km and polar radius 6386.6517km. The impacts of the spherical TOA and the spheroidal TOA on the global mean of the Earth radiation flux have been evaluated. The difference in global mean of the Earth radiation flux between the spherical TOA and spheroidal TOA is $-0.16 \text{ W} \cdot \text{m}^{-2}$ [CERES, 2017]. For MEO (Medium Earth Orbit) satellites, this only cause a difference of $10^{-8} \text{ W} \cdot \text{m}^{-2}$ in the Earth radiation flux that reaches the satellite's location. Thus, the TOA is assumed to be a sphere with a radius of $R_{\text{TOA}} = 6408.137 \text{ km}$ in this study.

In searching the visible area to the satellite, each cell has to be checked because the CERES data is in cells of 1° by 1° (there are 64800 cells in total). The searching process is slow in data processing. In this study, a triangular subdivision has been used to subdivide the TOA surface into different levels of spherical triangles. The lower the level, the larger the triangles and the faster the searching speed, but less accurate in the Earth radiation flux calculation. A compromise has to be made between the computation efficiency and the modelling accuracy.

3.2.2 Divide the TOA surface with a quad-tree structure

The division starts with a regular octahedron (with 6 vertices and 8 triangular faces) as shown in Fig. 3.6. All the 6 vertices are on the spherical surface and their longitudes and latitudes are listed in Tab. 3.2. Each side of the spherical triangles is a great circle arc.

The initial regular octahedron is set to be the level 0 division. To construct a quad-tree structure, each of the triangular face is subdivided into four triangles as shown in Fig. 3.7. The middle point of each side is chosen as a vertex of the next level triangle. If the coordinates of the 3 vertices of the raw triangle are expressed as \mathbf{x}_1 , \mathbf{x}_2 , and \mathbf{x}_3 , the coordinates of the middle points are computed

3. RADIATION FLUX MODELLING

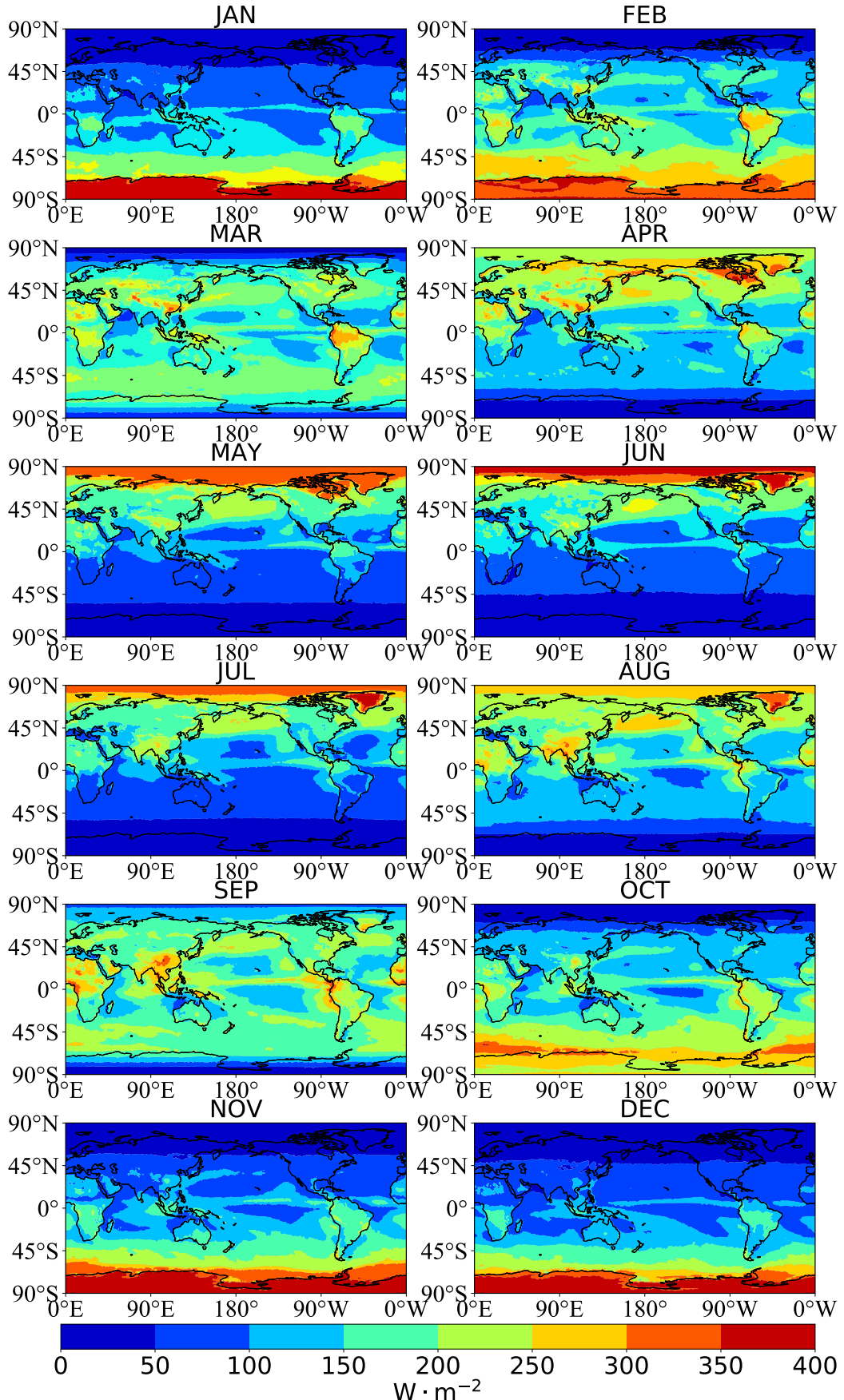


Figure 3.4: The monthly averaged SW flux from CERES grid files.

3. RADIATION FLUX MODELLING

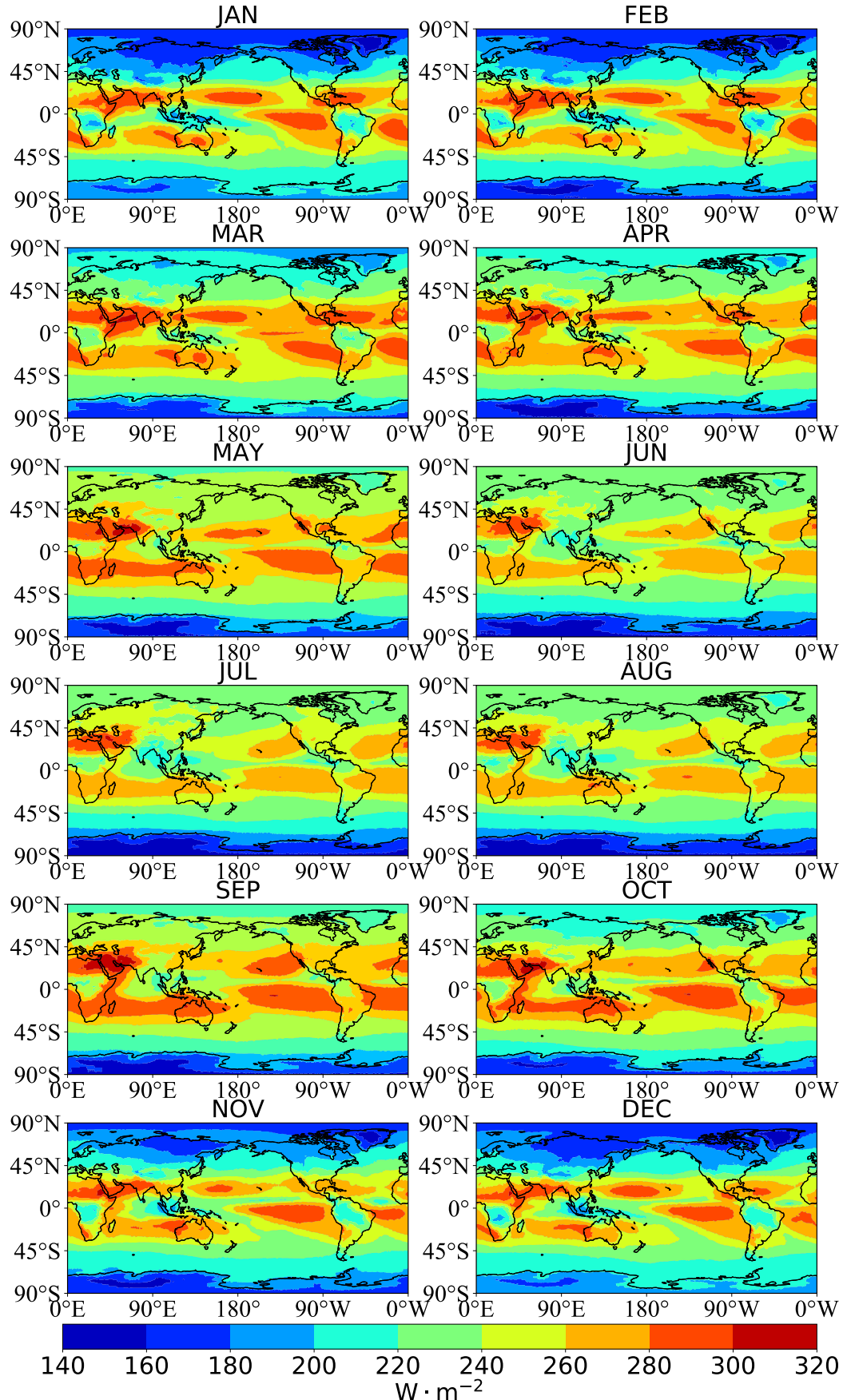


Figure 3.5: The monthly averaged LW flux from CERES grid files.

3. RADIATION FLUX MODELLING

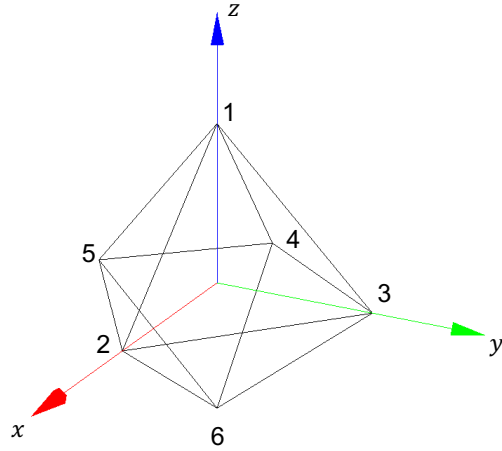


Figure 3.6: The initial regular octahedron for the division of the TOA.

Table 3.2: The coordinates of the vertices of the regular octahedron

vertex number	latitude	longitude
1	90	0
2	0	0
3	0	90
4	0	180
5	0	270
6	-90	0

Table 3.3: The list of faces for the regular octahedron

face number	vertex 1	vertex 2	vertex 3
1	1	2	3
2	1	3	4
3	1	4	5
4	1	5	2
5	2	6	3
6	3	6	4
7	4	6	5
8	5	6	2

3. RADIATION FLUX MODELLING

$$\begin{cases} \mathbf{x}_A = \frac{1}{2}(\mathbf{x}_1 + \mathbf{x}_2) \\ \mathbf{x}_B = \frac{1}{2}(\mathbf{x}_2 + \mathbf{x}_3) \\ \mathbf{x}_C = \frac{1}{2}(\mathbf{x}_1 + \mathbf{x}_3) \end{cases} \quad (3.5)$$

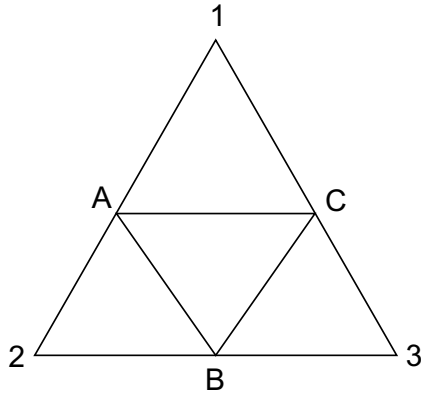


Figure 3.7: A triangle with vertices 1, 2, and 3 are divided into 4 small triangles by choosing the middle point of each side as a new vertex. A, B, and C are the middle points of each side.

The middle points A, B, and C are now on the triangular plane if their coordinates are calculated using Eq. 3.5. They have to be adjusted to be on the spherical surface. If the corresponding points of A, B, and C on the spherical surface are represented by A', B', and C', the coordinates of A', B', and C' are calculated by

$$\begin{cases} \mathbf{x}_{A'} = R_{TOA} \frac{\mathbf{x}_A}{\|\mathbf{x}_A\|} \\ \mathbf{x}_{B'} = R_{TOA} \frac{\mathbf{x}_B}{\|\mathbf{x}_B\|} \\ \mathbf{x}_{C'} = R_{TOA} \frac{\mathbf{x}_C}{\|\mathbf{x}_C\|} \end{cases} \quad (3.6)$$

where R_{TOA} is the radius of the spherical TOA.

This subdivision algorithm is applied to all the triangular faces. Figure 3.8 shows the process of subdivision from level 0 to level 5. Figure 3.9 shows the projection of all the triangles of level 2 subdivision. As the subdivision goes deeper levels, the areas of the triangular faces get smaller. If the triangles become smaller than the 1° by 1° cells, the calculation efficiency will not get improved. Thus, the level of subdivision has to be controlled to make each of the triangle larger than a cell of 1° by 1° . In this study, the maximum level of subdivision is set to be 6. The total number of triangles for level 6 is 32768 and the average area of the spherical triangles is 15565.932 km².

3.2.3 Fill each triangle with Earth radiation flux

After subdividing the TOA surface into triangles, the Earth radiation flux for each triangle is calculated according to the raw CERES grid data. The Earth radiation flux

3. RADIATION FLUX MODELLING

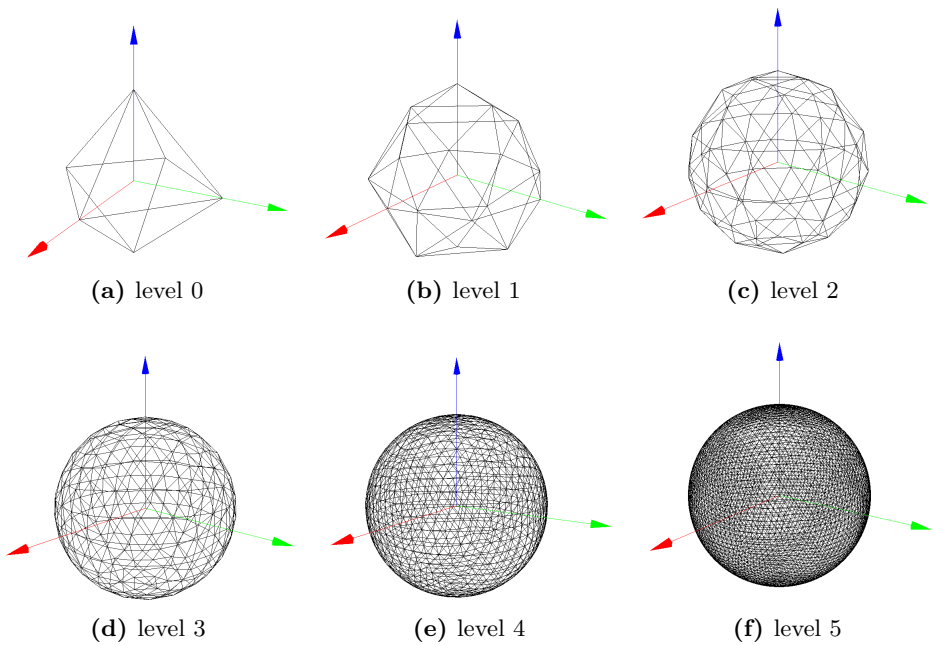


Figure 3.8: The subdivision of the spherical TOA from level 0 to level 5. The x, y, and z axis are represented by the red, green and blue arrows separately.

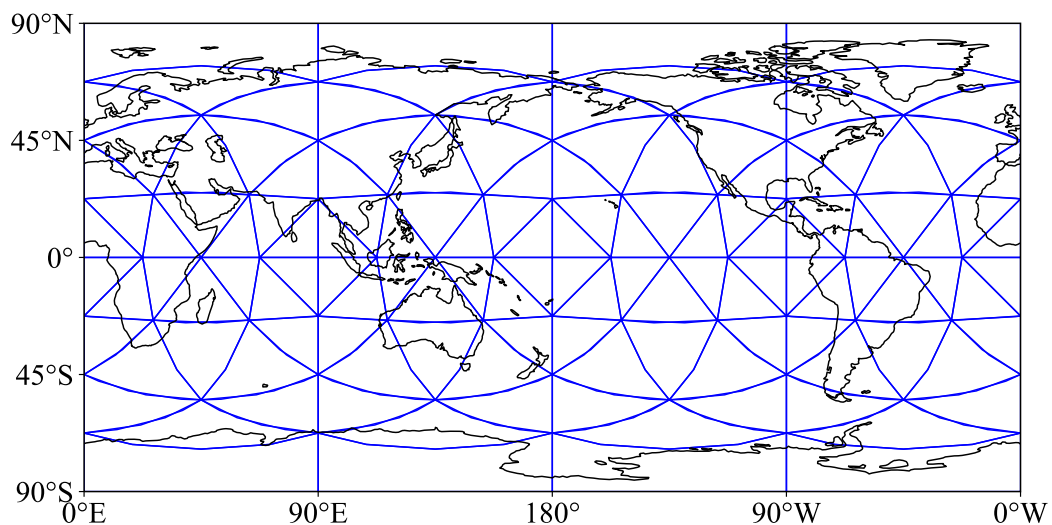


Figure 3.9: The triangles of level 2 under equidistant cylindrical projection

3. RADIATION FLUX MODELLING

for the triangle is assumed to be in the normal direction at the central point of the spherical triangle. The sizes of the triangles are larger than that of cells, one triangle may contain several cells.

One requirement for the calculation of Earth radiation flux at each triangle is that the radiation energy at the triangle should be equal to the sum of the radiation energy of all the cells inside the triangle. For the k^{th} triangle

$$\|\mathbf{W}_{e,\text{triangle},k}\| \cdot A_{\text{triangle},k} = \sum_{i=1}^M \|\mathbf{W}_{e,\text{cell},i}\| \cdot A_{\text{cell},i} \quad (3.7)$$

where

$\|\mathbf{W}_{e,\text{triangle},k}\|$ is the magnitude of mean Earth radiation flux (include both the SW and the LW) at the k^{th} triangle. i.e. $\|\mathbf{W}_{e,\text{triangle},k}\| = W_{e,\text{SW},k} + W_{e,\text{LW},k}$

$A_{\text{triangle},k}$ is the area of the triangle.

M is the total number of the cells inside (fully or partially) the triangle.

$\|\mathbf{W}_{e,\text{cell},i}\|$ is the magnitude of Earth radiation flux at the i^{th} cell. For the cells that are fully inside of the triangle, $A_{\text{cell},i}$ is the area of the cell, but for the cells that are partially inside the triangle, $A_{\text{cell},i}$ is the area of the part that are inside the triangle.

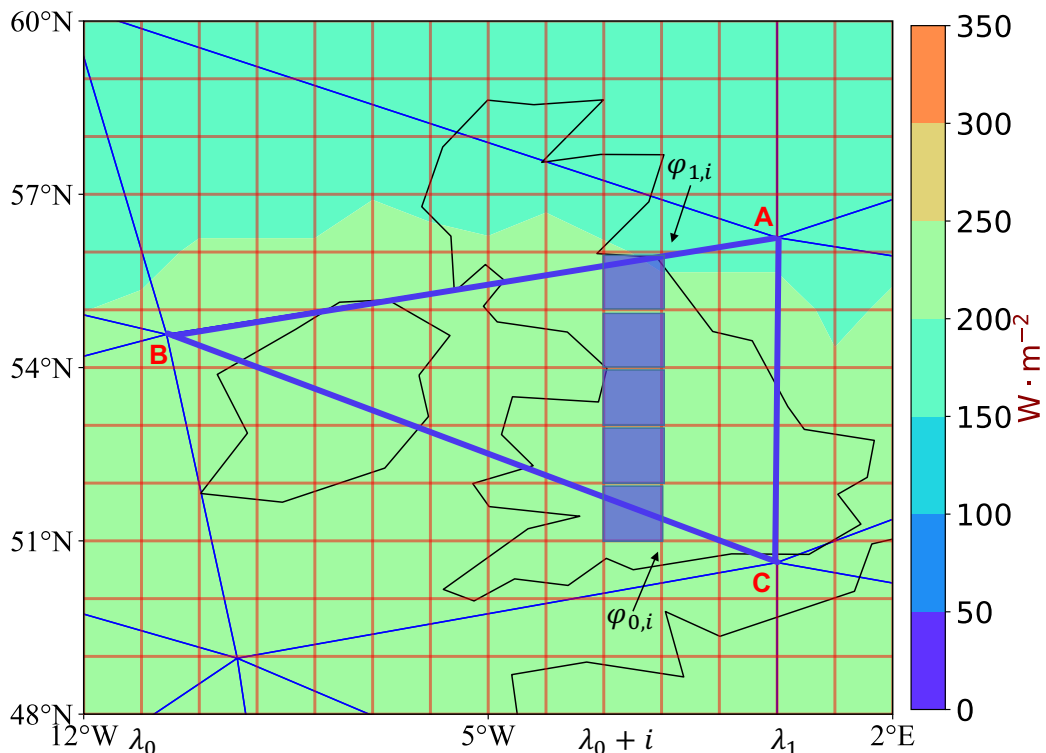


Figure 3.10: One level 4 triangle ABC is above the UK. It contains several cells of 1° by 1° . The short wave Earth radiation flux in June is shown. The boundaries of the triangle is shown in blue while the grid lines are shown in red.

One difficulty is to detect which cell is partially inside the triangle and the area calculation of the part that is inside the triangle. In this study, we introduced a “line scanning” algorithm to deal with this difficulty. To better describe the algorithm, one

3. RADIATION FLUX MODELLING

spherical triangle is projected using the equidistant cylindrical projection as shown in Fig. 3.10. Under the equidistant cylindrical projection, the meridians are projected to vertical straight lines of constant spacing (1° for the raw CERES grid files), and circles of latitude are projected to horizontal straight lines. There are two pairs of the scanning lines, the first pair is two adjacent meridians (because the spacing is 1° , only meridians with whole degrees are account for), the second pair is two lines of latitude (only account for whole degrees). The two meridians start from the minimum limit in longitude of the triangle and scan forward till they reach the maximum limit. In the scanning process, the intersections between the two meridians and the sides of the triangle are computed. The minimum and maximum in latitude of all the intersections form the range of the second pair of scanning lines. Similarly, two lines of latitude scan from the minimum till the maximum. In this scanning process, two lines of latitude and two meridians form a cell. The intersections between the 4 sides of the cell and 3 sides of the triangle together with 4 vertices of the cell form a list of candidate vertices. In the list, the vertices that are inside the triangle form a polygon, which is the part of the cell that is inside the triangle. The detail of the algorithm is described as follows:

- Find the minimum (λ_{min}) and maximum (λ_{max}) in the longitude for the triangle (in Fig. 3.10, the vertex which has the minimum longitude is vertex B while the vertex that has the maximum longitude is vertex A or C). The two scanning meridians start at longitude $\lambda_0 = \lfloor \lambda_{min} \rfloor$ and $\lambda_0 + 1$ respectively. The two scanning meridians end at longitude $\lambda_1 = \lceil \lambda_{max} \rceil$ and $\lambda_1 + 1$ separately.
- The number of meridians with whole degree between longitude λ_0 and λ_1 is N . Starting from λ_0 and $\lambda_0 + 1$, the two scanning meridians move one step (a step is 1° in this study) forward each time till they reach λ_1 and $\lambda_1 + 1$ respectively. For scanning meridians with longitude $\lambda_0 + i$ and $\lambda_0 + 1 + i$, $i \in (0, 1, 2, \dots, N - 1)$, the intersections between them and 3 sides of the triangles are calculated. Among all the intersections, the minimum latitude is $\varphi_{0,i}$ and the maximum latitude is $\varphi_{1,i}$. Both the 2 scanning meridians and 3 sides of triangle are arcs of great circle. The intersections between great circles on spherical surface are calculated using algorithm in [Bertels, 2005]. The details can also be found from appendix A.2.
- The number of latitude lines (whole degree) between $\varphi_{0,i}$ and $\varphi_{1,i}$ is M_i . We can construct two scanning lines of latitude with latitude $\varphi_{0,i} + j$ and $\varphi_{0,i} + j + 1$ separately, $j \in (0, 1, 2, \dots, M_i)$. Similarly, these two scanning lines move one degree forward till they strike $\varphi_{1,i}$ and $\varphi_{1,i} + 1$ respectively. A cell (the j^{th}) is formed using the two scanning line in latitude and the two meridians. Thus, the latitudes and longitudes of the 4 vertices for that cell are $V_{1,j} (\varphi_{0,i} + j, \lambda_0 + i + 1)$, $V_{2,j} (\varphi_{0,i} + j + 1, \lambda_0 + i + 1)$, $V_{3,j} (\varphi_{0,i} + j + 1, \lambda_0 + i)$, and $V_{4,j} (\varphi_{0,i} + j, \lambda_0 + i)$.
- A list of intersections is formed by checking the intersections between the 3 sides of the triangle and the 4 sides of the j^{th} cell. If any vertex of the cell is inside the triangle, the vertex is also added to the intersection list. The vertices in the

3. RADIATION FLUX MODELLING

intersection list actually represent a polygon that is inside the triangle (for cells that are totally inside the triangle, the intersections in the list are the 4 vertices of the cell). The area of the polygon can be calculated using the algorithm from [Bevis and Cambareri, 1987]. Appendix A.3 shows the details.

- The total Earth radiation power for the j^{th} cell is computed by using the area of the part that is inside the triangle times the Earth radiation flux of that cell from the CERES data. This applies to both the shortwave flux and longwave flux. Then, the average Earth radiation flux for the triangle is calculated using equation 3.7.

Apply the above steps to all the triangles, the raw CERES grid Earth radiation flux model is converted into triangular Earth radiation flux model.

3.2.4 The Earth radiation flux at a satellite's location

The approach of Earth radiation flux modelling divides the TOA surface into spherical triangles. In the triangular division, two aspects have to be considered in the calculation of the Earth radiation flux at a satellite's location. They are described as follows.

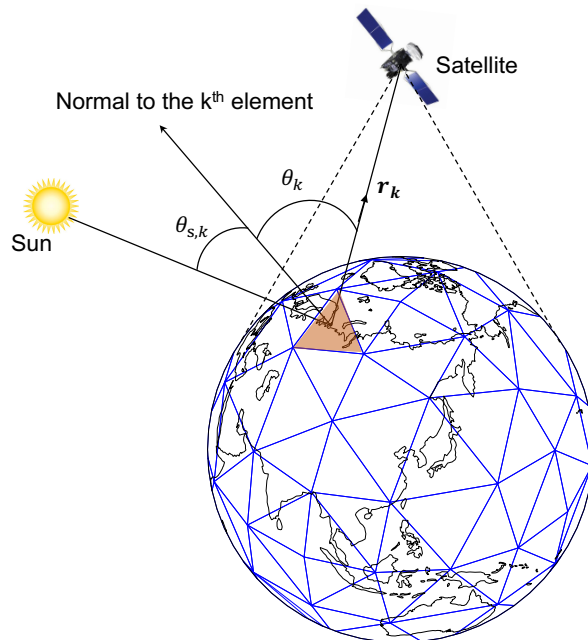


Figure 3.11: The TOA surface is divided into level 2 triangular network. For the k^{th} triangle that is visible to the satellite, the angle between the normal to that triangle and the Sun's direction is $\theta_{s,k}$, the angle between the viewing direction (from the centre of the triangle to the satellite) and the triangle's normal is θ_k

One is to work out which triangles are visible to the satellite (Earth radiation flux can reach a satellite only when the triangle is visible to the satellite). Situations are different for the LW and SW, as long as the triangle is visible, the LW radiation can reach the satellite, the SW radiation can reach the satellite only when the triangle is visible to the satellite and the triangle is visible to the Sun. As shown in Fig. 3.11,

3. RADIATION FLUX MODELLING

the angles between the normal to the k^{th} triangle and the Sun, the satellite are $\theta_{s,k}$, θ_k separately. The condition that a triangle is visible to the satellite and the Sun is

$$\begin{cases} \theta_{s,k} < \frac{\pi}{2} & ; \text{illuminated by the Sun} \\ \theta_k < \frac{\pi}{2} & ; \text{visible to the satellite} \end{cases} \quad (3.8)$$

The triangles that are visible to the satellite can be found out by searching over all the triangles. Among the visible triangles, those are illuminated by the Sun can be worked out by applying condition 3.8. For those triangles that are visible to the satellite and illuminated by the Sun, both the SW and LW are considered. For those triangles that are only visible to the satellite, only the LW is considered.

The other is how much the Earth radiation flux at the TOA is reduced when it reaches a satellite's location. The radiation flux of the k^{th} triangle is $\|\mathbf{W}_{e,\text{triangle},k}\|$. Because the TOA's surface is assumed to be Lambertian, the radiance (in the unit of $\text{W} \cdot \text{sr}^{-1} \cdot \text{m}^{-2}$) of the triangle is $\frac{1}{\pi}$ of the radiant power, i.e. $\frac{\|\mathbf{W}_{e,\text{triangle},k}\|}{\pi}$ [Knocke, 1989]. The cross-sectional area between the radiation flux and the satellite surface is $A_{\text{triangle},k} \cdot \cos \theta_k$. For a differential surface on the satellite with an area dA , the solid angle is $\frac{dA}{\|\mathbf{r}_k\|^2}$ (the vector from the centre of the triangle to the satellite is \mathbf{r}_k). Then the radiant power at the satellite is $\frac{\|\mathbf{W}_{e,\text{triangle},k}\| \cdot A_{\text{triangle},k} \cdot \cos \theta_k dA}{\pi \|\mathbf{r}_k\|^2}$ according to the definition of radiance. The radiation flux at the satellite's location of that triangle $\mathbf{W}_{e,k}$ is given by [Grey and Ziebart, 2014; Knocke, 1989; Li et al., 2017]

$$\mathbf{W}_{e,k} = \frac{\|\mathbf{W}_{e,\text{triangle},k}\|}{\pi \|\mathbf{r}_k\|^3} \cdot A_{\text{triangle},k} \cdot \cos \theta_k \cdot \mathbf{r}_k \quad (3.9)$$

The Earth radiation flux that reaches the satellite's location \mathbf{W}_e is calculated by summing $\mathbf{W}_{e,k}$ over all the visible triangles. i.e.

$$\mathbf{W}_e = \sum_{k=1}^P \mathbf{W}_{e,k} \quad (3.10)$$

where P is the number of triangles that are visible to the satellite.

3.2.5 Results on Earth radiation flux modelling

In the modelling of Earth radiation flux, the TOA surface is subdivided into different levels of spherical triangles. Accordingly, the CERES raw grids are converted into triangular mesh for both the LW and the SW. The tests on the new Earth radiation flux model are in 3 aspects. Firstly, the triangular representation of the Earth radiation flux model should be the same as the raw CERES grid files in theory. The differences between the triangular representation and the raw grid are computed to validate the accuracy of this transformation. Secondly, as the TOA surface is divided into 6 levels of triangles, the lower level division has lower accuracy. The accuracy in the Earth radiation flux of each level subdivision needs to be worked out. Thirdly, the main

3. RADIATION FLUX MODELLING

motivation of triangular division is to speed the computation of the Earth radiation flux at a satellite's location. Thus, the computation efficiency has to be evaluated.

The following sections are organised to give answers to questions in the above 3 aspects.

3.2.5.1 Validating the transformation from the raw CERES grid to the triangular mesh on the TOA's surface

The Earth radiation flux data is stored as grid (1° by 1°) in the raw CERES data. That slows down the computation of finding the visible cells to the satellite. To improve the efficiency of searching for visible area to the satellite, a quad-tree based triangulation mesh is introduced. The global mean Earth Radiation flux and the area of the TOA should be equal for these two representations because both the CERES grid and the triangular mesh are used to represent the TOA surface (the Earth radiation flux is attached to the cells in grid or triangles in the triangular mesh). These two indicators are used to test the quality of the transformation from the CERES grid to the triangular mesh.

The global area of a sphere with a radius of $R_{TOA} = 6408.137$ km is $A_0 = 516028205.131633$ km². For a subdivision of level n , the relative error in the global area is calculate by

$$\Delta A_{rel} = \frac{A_n - A_0}{A_0} \quad (3.11)$$

where A_n is the global area for level n subdivision.

Table 3.4 shows the the relative errors in the global area for different levels of subdivision. The magnitude of ΔA_{rel} is almost between 10^{-15} and 10^{-14} . This indicates that the triangular mesh representation of the TOA surface is of high quality.

Table 3.4: The relative error in area of TOA's surface for different levels of subdivision

Level	Rel. error	Level	Rel. error
Level 0	-1.24E-17%	Level 4	-1.61E-16%
Level 1	-3.27E-17%	Level 5	2.30E-16%
Level 2	-1.64E-17%	Level 6	1.51E-17%
Level 3	-6.43E-17 %		

The global total Earth radiation flux is calculated by adding up the Earth radiation flux of each TOA's element (this apply to both the CERES grid and triangular mesh). For triangular mesh of level n subdivision, the global mean Earth radiation flux is calculated by

$$W_{avg,n} = \frac{1}{A_0} \sum_{k=1}^{Q_n} \| \mathbf{W}_{e,triangle,k} \| A_{triangle,k} \quad (3.12)$$

where Q_n is the total number of triangles for level n subdivision. The global mean Earth radiation flux for the CERES cells W_{avg} is calculated using a similar approach

3. RADIATION FLUX MODELLING

as the above equation. The global mean Earth radiation flux for different months using CERES datasets are shown in Fig. 3.12. The difference between W_{avg} and $W_{avg,n}$ is shown in Table 3.5. For a certain month, different levels of subdivision get similar errors. But, for the same level of subdivision, different months get different relative errors, which means the errors are mainly caused by the temporal and spatial variation of the Earth radiation flux distribution. The largest errors shown at December is around $0.456 \times 10^{-6} \text{ W} \cdot \text{m}^{-2}$. Errors in such a magnitude at the TOA have a negligible influence on the Earth radiation at a satellite's location.

Table 3.5: The errors of global mean Earth radiation flux (both the SW and the LW) for different levels of subdivision. unit: $[10^{-6} \text{ W} \cdot \text{m}^{-2}]$

Month	Level 0	Level 1	Level 2	Level 3	Level 4	Level 5	Level 6
Jan.	-0.166	-0.167	-0.166	-0.166	-0.165	-0.166	-0.167
Feb.	-0.089	-0.089	-0.089	-0.089	-0.087	-0.088	-0.088
Mar.	0.158	0.158	0.158	0.158	0.157	0.156	0.155
Apr.	0.249	0.248	0.249	0.249	0.248	0.250	0.249
May	-0.354	-0.354	-0.353	-0.353	-0.353	-0.352	-0.351
Jun.	0.391	0.390	0.390	0.391	0.390	0.391	0.390
Jul.	0.282	0.281	0.281	0.282	0.280	0.281	0.280
Aug.	0.407	0.406	0.407	0.407	0.408	0.407	0.408
Sep.	-0.387	-0.386	-0.388	-0.386	-0.385	-0.384	-0.386
Oct.	-0.474	-0.473	-0.474	-0.474	-0.474	-0.473	-0.473
Nov.	-0.203	-0.202	-0.204	-0.203	-0.203	-0.204	-0.202
Dec.	0.456	0.455	0.455	0.456	0.455	0.456	0.455

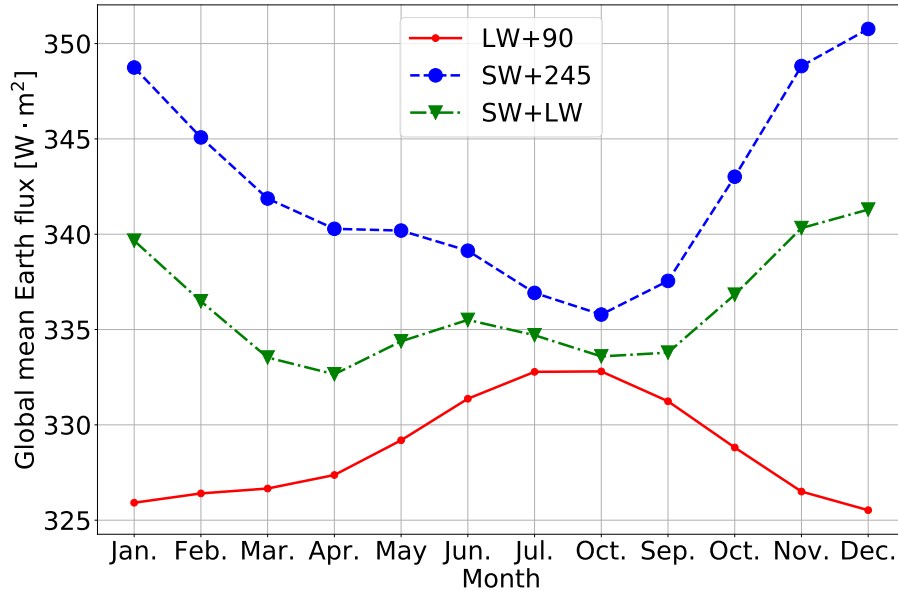


Figure 3.12: The variation of monthly averaged global mean Earth flux (on the TOA) derived from the CERES data. The SW has been offset by $245 \text{ W} \cdot \text{m}^{-2}$ and the LW has been offset by $90 \text{ W} \cdot \text{m}^{-2}$

3. RADIATION FLUX MODELLING

3.2.5.2 What is the accuracy in Earth radiation flux for different levels of subdivision at a satellite's location?

At a satellite's location, the errors in the Earth radiation flux for different levels of subdivision are calculated by taking the raw CERES dataset as the "truth". The differences in the Earth radiation flux (including both the SW and the LW) between the CERES grid and the triangular mesh of different levels of subdivision are worked out for the Galileo satellites.

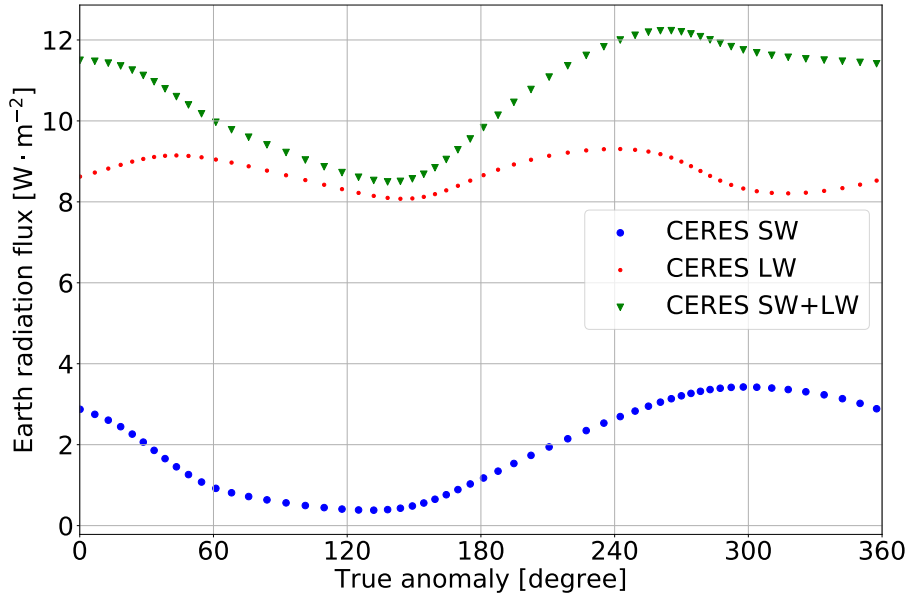


Figure 3.13: The variation of the LW and SW Earth radiation flux at a Galileo satellite's location derived from the CERES grid data

The test time is 11th March in 2015. Figure 3.13 shows the LW and SW Earth radiation flux derived from the CERES grid for a Galileo satellite E11. The average Earth radiation flux at Galileo satellite's location is around $11 \text{ W} \cdot \text{m}^{-2}$. The differences in the Earth radiation flux between the CERES grid and different levels of triangular divisions are shown in Fig. 3.14a and Fig. 3.14b. The statistics of the differences are shown in Tab. 3.6.

Table 3.6: The standard deviation and average of the difference between the CERES grid and different levels of subdivision in the Earth radiation flux (SW+LW), unit [$\text{W} \cdot \text{m}^{-2}$]

Level	mean	standard deviation
Level 0	0.4979	1.2333
Level 1	-0.1326	0.3485
Level 2	-0.1161	0.1025
Level 3	0.0990	0.0407
Level 4	0.0715	0.0207
Level 5	-0.0631	0.0169
Level 6	0.0627	0.0165

The main error source in the calculation of the Earth radiation flux at a satellite's

3. RADIATION FLUX MODELLING

location is the visible area to the satellite. Discrete division like the raw CERES grid and the triangular mesh leaves a saw-toothed boundary of the visible area as shown in Fig. 3.15. The errors in the visible area can be decreased by increasing the level of division. For the Galileo satellites, the level 3 division has a uncertainty of $0.04 \text{ W} \cdot \text{m}^{-2}$ (around 0.36% of the total Earth radiation flux), this only lead to an error of $0.003 \text{ nm} \cdot \text{s}^{-2}$, which has already reached the objective of this research (see 1.3.1).

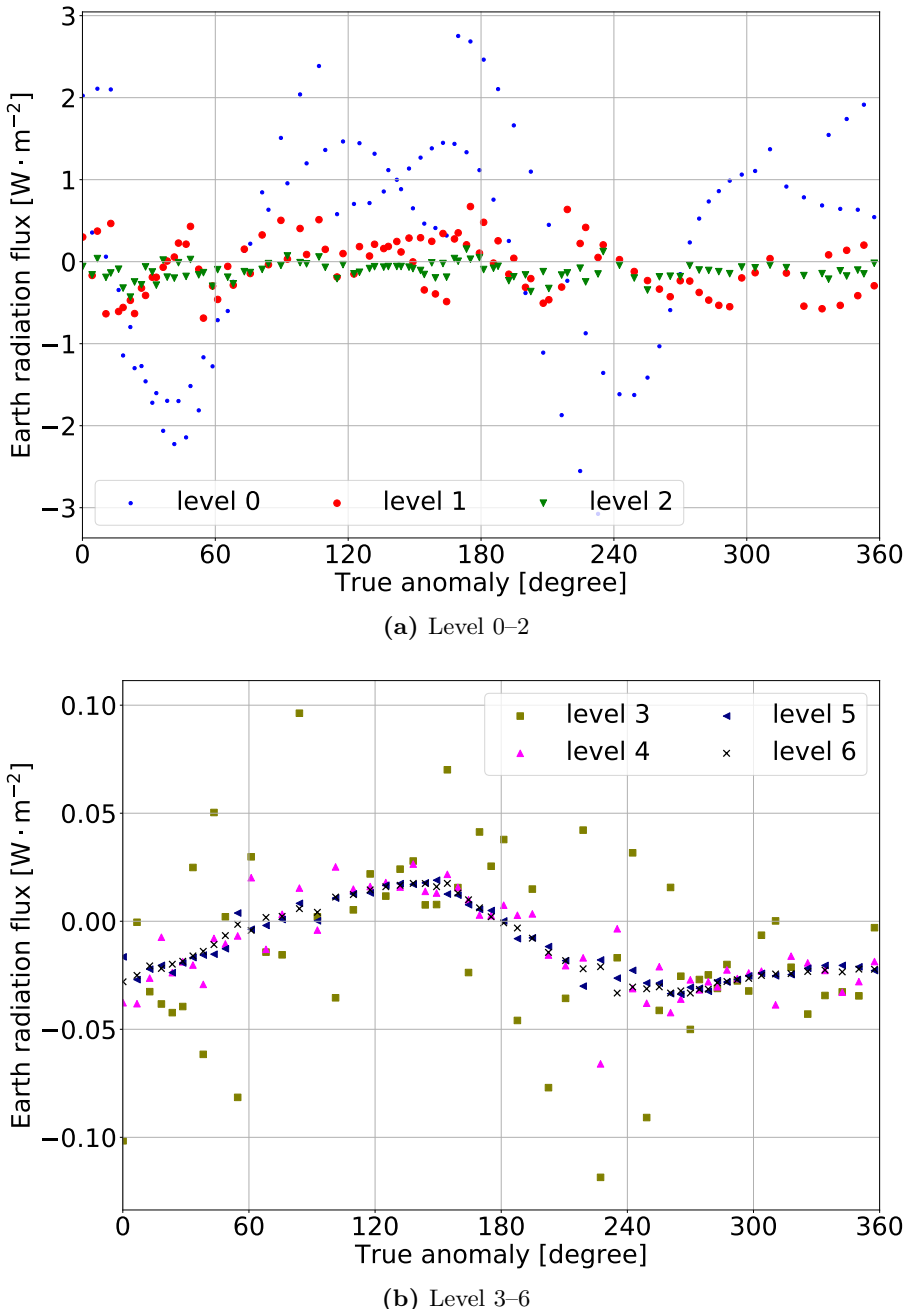


Figure 3.14: The difference in Earth radiation flux (SW+LW) between CERES grid and different level subdivision for Galileo E11 satellite during one orbit

3. RADIATION FLUX MODELLING

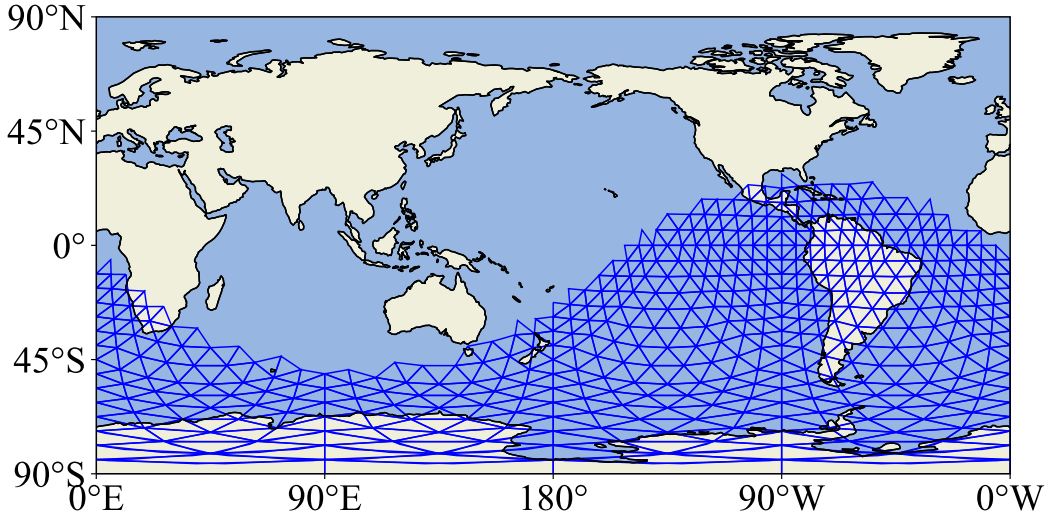


Figure 3.15: The visible triangles of E11 satellite at UTC 2015/03/11/19:59:44 with the level 4 subdivision triangular mesh. The blue triangles are showing the visible area.

3.2.5.3 What is the improvement of the subdivision in calculation efficiency?

The test is done on a personal computer with a CPU at a clock rate of 2.4 GHz. The average runtime are listed in Tab. 3.7. The maximum level (level 6) of division has a runtime of about two third of the CERES grid. Furthermore, level 3 division can meet the accuracy requirement in Earth radiation flux for the Galileo satellites. This indicates that the computation efficiency can be improved by over 100 times comparing with the CERES grid.

Table 3.7: The runtime of the different levels of subdivision [unit: ms]

Level	Runtime	Level	Runtime
Level 0	0.002	Level 4	0.2280
Level 1	0.004	Level 5	0.9175
Level 2	0.0155	Level 6	3.2115
Level 3	0.0615	CERES	6.556

3.3 Thermal radiation flux

All bodies that have temperatures larger than absolute zero emit electromagnetic radiation. The emission of the radiation causes a recoil force that is the so-called thermal radiation force. Thus, thermal radiation flux modelling is an important element in radiation pressure modelling.

Except for the direct solar radiation and Earth radiation sources, the thermal radiation also needs to be considered in the radiation pressure modelling. When the solar radiation and the Earth radiation illuminate on the satellite's surface, part of

3. RADIATION FLUX MODELLING

the radiation is absorbed by the satellite's surface. The absorbed radiation changes the internal energy of the surface material and the surface temperature changes as a consequence. The other thermal radiation source is from the satellite itself. The solar panels collect energy from the Sun and convert it into electrical energy. The power consumption by the satellite payload generates heat energy. The heat energy is then dumped into space by the radiators on the satellite surface. The heat dump at the radiators also changes the temperature at the surface of radiators.

In this section, the thermal radiation flux modelling due to the above two reasons are discussed.

3.3.1 Absorption from the Earth and solar radiation

The absorptivity of a surface material is used to describe how much radiation is absorbed. When the absorbed radiation is reradiated as thermal energy, the effective emittance of the material also needs to be known in order to work out how much of the radiation is reradiated. The solar panel is acting as an important component to provide energy for the whole satellite, and the thermal dynamics of the physical processes happened on the solar panels are more complex than that on the surface of the satellite bus. For the solar panels, a set of physical parameters have to be known, such as the surface temperature of the solar panels, how much energy is drawn from the solar panels and so on. Due to the complexity and a lack of parameters of the solar panels, the thermal effects on the solar panels are not modelled in this study.

Usually, most parts of the satellite bus are covered with Multi-Layer Insulation (MLI) material. It is used to protect the satellite bus from high temperature under the illumination of the Sun. The temperature T_{sc} inside the satellite bus is stable due to the active or inactive temperature control. Because the payloads are designed to work at room temperature, it is reasonable to assume T_{sc} to have a value of 298 K [Adhya, 2005]. The MLI material can insult heat energy with a high efficiency. However, radiant heat exchange does happen on the MLI surface. Thus, the radiation sources that affect the temperature of the MLI are the absorbed solar radiation, absorbed Earth radiation, and the thermal radiation from the internal satellite. The inner layer of the MLI (facing to the satellite bus) is assumed to be in the same temperature as the internal satellite bus [Adhya, 2005]. The temperature T_{MLI} of the outer layer MLI (facing to the space) can be computed by applying energy balance to the system. When the MLI surface is illuminated by radiation fluxes, T_{MLI} is computed by [Adhya, 2005]

$$T_{MLI}^4 = \frac{\alpha W \cos \theta + \varepsilon_{eff} \sigma T_{sc}^4}{\sigma(\varepsilon_{eff} + \varepsilon_{MLI})} \quad (3.13)$$

where

W : input radiation flux (include Solar radiation and Earth radiation flux at the satellite's location).

α : absorptivity of the MLI.

3. RADIATION FLUX MODELLING

θ : angle between the anti-incident radiation flux and the surface normal.

T_{sc} : temperature of the internal satellite bus.

σ : the Stefan-Boltzmann constant.

ε_{eff} : effective emittance of the MLI material.

ε_{MLI} : emittance of outer layer MLI surface.

The values of ε_{eff} , ε_{MLI} are not known for the Galileo satellites. However, those values for the GPS satellites are used in this study, i.e. $\varepsilon_{eff} = 0.02$ and $\varepsilon_{MLI}=0.84$ [Adhya, 2005; Miller et al., 2016].

If there is no radiation flux illuminating on the surface of the MLI, the temperature is computed by setting $W = 0$, that is

$$T_{MLI}^4 = \frac{\varepsilon_{eff} T_{sc}^4}{\varepsilon_{eff} + \varepsilon_{MLI}} \quad (3.14)$$

Once the surface temperature is calculated, the radiation flux going out from the outer layer MLI surface is calculated using the Stefan-Boltzmann law and assuming the radiation is diffusely emitted [Adhya, 2005]. Equivalently, the diffusely emitted (Lambertian assumption) radiation flux is expressed in the normal direction by applying a scaling factor $\frac{2}{3}$ [Fliegel et al., 1992; Ziebart, 2004], i.e.

$$\mathbf{W}_{t,m} = \frac{2}{3} \sigma \varepsilon_{MLI} T_{MLI}^4 \mathbf{n} \quad (3.15)$$

where

\mathbf{n} : the surface normal.

For the surface material that is not MLI, if the surface is illuminated under radiation flux, all the absorbed radiation energy is assumed to be emitted instantaneously with a Lambertian assumption. That is

$$\mathbf{W}_{t,o} = \frac{2}{3} \alpha W \cos \theta \mathbf{n} \quad (3.16)$$

When the surface is not illuminated by any radiation flux, the temperature of the surface is assumed to be as the same as that of outer space, i.e the cosmic microwave background. The force due to emitted photons at this temperature is ignored in this study.

3.3.2 The thermal radiation at radiators

Thermal radiation at radiators is thought to be one possible cause of the so called “y-bias” in orbit modelling [Ziebart et al., 2005]. The radiators at the -y and +y panel have different power in dumping heat energy. The unbalanced radiation will cause a net force, i.e. the “y-bias”. For the Galileo IOV satellites, there are radiators at the -y, +y, and +x panels of the satellite bus. For the Galileo FOC satellites, there are also radiators on the -z panel. The amount of the thermal radiation dumped at these radiators relies on the operating status of the satellite. In order to model the

3. RADIATION FLUX MODELLING

thermal radiation flux at these radiators, more information about how the satellites are operated needs to be known. In this study, the information is not available and the further research is therefore limited.

3.4 Antenna radiation power

For GNSS satellites, the navigation antenna is designed to be pointing to the Earth. The transmission of the navigation signal cause a recoil force, which is the so-called antenna thrust [Ziebart et al., 2005]. For GNSS satellites, the transmitted power can be measured with a high-gain antenna and knowledge about the properties of the transmit and receive antennas as well as the losses along the propagation path [Steigenberger et al., 2018].



Figure 3.16: 30-m dish antenna of the German Space Operation Centre (GSOC) at its ground station near Weilheim [Steigenberger et al., 2018]

Table 3.8: The average transmit power of navigation antenna for different Galileo satellites [Steigenberger et al., 2018]

Type	SVN	Transmit power [W]
IOV- n	E101-E104 until approximately 17 May 2014	160
IOV-r	E101 and E102 ¹	135
IOV-b	E103 (measured in Oct 2016)	95
FOC	E201-E214	265

A 30-m dish antenna (as shown in Fig. 3.16) of the German Aerospace Centre (DLR) located at its ground station in Weilheim was used to measure the transmit

3. RADIATION FLUX MODELLING

power for different types of GPS, GLONASS, Galileo, and BeiDou-2 satellites. The average transmit power of different Galileo satellites are shown in Tab. 3.8. There are 3 cases for the Galileo IOV satellites. “IOV-n” means the IOV satellites with nominal transmit power before July 2014; “IOV-r” means Galileo IOV satellites with reduced transmit power after July 2014; “IOV-b” means Galileo IOV satellites with status “all bands in temporary back-off” [Falcone, 2016] after July 2014. However, the Galileo satellites also carry TTC (Telemetry Track and Command) antenna and Search And Rescue (SAR) antenna. The impacts of these antennas need further study.

3.5 Summary

In this chapter, the modelling of 4 radiation sources (solar radiation, Earth radiation, thermal radiation and antenna transmit power) are discussed.

In the modelling of solar radiation flux, the variation of the TSI has been ignored, only the variation in solar radiation flux due to distance change between the Sun and satellite is considered. For Earth orbiters, the variation in the solar radiation flux is linear with the changes in the distance between the Sun and the satellite (see Equation. 3.4). The maximum variation can reach 6.68% (+3.34% at perihelion, -3.34% at aphelion).

In the modelling of Earth radiation flux, the CERES is used as a data source of Earth radiation flux. The TOA surface is divided into different levels of triangular mesh to speed up the searching of visible area to a satellite. The triangular division of the TOA has been validated in the global area and the global mean Earth radiation flux. Both these two indicators show a good quality of the triangular division. If the CERES grid is taken as the “truth”, the level 3 subdivision introduces errors less than 0.36 % in the accuracy of Earth radiation flux at a Galileo satellite’s location. Furthermore, the computation efficiency has been improved by over 100 times compared with the method using CERES grid.

The thermal radiation fluxes come from two main sources, one is the absorbed solar radiation and Earth radiation, the other is the heat dump of radiators on satellite body. The thermal flux modelling at the radiators requires information about the operating status of the satellite payloads. It is not studied due to a lack of such information. In the thermal flux modelling due to the absorbed radiation, two materials (the MLI and non-MLI material) are considered on the surface of the satellite body. When there is no radiation illuminating on the satellite surface, the surface temperature of the MLI material is determined by the heat transfer from the internal satellite body (see Eq. 3.14), the temperature of non-MLI material is assumed to be 2.7 K and the force effects can be ignored. When the satellite body is under the illumination of radiation flux, an energy balance equation is used to determine the surface temperature of the MLI material (see Eq. 3.13). Once the surface temperature of the MLI material is determined, the thermal radiation flux can be computed using equation 3.15. However, for the non-MLI material, all the absorbed radiation is assumed to be emitted

3. RADIATION FLUX MODELLING

instantaneously, the thermal radiation flux is computed using equation 3.16.

In the modelling of radiation flux from the navigation antenna, the measuring data in [Steigenberger et al., 2018] are used for both the IOV and FOC satellites. However, the transmit power of the SAR antenna is still unknown. Thus, the radiation force caused by the SAR antenna is not modelled.

Chapter 4

Solar radiation flux modelling during eclipses

The radiation flux as one important element in radiation pressure modelling has been discussed in chapter 3. However, when a satellite goes into eclipse, the solar radiation may be blocked by the Earth which causes a reduction in the solar radiation flux at a satellite's location. The reduction is described by a shadow function. This section will describe a new method to model the shadow function during the Earth's eclipses.

4.1 What is a shadow function?

Eclipses occur for both celestial bodies and artificial satellites. Solar eclipses reduce the solar irradiance at a satellite's location because all or part of the Sun is blocked by the occulting body. For artificial satellites, the occulting body can be the Earth or the moon. Eclipses caused by the Earth are far more frequent than those caused by the moon [Srivastava et al., 2015; Vallado, 2007]. However, lunar eclipses do affect the orbit of artificial satellites [Khalil and Abd, 2011; Song and Kim, 2016; Zhang et al., 2018]. In this study, we mainly focus on the eclipses caused by the Earth.

Three conditions define the eclipse state: full phase, penumbra, and umbra. Under conditions of full phase, the Sun is fully visible to the satellite, the only factor influencing the energy incident on the satellite is the satellite–Sun distance. The shadow function is the ratio of solar radiation incident on a satellite during penumbra to that at full phase. The value of the shadow function F_s for the three eclipse states is shown in Tab. 4.1. Orbital trajectory calculations rely upon modelling forces accurately. The shadow function as a scalar of the solar flux in radiation pressure modelling determines the magnitude of SRP during eclipse. Ignoring the variations in solar flux caused by shadow function effects will result in orbit errors at some level [Montenbruck and Gill, 2005; Vallado, 2007]. This is particularly important for missions that require cm-level orbit accuracy [Guo et al., 2016; Kucharski et al., 2017; Montenbruck et al., 2013; Robertson, 2015; Rodriguez-Solano, 2014; Sibthorpe et al., 2011].

When the solar radiation travels from the Sun to the satellite, if it is blocked

4. SOLAR RADIATION FLUX MODELLING DURING ECLIPSES

Table 4.1: The value of a shadow function

eclipse state	shadow function (F_s)
umbra	0
penumbra	$0 < F_s < 1$
full phase	1

by the Earth, the intensity of solar radiation is affected by the Earth's oblateness (geometrical problem) and the atmospheric effects (physical problem). Comparing with the conventional approaches, the method in this study accounts for the Earth's oblateness by treating it as an ellipsoid and use a simple linear function to describe the solar radiation reduction in the Earth's atmospheric due to refraction, scattering and absorption. In the shadow function modelling, the key to solve the geometrical problem is to work out how much of the solar disk is not blocked by the Earth, one important element in the physical problem is to compute how much solar radiation is reduced when the solar radiation goes through the Earth's atmosphere. Thus, the shadow function modelling is divided into a geometrical problem and a physical problem [Vokrouhlicky et al., 1993; 1994a]. A new shadow function model based on perspective projection and atmospheric effect called PPM_atm is put forward to solve the two problems [Li et al., 2019].

4.2 The geometrical problem

The main component of solving the geometrical problem is to work out how much of the solar disk is blocked by the solid Earth (the boundary of the Earth ellipsoid). The shape of the Earth is represented by the WGS-84 ellipsoid. The Sun is described by a sphere. The ECEF (Earth Centred Earth Fixed) frame is chosen as a global coordinate system to describe the problem. Thus, in mathematics, this is a computational geometry problem.

Problem description

The solid Earth can be represented by an ellipsoid (equatorial radius a and polar radius b) with equation

$$\mathbf{x}_e^T \mathbf{A} \mathbf{x}_e = 1 \quad (4.1)$$

where

$$\mathbf{A} = \begin{pmatrix} \frac{1}{a^2} & 0 & 0 \\ 0 & \frac{1}{a^2} & 0 \\ 0 & 0 & \frac{1}{b^2} \end{pmatrix}$$

\mathbf{x}_e is the coordinates of any point on the surface of the Earth ellipsoid.

The Sun is assumed to be a sphere with a radius of R_s and its centre \mathbf{r}_\odot is known

4. SOLAR RADIATION FLUX MODELLING DURING ECLIPSES

in the ECEF, the equation of the Sun is:

$$(\mathbf{x}_s - \mathbf{r}_\odot)^T (\mathbf{x}_s - \mathbf{r}_\odot) = R_s^2 \quad (4.2)$$

where \mathbf{x}_s represents any point on the surface of the Sun.

For a satellite that is orbiting around the Earth, its position is known to be \mathbf{r} in ECEF. Under the assumption that there is a camera on the satellite's centre of mass and the camera is looking at the Sun's centre of mass, two questions need to be answered.

- In the eye of the satellite, whether the Sun is blocked by the Earth?
- If part of the Sun is blocked by the Earth, how much of the solar disk is not blocked?

Problem Analysis

In facing these problems, one natural way of thinking is to use the perspective projection approach. Perspective projection is a 3D projection that makes objects appear as they would effectively to the human eye. To solve these questions using perspective projection, some coordinates system must be established in rigorous mathematics. In addition, some elements about perspective projection have to be introduced, such as the viewpoint, the orientation of the camera, the position of the display image.

Using the perspective projection, both the Sun and the Earth are projected onto an image plane. On the image plane, if the projection of the Earth intersects the projection of the Sun, the Sun is blocked by the Earth. So one key is to work out the equations of the perspective projections for the Earth and the Sun. As for the second question, because the satellite is staring at the Sun's centre of mass, the projection of the Sun on the image is always a circle, this is relatively a simple situation to deal with. Thus, the main task is to work out the area of a circle that is not blocked by the projection of the Earth.

According to the above analysis, the solution to this problem are described in the following subsections.

4.2.1 Definition of Image Space Frame

The equations of the Sun, the Earth and the position of the satellite are all described in the ECEF. The centre of mass of the satellite is treated as a viewpoint and it is staring at the Sun's centre of mass. An image plane is placed at a distance of γ from the viewpoint and is perpendicular to the satellite–Sun direction. Perspective projections turn 3D objects into planar shapes on the image plane. Thus, the Image Space Frame (ISF) is defined to describe the equations of the projections on the image plane.

Figure 4.1 shows the definition of ISF and the geometrical relations amongst the Sun, the Earth, and the satellite. The image plane is at a distance of γ from the satellite. We define the origin (denoted as \mathbf{o} in ECEF) of the ISF to be the projection

4. SOLAR RADIATION FLUX MODELLING DURING ECLIPSES

of the Sun's centre (PSC) on the image plane, z-axis (denoted as a unit vector \mathbf{n} in ECEF) of the ISF to be along the vector from the Sun to the satellite, x-axis (denoted as a unit vector \mathbf{u} in ECEF) of the ISF to be from the origin to the projection of Earth's mass centre (PEC), y-axis (denoted as a unit vector \mathbf{v} in ECEF) lies in the image plane and completes the right-hand coordinate system. The 3 unit vectors \mathbf{u} , \mathbf{v} , \mathbf{n} , and the origin of the ISF \mathbf{o} are defined as follows if the satellite's position \mathbf{r} and the Sun's position \mathbf{r}_\odot are known.

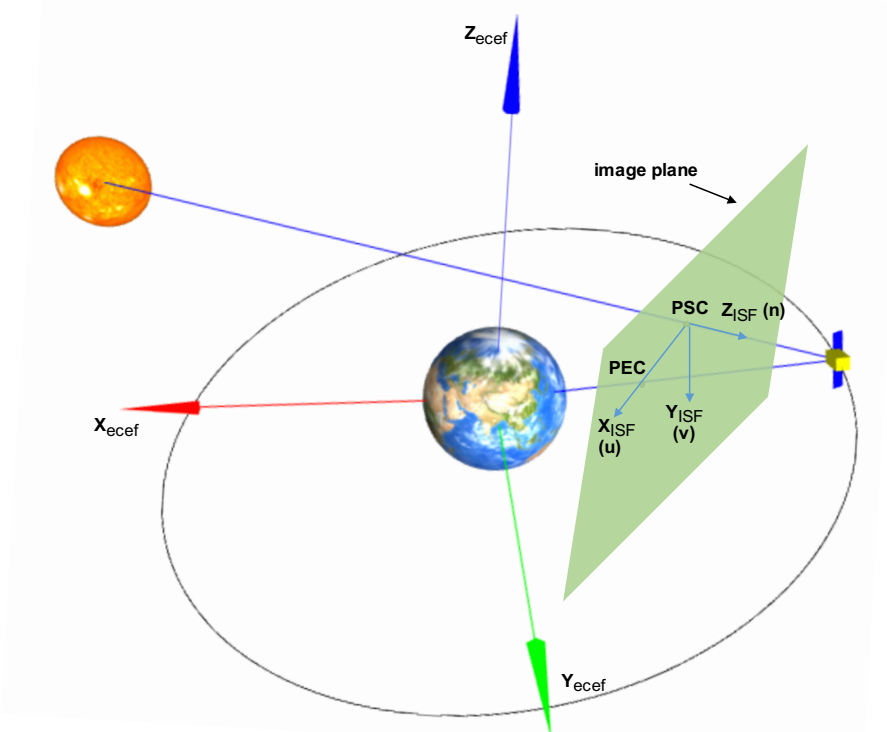


Figure 4.1: The basic geometrical relations among the Sun, the Earth and the satellite. The definition of the ISF (Image Space Frame) is also shown.

The unit vector along the ISF z-axis is

$$\mathbf{n} = \frac{\mathbf{r} - \mathbf{r}_\odot}{\|\mathbf{r} - \mathbf{r}_\odot\|} \quad (4.3)$$

The coordinates of the ISF origin \mathbf{o} is

$$\mathbf{o} = \mathbf{r} - \gamma \mathbf{n} \quad (4.4)$$

where γ is the distance from the satellite to the image plane.

The unit vector \mathbf{u} of x-axis can be worked out from the geometrical relation amongst PSC, PEC and the satellite (See Fig. 4.2). Therefore,

$$\mathbf{u} = \frac{\mathbf{r} - (\mathbf{n} \cdot \mathbf{r})\mathbf{n}}{\|\mathbf{r} - (\mathbf{n} \cdot \mathbf{r})\mathbf{n}\|} \quad (4.5)$$

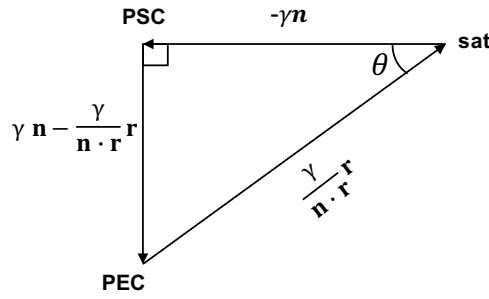


Figure 4.2: The geometrical relation among the PEC, PSC and the satellite. Based on this, the unit vector \mathbf{u} (normalization of vector from PSC to PEC) can be worked out.

Once \mathbf{u} and \mathbf{n} are confirmed, the unit vector along the positive y-axis of the ISF \mathbf{v} is computed

$$\mathbf{v} = \mathbf{n} \times \mathbf{u} \quad (4.6)$$

However, the above definition of the ISF can be singular when the centre of the Sun, the centre of the Earth, and the satellite are collinear, i.e. $\mathbf{r} - (\mathbf{n} \cdot \mathbf{r})\mathbf{n} = 0$. In this case, the eclipse state is either full phase (the satellite is between the Sun and the Earth) or umbra (the Earth is between the Sun and the satellite).

4.2.2 Existence of the Earth's image on the projection plane

The solution to the geometrical problem is worked out according to the perspective projection. However, the Earth's image on the projection plane may not exist when the projection plane is between the Sun and the Earth. Therefore, before starting the calculation of perspective projection, the condition of the existence of the Earth's image has to be checked.

We define a plane including the centre of mass of the Sun, the satellite and the Earth. In this plane, we draw a line through the centres of mass of the satellite and the Sun (see line S_1S_2 in Fig. 4.3). There exist two planes which are perpendicular to the line and are tangent to the Earth (planes S_1P_1 and S_2P_2 in Fig. 4.3, S_1 and S_2 are the intersections between the line and the two planes). The sun-side of line S_1S_2 is defined as the front. There are three possibilities for the position of the satellite on line S_1S_2 : (1) the satellite is in front of S_1 ; (2) the satellite is between S_1 and S_2 ; (3) the satellite is behind S_2 . The first case is full phase. However, for the latter two cases, the perspective projection algorithm can be used. The keys to distinguish amongst the three possibilities is the positions of S_1 and S_2 . They are determined as follows:

Let the coordinates of P_1 and P_2 be \mathbf{x}_{P_i} , $i \in 1, 2$. Let the coordinates of S_1 and S_2 be \mathbf{x}_{S_i} , $i \in 1, 2$. The parametric representation of \mathbf{x}_{S_i} is

$$\mathbf{x}_{S_i} = \mathbf{r} - t\mathbf{n} \quad (4.7)$$

where t is an unknown parameter.

4. SOLAR RADIATION FLUX MODELLING DURING ECLIPSES

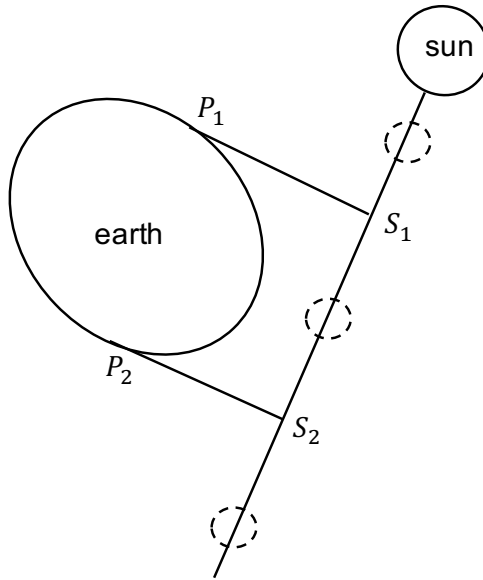


Figure 4.3: The relative positions of the satellite, the Earth, and the Sun. Point S_1 and S_2 split line S_1S_2 into three segments. The dashed circles are the possible positions of the satellite on the line. S_1P_1 and S_2P_2 are tangent planes that touch the Earth at points P_1 and P_2 .

Because planes S_iP_i ($i \in 1, 2$) are tangent to the Earth ellipsoid and touch the Earth at P_1 and P_2 , the normal to the Earth at P_i are perpendicular to planes S_iP_i . Meanwhile, line S_1S_2 (which is also in the direction of vector \mathbf{n}) is perpendicular to planes S_iP_i . Therefore, the normal to the Earth at P_i are parallel to vector \mathbf{n} , which yields

$$\mathbf{A}\mathbf{x}_{\mathbf{P}_i} = s\mathbf{n} \quad (4.8)$$

where s is a parameter for the parallel condition ($s \neq 0$). \mathbf{A} is a matrix describing the Earth ellipsoid (see equation 4.1).

Because vector \mathbf{n} is perpendicular to the planes S_iP_i , \mathbf{n} is also perpendicular to the vectors from point S_i to point P_i that lie in plane S_iP_i . This yields

$$(\mathbf{x}_{\mathbf{P}_i} - \mathbf{x}_{\mathbf{S}_i})^T \mathbf{n} = 0, \quad i \in 1, 2 \quad (4.9)$$

Because P_i are on the surface of Earth ellipsoid, equation 4.8 can be substituted into equation 4.1. That yields

$$s^2 \mathbf{n}^T \mathbf{A}^{-1} \mathbf{n} = 1 \quad (4.10)$$

There are two solutions of parameter s to equation 4.10. They describe the positions of P_1 and P_2 separately. Thus, the positions of P_1 and P_2 can be obtained:

$$\mathbf{x}_{\mathbf{P}_i} = \pm s \mathbf{A}^{-1} \mathbf{n} \quad (4.11)$$

Substituting equation 4.11 and equation 4.7 into equation 4.9 yields

$$\mathbf{r}^T \mathbf{n} - t \mathbf{n}^T \mathbf{n} = \pm s \mathbf{n}^T \mathbf{A}^{-1} \mathbf{n} \quad (4.12)$$

4. SOLAR RADIATION FLUX MODELLING DURING ECLIPSES

From equation 4.10, we see

$$\mathbf{n}^T \mathbf{A}^{-1} \mathbf{n} = \frac{1}{s^2} \quad (4.13)$$

Thus, parameter t can be solved by

$$t = \frac{1}{\mathbf{n}^T \mathbf{n}} (\mathbf{r}^T \mathbf{n} \mp \frac{1}{s}) \quad (4.14)$$

Parameters s and t both have two solutions which correspond to the positions of S_1 and S_2 . Once the positions of S_1 and S_2 are calculated, those three cases can be distinguished by the variation range of the satellite–Sun distance. We define the distance from the Sun to S_1 as d_{S_1} , the distance from the Sun to S_2 as d_{S_2} and the distance from the Sun to the satellite as d . In the first case, the satellite cannot “see” the Earth, and it is denoted as "no image" in the following description. In the second case, the satellite only “sees” part of the Earth. Thus, it is described as "partial image". In the third case, the satellite can “see” the whole Earth, and it is denoted as "full image".

$$\begin{cases} \text{no image}, & d \leq d_{S_1} \\ \text{partial image}, & d_{S_1} < d < d_{S_2} \\ \text{full image}, & d \geq d_{S_2} \end{cases} \quad (4.15)$$

Note that for the first case, the satellite is in full phase. However, for the second and third cases, the eclipse state still needs to be confirmed by the following perspective projection calculation.

4.2.3 Perspective projection of the Earth and the Sun onto the image plane

The projection of the Sun on the image plane is always a circle because the satellite is staring at the centre of the Sun and the Sun is assumed to be a sphere in this study. When the satellite can ‘see’ the whole or part of the Earth, what is the shape of the Earth’s projection on the image plane? The answer can be worked out by using the perspective projection algorithm. As mentioned in the problem analysis, only when the equations of the perspective projects of the Sun and the Earth are known, the intersections between them can be worked out. The first question in the problem description can be answered based on the intersections. The coordinates of the intersections also provide key information for answering the second question.

For the situation when the ellipsoid is in front of the viewpoint (the full image case), [Eberly \[1999\]](#) proposed a method to calculate the equation of perspective projection of the ellipsoid. However, the approach needs to be extended to the partial image situation.

In general, the visible boundary of an ellipsoid is composed of points on the surface that have normals perpendicular to the line of sight from the satellite to the boundary points. Let \mathbf{g} be a unit vector which starts from the satellite to arbitrary boundary

4. SOLAR RADIATION FLUX MODELLING DURING ECLIPSES

points (i.e. a vector in the line of sight) . The coordinates of arbitrary points on the visible boundary are described in a parametric equation:

$$\mathbf{x}_a = \mathbf{r} + p\mathbf{g} \quad (4.16)$$

where p is a parameter representing the distance from the satellite to the boundary point. Because the satellite cannot be on the Earth's surface, parameter $p \neq 0$.

Necessarily all the boundary points are on the surface of the Earth. Their coordinates also satisfy the equation of the Earth ellipsoid. Substituting equation 4.16 into equation 4.1 yields

$$p^2\mathbf{g}^T\mathbf{A}\mathbf{g} + p(\mathbf{g}^T\mathbf{A}\mathbf{r} + \mathbf{r}^T\mathbf{A}\mathbf{g}) + \mathbf{r}^T\mathbf{A}\mathbf{r} = 1 \quad (4.17)$$

Equation 4.17 is a quadratic with respect to parameter p . Because the vectors in line of sight are tangent to the Earth's surface, the line of sight vectors only have one intersection with the Earth. That means the discriminant of the quadratic (equation 4.17) is 0.

$$(\mathbf{g}^T\mathbf{A}\mathbf{r})^2 - \mathbf{g}^T\mathbf{A}\mathbf{g}(\mathbf{r}^T\mathbf{A}\mathbf{r} - 1) = 0 \quad (4.18)$$

Equation 4.18 can also be expressed as

$$\mathbf{g}^T\mathbf{M}\mathbf{g} = 0 \quad (4.19)$$

where

$$\mathbf{M} = \mathbf{A}\mathbf{r}\mathbf{r}^T\mathbf{A}^T - (\mathbf{r}^T\mathbf{A}\mathbf{r} - 1)\mathbf{A}$$

Equation 4.19 is the condition that all of the vectors in line of sight (\mathbf{g}) should satisfy.

The points on the visible boundary, the projections of these points on the image plane and the viewpoint (the mass centre of the satellite) are on the line of sight. Let \mathbf{x}_b be the coordinates of the projection of the boundary points on the image plane, then, the vector $\mathbf{x}_b - \mathbf{r}$ is at the same direction as \mathbf{g} , and it should satisfy equation 4.19. That is

$$(\mathbf{x}_b - \mathbf{r})^T\mathbf{M}(\mathbf{x}_b - \mathbf{r}) = 0 \quad (4.20)$$

Because the projections are two dimensional in the ISF (see definition at section 4.2.1), the coordinates of the projections can also be described in the following form

$$\mathbf{x}_b = \mathbf{o} + \alpha\mathbf{u} + \beta\mathbf{v} \quad (4.21)$$

where \mathbf{u} and \mathbf{v} are the unit vectors of two ISF axes, \mathbf{o} is the origin of the ISF, α and β are the two dimensional coordinates of these projection points in ISF. Substituting equation 4.21 and equation 4.4 into equation 4.20 yields

$$k_0\alpha^2 + 2k_1\alpha\beta + k_2\beta^2 + k_3\alpha + k_4\beta + k_5 = 0 \quad (4.22)$$

4. SOLAR RADIATION FLUX MODELLING DURING ECLIPSES

where

$$\begin{cases} k_0 = \mathbf{u}^T \mathbf{M} \mathbf{u} \\ k_1 = \mathbf{u}^T \mathbf{M} \mathbf{v} \\ k_2 = \mathbf{v}^T \mathbf{M} \mathbf{v} \\ k_3 = -2\gamma \mathbf{u}^T \mathbf{M} \mathbf{n} \\ k_4 = -2\gamma \mathbf{v}^T \mathbf{M} \mathbf{n} \\ k_5 = \gamma^2 \mathbf{n}^T \mathbf{M} \mathbf{n} \end{cases}$$

In equation 4.22, γ is the distance from the satellite to the image plane. Equation 4.22 describes the projection of the Earth on the image plane. This quadratic is in a general form of conical curves. Equation 4.22 can also be written in the following form:

$$\chi^T \mathbf{B} \chi + \delta^T \chi + k_5 = 0 \quad (4.23)$$

where

$$\begin{cases} \chi = (\alpha, \beta)^T \\ \delta = (k_3, k_4)^T \\ \mathbf{B} = \begin{pmatrix} k_0 & k_1 \\ k_1 & k_2 \end{pmatrix} \end{cases}$$

The shape of the conical curve is determined by the determinant of matrix \mathbf{B} .

$$\begin{cases} \text{ellipse, } \|\mathbf{B}\| > 0 \\ \text{parabola, } \|\mathbf{B}\| = 0 \\ \text{hyperbola, } \|\mathbf{B}\| < 0 \end{cases} \quad (4.24)$$

The parabola case is an instantaneous state in the variation from an ellipse to a hyperbola, it is not discussed in this study. However, neither equation 4.23 nor equation 4.22 is in its standard form of conical curves. For the ellipse and hyperbola cases, a rotation and translation are applied to equation 4.23 to achieve the standard form. The eigendecomposition of real symmetric matrix \mathbf{B} is

$$\mathbf{B} = \mathbf{Q} \mathbf{D} \mathbf{Q}^T = \mathbf{Q} \mathbf{D} \mathbf{Q}^{-1} \quad (4.25)$$

where \mathbf{D} is a two dimensional diagonal matrix whose diagonal elements are the corresponding eigenvalues (i.e. $\mathbf{D} = \text{diag}\{\lambda_1, \lambda_2\}$), \mathbf{Q} is an orthogonal matrix whose i^{th} column is the i^{th} eigenvector.

Let $\phi = \mathbf{Q}^T \chi + \frac{1}{2} \mathbf{D}^{-1} \mathbf{Q}^T \delta$, equation 4.23 becomes

$$\phi^T \mathbf{D} \phi = \frac{1}{4} \delta^T \mathbf{B}^{-1} \delta - k_5 \quad (4.26)$$

Equation 4.26 is in the standard form of conical curves and describes the shape of the projection of the Earth on the image plane.

4. SOLAR RADIATION FLUX MODELLING DURING ECLIPSES

However, for the Sun (a sphere), the projection on the image plane is a circle. The radius of the circle R_0 is given

$$\frac{\gamma}{\|\mathbf{r} - \mathbf{r}_\odot\|} = \frac{R_0}{R_s} \quad (4.27)$$

That is

$$R_0 = \frac{\gamma R_s}{\|\mathbf{r} - \mathbf{r}_\odot\|} \quad (4.28)$$

In order to describe the circle and the conical curve in the same coordinate system, the equation of the circle has to be translated and rotated (The rotation transformation has no effect to the equation of the circle because the origin of the coordinate system before transformation lies at the centre of the circle). After performing the same transformation as the conical curve, the equation of the circle is

$$(\omega - \frac{1}{2}\mathbf{D}^{-1}\mathbf{Q}^T\delta)^T(\omega - \frac{1}{2}\mathbf{D}^{-1}\mathbf{Q}^T\delta) = R_0^2 \quad (4.29)$$

where ω is a 2-vector coordinates of any point on the projected circle after the transformation.

4.2.4 Solve the intersections between the projections of the Earth and the Sun

The intersections between projections of the Earth and the Sun can be determined by combining their equations together. Equation 4.26 and equation 4.29 form two simultaneous equations.

$$\begin{cases} (\mathbf{x} - \frac{1}{2}\mathbf{D}^{-1}\mathbf{Q}^T\delta)^T(\mathbf{x} - \frac{1}{2}\mathbf{D}^{-1}\mathbf{Q}^T\delta) = R_0^2 \\ \mathbf{x}^T\mathbf{D}\mathbf{x} = \frac{1}{4}\delta^T\mathbf{B}^{-1}\delta - k_5 \end{cases} \quad (4.30)$$

where \mathbf{x} is the coordinates of intersections between the circle and the conical curve.

The above equations 4.30 are also expressed as follows:

$$\begin{cases} (x - \frac{1}{2}t_x)^2 + (y - \frac{1}{2}t_y)^2 = R_0^2 \\ (\lambda_1 x^2 + \lambda_2 y^2) = \Omega - k_5 \end{cases} \quad (4.31)$$

where $\Omega = \frac{k_2 k_3^2 - 2k_1 k_3 k_4 + k_0 k_4^2}{4(k_0 k_2 - k_1^2)}$; $\mathbf{D}^{-1}\mathbf{Q}^T\delta = (t_x, t_y)^T$; $\mathbf{x} = (x, y)^T$. In order to solve equation 4.31, variable x and y are related to an unknown parameter η

$$\begin{cases} x = \frac{1 - \eta^2}{1 + \eta^2} R_0 + \frac{1}{2}t_x \\ y = \frac{2\eta}{1 + \eta^2} R_0 + \frac{1}{2}t_y \end{cases} \quad (4.32)$$

Substitute equation 4.32 into equation 4.31, a quartic with respect to parameter η is

4. SOLAR RADIATION FLUX MODELLING DURING ECLIPSES

obtained

$$a\eta^4 + b\eta^3 + c\eta^2 + d\eta + e = 0 \quad (4.33)$$

where

$$\begin{cases} a = \lambda_1(R_0 - \frac{1}{2}t_x)^2 + \frac{1}{4}\lambda_2t_y^2 - \Omega + k_5 \\ b = 2\lambda_2R_0t_y \\ c = \lambda_1(\frac{1}{2}t_x^2 - 2R_0^2) + \lambda_2(\frac{1}{2}t_y^2 + 4R_0^2) - 2\Omega + 2k_5 \\ d = 2\lambda_2R_0t_y \\ e = \lambda_1(R_0 + \frac{1}{2}t_x)^2 + \frac{1}{4}\lambda_2t_y^2 - \Omega + k_5 \end{cases}$$

The quartic can be solved using Ferrari's method. The detailed algorithm can be found in [Nonweiler \[1968\]](#). Once parameter η is obtained, the coordinates of the intersections between the Sun's image and the Earth's image can be computed using equation 4.32.

Now, we can fully answer the first question in the problem description. The answer is:

- If the quartic has two real solutions, the Sun is blocked by the Earth.
- If the quartic has no real solutions, there are two situations to deal with. The first situation is the centre of the circle (the projection of the Sun) is outside of the conical curve (the projection of the Earth), the Sun is not blocked by the Earth in this case and it is full phase. The second situation is the centre of the circle is fully inside the conical curve, this means the Sun is totally blocked by the Earth and it is umbra.

If equation 4.33 has real solutions, the Sun is partly blocked by the Earth and it is the penumbra state. The second question (How much of the Sun disk is not blocked?) in the problem description can be answered based on the overlapping area between the conical curve and the circle. The method of calculating the overlapping area is discussed in the next section.

4.2.5 Calculate the overlapping area

In the penumbra case, part of the solar disk is blocked by the Earth's image. The total area of the solar disk is split into the bright part (denoted as A_b) and the shaded part (denoted as A_s). i.e.

$$A_b + A_s = \pi R_0^2 \quad (4.34)$$

The area calculation is different for the hyperbolic and elliptical image of the Earth. For both the ellipse case and the hyperbola case, the calculation processes are separated according to the condition that if the centre of the Sun's image is inside the Earth's image or not. The condition that the Sun's image is inside the Earth's image is given

4. SOLAR RADIATION FLUX MODELLING DURING ECLIPSES

by

$$\begin{cases} \text{ellipse ; } & \frac{\Omega}{\Omega - k_5} \leq 1 \\ \text{hyperbola ; } & \frac{\Omega}{\Omega - k_5} \geq 1 \end{cases} \quad (4.35)$$

The centre of the circle is on the ellipse or the hyperbola when $\frac{\Omega}{\Omega - k_5} = 1$.

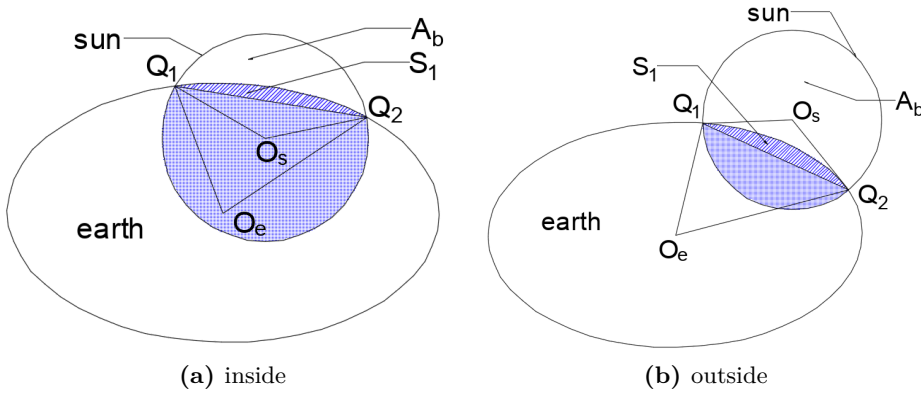


Figure 4.4: The situation where the Earth's image is an ellipse. Figure 4.4a is for that the centre of the solar disk is inside the Earth's image and Fig. 4.4b is for that the centre of the solar disk is outside the Earth's image. Q_1 and Q_2 are the two intersections between the ellipse and the circle. O_e and O_s are the projections of the centres of the Earth and the Sun separately.

Figure 4.4 and Fig. 4.5 show the two situations for the ellipse and hyperbola cases separately. The area of the bright part $A_{b,e,in}$ and the area of the shadow part $A_{s,e,in}$ of the ellipse situation in Fig. 4.4a are computed by

$$\begin{cases} A_{b,e,in} = S_{\widehat{Q_1 Q_2 O_s}} - S_{\triangle Q_1 Q_2 O_s} - S_1 \\ A_{s,e,in} = \pi R_0^2 - A_{b,e,in} \end{cases} \quad (4.36)$$

where

$S_{\widehat{Q_1 Q_2 O_s}}$: the area of the circular sector $Q_1 Q_2 O_s$.

$S_{\triangle Q_1 Q_2 O_s}$: the area of the triangle $Q_1 Q_2 O_s$.

S_1 : the area of the elliptical arch as shown in Fig. 4.4. Its calculation method can be found in [Hughes and Chraibi \[2012\]](#).

The area of the bright part $A_{b,e,out}$ and the area of the shadow part $A_{s,e,out}$ of the ellipse situation in Fig. 4.4b are computed by

$$\begin{cases} A_{b,e,out} = \pi R_0^2 - A_{s,e,out} \\ A_{s,e,out} = S_{\widehat{Q_1 Q_2 O_s}} - S_{\triangle Q_1 Q_2 O_s} + S_1 \end{cases} \quad (4.37)$$

The area of the bright part $A_{b,h,in}$ and the area of the shadow part $A_{s,h,in}$ of the

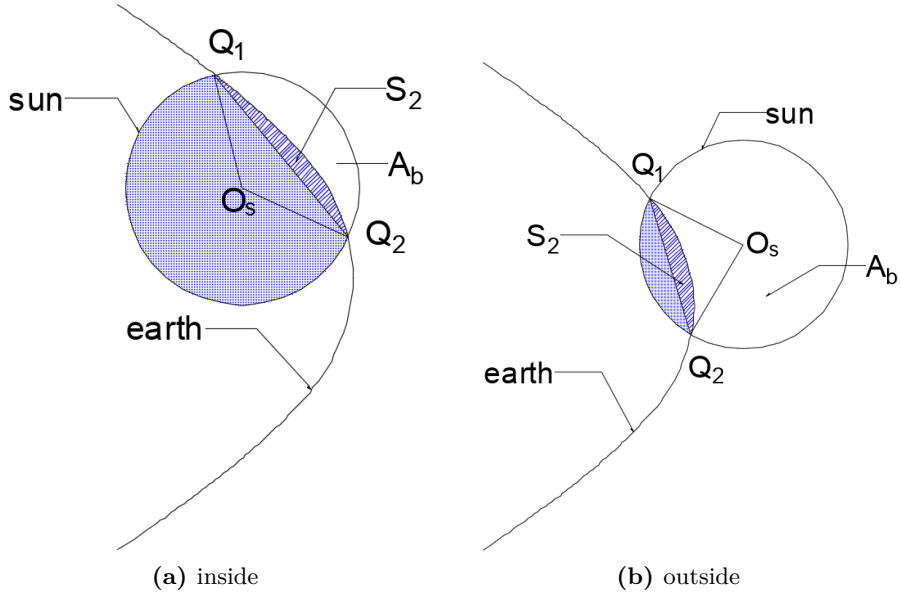


Figure 4.5: The situation where the Earth's image is a hyperbola. Figure 4.5a is for that the centre of the solar disk is inside the Earth's image and Fig. 4.5b is for that the centre of the solar disk is outside the Earth's image. Q_1 and Q_2 are the two intersections between the hyperbola and the circle. O_e and O_s are the projections of the centres of the Earth and the Sun separately.

hyperbola situation in Fig. 4.5a are computed by

$$\begin{cases} A_{b,h,in} = \widehat{S_{Q_1 Q_2 O_s}} - S_{\Delta Q_1 Q_2 O_s} - S_2 \\ A_{s,h,in} = \pi R_0^2 - A_{b,h,in} \end{cases} \quad (4.38)$$

where $\widehat{S_{Q_1 Q_2 O_s}}$ and $S_{\Delta Q_1 Q_2 O_s}$ have the same meanings as equation 4.36. S_2 is the area of elliptical arch as shown in Fig. 4.5.

The area of the bright part $A_{b,h,out}$ and the area of the shadow part $A_{s,h,out}$ of the hyperbola situation in Fig. 4.5b are computed by

$$\begin{cases} A_{b,h,out} = \pi R_0^2 - A_{s,h,out} \\ A_{s,h,out} = \widehat{S_{Q_1 Q_2 O_s}} - S_{\Delta Q_1 Q_2 O_s} + S_2 \end{cases} \quad (4.39)$$

This subsection describes the algorithm to calculate the unblocked area of the solar disk for both ellipse and hyperbola cases. The results can answer the second question in the problem description rigorously in mathematics.

4.3 The physical problem

Except for the geometrical problem, the shadow function modelling involves a physical problem as well. The physical processes of atmospheric effects like scattering, refraction, and absorption should be considered [Vokrouhlicky et al., 1993; 1994a;b]. But, it is very complex to consider the rigorous physical process in the modelling. Robertson

4. SOLAR RADIATION FLUX MODELLING DURING ECLIPSES

[2015] came up with a highly physical approach (not entirely rigorous but with some assumptions) to deal with it. In this study, we provide a simple approach to simulate the reduction of solar radiation due to the atmospheric effects.

One basic fact is that due to the atmospheric absorption, scattering and refraction, the solar radiation intensity (brightness) in the Earth's atmosphere is reduced. Denser air causes more reduction. The air density of the Earth's atmosphere is reduced from the Earth's surface to the TOA. Based on these facts, a function with respect to the depth in the atmosphere is used to describe the reduction of the solar radiation in the atmosphere.

The method proposed in this study has some assumptions and they are listed as follows:

- The TOA is assumed to be an ellipsoid that wraps the solid Earth ellipsoid (WGS-84 [Hofmann-Wellenhof et al., 1993]). The atmospheric effects to the reduction of solar radiation can be ignored at an altitude higher than 50 km [Robertson, 2015], therefore, the height of TOA in this shadow function modelling is set to be 50 km. The equatorial radius of the TOA is $a = 6428.137$ km, and the polar radius of the TOA is $b = 6406.584673$ km. With these assumptions, the TOA can be perspectively projected onto the image plane.
- The air density inside TOA is assumed to be centrally symmetric with the centre of Earth. This assumption makes the air density only relate to the depth in the atmosphere. The solar radiation does not get reduced outside of the TOA. The solar radiation flux becomes 0 for the part of the solar disk that is blocked by the solid Earth.
- On the image plane, for the points inside the projection of the atmosphere, the closer to the solid Earth, the more reduction of the solar radiation. The variation is assumed to be linear, that is, at the boundary of the TOA's projection, the radiation reduction coefficient is 1 (no reduction), at the boundary of the projection of the solid Earth, the radiation coefficient is 0 (the solar radiation flux reduced to 0).

Based on the above assumptions, a function $f(h)$ about the radiation reduction coefficient inside the atmosphere is defined (This function describes the ratio between current solar radiation intensity and that outside the atmosphere). The thickness H_0 (as shown in Fig. 4.6) of the atmosphere on the image can be different (because of distortions in perspective projection) depends on different positions of the satellite. For any point that has a distance h to the solid Earth in the direction from the centre of the Earth O_e to the centre of the Sun O_s on the image, the radiation reduction function inside the atmosphere is defined

$$f(h) = (\mu_2 - \mu_1) \frac{h}{H_0} + \mu_1 \quad (4.40)$$

4. SOLAR RADIATION FLUX MODELLING DURING ECLIPSES

where μ_1 is the radiation reduction value at the boundary of the solid Earth, μ_2 is the radiation reduction at the boundary of the atmosphere. At the boundary of the solid Earth, the solar radiation is thought to be blocked by the solid Earth ($\mu_1 = 0$); at the boundary of the TOA, the solar radiation is not blocked ($\mu_2 = 1$).

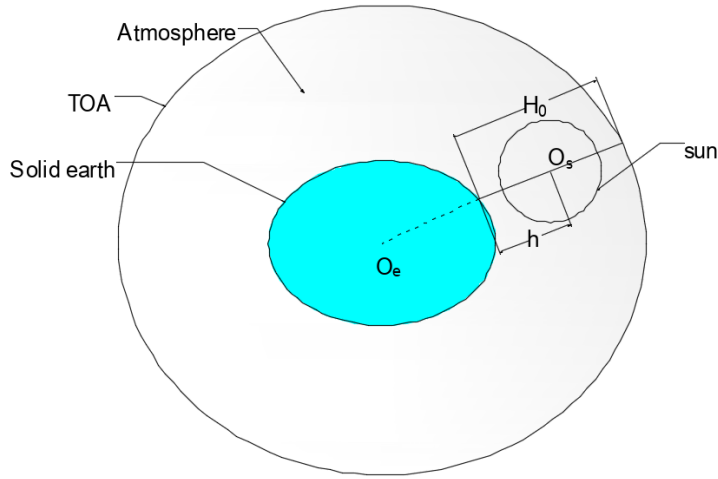


Figure 4.6: The projection (the ellipse case) of the solid Earth, the TOA and the Sun on the image. In this figure, the Sun's image is totally inside the atmosphere. O_e is the centre of the Earth's image, O_s is the centre of the Sun's image. The point that for the calculation of the radiation reduction lies exactly at the centre of the Sun in this figure, but it could be anywhere (inside the atmosphere's image) on the line O_eO_s .

This section gives out a simple approximation of the atmospheric effect to the solar radiation reduction. Comparing with the highly physical method discussed in [Robertson, 2015], the approach in this study is much easier to be implemented and can also produce good results in the shadow function modelling. The values of the shadow function are calculated by combining together the solutions to the geometrical problem and the physical problem.

4.4 The calculation of shadow function

The Sun's image will firstly intersect the TOA's image, then, it intersects the solid Earth's image in the process from the full phase to the umbra state. By applying the perspective projection algorithm, the coordinates of the intersections and the visible area of the solar disk are computed. The shadow function is a ratio between the solar radiation flux in the penumbra and that in full phase. The calculation of radiation flux that goes through the solar disk in umbra is calculated by the average radiation reduction coefficient of the solar disk times the area that is inside the atmosphere. In this way, the visible area of the solar disk and the solar radiation reduction function are combined to calculate the shadow function.

4. SOLAR RADIATION FLUX MODELLING DURING ECLIPSES

On the image composed by the projections of the TOA, the Earth, and the Sun; the relative positions between them are shown in Fig. 4.7. There are 5 possible cases for the position of the Sun on the image [Vokrouhlicky et al., 1993]. Case a indicates that the satellite is in full phase, the shadow function should be 1.0. Case e indicates that the satellite is in umbra, the shadow function is 0. Case b, c, and d indicate the satellite is in penumbra. The shadow function is calculated differently for these 3 cases. As shown in Fig. 4.8, G_1 and G_2 are the lower boundary and upper boundary of the Sun's image in the atmosphere in the direction from the centre of the solid Earth to centre of the solar disk. The coordinates of G_1 and G_2 are the intersections between a line (from the centre of the solid Earth's projection to the centre of the solar disk) and the solid Earth's projection, the solar disk separately. The solar radiation reduction $f(h_G)$ for the area of the solar disk that is in the atmosphere is the average of the solar radiation reduction at G_1 and G_2 . That is

$$f(h_G) = \frac{f(h_{G_1}) + f(h_{G_2})}{2} \quad (4.41)$$

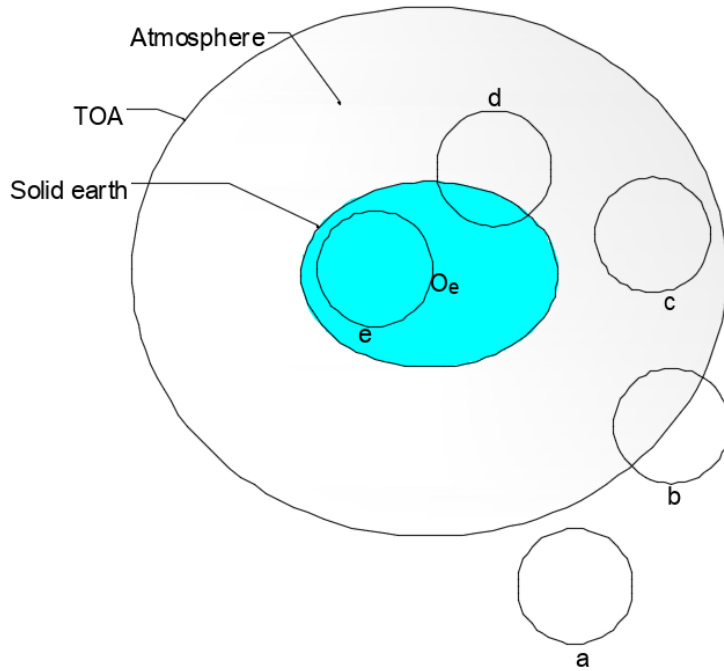


Figure 4.7: The 5 possible situations of the relative positions among the projections of the TOA, the Earth and the Sun. The circles represent the possible positions of the Sun's projection. Case a means the Sun is fully outside the TOA. Case b means part of the Sun's projection has entered Earth's atmosphere. Case c means the Sun's projection is fully in the projection of the atmosphere while case d means part of the Sun's projection is blocked by the solid Earth. Case e means the solar disk is fully blocked by the solid Earth.

case a

The satellite can see the full solar disk and the solar disk is not blocked by the atmo-

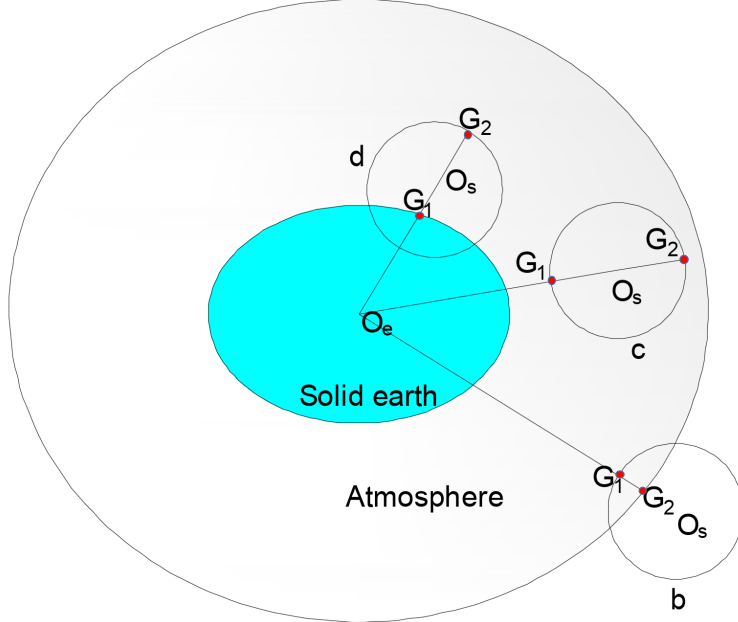


Figure 4.8: The cases b, c, and d in details. G₁ and G₂ are the lower boundary and upper boundary for the overlapping part between the Sun's image and the TOA's image.

sphere. The shadow function is

$$F_s = 1 \quad (4.42)$$

case b

In case b, part of the solar disk has entered the atmosphere's image as shown in Fig. 4.8. The area of the solar disk that is inside the atmosphere is $A_{s,b}$, and the area outside of the atmosphere's image is $A_{b,b}$. For the area inside the atmosphere, the solar radiation flux is $f(h_G)A_{s,b}$. For the area outside of the atmosphere, the solar radiation flux is $A_{b,b}$. In this case, because G_2 is at the boundary of the atmosphere, the solar radiation reduction coefficient at G_2 is $\mu_2=1$. The shadow function is calculated by

$$F_s = \frac{0.5(f(h_{G_1}) + \mu_2)A_{s,b} + A_{b,b}}{\pi R_0^2} \quad (4.43)$$

case c

In case c, the whole solar disk is inside the atmosphere's image. The shadow function is computed by

$$F_s = \frac{f(h_{G_1}) + f(h_{G_2})}{2} \quad (4.44)$$

case d

In case d, part of the solar disk is blocked by the solid Earth's image, part of the solar disk is inside the atmosphere's image. The area of the solar disk blocked by the Earth's image is $A_{s,d}$ while the area that is in the atmosphere is $A_{b,d}$. The solar radiation reduction coefficient for the area that is blocked by the solid Earth is 0. In the case

4. SOLAR RADIATION FLUX MODELLING DURING ECLIPSES

d in Fig. 4.8, G_1 lies on the boundary of the solid Earth's image, the solar radiation reduction coefficient is μ_1 ($\mu_1 = 0$). Thus the shadow function is given by

$$F_s = \frac{0.5(f(h_{G_2}) + \mu_1)A_{b,d}}{\pi R_0^2} \quad (4.45)$$

case e

For case e, the whole solar disk is blocked by the solid Earth, the shadow function is given

$$F_s = 0 \quad (4.46)$$

4.5 Algorithm implementation of the shadow function modelling

The core of shadow function modelling algorithm is the perspective projection. The inputs of the shadow function model is the position of the satellite, the position of the Sun and the output is the value of the shadow function. This section will firstly introduce the frame of the shadow function modelling in the first place, then the algorithm flow of the perspective projection.

Figure 4.9 shows the frame of the shadow function modelling algorithm. At the beginning of the algorithm, some parameters about the dimensions of the solid Earth ($a = 6378.137$ km, $b = 6356.752314$ km), and the height of the TOA (50 km) are initialized. The perspective projection algorithm is applied to the solid Earth and the TOA separately. There are 2 tests between the solar disk and the TOA or the solid Earth on the image plane. One is to test if the solar disk intersects the projection of the solid Earth or the TOA, the other is to test if the centre of the solar disk is inside the projection of the solid Earth or the TOA. The 5 cases discussed in section 4.4 are distinguished as shown in Tab. 4.2.

For each of the 5 cases, the distance from the Earth's centre to the boundary of the TOA on the image and the distances (h_{G_1} and h_{G_2}) from G_1 and G_2 to the centre of the solid Earth's projection are output from the perspective projection function. The thickness of TOA H_0 on the image is also worked out. Once these parameters are obtained, the shadow function can be calculated according to the Equations from Eq. 4.42 to Eq. 4.46.

In the perspective projection function, the TOA and the solid Earth are expressed as ellipsoids (spheroids) with different parameters. The inputs and outputs of the perspective projection function are described as follows:

Inputs:

a : equatorial radius of the ellipsoid;

b : polar radius of the ellipsoid;

\mathbf{r}_\odot : the position of the Sun;

\mathbf{r} : the position of the satellite;

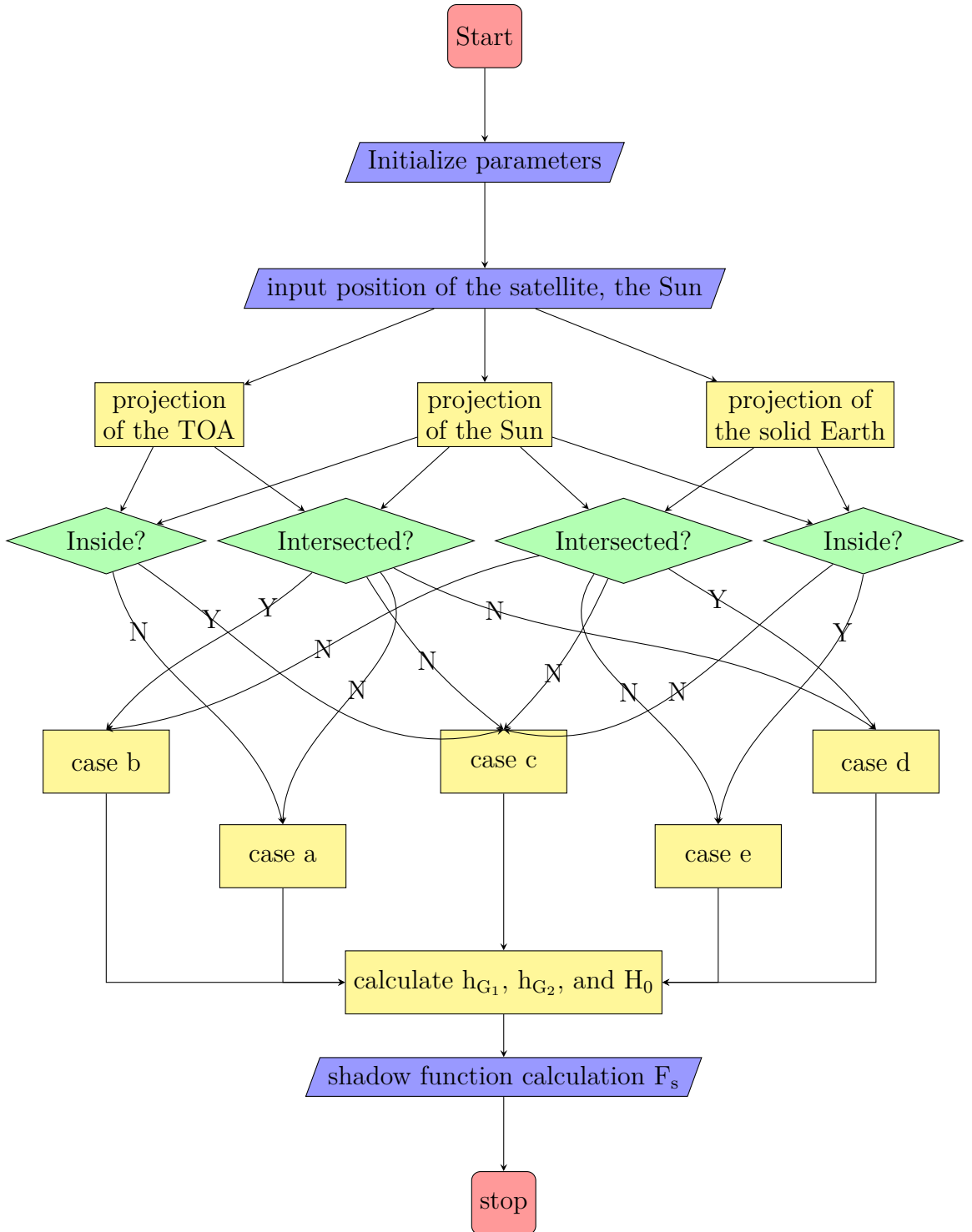


Figure 4.9: The algorithm flow of the shadow function modelling

4. SOLAR RADIATION FLUX MODELLING DURING ECLIPSES

Table 4.2: The conditions for the 5 cases

Cases	Intersection		Inside	
	solid Earth	TOA	solid Earth	TOA
case a		No		No
case b	No	Yes		
case c	No	No	No	Yes
case d	Yes	No		
case e	No		Yes	

Outputs:

r_{state} : the intersection state; the possible values are listed as follows:

$r_{state} = 0$, no intersection and the centre of the solar disk is outside the projection of the ellipsoid (solid Earth or the TOA);

$r_{state} = 1$, hyperbolic intersection;

$r_{state} = 2$, elliptic intersection;

$r_{state} = -1$, no intersection and the centre of the solar disk is inside the ellipsoid's projection;

A_b : the area of the solar disk that is not bocked by the ellipsoid;

h_{G_1} : the distance from the centre of the Earth to point G_1 .

h_{G_2} : the distance from the centre of the Earth to point G_2 .

The algorithm flow of the perspective projection is shown in Fig. 4.10. The first step is to build the ISF (Image Space Frame). Then check if the ellipsoid's image exist on the image plane (i.e. the condition $d < d_{S_1}$). If the condition is met, it is full phase and $r_{state} = 0$, which is the case a in the framework of the shadow function modelling algorithm in Fig. 4.9. If the condition is not met, the key part (solve the quartic Eq. 4.33) of the perspective projection is executed. If no real solution is found for the quartic, there are two cases according to the test that whether the centre of the solar disk is inside or outside of the image of the ellipsoid. For the situation that the centre of the solar disk is inside the ellipsoid's image, $r_{state} = -1$; $r_{state} = 0$ for the situation that the centre of the solar disk is outside the ellipsoid's image. If real solutions to the quartic are found, the area of the bright part (not blocked by the ellipsoid) of the solar disk is calculated differently according to the shape of the ellipsoid's image (ellipse or hyperbola). $r_{state} = 1$ for the hyperbola case and $r_{state} = 2$ for the ellipse case.

In order to make a better contribution to the community, the working code (C++) of the model PPM_atm is published on github at this link: http://github.com/whulizhen/PPM_atm_shadow_function.git.

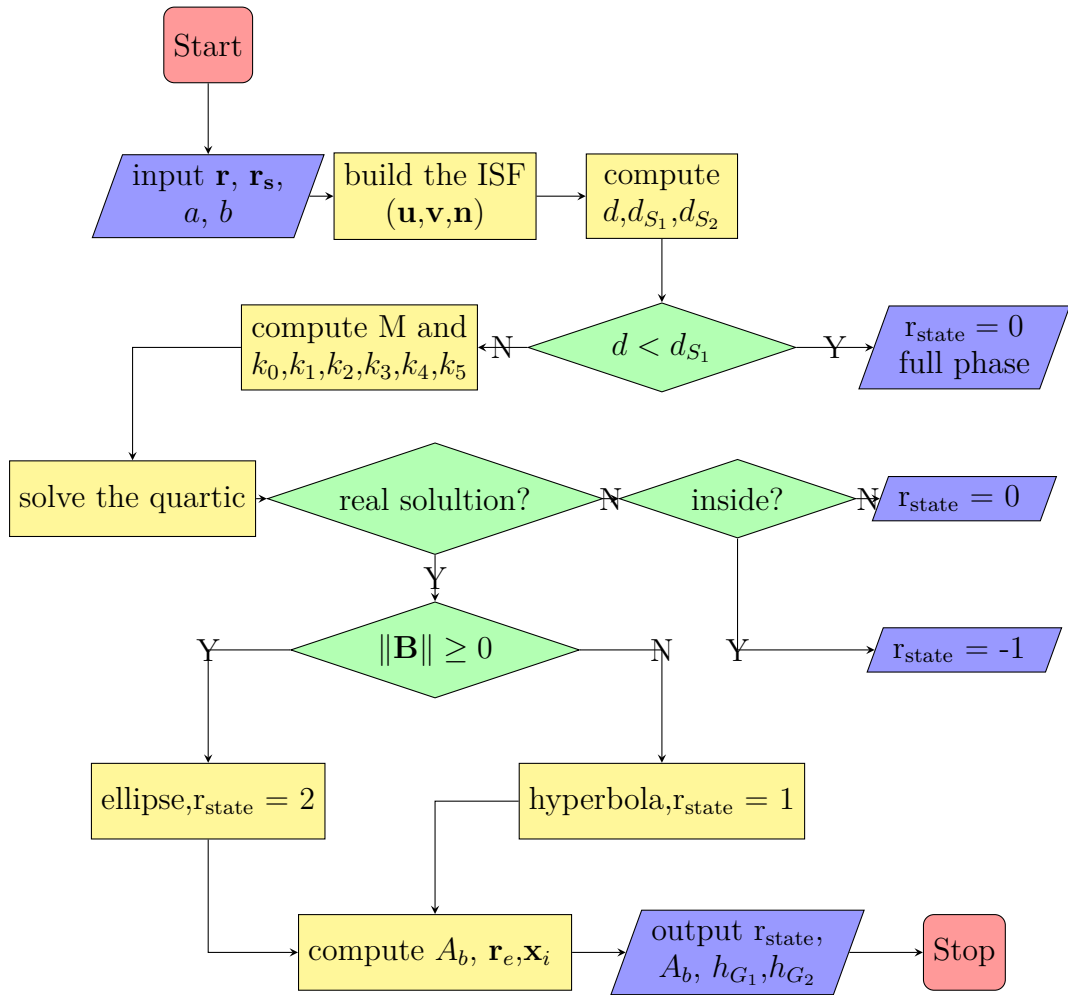


Figure 4.10: The algorithm flow of the perspective projection

4.6 Results

The modelled shadow function is compared to the GRACE accelerometer measurements – essentially as a consistency check, although we treat the GRACE data as the “truth”. The GRACE spacecraft [Tapley et al., 2004] carry accelerometers to record the non-gravitational forces and thruster events. The transition from full phase to umbra causes variations in solar radiation pressure on the GRACE spacecraft, thus, the accelerometer measurements can reveal the variation of the shadow function. GRACE level-1B products record all the available measurements of the accelerometers [Case et al., 2010]. Therefore, the level-1B accelerometer data (calibrated using the *a priori* calibration parameters in Bettadpur [2009]) are used as a baseline to validate the accuracy of the shadow function model.

In the tests, we introduce 5 different shadow function models (the PPM, the PPM_atm, the SECM, the SECM_atm, the “linear”). The shadow function models are listed as follows:

- PPM_atm: it considers both the Earth’s oblateness and the atmospheric effects in the modelling.
- PPM: it considers only the Earth’s oblateness and ignores the atmospheric effects in the modelling.
- SECM: it uses a sphere (a radius of 6371 km) to represent the solid Earth. Thus, it ignores both the Earth’s oblateness and the atmospheric effects.
- SECM_atm: it uses a sphere (a radius of 6371 km) to represent the solid Earth. It ignores the Earth’s oblateness but includes the atmospheric effects in the modelling.
- linear: The “linear” shadow function is implemented to compare extend the method in Adhya et al. [2004]. There is no shadow function proposed in Adhya et al. [2004], only the penumbra entry/exit time is determined considering the Earth’s oblateness. This “linear” shadow function just simply connects the penumbra entry and exit time and reduce its value from 1 to 0.

4.6.1 The GRACE accelerometer observations and shadow function

GRACE is one of the missions under the NASA Earth System Science Pathfinder (ESSP) program which is used to accurately map variations in Earth’s gravity field. It consists of two identical spacecraft that fly about 220 km apart in a polar orbit at a height of about 500 km (as shown in Fig. 4.11). They were launched on March 17, 2002 and designed to have a lifespan of 5 years. The two spacecraft carry accelerometers to measure the non-conservative forces (including atmospheric drag and radiation pressure). There are gravitational force and non-gravitational forces acting on the

4. SOLAR RADIATION FLUX MODELLING DURING ECLIPSES

spacecraft. The centre of the proof-mass of the accelerometer is placed at the spacecraft centre of gravity [Touboul et al., 1999]. In this way, the motion of the proof-mass of the accelerometer relative to the spacecraft centre of gravity is only driven by the non-gravitational force [Klinger and Mayer-Gürr, 2016]. The motion of the proof-mass is then measured and output as voltage measurements.

During the transition from full phase to umbra or vice versa, the reduction in the solar radiation can cause reduction in the solar radiation pressure which can be recorded by the accelerometers on board. The mission analysis centre made the level-1B products public which contains all the available measurements from the accelerometers [Case et al., 2010].



Figure 4.11: The two GRACE satellites on a polar orbit.

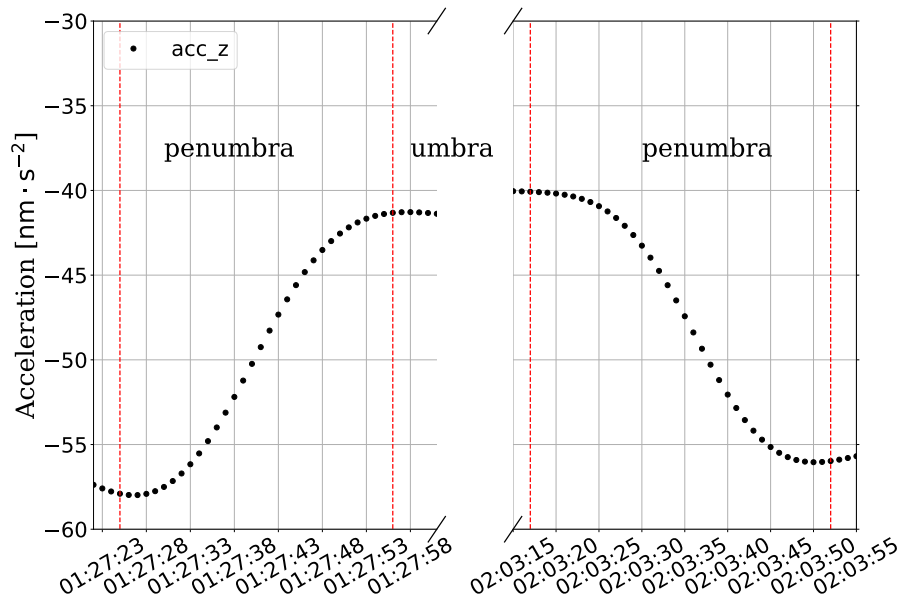


Figure 4.12: The z component of accelerometer observations in satellite frame of GRACE-A satellite. The epochs are in GPS time [H:M:S].

4. SOLAR RADIATION FLUX MODELLING DURING ECLIPSES

When the GRACE satellites are in eclipse, the sun elevation over their orbital planes are usually small. In these cases, the solar radiation pressure is mainly in the z-axis of the satellite frame (also the z axis of the science reference frame which is where all the Level-1B data products are specified in [Bettadpur, 2012]). Thus, the z component of the accelerometer observations are used to obtain an acceleration derived shadow function $F_{s,acc}$. It is computed by normalising the acceleration observations with Eq. 4.47.

$$F_{s,acc} = \frac{\zeta_t - \zeta_0}{\zeta_1 - \zeta_0} \quad (4.47)$$

where ζ_t is the acceleration, ζ_0 is the acceleration at umbra and ζ_1 is the acceleration at full phase.

Figure 4.12 shows one eclipse event for GRACE-A satellite on Jan. 20th 2007. The left half shows the variations of acceleration from full phase to umbra while the right half shows the accelerations from umbra to full phase. It shows that the accelerometer observations contain clear signals of shadow function.

4.6.2 GRACE results

The data used in this study are the accelerometer observations of GRACE-A satellite on January 20th 2007. There are 16 eclipse events on that day. The total number of penumbra transitions is 30. The entry/exit time for the penumbra are shown in Tab. 4.3. The accelerations for all these 30 penumbra transitions are converted into shadow function $F_{s,acc}$ according to Eq. 4.47. The 5 shadow function models are compared to $F_{s,acc}$ and the differences between them are calculated separately. Figure 4.13a (from full phase to umbra) and Fig. 4.13b (from umbra to full phase) show the comparisons for 2 penumbra transitions.

If the values of $F_{s,acc}$ are taken as the “truth”, the differences between the other 5 shadow functions models and $F_{s,acc}$ are the errors of these models. The mean and standard deviation of the errors for the 5 shadow function models are shown in Tab. 4.4.

Among all the 5 shadow function models, the newly developed model PPM_atm is the closest to the “observed” $F_{s,acc}$. Results in Tab. 4.4 show that the PPM_atm has an error of about 0.79% while the widely used SECM 11.07%. The accuracy of the shadow function can be improved by a factor of 10 using the PPM_atm.

4.6.3 Galileo results

The Galileo satellites do not carry accelerometers. There are no direct observations for the shadow function. Based on the results from GRACE-A satellite that the PPM_atm is the closest to the observations, we can take the PPM_atm as the “truth” and compare it with the other shadow function models. This can help to analyse the errors in different shadow function models.

4. SOLAR RADIATION FLUX MODELLING DURING ECLIPSES

Table 4.3: The penumbra entry/exit time (in GPS time) for GRACE-A satellite on 20th January, 2007 (time format: H:M:S).

event #	entry1	exit1	entry2	exit2
1			00:29:24	00:29:52
2	01:27:25	01:27:55	02:03:21	02:03:51
3	03:01:24	03:01:53	03:37:22	03:37:50
4	04:35:24	04:35:52	05:11:21	05:11:49
5	06:09:22	06:09:55	06:45:20	06:45:48
6	07:43:22	07:43:50	08:19:20	08:19:47
7	09:17:22	09:17:49	09:53:19	09:53:46
8	10:51:20	10:51:52	11:27:18	11:27:45
9	12:25:20	12:25:48	13:01:17	13:01:44
10	13:59:19	13:59:47	14:35:16	14:35:44
11	15:33:17	15:33:46	16:09:15	16:09:43
12	17:07:17	17:07:45	17:43:14	17:43:42
13	18:41:16	18:41:44	19:17:13	19:17:41
14	20:15:15	20:15:43	20:51:12	20:51:40
15	21:49:14	21:49:42	22:25:12	22:25:39
16	23:23:13	23:23:40		

Table 4.4: The error statistics of different shadow function models based on the comparison with $F_{s,acc}$ for GRACE-A satellite (over 30 penumbra transitions)

Shadow function Model	mean	standard deviation
PPM	0.2314	0.2417
PPM_atm	-0.0079	0.0220
SECM	0.1107	0.1741
SECM_atm	-0.1350	0.0899
linear	0.2427	0.2564

Table 4.5: The error statistics of the differences between the PPM_atm and the other shadow function models for Galileo E11 (over 34 penumbra transitions)

Shadow function Model	mean	standard deviation
SECM	0.0528	0.0306
PPM	0.0657	0.0374
SECM_atm	-0.0131	0.0071
linear	0.0651	0.0435

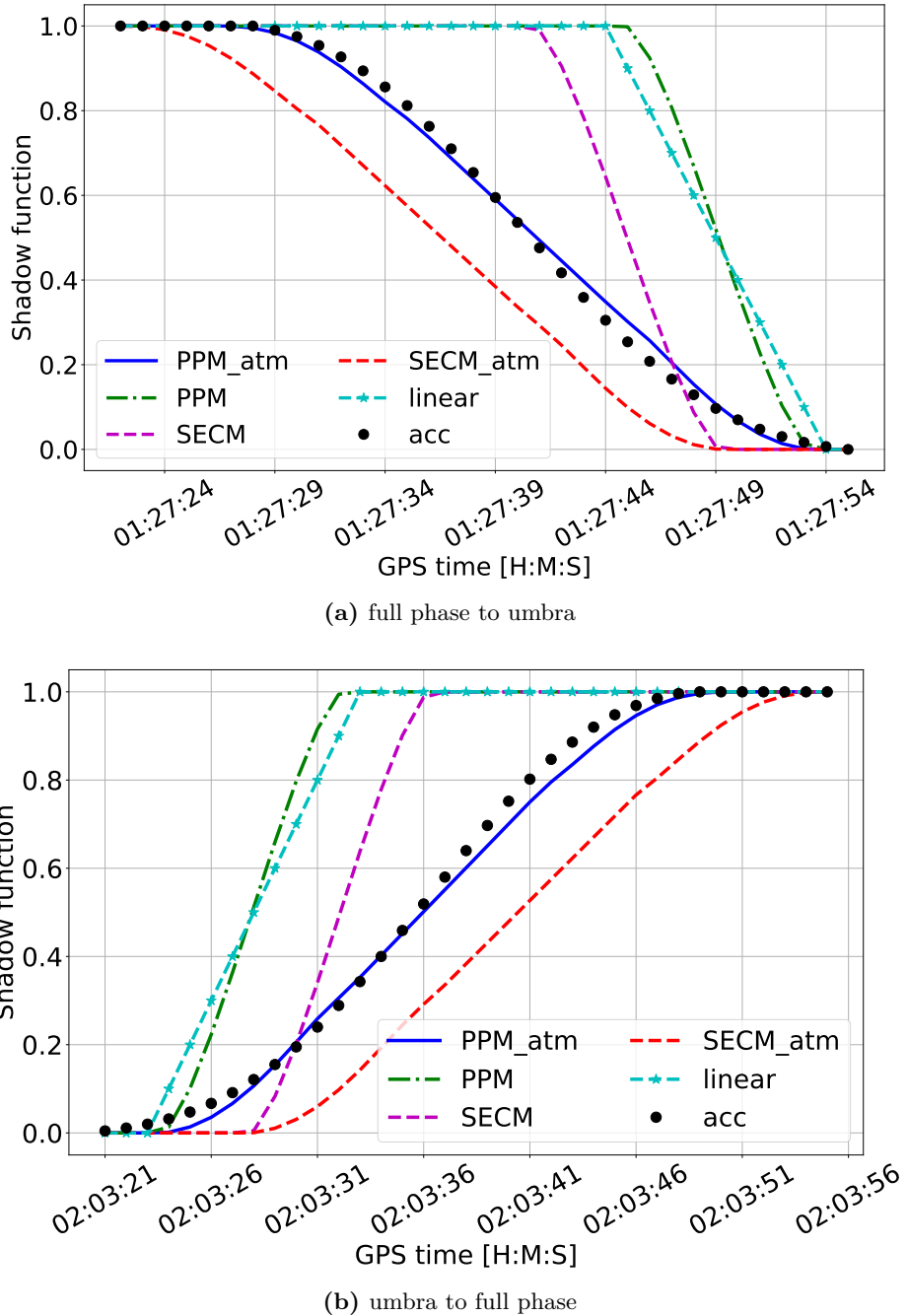


Figure 4.13: The changes of shadow function during one eclipse event for GRACE-A satellite on Jan 20th, 2007

4. SOLAR RADIATION FLUX MODELLING DURING ECLIPSES

In this experiment, one Galileo IOV satellite (E11) is chosen. The precise orbit of the Galileo satellites are provide by the CODE. There are 17 eclipse events (34 penumbra transitions) for E11 from 6th to 15th January, 2015 (see Tab. 4.6). Figure 4.14 shows the variations of shadow function for different models during one eclipse event on January 11th, 2015. The statistics of the differences between the other 4 models and the PPM_atm are shown in Tab. 4.5. Among the models SECM, PPM, and SECM_atm, the SECM_atm is the closest to the PPM_atm. This also means that the models with the atmospheric effects are closer to each other, i.e. the atmospheric effects are more important than the Earth's oblateness in the shadow function modelling.

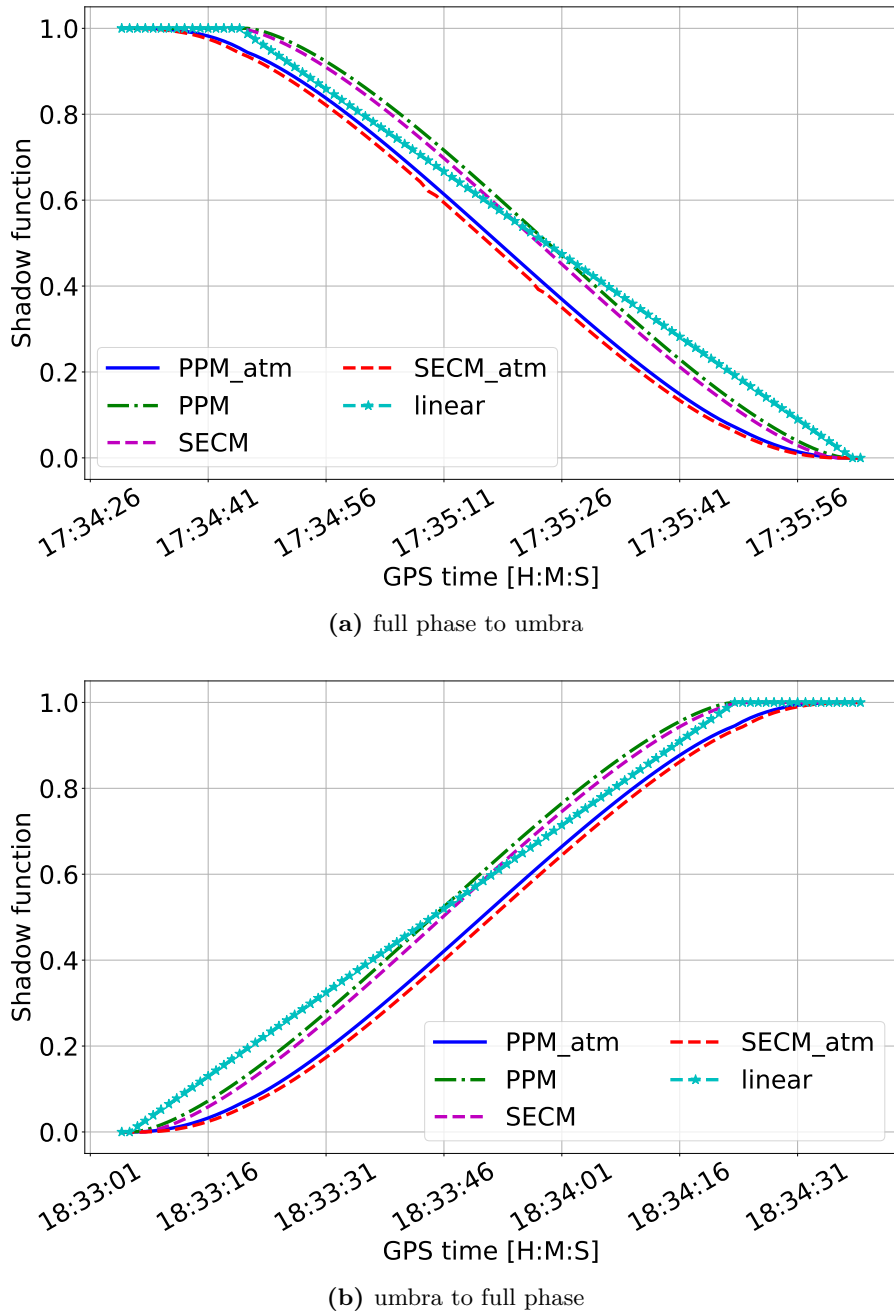


Figure 4.14: The variations of shadow function during one eclipse event for Galileo E11 on Jan 11th, 2015

4. SOLAR RADIATION FLUX MODELLING DURING ECLIPSES

Table 4.6: The penumbra entry/exit time (in GPS time, time format: Y/M/D:h:m:s) for Galileo E11 from 6th to 15th January, 2015.

penumbra #	entry	exit	duration (second)
1	2015/01/06/10:48:12	2015/01/06/10:49:49	97
2	2015/01/06/11:42:29	2015/01/06/11:44:06	97
3	2015/01/07/00:53:07	2015/01/07/00:54:43	96
4	2015/01/07/01:48:21	2015/01/07/01:49:57	96
5	2015/01/07/14:58:07	2015/01/07/14:59:41	94
6	2015/01/07/15:54:10	2015/01/07/15:55:44	94
7	2015/01/08/05:03:09	2015/01/08/05:04:43	94
8	2015/01/08/05:59:54	2015/01/08/06:01:27	93
9	2015/01/08/19:08:15	2015/01/08/19:09:48	93
10	2015/01/08/20:05:35	2015/01/08/20:07:07	92
11	2015/01/09/09:13:25	2015/01/09/09:14:56	91
12	2015/01/09/10:11:12	2015/01/09/10:12:44	92
13	2015/01/09/23:18:37	2015/01/09/23:20:08	91
14	2015/01/10/00:16:46	2015/01/10/00:18:17	91
15	2015/01/10/13:23:52	2015/01/10/13:25:23	91
16	2015/01/10/14:22:16	2015/01/10/14:23:47	91
17	2015/01/11/03:29:11	2015/01/11/03:30:41	90
18	2015/01/11/04:27:43	2015/01/11/04:29:14	91
19	2015/01/11/17:34:33	2015/01/11/17:36:03	90
20	2015/01/11/18:33:07	2015/01/11/18:34:37	90
21	2015/01/12/07:39:57	2015/01/12/07:41:28	91
22	2015/01/12/08:38:27	2015/01/12/08:39:58	91
23	2015/01/12/21:45:25	2015/01/12/21:46:56	91
24	2015/01/12/22:43:45	2015/01/12/22:45:15	90
25	2015/01/13/11:50:56	2015/01/13/11:52:27	91
26	2015/01/13/12:48:58	2015/01/13/12:50:30	92
27	2015/01/14/01:56:30	2015/01/14/01:58:02	92
28	2015/01/14/02:54:09	2015/01/14/02:55:41	92
29	2015/01/14/16:02:07	2015/01/14/16:03:40	93
30	2015/01/14/16:59:16	2015/01/14/17:00:48	92
31	2015/01/15/06:07:48	2015/01/15/06:09:22	94
32	2015/01/15/07:04:19	2015/01/15/07:05:53	94
33	2015/01/15/20:13:33	2015/01/15/20:15:08	95
34	2015/01/15/21:09:19	2015/01/15/21:10:54	95

4.7 Summary

In this chapter, a shadow function model (the PPM_atm) that describes the solar radiation flux reduction when satellites are in eclipse is put forward. The newly developed model PPM_atm considers the Earth's oblateness (the geometrical problem) and the Earth's atmospheric effects (the physical problem) in the modelling. The geometrical problem is solved using perspective projection and the physical problem is dealt with a simple linear solar radiation reduction function. The combination of these two produces

4. SOLAR RADIATION FLUX MODELLING DURING ECLIPSES

the PPM_atm.

The performance of the PPM_atm is evaluated using the GRACE-A accelerometer observations. In addition, several other shadow function models like the SECM, SECM_atm, PPM and the “linear” model are developed and compared with the PPM_atm. The accelerometer observations over 30 penumbra transitions of GRACE-A satellite show that the errors in the PPM_atm have an average of -0.0079 and standard deviation of 0.0220. This indicates that the PPM_atm has a better accuracy than the widely used SECM by a factor of 10 (see Tab. 4.4).

There is no direct way to assess the performance of the PPM_atm on Galileo satellites due to the fact that the Galileo satellites do not carry accelerometers. According to the results from GRACE-A satellite, it is reasonable to take the PPM_atm as the “truth”. In this way, the errors of the other 4 shadow function models are computed for Galileo E11 satellite over 36 penumbra transitions. The statistics are shown in Tab. 4.5. The SECM has about 5.28% error while the SECM_atm has only -1.31% error. Furthermore, the PPM has larger error than the SECM as shown in both Tab. 4.4 and Tab. 4.5. The PPM only consider the Earth’s oblateness and ignore the atmospheric effects in modelling. The SECM uses a sphere to represent the shape of the Earth and ignores the atmospheric effects as well. This means the SECM have errors in solving both the geometrical problem and the physical problem. Based on the fact that the SECM is better than the PPM but worse than the PPM_atm, we can conclude that the errors in approximating the Earth’s shape and the errors in modelling the atmospheric effects can cancel to some degree.

4. SOLAR RADIATION FLUX MODELLING DURING ECLIPSES

Chapter 5

Interactions between radiation flux and satellite surface

According to how the radiation flux is generated, the interactions between radiation flux and the satellite surfaces are classified into two types: the active and passive. The active means that the surface itself emits radiation flux while the passive case means the radiation flux is from the outside of the satellite. In this study, the forces such as direct solar radiation pressure, Earth radiation pressure are generated by the passive interactions between the radiation flux and the surfaces. The antenna thrust and the thermal re-radiation pressure due to the re-radiation of the absorbed solar and Earth radiation belong to the active classification.

In this chapter, we firstly introduce the physical foundation of radiation pressure, including both the active and the passive cases. Then, the information on Galileo IOV and FOC satellites including the 3D surface model, optical properties, and mass are introduced. Based on structures of the Galileo IOV and FOC satellites, the radiation force computation is separated into two parts: the modelling of the solar panels and the computation for the satellite bus. The physical formula is directly applied in calculation of the direct solar radiation pressure and direct Earth radiation pressure due to a simple geometry of the solar panels. A ray tracing approach is applied to the satellite bus to deal with the complex geometry. In order to make the models easy to use, a user algorithm is described.

5.1 Physical foundation of radiation pressure

Physical foundation is the basis of radiation pressure modelling. The theory of radiation pressure was revealed by Maxwell as an assertion based on his theory of electromagnetism. The radiation pressure phenomenon was then validated in experiments by [Lebedev \[1901\]](#); [Nichols and Hull \[1902\]](#). According to Maxwell's theory, an electromagnetic wave carries momentum which can be transferred to a reflecting or absorbing surface hit by the wave. The momentum exchange generates a force on the surface. By applying Einstein's special theory of relativity and the theorem of impulse, the force

5. INTERACTIONS BETWEEN RADIATION FLUX AND SATELLITE SURFACE

generated by the electromagnetic wave is obtained.

The momentum of a photon of frequency f is given by

$$p = \frac{hf}{c} \quad (5.1)$$

where h is Planck's constant, c is the light speed.

5.1.1 The active case

In the modelling of the active case, assume there are N_f photons of frequency f emitting out from a surface of unit area at a unit time in the surface normal direction (\mathbf{n}). According to the conservation of momentum of the system consisting of radiation flux and the surface, the momentum exchange at a unit time $\Delta\mathbf{p}_f$ is calculated by

$$\frac{N_f hf}{c} \mathbf{n} + \Delta\mathbf{p}_f = 0 \quad (5.2)$$

Equation 5.2 is integrated over the solar radiation spectrum (assume the wavelength range is from 0 to ∞). The momentum change can be expressed

$$\Delta\mathbf{P} = - \int_0^\infty \frac{N_f hf}{c} df \mathbf{n} \quad (5.3)$$

The momentum change at a unit time is actually a force. Thus, the radiation force is

$$\mathbf{F} = - \int_0^\infty \frac{N_f hf}{c} df \mathbf{n} \quad (5.4)$$

The radiant power ($\int_0^\infty N_f hf df$) is the irradiance times the area that is normal to the flux. In the active case, the radiation flux is assumed to be in the normal of the surface. Thus, the force is also expressed:

$$\mathbf{F} = - \frac{WA}{c} \mathbf{n} \quad (5.5)$$

where W is the radiation flux (in the unit of $\text{W} \cdot \text{m}^{-2}$), A is the surface area.

5.1.2 The passive case

In the modelling of the passive case, the incident radiation flux has a amount of N_f photons of frequency f going through a unit area at a unit time. When the incident radiation flux hits the surface, the radiation flux gets reflected and absorbed as shown in Fig. 5.1. Assume the number of photons that are reflected is $\nu_f N_f$. Within the reflected, there are $\mu_f \nu_f N_f$ photons getting specularly reflected and the rest gets diffusely reflected. In the calculation of diffuse reflection, the surface is assumed to be Lambertian which means the intensity of the diffusely reflected flux falls off by a factor of $\cos \theta$ away from the normal to the surface. Thus, the proportion of diffusely reflected radiation that is emitted normal to the surface is $\frac{2}{3}$ [Fliegel et al., 1992; Ziebart, 2004].

5. INTERACTIONS BETWEEN RADIATION FLUX AND SATELLITE SURFACE

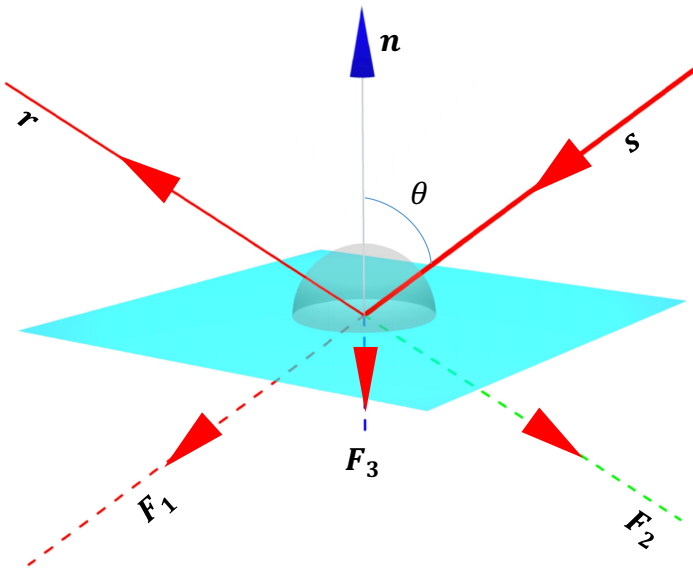


Figure 5.1: The force effects due to incident rays (incident angle θ) on a plane. The incident rays are in \mathbf{s} direction, the normal to the plane is \mathbf{n} and the specular reflection direction is \mathbf{r} . The diffusely reflected radiation is distributed in a semi-sphere but the force \mathbf{F}_3 is in $-\mathbf{n}$ direction. The direct hit of the incident rays generate force \mathbf{F}_1 and the specularly reflected rays generate force \mathbf{F}_2 .

Similarly, the conservation of momentum is applied to the radiation flux and the surface which yields

$$\frac{N_f h f}{c} \mathbf{s} = \nu_f \mu_f \frac{N_f h f}{c} \mathbf{r} + \frac{2}{3} \nu_f (1 - \mu_f) \frac{N_f h f}{c} \mathbf{n} + \Delta \mathbf{p}_f \quad (5.6)$$

where

\mathbf{s} : the incident unit vector.

\mathbf{r} : the unit vector of specularly reflected ray, $\mathbf{r} = \mathbf{s} - 2(\mathbf{s} \cdot \mathbf{n})\mathbf{n}$.

The momentum exchange is also integrated over the whole radiation spectrum and yields:

$$\Delta \mathbf{P} = \int_0^\infty \frac{N_f h f}{c} \left\{ \mathbf{s} - \nu_f \mu_f \mathbf{r} - \frac{2}{3} \nu_f (1 - \mu_f) \mathbf{n} \right\} df \quad (5.7)$$

The power of incident radiation flux (in the units of W) is

$$E = \int_0^\infty N_f h f df \quad (5.8)$$

In the passive case, the power of specularly reflected radiation E_s and the power of diffusely reflected radiation are expressed

$$\begin{cases} E_s = \int_0^\infty \nu_f \mu_f N_f h f df \\ E_d = \int_0^\infty \nu_f (1 - \mu_f) N_f h f df \end{cases} \quad (5.9)$$

5. INTERACTIONS BETWEEN RADIATION FLUX AND SATELLITE SURFACE

The reflectivity ν and specularity μ of the surface over the whole spectrum are defined as follows:

$$\begin{cases} \nu\mu = \frac{E_s}{E} \\ \nu(1 - \mu) = \frac{E_d}{E} \end{cases} \quad (5.10)$$

Therefore

$$\begin{cases} \nu = \frac{E_s + E_d}{E} \\ \mu = \frac{E_s}{E_s + E_d} \end{cases} \quad (5.11)$$

optical properties ν and μ are important in the calculation of radiation force, usually they are measured in laboratory for various materials within the solar radiation spectrum.

Similar as the active case, the force is computed from $\Delta\mathbf{P}$. The difference is that the radiation flux may not be in the surface normal. Given the surface area A and the incident angle θ , the cross-sectional area that is normal to the flux is $A \cos \theta$. Thus

$$\mathbf{F} = \frac{WA \cos \theta}{c} \left\{ \mathbf{s} - \nu\mu \mathbf{r} - \frac{2}{3}\nu(1 - \mu)\mathbf{n} \right\} \quad (5.12)$$

where W is the incident radiation flux and $\cos \theta = -\mathbf{s} \cdot \mathbf{n}$

Equation 5.5 and Eq. 5.12 are the foundation of radiation pressure calculation, they will be used in the computation of the solar radiation pressure, thermal radiation pressure, Earth radiation pressure, and antenna thrust.

5.2 Galileo satellites information description

OHB System is the industrial prime contractor responsible for the total of 22 Galileo FOC satellites. EADS Astrium (now Airbus Defence and Space) manufactured the Galileo IOV satellites. The obtaining of information on Galileo satellites' design and engineering parameters have to be authorized by the European Commission. In this study, we have obtained a series of documents on the satellite's design and test reports (reports on the attitude performance tests, thermal control tests). We extracted useful information from these documents for radiation pressure modelling.

5.2.1 General structures of the Galileo IOV and FOC satellites

Both Galileo IOV and FOC satellites have a pair of solar panels and a satellite bus (see Fig. 5.2). The solar panels are in a simple geometry which makes the modelling of direct solar and Earth radiation pressure easier than the satellite bus. However, the operating status of the solar cells and the power drawn on the solar panels make the thermal radiation pressure modelling complex. The satellite bus is in a complex shape and its surface is covered with different materials, making it difficult in computing the radiation forces.

5. INTERACTIONS BETWEEN RADIATION FLUX AND SATELLITE SURFACE



Figure 5.2: The artists' view of Galileo IOV (left) and FOC (right) satellites [ESA, 2015].

In this study, the solar panels are treated as a plane in the modelling of direct solar and Earth radiation pressure. The Sun-facing side of the solar panels is covered by solar cells to collect energy while the rear side is made of different material from the sun-facing side. This makes the optical properties different for the sun-facing side and rear side of the solar panels. Under the nominal attitude, the sun-facing side is always facing the Sun and be illuminated by both the solar and Earth radiation, the rear side is only illuminated by the Earth radiation. The sun-facing side and rear side of the solar panels have different temperatures and the temperature gradient causes a force. But, the solar panel surface temperature is affected by the satellite power draw. Due to a lack of the duty cycle information of the solar panels, the thermal gradient force on the solar panels is not modelled.

The satellite bus is where all the payload stored in. Its shape is much like a “box” for all the Galileo satellites. The satellite bus structures of the IOV and FOC satellites are shown in Fig. 5.3a and 5.3b separately. In radiation pressure modelling, its surface materials are classified into 3 types: the MLI, the radiators and non-MLI material. These three types of materials are different in modelling the thermal radiation flux (see chapter 3.3). The MLI is a main contributor to thermal radiation forces. There are large radiators (almost the whole y panel is covered by radiators) on the $+y$ and $-y$ panels. The $+x$ panel is mounted with radiators to provide a stable temperature for the atomic clocks. There are radiators on the $+z$ panels of the FOC satellite bus but not the IOV satellite bus. The imbalance in the power of radiators between $-y$ and $+y$ panels are thought to be a source of the so-called “ y -bias”. The $+x$ and $+z$ radiators (FOC satellite only) can also cause corresponding forces. The Laser Retro-reflector Array (LRA) is mounted on the $+z$ panel for the laser tracking purpose. When radiation flux illuminates on LRA, the radiation flux is bounced exactly opposite to the incident direction. This makes the LRA different from the other surface materials in the computation of radiation pressure. The solar panels are linked to the satellite body through a yoke-arm. The rotation of the yoke-arm is driven by the SADM (Solar Array Driving Mechanism). The surface of the yoke-arm should also be accounted for in the modelling. The other structures that contribute to the radiation pressure modelling

5. INTERACTIONS BETWEEN RADIATION FLUX AND SATELLITE SURFACE

are the antennas. The main parts are the SAR (Search And Rescue), TTC (Telemetry Track and Command) and NAV (Navigation) antennas. The power transmitted from these antennas causes the so-called antenna thrust.

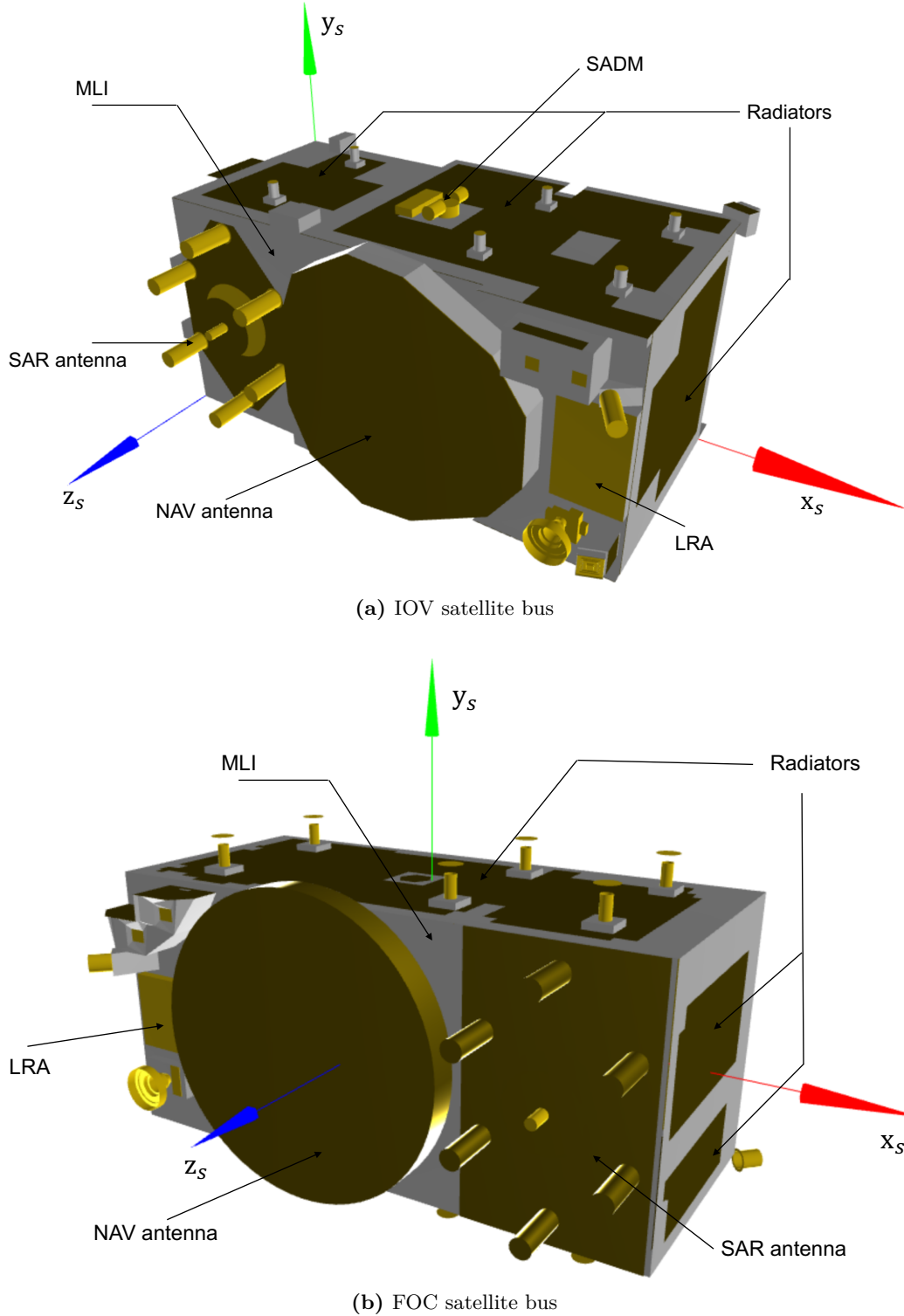


Figure 5.3: The structures of the Galileo IOV and FOC satellite bus

The radiation pressure (direct solar and Earth radiation pressure) on the solar panels are computed by directly applying the passive case formulae (Eq. 5.12). The

5. INTERACTIONS BETWEEN RADIATION FLUX AND SATELLITE SURFACE

complex shape and multiple surface materials of the satellite bus can be dealt with the ray tracing technique.

5.2.2 The satellite geometry and optical properties

The information on the satellite geometry and optical properties are provided in two forms. One is the the box-wing model which uses a box to represent the satellite bus and a plane to describe the solar panels. The other is a detailed 3D surface model of the satellite bus with optical properties for each of the component and documents describing the optical properties of the solar panels.

In the box-wing model, the area, material and optical properties of each facet are provided. The dimensions and the optical properties for Galileo IOV and FOC satellites are described in Tab. 5.1 and Tab. 5.2 separately. The dimensions of the satellite bus are slightly different. The area of the y panel is 3.0 m^2 for IOV satellite but 2.783 m^2 for FOC satellite. The area of the z panel is 3.0 m^2 for IOV satellite but 3.036 m^2 for FOC satellite. Both the IOV and FOC satellites have a same size in the x panel. Although the optical properties are provided in the case of BOF (Beginning Of Life) and EOF (End Of Life), there is worry in the data because most of the terms share the same values for the BOF and EOF. We only take the optical properties for the BOF in the computation. As for the optical properties of the solar cells on the solar panels, there is a big difference between the loaded solar cells and unloaded solar cells (this depends on the duty cycle of the solar panels). The reflectivity of the loaded solar cells is 0.3 (As shown in Tab. 5.1 and Tab. 5.2). When the solar cells are unloaded, the reflectivity becomes 0.1. Due to a lack of the operating status of the solar panels, an average value ($\nu = 0.2$) of the reflectivity is applied in this study.

The detailed 3D surface model is called RTMM (Reduced Thermal Mathematical Model), which is originally used in the spacecraft thermal analysis. In this model, the satellite bus geometry is described using the ESARAD language¹. Each of the component is attached with a set of optical properties including reflectivity, specularity, emissivity and transmissivity. The ESARAD description has to be converted to an user file (a special text file defining the satellite components) as an input to the ray tracing approach. The visualization of the satellite bus (Fig. 5.3a and Fig. 5.3b) are generated from the RTMM. This model is much detailed than the box-wing model even though it may have inaccurate optical properties and spacecraft components compared with the real-world satellites.

5.2.3 Satellite mass information

According to the satellite design data and model description documents, the mass of 4 IOV satellites are 696.815 kg, 694.779 kg, 695.0 kg and 695.0 kg separately at BOL. All the FOC satellites have a mass of 732.8 kg at BOL. What listed in the Tab. 5.3

¹A computer language used to define surfaces, optical properties in the thermal modelling software ESATAN-TMS Workbench

5. INTERACTIONS BETWEEN RADIATION FLUX AND SATELLITE SURFACE

Table 5.1: The basic geometry and optical parameters for Galileo IOV satellite [ν : reflectivity, μ : specularity]

Surface	Material	Area (m ²)	BOF		EOF	
			ν	μ	ν	μ
+X	Carbon filled Kapton (MLI)	0.54	0.06	0.0	0.06	0.0
	Optical surface radiator	0.78	0.9	0.8	0.75	0.8
-X	Carbon filled Kapton (MLI)	1.32	0.06	0.0	0.06	0.0
	Carbon filled Kapton (MLI)	1.0	0.06	0.0	0.06	0.0
+Y	Optical surface radiator	2.0	0.9	0.8	0.75	0.8
	Carbon filled Kapton (MLI)	1.03	0.06	0.0	0.06	0.0
-Y	Optical surface radiator	1.97	0.9	0.8	0.75	0.8
	Carbon filled Kapton (MLI)	1.72	0.06	0.0	0.06	0.0
+Z	Germanium coated black Kapton	1.28	0.9	0.8	0.75	0.8
	Carbon filled Kapton (MLI)	3.00	0.06	0.0	0.06	0.0
$\pm Y$ wing	Solar cells	3.88	0.30	0.8	0.30	0.8
	Kapton HN (Insulation layer)	1.53	0.1	1.0	0.1	1.0

Table 5.2: The basic geometry and optical parameters for Galileo FOC satellite [ν : reflectivity, μ : specularity]

Surface	Material	Area (m ²)	BOF		EOF	
			ν	μ	ν	μ
+X	XC160mil foils (MLI)	0.44	0.07	0.0	0.07	0.0
	Optical surface radiator	0.88	0.92	0.793	0.92	0.793
-X	XC160mil foils (MLI)	1.32	0.07	0.0	0.07	0.0
	XC160mil foils (MLI)	1.129	0.07	0.0	0.07	0.0
+Y	Optical surface radiator	1.654	0.92	0.793	0.92	0.793
	XC160mil foils (MLI)	1.244	0.07	0.0	0.07	0.0
-Y	Optical surface radiator	1.539	0.92	0.793	0.92	0.793
	XC160mil foils (MLI)	1.053	0.07	0.0	0.07	0.0
+Z	Al2024 T81	1.969	0.43	0.512	0.43	0.512
	XC160mil foils (MLI)	2.077	0.07	0.0	0.07	0.0
$\pm Y$ wing	Optical surface radiator	0.959	0.92	0.793	0.92	0.793
	Solar cells	3.88	0.30	0.8	0.30	0.8
	Kapton HN (Insulation layer)	1.53	0.1	1.0	0.1	1.0

5. INTERACTIONS BETWEEN RADIATION FLUX AND SATELLITE SURFACE

are the mass and COM (Centre Of Mass) of both IOV and FOC satellites sourced from [European Global Navigation Satellite Systems Agency \[2017a\]](#). The mass data for IOV satellites are measured at May, 2013 while the mass data for FOC satellites are measured at November, 2016.

Table 5.3: The mass and COM of Galileo IOV and FOC satellites

GSAT	Type	SV ID	Mass [kg]	COM x [mm]	COM y [mm]	COM z [mm]
0101	IOV	11	696.815	1205.90	628.90	553.40
0102	IOV	12	694.779	1205.30	628.80	551.40
0103	IOV	19	695.000	1205.29	629.58	552.81
0104	IOV	20	695.000	1205.32	628.96	551.51
0201	FOC	18	660.977	316.89	-13.48	561.91
0202	FOC	14	662.141	311.61	-12.60	562.31
0203	FOC	26	705.688	259.54	-9.24	561.17
0204	FOC	22	705.914	261.14	-9.24	561.16
0205	FOC	24	708.789	258.56	-9.88	565.46
0206	FOC	30	707.740	259.23	-9.51	565.26
0207	FOC	07	706.648	261.17	-9.52	565.29
0208	FOC	08	709.138	261.08	-10.43	565.28
0209	FOC	09	707.882	261.49	-9.60	565.00
0210	FOC	01	706.679	262.18	-9.61	565.28
0211	FOC	02	707.638	263.08	-10.23	565.27
0212	FOC	03	709.911	257.23	-9.88	565.27
0213	FOC	04	708.765	262.66	-10.33	565.27
0214	FOC	05	709.761	261.60	-9.42	565.27

5.3 The ray tracing technique

5.3.1 State of the art in ray tracing

Ray tracing is a rendering technique used to generate images that are of significantly higher quality than images produced through rasterization techniques. However, one serious disadvantage of ray tracing is performance. This can be overcome to some extent with the continuing improvement of hardware (CPU and GPU). Optimising how data are stored and retrieved can also greatly improve performance [[Forrest, 2003](#)]. Those optimisations fall under two different categories: spatial subdivision techniques and object hierarchies. Examples of these two are the K-Dimensional Tree and Bounding Volume Hierarchy, respectively [[Wald et al., 2007](#)].

A wide range of commercial software is available for ray tracing, such as Autodesk 3ds Max, Autodesk Maya, Blender and V-ray. These software are highly optimised. However, they are all designed to produce high quality images. For a specific science application, it is impractical to make use of the commercial software. For example, one reason is to do with how the interaction between the surfaces and the fluxes is handled. Commercial image rendering software is concerned with the reflective prop-

5. INTERACTIONS BETWEEN RADIATION FLUX AND SATELLITE SURFACE

erties with respect to colour and brightness. In contrast, radiation pressure modelling is only concerned with force computation. In addition, there are also differences in the representation of objects. Therefore, it is necessary to have our own ray tracing software for radiation pressure modelling. The research outcomes and approaches from the field of computer graphics can also be used in the implementation of radiation pressure modelling software.

The ray tracing technique is used to deal with the complex shape of satellite bus and the interactions between satellite surfaces and radiation fluxes. In this study, a BVH-based ray tracer is implemented. It makes the computation run 30–50 times faster compared with traditional ray tracing [Li et al., 2018]. The following sections will discuss the elements of ray tracing technique including: 1. the representation of satellite’s geometry; 2. the simulation of radiation flux; 3. the intersections between rays and primitives; 4. the application of BVH in ray tracing; 5. the uncertainty analysis of ray tracing results.

5.3.2 The representation of the satellite’s geometry

Regarding the description of satellite bus geometry, one way is to use a tessellation approach which represents complex geometry with a model consisting of planar triangles [Grey et al., 2017]. However, this tessellation approach introduces errors in the curved surfaces such as spheres, cylinders, parabolic dishes and so on. Therefore, in this study, the satellite bus geometry is represented by primitives such as planar polygon & circle & ring, cylinder, cone, sphere [Ziebart, 2001; 2004]. These simple geometries can be described by rigorous mathematical equations and the intersections between rays and surfaces can be accurately computed.

In order to apply the BVH in ray tracing, all the components have to be surrounded by volumes, this can help to speed up the intersection searching process. In this study, the AABB (Axis Aligned Bounding Box) is used as the surrounding volume. The orientation of the AABB is aligned to the three axes of the satellite BFS. The AABB for every primitive is stored as the minimum and maximum coordinates in x, y and z. For each primitive, it also needs a Local Body System (LBS) to describe the geometry. The transformation matrix between the local body coordinate system and the satellite body fixed frame is computed when building each primitive. The definitions of LBS and the AABB for each primitive are shown in Table 5.4. The details about the construction of LBS and AABBs for each primitive are described in the following text.

In the ray tracing software, a spacecraft structure source file (i.e. the user file) is used to store the geometry and the optical properties. In this study, we follow the definition described by Ziebart [2004]. The geometry models of Galileo IOV and Galileo FOC satellites described by the user file are rendered in 3D and shown in Fig. 5.4.

The global coordinate system for the geometry modelling is the BFS (Body Fixed System) of the satellite which means all the components in the user file are expressed in the BFS. The following text described how to build the LBS for each primitive . Once

5. INTERACTIONS BETWEEN RADIATION FLUX AND SATELLITE SURFACE

Table 5.4: The definition of local body frame and AABB for all the primitives

Geometry	Representation	Local body frame	AABB
Polygon	all vertices in counter clockwise order		
Circle	radius, centre, two vertices on the circle in counter clockwise order		
Ring	centre, inner radius, outer radius, two vertices on the outer circle in counter clockwise		
Cone	bottom vertex, top vertex, radius, two vertices on the bottom circle in counter clockwise order		
Sphere	centre, radius		
Cylinder	top vertex, bottom vertex, radius, any vertex on the circumference of bottom circle		

5. INTERACTIONS BETWEEN RADIATION FLUX AND SATELLITE SURFACE

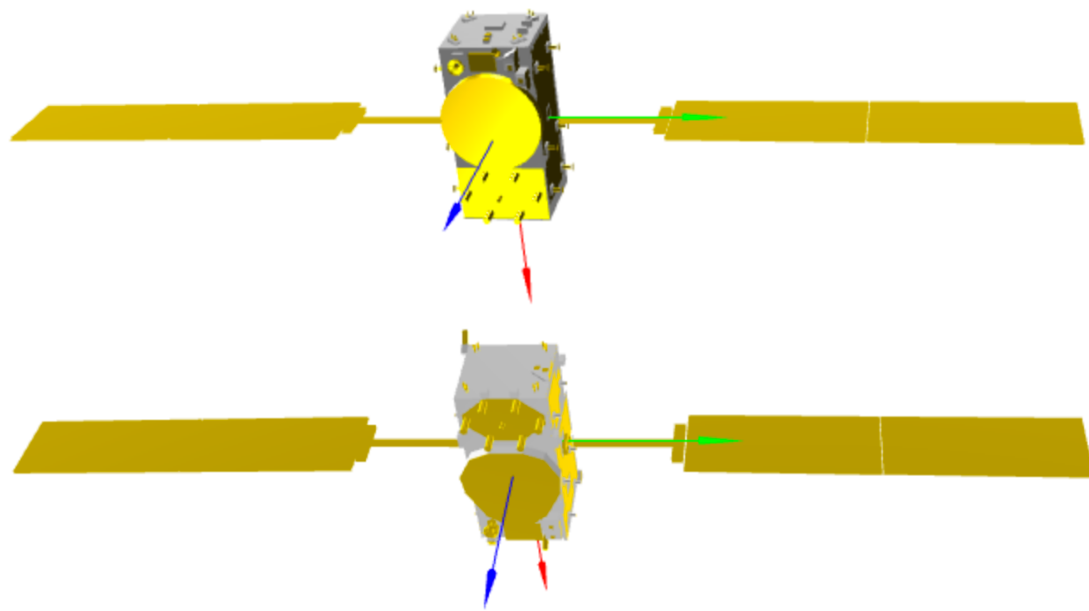


Figure 5.4: The rendered geometry of the Galileo IOV and FOC satellite based on the primitives in Table 5.4.

the LBS is constructed, the connection between the LBS and BFS for each primitive is built, a rotation and translation can be applied to convert between them.

5.3.2.1 Planar circle & ring

The origin of the LBS is defined at the centre of a circle or a ring (expressed in BFS). The spacecraft structure source file (user file) includes any two vertices on the perimeter (the two vertices are on the external circle of a ring) in counter clock order. So the x-axis of the LBS is defined from the centre of the circle (or the ring) to the first vertex on the perimeter. Three points (a centre + two vertices on the perimeter) determine the normal to the plane where the circle or the ring is in. The normal to the plane is used as the z-axis of the LBS. The y-axis of the LBS completes a right-hand system.

5.3.2.2 Planar polygon

A polygon is represented by a series of vertices in the counter clockwise order. Thus, the first vertex is chosen as the origin of the LBS. The vector from the first vertex to the second vertex is used as the x-axis of the LBS. The vector from the origin to the third vertex lies in the plane where the polygon is in. The crossproduct of that vector and the vector in x-axis produces the normal to the plane. The normal acts as the z-axis of the LBS. The y-axis of the LBS completes a right-hand system.

5.3.2.3 Cone

In this study, a cone is represented by a vertex on the top, the centre of the bottom circle, the radius of the circle on the bottom, and two vertices in counter clockwise

5. INTERACTIONS BETWEEN RADIATION FLUX AND SATELLITE SURFACE

order on the perimeter of the bottom circle. Note that the cone does not include the circle on the bottom (If necessary, the circle on the bottom is another component which is represented by a primitive of planar circle). The centre of the cicle on the bottom is used as the origin of the LBS. The vector from the origin to the first vertex on the perimeter is used as the x-axis of the LBS. The vector from the origin to the vertex on the top make z-axis and y-axis completes the right-hand system.

5.3.2.4 Cylinder

A cylinder is represented by the centres of the top and bottom circle, a vertex on the perimeter of the bottom circle, and its radius. Note that the cylinder is open capped which means the cylinder does not include the top and bottom circles. The origin of the LBS is defined at the centre of the bottom circle. The x-axis of LBS is defined from the origin to the vertex on the bottom circle. The z-axis is from the origin to the top vertex while y-axis completes the right-hand system.

5.3.2.5 Sphere

Spheres are symmetric shapes, the three axes of the LBS for spheres are defined the same as the BFS of the satellite. Only the origin of the LBS is defined at the centre of the sphere. Thus, a sphere is described by the centre and its radius.

5.3.3 Simulation of radiation flux in ray tracing

The radiation fluxes need to be simulated in the ray tracing are the solar and Earth fluxes. The Sun is far from the Earth, all the rays from the Sun to the Earth are assumed to be parallel. The Earth radiation at a satellite's location is assumed to be distributed on a spherical surface (with a radius of the distance from the satellite to the Earth). The dimension (about 10 m) of an artificial satellite is small comparing with the satellite-Earth distance (30,000,000 m), the impacts of curvature on the flux direction at a satellite's location can be ignored. Thus, all the Earth radiation flux are assumed parallel as well. In this study, a pixel array is used to simulate the radiation flux following [Ziebart \[2004\]](#). All the rays start from the plane of the pixel array. The centre of each pixel is set to be the start of the ray. The normal to the pixel array plane is used as the direction of radiation flux.

There are a series of questions on the establishment of the pixel array. They are listed below:

- How to express the normal to the pixel array (the direction of the radiation flux) in the BFS?
- How to decide the dimension (the length and width) of the pixel array?
- How to locate each pixel in the pixel array? This involves the establishment of the Pixel Array System (PAS) and the coordinates conversion between the PAS and BFS.

5. INTERACTIONS BETWEEN RADIATION FLUX AND SATELLITE SURFACE

The answers to these questions will shape the process of simulating radiation flux in ray tracing technique for radiation pressure modelling.

5.3.3.1 Description of the direction of radiation flux

In the satellite BFS, any direction can be described by two angular parameters, i.e. the latitude φ and longitude λ (see Fig. 5.5). This can also be used to describe the direction of radiation flux.

The vector from the origin of PAS (the simulated position of the radiation source) to the origin of the BFS is defined to be the direction of radiation flux. This vector \mathbf{s} can be expressed with two angular arguments

$$\mathbf{s} = (-\cos \varphi \cos \lambda, -\cos \varphi \sin \lambda, -\sin \lambda)^T \quad (5.13)$$

5.3.3.2 Definition of the PAS

The PAS is used to describe the location of each pixel on the pixel array. Because all the calculations are done in the satellite's BFS, a connection between the BFS and the PAS has to be established. Assume the pixel array is placed at $d_0 = 100$ m away from the spacecraft. We can build the PAS by rotating and translating the BFS as shown in Fig. 5.5. The steps are given as follows:

- Rotate the x-axis of BFS around the z-axis of BFS with angle λ in counter clockwise order. Make x-axis of BFS lies in the projection from the radiation source to the satellite in the x-y plane of the BFS.
- Rotate z-axis of the BFS around BFS's y-axis with angle $\frac{3\pi}{2} - \varphi$ in counter clockwise order so that the z-axis is pointing from the radiation source to the satellite.
- Move the origin of BFS to the simulated position of the radiation source.

Therefore, the transformation in coordinates between the BFS (\mathbf{x}_{BFS}) and the PAS (\mathbf{x}_{PAS}) is:

$$\mathbf{x}_{\text{PAS}} = \mathbf{R} \cdot \mathbf{x}_{\text{BFS}} + \mathbf{x}_0 \quad (5.14)$$

where

$$\mathbf{R} = \begin{pmatrix} -\sin \varphi \cos \lambda & -\sin \varphi \sin \lambda & \cos \lambda \\ -\sin \lambda & \cos \lambda & 0 \\ -\cos \varphi \cos \lambda & -\cos \varphi \sin \lambda & -\sin \varphi \end{pmatrix}$$

and

$$\mathbf{x}_0 = \left(-d_0 \cos \varphi \cos \lambda \quad -d_0 \cos \varphi \sin \lambda \quad -d_0 \sin \lambda \right)^T$$

5.3.3.3 Determine the size of the pixel array

The size of pixel array is represented by the length (along the PAS x-axis) and width (along the PAS y-axis) of the pixel array. One principle of determining the size of the

5. INTERACTIONS BETWEEN RADIATION FLUX AND SATELLITE SURFACE

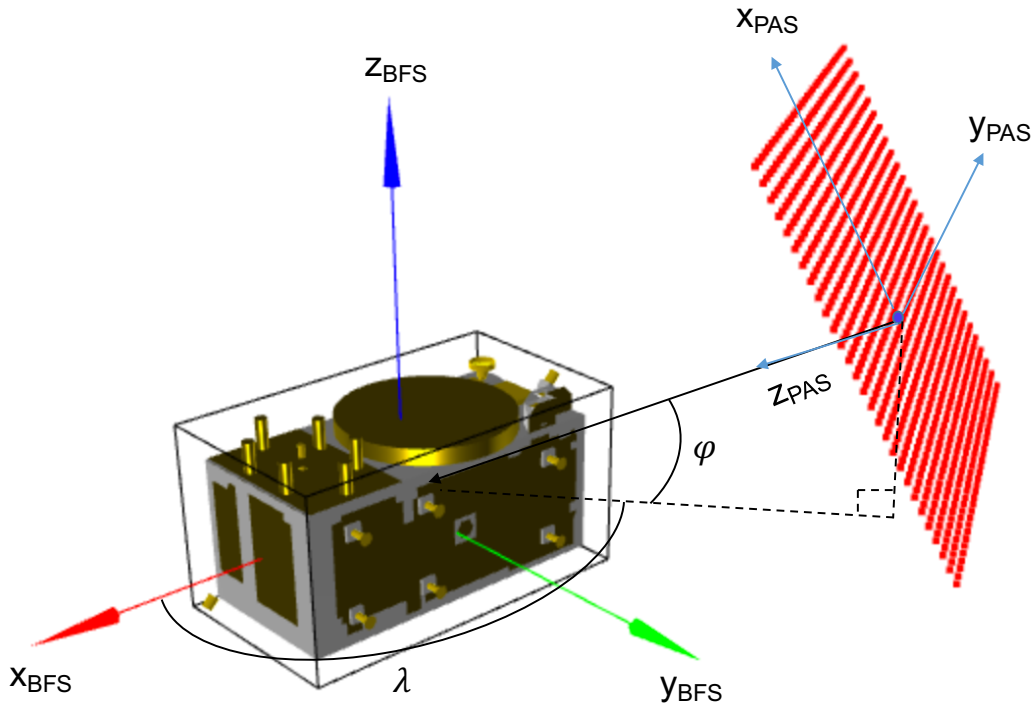


Figure 5.5: The definition of PAS (Pixel Array System) for one Galileo IOV satellite bus. The radiation flux direction is represented by latitude φ and longitude λ in BFS. The boundary of the AABB of the spacecraft is shown in black.

pixel array is to make sure that the rays started from the pixel array can fully cover the cross-sectional area of the satellite. The size of the pixel array is calculated by converting the AABB of the whole satellite into the PAS, then the ranges of x and y coordinates in the PAS are found. The steps are as follows:

- The AABB of the satellite has 8 vertices. The coordinates of all the 8 vertices are converted into the PAC.
- Find the maximum and minimum coordinates in x, y and z of the PAC for the 8 vertices.
- The length in the pixel array x direction is the difference between the maximum coordinates and minimum coordinates in x-axis while the length in the pixel array y direction is the difference between the maximum coordinates and the minimum coordinates in y-axis.

5.3.3.4 Locate each pixel on the pixel array

The centre of each square pixel on the pixel array is used as the start of the ray. The position of each pixel has to be calculated in the BFS. Given the pixel spacing, the length (l), and width (w) of the pixel array, the number of pixels in both x and y direction of the PAS can be calculated. The first pixel of the pixel array is defined to have the minimum x and y coordinates in the PAS. Start from the first pixel, the

5. INTERACTIONS BETWEEN RADIATION FLUX AND SATELLITE SURFACE

coordinates $(\mathbf{x}_{i,j})$ of the centre of pixel with index i in x and j in y are given

$$\mathbf{x}_{i,j} = \mathbf{x}_1 + i \cdot \delta_0 \mathbf{e}_x + j \cdot \delta_0 \mathbf{e}_y \quad (5.15)$$

where \mathbf{x}_1 is the coordinates of the centre of the first pixel; $\mathbf{x}_1 = (-\frac{l}{2}, -\frac{w}{2}, 0)^T$, δ_0 is the pixel spacing, $\mathbf{e}_x = (1, 0, 0)^T$ and $\mathbf{e}_y = (0, 1, 0)^T$.

The coordinates $\mathbf{x}_{i,j}$ in the PAS are then converted into BFS using the connection between the BFS and PAS (see Equation 5.14).

5.3.4 The ray-primitive intersection

The intersections between the ray and the primitives can be computed by combining the equations of a ray and a primitive. The parametric equation of a ray in the BFS can be expressed

$$\mathbf{x} = \mathbf{a} + t\mathbf{d} \quad (5.16)$$

where \mathbf{a} is the coordinates of the start, \mathbf{d} is the unit vector in the ray direction, t is a parameter for the ray. The vector \mathbf{a} and \mathbf{d} can also be written in their scalar forms: $\mathbf{d} = (d_x, d_y, d_z)^T$, and $\mathbf{a} = (a_x, a_y, a_z)^T$.

The intersection between a ray and a primitives is calculated by solving the simultaneous equations composed by the equation of the ray and the equation of the primitive. Because the equation of ray is expressed in the BFS while the equation of primitive is expressed in the LBS, the first step is to convert the equation of ray into the LBS of a primitive. For the equation of ray, we only need to convert \mathbf{a} and \mathbf{d} into the corresponding LBS. After the conversion, the values of \mathbf{a} and \mathbf{d} are already different from the previous ones. For the convenience of description, they are still denoted as the same symbols though they are different for different primitives. Once the intersections are computed, they are converted back from different LBSs into the BFS using Eq. 5.14. The following text will describe how to calculate the intersections of a ray with different primitives.

5.3.4.1 Planar polygon & circle & ring

The intersection calculation for planar geometries requires two steps. The first step is to get the candidate which is the intersection between the ray and the plane. The next step is to check if the candidate intersection is inside the range of the shape (polygon, circle, or ring). If the normal to the plane for the planar geometries is \mathbf{n} , the equation of the plane in the LBS is expressed

$$\mathbf{n}^T \mathbf{x} = 0 \quad (5.17)$$

The simultaneous equations of the ray (in LBS) and the plane are

$$\begin{cases} \mathbf{n}^T \mathbf{x} = 0 \\ \mathbf{x} = \mathbf{a} + t\mathbf{d} \end{cases} \quad (5.18)$$

5. INTERACTIONS BETWEEN RADIATION FLUX AND SATELLITE SURFACE

The parameter t can be solved

$$t = -\frac{\mathbf{n}^T \mathbf{a}}{\mathbf{n}^T \mathbf{d}} \quad (5.19)$$

Note that if \mathbf{n} is perpendicular to \mathbf{d} (i.e. $\mathbf{n}^T \mathbf{d} = 0$), the ray is assumed to have no intersection with the plane because the ray is parallel to the plane. In fact, parameter t represents the distance from the start of the ray to the intersection, only positive values are accepted. Negative t means the ray intersects the plane from the opposite direction and this situation won't happen in physics.

Once t is solved, the candidate intersection is obtained. The next step is to confirm the solution (i.e. to test if the candidate lies in the range of the shape). This process is different for the polygon, the circle and the ring.

We only need to check the distance from the candidate to the centre of the circle. If the distance is less than or equal to the radius of the circle, the candidate is accepted as the final intersection.

As for the rings, the validation is similar to that of the circles. In order to make sure that the intersection lies in the ring, the distance from the candidate to the centre of the ring has to be larger than the the radius of the inner circle but less than the radius of the outer circle.

As for the polygons, the check of the candidate intersections involves the theory of winding number in topology. The winding number of a closed curve in a plane around a given point is an integer representing the total number of times that curve travels counter clockwise around the point. If the winding number of a polygon for the candidate is 0, the candidate is outside the polygon otherwise it is inside the polygon and should be accepted [Hormann and Agathos, 2001].

5.3.4.2 Sphere

The equation of a sphere in LBS is described

$$\mathbf{x}^T \mathbf{x} = R^2 \quad (5.20)$$

where R is the radius of the sphere.

The simultaneous equations of the ray and the sphere are

$$\begin{cases} \mathbf{x}^T \mathbf{x} = R^2 \\ \mathbf{x} = \mathbf{a} + t\mathbf{d} \end{cases} \quad (5.21)$$

A quadratic with respect to parameter t is generated from Eq. 5.21.

$$\mathbf{d}^T \mathbf{d} t^2 + 2\mathbf{d}^T \mathbf{a} t + \mathbf{a}^T \mathbf{a} - R^2 = 0 \quad (5.22)$$

Similarly, only positive t is accepted. The smaller t is chosen as the solution if the quadratic has two real solutions.

5. INTERACTIONS BETWEEN RADIATION FLUX AND SATELLITE SURFACE

5.3.4.3 Cylinder

The equation of a cylinder in its LBS can be expressed

$$\begin{cases} x^2 + y^2 = R^2 \\ 0 \leq z \leq h \end{cases} \quad (5.23)$$

where R is the radius of the circle on the bottom of the cylinder, h is the height, x , y , and z are the coordinates of vertices on the cylindrical surface. The simultaneous equations of the ray (see its scalar form in Eq. 5.16) and the cylinder generate a quadratic

$$At^2 + Bt + C = 0 \quad (5.24)$$

where

$$\begin{aligned} A &= x_d^2 + y_d^2 \\ B &= 2(x_d x_a + y_d y_a) \\ C &= x_a^2 + y_a^2 - R^2 \end{aligned}$$

The smaller t is accepted as the solution if quadratic 5.24 has two real solutions. It is also necessary to check the z component of the solution and make it meet the condition $0 \leq z \leq h$.

5.3.4.4 Cone

The equation of a cone in its LBS is

$$\begin{cases} z - h = -\frac{h}{R} \sqrt{x^2 + y^2} \\ 0 \leq z \leq h \end{cases} \quad (5.25)$$

where h is the height of the cone, R is the radius of the circle on the bottom. The simultaneous equations of the ray (see its scalar form in Eq. 5.16) and the cone generate a quadratic similar to Eq. 5.24 but with different coefficients A , B , and C . In this case,

$$\begin{aligned} A &= z_d^2 - \frac{h^2}{R^2}(x_d^2 + y_d^2) \\ B &= 2(z_d z_a - h z_d - \frac{h^2}{R^2}(x_d x_a + y_d y_a)) \\ C &= z_a^2 + h^2 - 2h z_a^2 - \frac{h^2}{R^2}(x_a^2 + y_a^2) \end{aligned}$$

Still, the smaller t is accepted as the solution and the z component of the intersection has to be checked to meet condition $0 \leq z \leq h$.

5.3.5 Applying BVH in radiation pressure modelling

The slowest part of traditional ray tracing algorithm is to search for the intersection between the rays and the primitives. The radiation pressure modelling with traditional ray tracing has to search all the components of the satellite to find the correct intersection for each ray [Ziebart, 2001]. The searching process can be speeded up using Bounding Volume Hierarchy (BVH) data structure to organize the satellite components. All the satellite components are organised in a binary tree with each node

5. INTERACTIONS BETWEEN RADIATION FLUX AND SATELLITE SURFACE

contains an AABB. The application of BVH into the ray tracing includes two parts: one is the construction of the BVH data structure; the other is the traversal of the BVH to search for the intersection.

Why we need to speed up the computation

The ray tracing process can be slow in calculation especially for satellites with thousands of components. Take a 5 m by 5 m plane as an example, if the spacing of the pixel array is set to be 1 mm, the total number of rays can be 2.5×10^7 for only one direction of the radiation flux. In the calculation, radiation flux is simulated on a sphere around the satellite. If the angle spacing is 1 degree, there are $360 \times 180 = 64800$ directions to calculate. For this simple plane, the amount of rays to be traced is at the level of 10^{12} . Previous computation on a GPS IIR satellite model with a 5 mm pixel spacing on an AMD Athlon 1800 processor desktop PC took around 10 days [Sibthorpe, 2006]. Although the computation ability of modern computers have been improved a lot in the recent years, the computation efficiency will benefit from a faster algorithm.

In addition, the ray tracing approach requires large number of inputs about the optical properties of the satellite's surface and the geometry of the satellite. These information can not be delivered completely correct at once. Several iterations in the modelling process are needed in practice. For the sake of modelling efficiency, the computation process has to be speeded up.

5.3.5.1 The Construction of BVH

Since all the components of the satellite geometry are surrounded by AABBs, the AABB for the whole satellite is easily found by grouping the AABBs of all the components. The root node of the BVH is the AABB of the whole satellite bus. The establishment of the BVH is a process of partitioning the root AABB into different levels of sub-volumes and store them into a binary tree. For each AABB, its geometric centre is chosen as its reference point. The key factor that affects the efficiency of a BVH is how the partition plane is chosen. There are many algorithms of choosing the partition plane in an optimized way [Sopin et al., 2011]. Because how to improve the efficiency of a BVH in ray tracing is not the focus of this study, a widely used approach is applied in this study. This method is in two steps. The first step is to choose the longest side (this side can either be along x, y or z-axis) of the AABB. Step two is to choose a partition plane and make it go through the middle point of the longest side and be perpendicular to the longest side. For each partition, the AABB is divided into two sub-volumes. The steps of building a BVH are as follows:

- Let the AABB of the whole satellite bus geometry be the root node.
- Choose the partition plane for the root node.
- Loop over all the geometry components inside the AABB, if the reference point of the AABB lies on the left side of the partition plane, the components are stored

5. INTERACTIONS BETWEEN RADIATION FLUX AND SATELLITE SURFACE

in the left child, otherwise the components are sent to the right child.

- Repeat step 1 to step 3 for both the left and right child till the number of components of the children is 1. The nodes that have only one component are treated as leaf nodes.

5.3.5.2 Traversal of the BVH and intersection check

The traversal of a BVH is the key part of searching the intersections between rays and the satellite components. All the nodes of the BVH are AABBs that contain components. If a ray misses the AABB, it will not hit any components inside the AABB. If the ray hits the AABB of that node, all the children of that node should be checked till it reaches the leaf node. There is only one component inside a leaf node, the corresponding intersection algorithm can be applied for different primitives. The closest intersection to the start of the ray is chosen as the final solution. The steps for the traversal of the BVH are as follows:

- Start from the root of the BVH, if the ray hits the AABB, then check the left child and the right child. Otherwise, the ray will not hit any part of the spacecraft.
- Repeat the above step till it reaches the leaf nodes. The intersection algorithm for the primitive inside the leaf nodes will be executed if the ray hits the leaf AABB, the distance from this intersection to the start of the ray is record.
- Finally, the real intersection is the one that is closest to the start of the ray.

Once the intersection is determined for a ray, the optical properties (reflectivity ν and specularity μ) of the material that the ray hits are known. Based on the coordinates of the intersection, the incident ray, and the optical properties of the hit material, a core function is executed to calculate the radiation pressure for that ray. The resultant force is computed by summing the results of all the intersected rays.

5.3.5.3 Core function in the ray tracing

The above description of the ray tracing approach can be applied generally. What makes the ray tracer have different function is the core function in the ray tracing. A core function is a function that describes what happened on the intersection between a ray and the surface. In the radiation pressure modelling, a core function is used to calculate the direct radiation pressure (including the solar and Earth radiation pressure depends on the radiation sources) and the thermal re-radiation pressure for 2 types of materials (the MLI and non-MLI on the satellite bus). The inputs to the core function are the ray direction, radiation flux of the ray, coordinates of the intersection, and the optical properties of the material. The outputs are the force due to the direct radiation pressure and thermal re-radiation pressure. In this way, the ray tracing approach combine together the modelling of direct solar radiation pressure and thermal re-radiation pressure.

5. INTERACTIONS BETWEEN RADIATION FLUX AND SATELLITE SURFACE

For all the materials (both MLI and non-MLI), the direct radiation pressure is computed using Eq. 5.12. In addition, the re-radiated thermal fluxes are computed for the MLI and non-MLI material according to Eq. 3.15 and Eq. 3.16 separately. Once the radiated thermal fluxes are computed, the re-radiation thermal force is computed by Eq. 5.5. The above descriptions contain all the contents of the core function in radiation pressure modelling.

5.3.5.4 Multiple reflections

In order to cope with the multiple reflections in the ray tracing, the specular reflection rays are used as the incident rays for the next reflection. There are two key points in the calculation: one is the direction of the specular reflection; the other is the specularly reflected radiation flux. Once the incident ray direction \mathbf{s} and the surface normal \mathbf{n} is known, the specularly reflected direction \mathbf{r} can be computed

$$\mathbf{r} = \mathbf{s} - 2(\mathbf{s} \cdot \mathbf{n})\mathbf{n} \quad (5.26)$$

As for the radiation flux of the specularly reflected rays, they should be scaled by the reflectivity (ν) and specularity (μ) of the material that the incident ray intersects. For the $i + 1^{\text{th}}$ reflection, the magnitude of the radiation flux W_{i+1} is given by

$$W_{i+1} = \nu_i \mu_i W_i \quad (5.27)$$

where W_i is the radiation flux of the i^{th} reflection ray, ν_i and μ_i are the reflectivity and specularity of the material which the i^{th} reflection ray intersects.

In the multiple reflection computation, we only consider the specular reflected rays. The workload in computation increases enormously if the multiple reflections for the diffusely reflected rays are accounted for. In this study, the first order of diffusely reflected rays are considered in the calculation of passive radiation pressure (see Eq. 5.12). However, the multiple reflection computation is ignored in the active radiation pressure calculation. This is because the active radiation pressure is mainly generated on the thermal radiators and the navigation antenna, these surfaces are facing the space and have very few multiple reflections.

5.3.6 Parameters choice in ray tracing and improvement in computation efficiency

There are two input parameters to set up the ray tracing, including the pixel spacing and the maximum number of reflections. Smaller pixel spacing and more reflections can improve the computation accuracy but lead to longer runtime. In order to balance between modelling efficiency and accuracy, the choices of pixel spacing and the maximum of reflections have to be optimized. The following text will discuss the choices of the pixel spacing and the maximum reflections based on tests for Galileo IOV and FOC satellites. In addition, the improvement in computation efficiency is discussed based on

5. INTERACTIONS BETWEEN RADIATION FLUX AND SATELLITE SURFACE

the above optimized pixel spacing and maximum reflections. Both the Galileo IOV and FOC satellites are assuming to be in their nominal attitudes. In this way, the longitude of the Sun in body fixed frame is fixed to be 180° while the latitude varies from -90° to 90° . The mass is set to be 700 kg for both the IOV and FOC satellites.

5.3.6.1 Pixel spacing

In this experiment, 4 choices (1 m, 1 dm, 1 cm and 1 mm) of the pixel spacing are tested. In order to assess the modelling accuracy of these 4 pixel spacings, a pixel spacing of 0.1 mm is used as the “truth” in comparison. The differences in acceleration between the 4 different pixel spacings and 0.1 mm are used to assess the errors in these 4 pixel spacings. In this test, the maximum number of reflections is set to be 1, which makes pixel spacing the only variable. The differences in magnitude of acceleration are shown in Fig. 5.6. The statistics of them are presented in Tab. 5.5.

Table 5.5: The error statistics for different pixel spacings. unit: $[\text{nm} \cdot \text{s}^{-2}]$

satellite	method	1 m	1 dm	1 cm	1mm
IOV	mean	-4.971	-0.007	7.64E-4	1.29E-5
IOV	std.	8.145	0.484	0.036	0.004
FOC	mean	0.558	0.174	0.0232	-8.85E-4
FOC	std.	4.218	0.434	0.047	0.004

The computation results show that standard deviation of the errors of acceleration derived from 1 mm pixel spacing is less than $0.01 \text{ nm} \cdot \text{s}^{-2}$ for both the IOV and FOC satellites. Although the 1 mm pixel spacing increases the runtime by a factor of 100, the accuracy has been increased by a factor of 10 compared with the 1 cm pixel spacing. The maximum error of 1 mm spacing is lower than $0.01 \text{ nm} \cdot \text{s}^{-2}$ which indicates that a spacing of 1mm has reached the objective of this research (see 1.3.1). Thus, the pixel spacing is set to be 1 mm in this study.

5.3.6.2 Maximum number of reflections

The 1st reflection is defined as the incident ray hits and bounces off but not any further intersections. In the test of maximum reflections, the accelerations derived from 10-reflection are treated as the “truth” in comparison. In this test, the pixel spacing is set to be 1 mm according to the test results of previous section. This problem is investigated in two aspects: one is the proportion of intersection number, the other is the difference in acceleration.

Figure 5.7 shows the ratio of total intersection number between 10-reflection and different numbers of reflections. It shows that the first reflection can only capture 85% (FOC) and 87% (IOV) of the total intersections. There is a significant improvement (7%) from 1-reflection to 2-reflection. The 3-reflection results capture 3% more intersections. Starting from 3 reflections, the improvement gets less as the number of reflection increases. From this point of view, the 3 reflections can capture over 95% of

5. INTERACTIONS BETWEEN RADIATION FLUX AND SATELLITE SURFACE

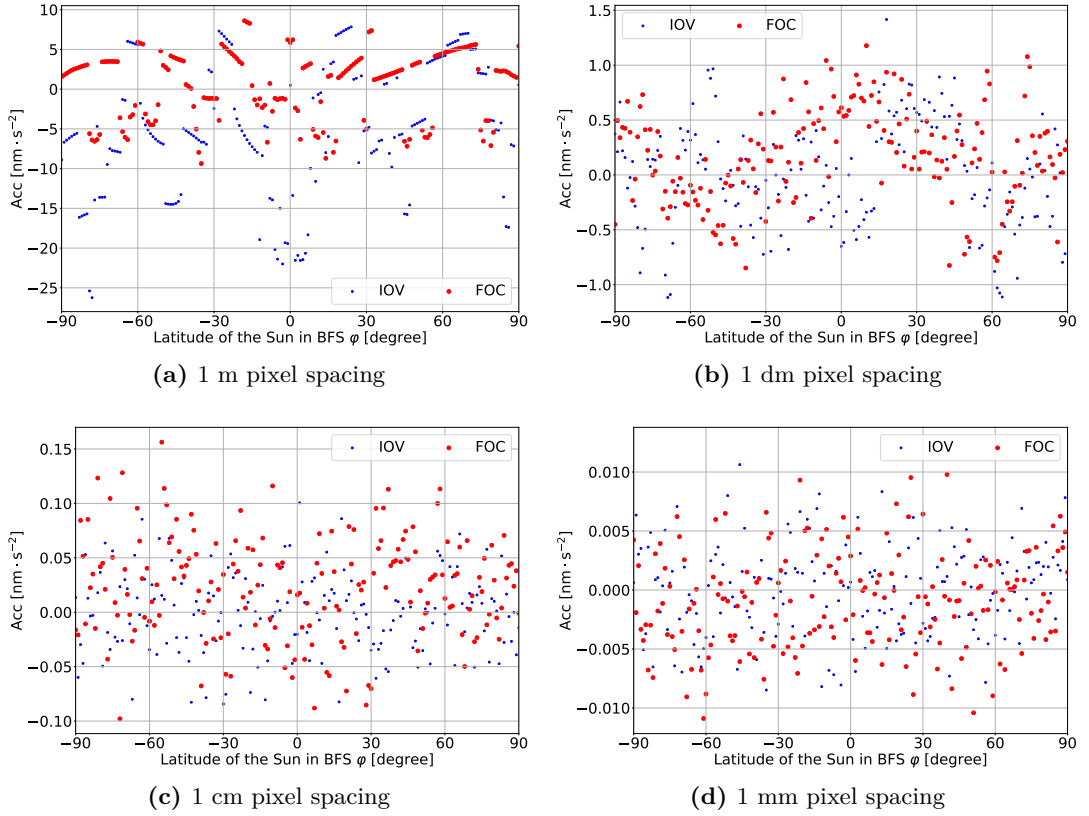


Figure 5.6: The differences in magnitude of acceleration between 0.1 mm pixel spacing and the other 4 pixel spacings. Red dots represent FOC satellite while blue dots stand for IOV satellite.

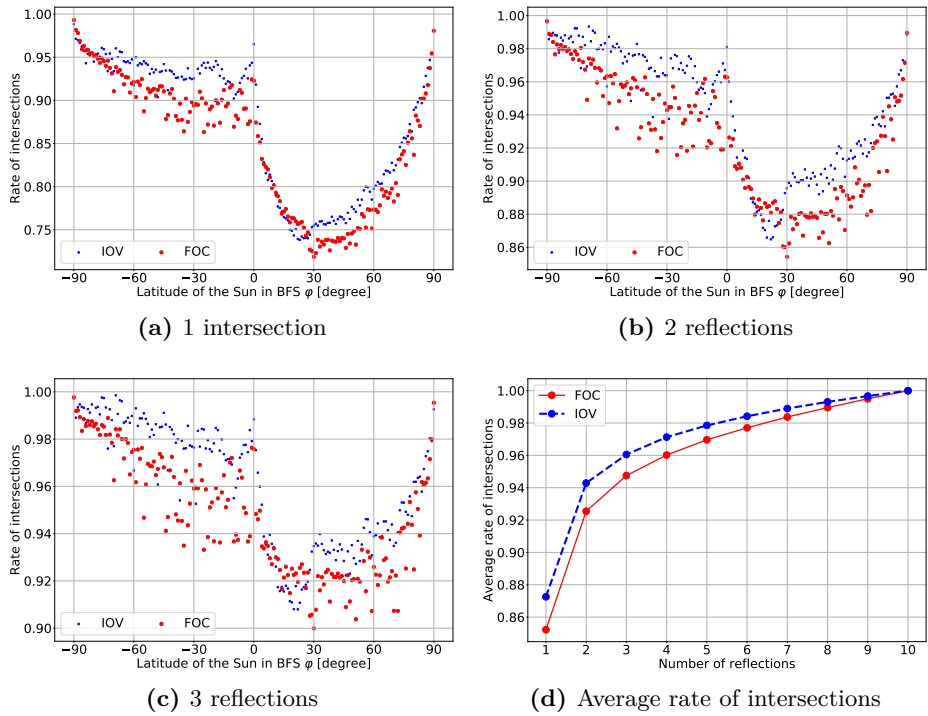


Figure 5.7: The rate of intersection number between different reflections and the 10th reflection. Red dots represent FOC satellite while blue dots stand for IOV satellite.

5. INTERACTIONS BETWEEN RADIATION FLUX AND SATELLITE SURFACE

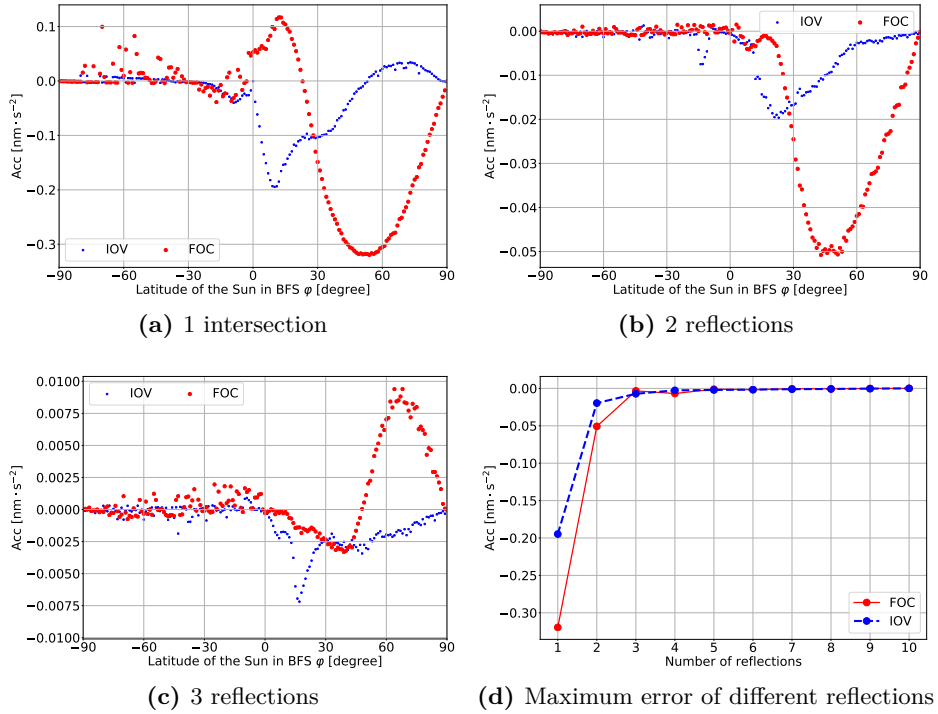


Figure 5.8: The differences in magnitude of acceleration between 10 reflections and the other number of reflections. Red dots represent FOC satellite while blue dots stand for IOV satellite.

the total intersections. The results in the $+z$ panel ($\varphi > 0$) shows more improvements in increasing the number of reflections than the $-z$ panel due to more complex geometry.

Figure 5.8 shows the differences in the magnitude of acceleration between the “truth” (10 reflections) and other number of reflections. The maximum error can reach to -0.3 (FOC) and -0.2 (IOV) $\text{nm} \cdot \text{s}^{-2}$ for the 1 reflection. As the number of reflections increase, the maximum error decreases. For the 3 reflections, the maximum error reduce to -0.0033 (FOC) and -0.0072 (IOV) $\text{nm} \cdot \text{s}^{-2}$. When the number of reflections is larger than 3, the improvement in the acceleration is not significant.

Based on the above calculations, we can conclude that the maximum number of reflections should be set to 3 in the radiation pressure modelling of the Galileo IOV and FOC satellites. The maximum error of accelerations is less than $0.01 \text{ nm} \cdot \text{s}^{-2}$ for both the IOV and FOC satellites.

5.3.6.3 Improvement in computation efficiency

The improvement in the computation efficiency of applying the BVH structure to the ray tracing is evaluated by comparing the runtime using the ray tracing without BVH and raw UCL (University College London) solar radiation pressure modelling software [Ziebart and Dare, 2001; Ziebart, 2001], which has no speed-up structure. The software developed in this study has optimizations in coding and should be more efficient than the raw UCL software even though both of them do not have acceleration structure.

The average runtime (on a personal computer) of 181 different radiation flux di-

5. INTERACTIONS BETWEEN RADIATION FLUX AND SATELLITE SURFACE

rections is used as an indicator to measure the speedup rate. Different sizes (1 dm, 1 cm, and 1 mm) of pixel spacing are also considered in this test. The test results are shown in Tab. 5.6.

Table 5.6: The speedup test for Galileo IOV and FOC satellite bus

satellite	pixel spacing	UCL raw	without BVH	with BVH
IOV	1 dm (ms)	75.60	35.45	1.11
IOV	1 cm (s)	5.30	3.30	0.10
IOV	1 mm (min)	8.09	8.79	0.15
FOC	1 dm (ms)	76.82	36.21	1.81
FOC	1 cm (s)	5.49	2.92	0.14
FOC	1 mm (min)	7.48	5.66	0.23
IOV	avg. speedup	1	1.75	59.39
FOC	avg. speedup	1	1.77	38.06

As Tab. 5.6 shows, the approach with BVH is 30-50 times more efficient than the raw UCL software. Due to the optimizations in coding, the approach without BVH is about 2 times more efficient than the raw UCL software.

5.3.7 Uncertainty analysis of the ray tracing approach

The material optical property (reflectivity and specularity) is a major factor that affects the accuracy of the radiation pressure computation. In the ray tracing, the uncertainties in the optical properties are propagated to the resultant force. Direct radiation pressure (including solar and Earth radiation) as the principal component is taken as an example to study the propagation of the uncertainties. The uncertainties in the direct radiation pressure are linked to the uncertainties in the reflectivity and specularity by the computation of passive radiation pressure (see Eq. 5.12). Therefore, the task of uncertainty analysis of the ray tracing is to find the answer to the following question.

Given the standard deviation of the reflectivity (δ_ν) and the specularity (δ_μ) for each material, if the reflectivity and specularity of every material are assumed to be independent to each other, what is the covariance matrix of the resultant force derived from the ray tracing?

The output of the ray tracing is a sum of radiation force from all the intersections for a specific radiation flux. If the covariance matrix of the force due to the i^{th} intersection is known as $\mathbf{D}_{\mathbf{F}_i}(\nu, \mu)$, the relation between the covariance matrix of the resultant force $\mathbf{D}_{\mathbf{F}}$ in that direction and $\mathbf{D}_{\mathbf{F}_i}(\nu, \mu)$ is given

$$\mathbf{D}_{\mathbf{F}} = \sum_{i=1}^{i=N} \mathbf{D}_{\mathbf{F}_i}(\nu, \mu) \quad (5.28)$$

where N is the total number of intersections.

For the i^{th} intersection, δ_{F_i} is related to the standard deviation of the optical properties δ_ν and δ_μ . The passive radiation pressure computation (i.e. Eq. 5.12) is

5. INTERACTIONS BETWEEN RADIATION FLUX AND SATELLITE SURFACE

non-linear with respect to ν and μ . It is expanded to the first order at ν_0 and μ_0 using a Taylor series. ν_0 and μ_0 are the average values of reflectivity and specularity.

$$\mathbf{F}_i(\nu, \mu) = \mathbf{F}_i(\nu_0, \mu_0) + \frac{\partial \mathbf{F}_i(\nu, \mu)}{\partial \nu} d\nu + \frac{\partial \mathbf{F}_i(\nu, \mu)}{\partial \mu} d\mu \quad (5.29)$$

where $d\nu = \nu - \nu_0$, $d\mu = \mu - \mu_0$

$$\begin{cases} \frac{\partial \mathbf{F}_i(\nu, \mu)}{\partial \nu} &= \frac{WA \cos \theta}{c} \left(-\mu \mathbf{r} - \frac{2}{3}(1-\mu) \mathbf{n} \right) \\ \frac{\partial \mathbf{F}_i(\nu, \mu)}{\partial \mu} &= \frac{WA \cos \theta}{c} \left(-\nu \mathbf{r} + \frac{2}{3}\nu \mathbf{n} \right) \end{cases}$$

Equation 5.29 can also be written as:

$$\mathbf{F}_i(\nu, \mu) = \left(\frac{\partial \mathbf{F}_i(\nu, \mu)}{\partial \nu}, \frac{\partial \mathbf{F}_i(\nu, \mu)}{\partial \mu} \right)_{3 \times 2} \begin{pmatrix} d\nu \\ d\mu \end{pmatrix} + \mathbf{F}_i(\nu_0, \mu_0) \quad (5.30)$$

Therefore,

$$\mathbf{D}_{\mathbf{F}_i}(\nu, \mu)_{3 \times 3} = \left(\frac{\partial \mathbf{F}_i(\nu, \mu)}{\partial \nu}, \frac{\partial \mathbf{F}_i(\nu, \mu)}{\partial \mu} \right) \begin{pmatrix} \delta_\nu^2 & 0 \\ 0 & \delta_\mu^2 \end{pmatrix} \left(\frac{\partial \mathbf{F}_i(\nu, \mu)}{\partial \nu}, \frac{\partial \mathbf{F}_i(\nu, \mu)}{\partial \mu} \right)^T \quad (5.31)$$

where

$$\mathbf{D}_{\mathbf{F}_i}(\nu, \mu)_{3 \times 3} = \begin{pmatrix} \delta_x^2 & \delta_{xy} & \delta_{xz} \\ \delta_{xy} & \delta_y^2 & \delta_{yz} \\ \delta_{xz} & \delta_{yz} & \delta_z^2 \end{pmatrix} \quad (5.32)$$

δ_x^2 , δ_y^2 , and δ_z^2 are the variance of the final radiation pressure in the BFS x, y, and z components. δ_{xy} , δ_{yz} , and δ_{xz} are the corresponding covariance.

In the data provided, the standard deviation of optical properties for all components are not available. In order to analyse how the uncertainties in the optical properties are propagated to the resultant force, all the components of the satellites are assumed to have the same standard deviation in the reflectivity and specularity ($\delta_\mu = \delta_\nu = \delta$). One Galileo IOV and one Galileo FOC satellites are tested. The standard deviation of the optical properties are set to be 1.0, 0.1, 0.01, and 0.001 separately. The satellite mass is set to be 700 kg for both the IOV and FOC satellites.

The average of the covariance matrix for 181 different directions ($\lambda = 180$, ϕ varies between -90 and 90) is computed. As shown in Eq. 5.28, it seems the covariance of the resultant force is related to the total number of intersections (N). In order to validate this, we perform a test to show the variations of the covariance with respect to the pixel spacing (the smaller pixel spacing causes larger number of intersections). In this test, the standard deviation of the optical properties is set to be $\delta = 0.1$, the pixel spacing varies among 1 dm, 1 cm, and 1 mm. The covariances of the resultant force are shown in Tab. 5.7.

As shown in Tab. 5.7, the covariances of the resultant force are not related to

5. INTERACTIONS BETWEEN RADIATION FLUX AND SATELLITE SURFACE

Table 5.7: The covariances of resultant force for the Galileo IOV and FOC satellites ($\delta = 0.1$), unit: $\text{nm} \cdot \text{m}^{-2}$

satellite	intersection #	pixel size	δ_x^2	δ_y^2	δ_z^2	δ_{xy}	δ_{yz}	δ_{xz}
IOV	5.19E+02	1 dm	0.69	2.7E-2	1.36	2.2E-3	1.8E-3	0.16
IOV	4.67E+04	1 cm	0.70	3.1E-2	1.34	5.6E-4	-5.3E-4	0.15
IOV	4.59E+06	1 mm	0.70	3.3E-2	1.33	5.8E-4	-5.4E-3	0.15
FOC	5.30E+02	1 dm	0.84	3.6E-2	1.49	6.5E-3	4.9E-3	0.11
FOC	4.57E+04	1 cm	0.83	3.9E-2	1.49	3.5E-3	7.2E-4	0.12
FOC	4.53E+06	1 mm	0.83	4.2E-2	1.49	3.8E-3	7.9E-4	0.12

the total number of intersections (or the pixel size). This is because larger number of intersections also cause smaller cross-sectional area. The total cross-sectional area between the radiation flux and the satellite is not to do with the pixel size. The covariances keep stable for different pixel sizes.

Table 5.8: The covariances of resultant force for the Galileo IOV and FOC satellites (pixel size: 1 cm). unit: $\text{nm} \cdot \text{m}^{-2}$

satellite	δ	δ_x^2	δ_y^2	δ_z^2	δ_{xy}	δ_{yz}	δ_{xz}
FOC	1.0	83.59	3.93	149.53	3.47E-1	7.24E-2	11.67
FOC	0.1	0.84	3.92E-2	1.50	3.47E-3	7.24E-4	1.17E-1
FOC	0.01	8.36E-3	3.92E-4	1.49E-2	3.47E-5	7.24E-6	1.17E-3
FOC	0.001	8.36E-5	3.92E-6	1.49E-4	3.47E-7	7.24E-8	1.17E-5
IOV	1.0	70.29	3.09	134.14	5.64E-2	-5.53E-2	15.28
IOV	0.1	0.70	3.09E-2	1.34	5.64E-4	-5.53E-4	0.15
IOV	0.01	7.03E-3	3.09E-4	1.34E-2	5.64E-6	-5.53E-6	1.53E-3
IOV	0.001	7.03E-5	3.09E-6	134E-4	5.64E-8	-5.53E-8	1.53E-5

The covariances of the resultant force are strongly related to the standard deviation of the optical properties. In the following test, the pixel size is set to be 1 cm. The standard deviation of optical properties δ varies among 1.0, 0.1, 0.01, and 0.001. As shown in Tab. 5.8, in order to make the standard deviation of the resultant force less than $0.1 \text{ nm} \cdot \text{m}^{-2}$, the standard deviation of the optical properties has to be less than 0.01.

5.4 Radiation pressure modelling for the solar panels

The solar panels of Galileo satellites are in simple geometry and the direct solar and Earth radiation pressure can be calculated in an analytical way (The ray tracing method is used to capture the details of the complex geometry of the satellite bus). There are also thermal gradient force (due to the temperature difference between the front and rear of the solar panels) on the solar panels. However, the temperature calculation of the solar panels needs more engineering and working status parameters. In this study, the corresponding information is not available.

5. INTERACTIONS BETWEEN RADIATION FLUX AND SATELLITE SURFACE

The modelling of radiation pressure for the solar panels mainly includes the direct solar radiation pressure and direct Earth radiation pressure. The following section will discuss the modelling methods and give computation results.



Figure 5.9: The Sun-facing side of the stowed solar panels for two Galileo FOC satellites.
credit: space in images [ESA, 2015].

5.4.1 Direct solar radiation pressure modelling

The solar panels are perpendicular to solar radiation flux under nominal attitude for Galileo satellites. There is only one side (72% is covered by solar cells) of the solar panels that faces the Sun. The rear side of the solar panel is different from the sun-facing side in material as shown in Fig. 5.9 and Fig. 5.10.

The calculation method is obtained by applying Eq. 5.12 to the solar panels and consider that the solar panels are always perpendicular to the solar flux (in Eq. 5.12, $\theta = 0$). The direct solar radiation pressure for solar panels $\mathbf{F}_{p,s}$ is

$$\mathbf{F}_{p,s} = \frac{A_p}{c} \left(1 + \frac{2}{3}\nu_p + \frac{1}{3}\nu_p\mu_p\right) \mathbf{W}_s \quad (5.33)$$

5. INTERACTIONS BETWEEN RADIATION FLUX AND SATELLITE SURFACE

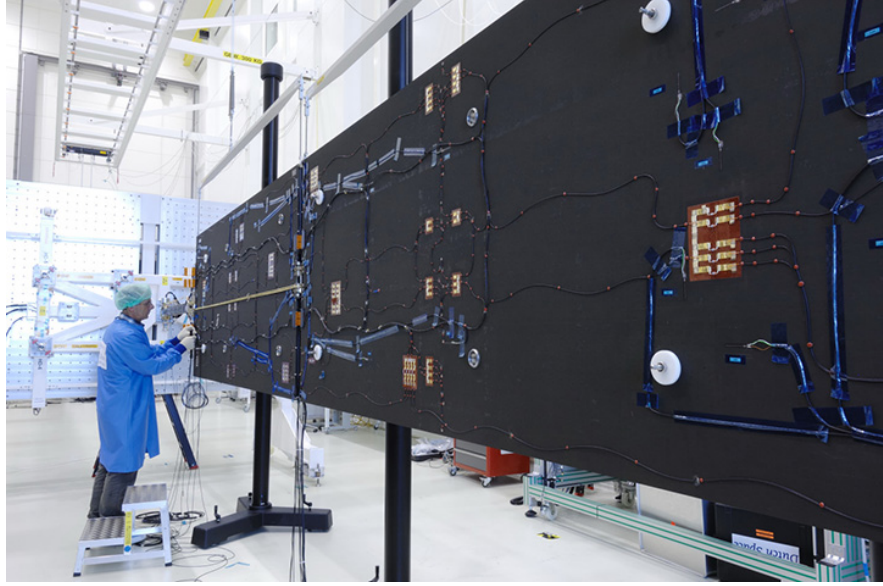


Figure 5.10: The rear side of the solar panels for one Galileo FOC satellite. credit: space in images [ESA, 2015].

where c is the light speed, \mathbf{W}_s is the incident solar radiation flux, A_p is the area of solar panels, ν_p and μ_p are the reflectivity and specularity of the solar panels.

5.4.2 Direct Earth radiation pressure modelling

In the modelling of direct Earth radiation pressure, both the Sun-facing side and rear side of the solar panels can be illuminated by the Earth radiation flux. The Earth radiation flux is divided into the SW and LW components (see chapter 3.2). The SW is mainly from the reflection of solar radiation and the solar panels should have the same optical properties for solar radiation and the SW Earth radiation. However, the LW is mainly the thermal (infrared) radiation and the optical properties of the solar panels to the thermal radiation are different from that to the SW. However, in this study, the optical properties of Galileo satellite's surfaces to the LW are not known, in the actual computation, the optical properties for the solar radiation are used instead.

Under the nominal attitude of the Galileo satellites, both the Sun-facing side and the rear side can be illuminated by the Earth radiation. The direct Earth radiation pressure (for both the SW and the LW) is computed using Eq. 5.12, i.e.

$$\mathbf{F}_{p,e} = -\frac{A_p \mathbf{n}^T \mathbf{W}_e}{c} \left\{ (1 - \nu_p \mu_p) \frac{\mathbf{W}_e}{\|\mathbf{W}_e\|} + 2\nu_p \mu_p (\mathbf{n}^T \frac{\mathbf{W}_e}{\|\mathbf{W}_e\|}) \mathbf{n} - \frac{2}{3} \nu_p (1 - \mu_p) \mathbf{n} \right\} \quad (5.34)$$

where \mathbf{W}_e is the incident Earth radiation flux, \mathbf{n} is the normal to the solar panel surface that is illuminated by the Earth radiation flux.

5. INTERACTIONS BETWEEN RADIATION FLUX AND SATELLITE SURFACE

5.5 Radiation pressure modelling for the satellite bus

The modelling of radiation pressure for the satellite bus mainly includes direct solar radiation pressure, direct Earth radiation pressure, and thermal re-radiation pressure (mainly caused by the MLI). They are calculated in the ray tracing (the core function) because of the complex shape of the satellite bus. For a given radiation source, the ray tracing can give out a resultant force.

Even though the ray tracing process has been speeded up by introducing the BVH structure, the ray tracing is time consuming if it is directly used to calculate radiation pressure in a satellite's trajectory computation. In this study, the radiation pressure models of the satellite bus are generated in a pre-computation and stored in grid files indexed by the latitude and longitude of the radiation flux direction. In the pre-computation, the TSI (Total Solar Irradiance, $E_s = 1361 \text{ W} \cdot \text{m}^{-2}$) is used as the magnitude of radiation flux. In the calculation of the direct Earth radiation pressure, the optical properties of all the satellite components for the LW are the same as that for the solar radiation just as how we dealt with the solar panels.

Once the grid files are generated, the satellite's acceleration due to the radiation pressure on the satellite's bus is computed by a bilinear interpolation. The following text will discuss both of them.

5.5.1 Grid files generation

There are 3 grid files storing the 3 components (x, y, and z in the satellite BFS) of the radiation pressure derived acceleration for a satellite bus. The direction of a radiation flux is represented by a latitude and a longitude in the BFS. Assume the radiation sources are distributed on a sphere, which means there are 360 longitudes and 180 latitudes for the directions of the radiation fluxes. With a spacing of 1° in both the longitude and latitude, there are 181 columns (-90° to 90°) and 361 rows (0° to 360°) in each of the grid files. The longitude is always 180° for Galileo satellites under nominal attitude. The coverage of all the possible radiation flux directions is helpful to deal with the non-nominal attitude situations.

Table 5.9: The parameters in generating the grid files

items:	value
nominal satellite mass (m_0):	700.0 kg
magnitude of radiation flux:	$1361 \text{ W} \cdot \text{m}^{-2}$
maximum reflection number:	3
pixel spacing:	1 mm

The parameters about the generation of grid files are in Tab. 5.9. In the generation of the grid files, the nominal satellite mass m_0 is set to be 700 kg, the magnitude of the radiation flux is set to be $1361 \text{ W} \cdot \text{m}^{-2}$. Figure 5.11 shows the accelerations in x, y, and z due to radiation pressure for the satellite bus of Galileo IOV and FOC satellites.

5. INTERACTIONS BETWEEN RADIATION FLUX AND SATELLITE SURFACE

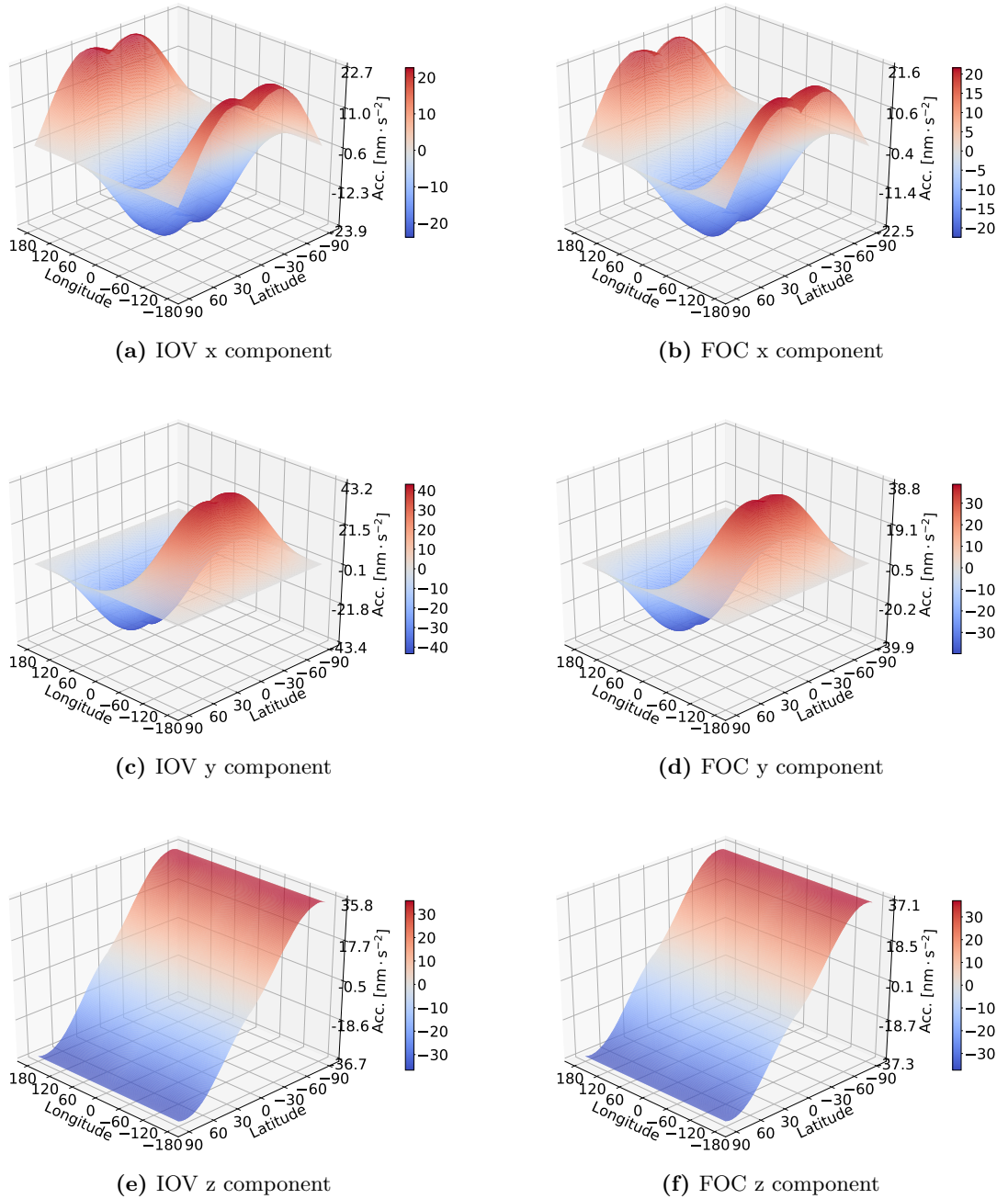


Figure 5.11: The accelerations (the grid files) of the Galileo IOV and FOC satellite bus derived from the ray tracing.

5. INTERACTIONS BETWEEN RADIATION FLUX AND SATELLITE SURFACE

The accelerations derived from the grid files have to be scaled to the actual satellite mass and the magnitude of radiation flux. This will be discussed in the user algorithm.

5.5.2 User algorithm of the grid files

A user algorithm is a process that describes how to compute the acceleration using the grid files. A user can calculate the radiation pressure derived acceleration (due to direct solar and Earth radiation pressure and thermal re-radiation pressure) of the satellite bus using the grid files generated in section 5.5.1 for any radiation fluxes. There are two steps in the user algorithm. The first step is to obtain nominal accelerations in the x,y and z of the satellite BFS by a bilinear interpolation. The next step is to scale the interpolated acceleration according to the real satellite mass and the actual radiation flux. The algorithm flow is shown in Fig. 5.12.

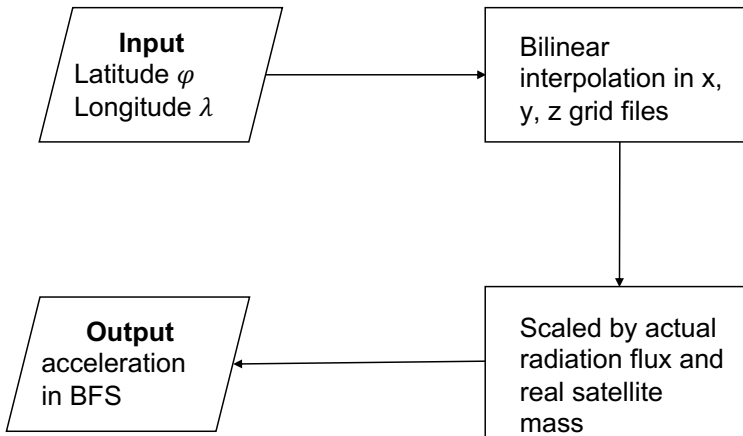


Figure 5.12: The user algorithm for the calculation of the radiation pressure acceleration due to any radiation flux using the grid files

In this algorithm, if the direction of the radiation flux is represented by latitude φ and longitude λ , the magnitude of the actual radiation flux (solar or Earth radiation) is W , the real satellite mass is m , the output acceleration is obtained by

$$\mathbf{F}_b = \frac{Wm_0}{mE_s} (a_x(\varphi, \lambda), a_y(\varphi, \lambda), a_z(\varphi, \lambda))^T \quad (5.35)$$

where E_s is the TSI, m_0 is the nominal mass (700.0 kg) in the generation of the grid files, $a_x(\varphi, \lambda)$, $a_y(\varphi, \lambda)$, $a_z(\varphi, \lambda)$ are the results from the bilinear interpolation in x, y, and z components.

One issue in the user algorithm is that there exist errors in the bilinear interpolation. We designed a test to investigate how much errors are introduced by the user algorithm (mainly from the bilinear interpolation). In this test, 10,000 radiation flux directions (a series of latitude and longitude) are generated randomly. The accelerations for these 10,000 radiation fluxes can be computed by the ray tracing or the bilinear interpolation using the grid files. The results from the ray tracing are taken as the “truth” and the differences between the ray tracing and the bilinear interpolation accelerations are used to assess the accuracy of the user algorithm.

5. INTERACTIONS BETWEEN RADIATION FLUX AND SATELLITE SURFACE

The statistics of the differences in x, y, and z components are shown in Tab. 5.10 for both the Galileo IOV and FOC satellites. The medium value is the 5000th value if all the values are sorted from smallest to the largest. The proportion of the differences that are in the range of -0.1 to 0.1 nm · s⁻² is also computed. The histograms of the differences are shown in Fig. 5.13.

Table 5.10: The statistics of the differences for 10,000 samples, unit: [nm · s⁻²]

Item	x (IOV)	y (IOV)	z (IOV)	x (FOC)	y (FOC)	z (FOC)
mean	-1.65E-04	-1.77E-04	2.69E-04	-3.81E-05	2.99E-04	8.48E-05
std.	3.35E-02	3.59E-02	2.08E-02	2.99E-02	3.12E-02	2.02E-02
min.	-0.42	-0.43	-0.31	-0.37	-0.40	-0.19
max.	0.41	0.45	0.22	0.38	0.36	0.20
medium	-5.04E-04	-3.57E-04	-8.71E-05	-1.65E-04	4.21E-04	-6.61E-05
proportion	98.60%	98.41%	99.62%	99.10%	99.05%	99.41%

5.6 The other force effects

Except for the radiation forces discussed above, there exist other forces acting on the Galileo satellites. These mainly include the antenna thrust caused by the transmitted power from the antennas on the satellite bus and the Lorenz force caused by the charged surfaces of the satellite moving in the Earth's geomagnetic field.

5.6.1 Antenna thrust

The antenna thrust on the Galileo satellites including two parts: one is from the navigation antenna; the other is from the SAR (Search And Rescue) antenna. As discussed in chapter 3.4, only the transmitted power of navigation antenna is known, thus, the antenna thrust for the SAR antenna is not considered in this study.

As long as the antenna transmission power is known, the recoil force F_a can be calculated using Eq. 5.5.

$$\mathbf{F}_a = -\frac{\mathbf{W}_a}{c} \quad (5.36)$$

where \mathbf{W}_a is the transmitted power (pointing from the satellite to the Earth) in Watts, c is the light speed.

The magnitude of antenna thrust mainly depends on the transmitted power. For the Galileo satellites, the antenna thrust can reach to 0.96 nm · s⁻². It is mainly in the radial direction and can cause about 2 cm change in the semi-major axis of the orbit during one orbital period [Steigenberger et al., 2018].

5.6.2 Lorenz force

A charged artificial satellite (due to plasmas, high energy electrons) moving relative to a magnetic field accelerates in a direction perpendicular to its velocity and the magnetic

5. INTERACTIONS BETWEEN RADIATION FLUX AND SATELLITE SURFACE

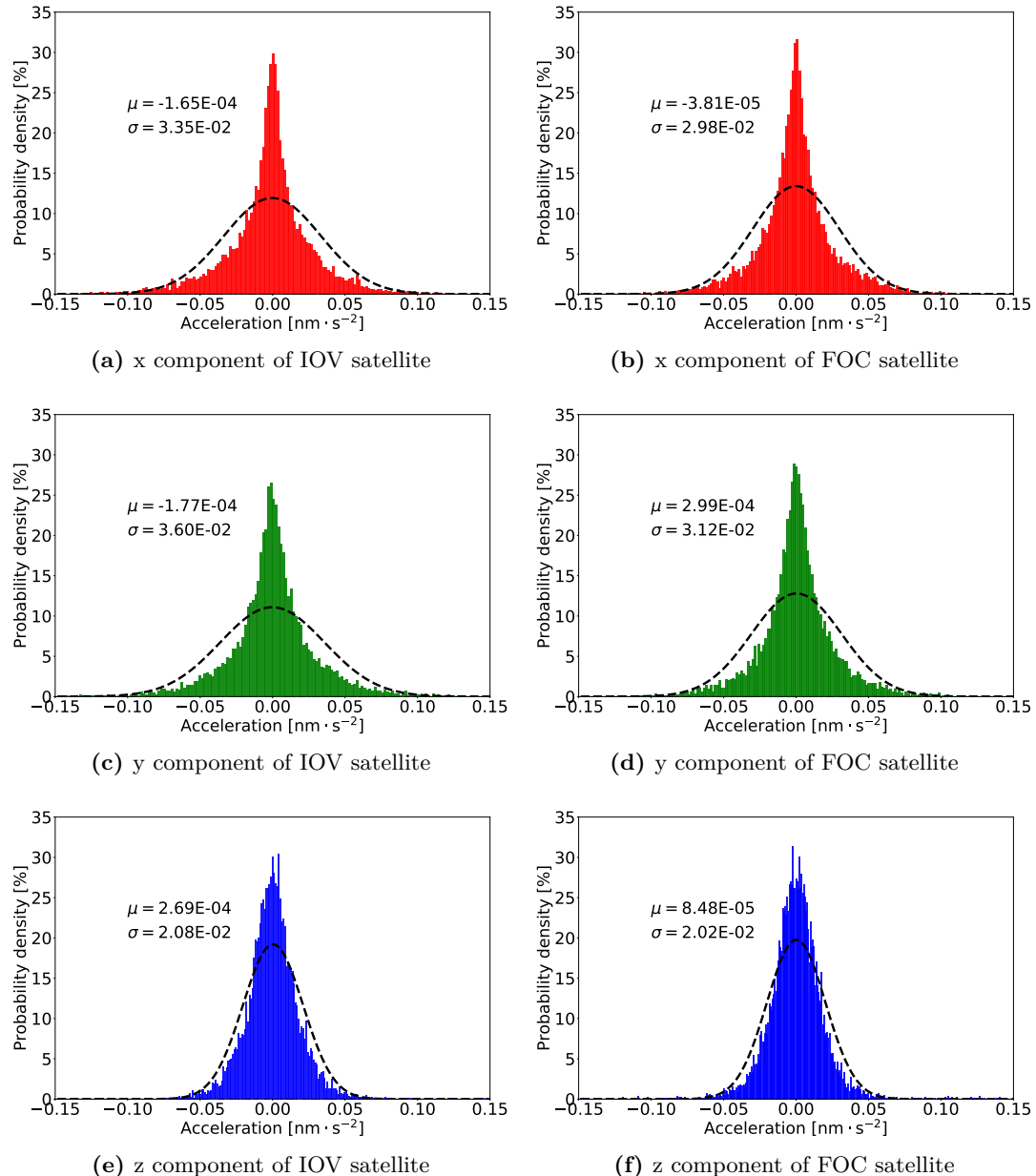


Figure 5.13: The histograms of the differences in x, y, and z component for Galileo IOV and FOC satellites. The dash line is the PDF of normal distribution with corresponding mean μ and standard deviation σ .

5. INTERACTIONS BETWEEN RADIATION FLUX AND SATELLITE SURFACE

field due to the Lorentz force. The equation for calculating the Lorentz force \mathbf{F}_L is given [Abdel-Aziz, 2007; Abdel-Aziz and Khalil, 2014]

$$\mathbf{F}_L = Q \cdot \mathbf{v} \times \mathbf{B} \quad (5.37)$$

where \mathbf{v} is the velocity of the satellite, \mathbf{B} is the vector of the magnetic field of the Earth, Q is the satellite's electric charge.

Usually, the surface charge on a satellite is very small, for LAGEOS satellite, the estimation of the charge gives 10^{-9} C as an approximate maximum [Vokrouhlický, 1989]. A value of -3×10^{-11} C was used for the analysis on its impacts to the orbit [Abdel-Aziz, 2007; Vokrouhlický, 1989]. The results showed that it leads to changes in the semi-major axis by 1 m after 30 days [Abdel-Aziz and Khalil, 2014]. Generally speaking, the Lorentz force due to the surface charge is a weak effect and it is ignored in this study.

5.7 Summary

In this chapter, the interactions between radiation fluxes and the satellite's surfaces are modelled. Firstly, the physical mechanism of the interactions between radiation flux and a satellite's surfaces are introduced. Then, a description about the satellites' information is presented. Based on the structure of Galileo satellites, the radiation pressure modelling is divided into two parts: one is the direct solar and Earth radiation pressure modelling on the solar panels, the other part is the radiation pressure computation (direct radiation pressure and thermal re-radiation pressure) on the satellite bus. A ray tracing technique that uses BVH as an acceleration structure is used to deal with the interactions between radiation fluxes with complex satellite surfaces (the satellite bus). In this chapter, the modelling results of the satellite bus derived from the ray tracing are stored in grid files and a user algorithm is provided to efficiently use the high precision ray tracing results. In addition, the modelling methods of antenna thrust and Lorenz force are also discussed.

This study is the first to apply the BVH data structure to radiation pressure modelling. By increasing the speed of radiation pressure modelling, it becomes easier to analyse the effect of multiple reflections and the choice of pixel array spacing. This is also the first time to reveal the impact of acceleration caused by multiple reflections on satellite's orbit.

The key findings of this chapter are as follows:

- The modelling of direct solar and Earth radiation pressure for the solar panels are presented. A ray tracing approach is used to model the direct solar and Earth radiation pressure and thermal re-radiation pressure for the satellite bus with complex shape.
- By introducing the BVH structure in the modelling of radiation pressure using ray tracing, the computation efficiency can be improved by a factor of 50.

5. INTERACTIONS BETWEEN RADIATION FLUX AND SATELLITE SURFACE

- The user algorithm of the grid files is in good accuracy. Over 99% of the errors introduced by the user algorithm are in the range of -0.1 to 0.1 $\text{nm} \cdot \text{s}^{-2}$.
- The uncertainty analysis of the ray tracing approach shows that the standard deviation of the optical properties has to be in the magnitude of 0.01 if the standard deviation of the computed acceleration is required to be less than 0.1 $\text{nm} \cdot \text{s}^{-2}$ for both Galileo IOV and FOC satellites.

Chapter 6

Empirical representation of solar radiation pressure

The analytical modelling approaches discussed in chapter 5 contain errors due to the un-modelled force effects and inaccuracy of inputs such as the radiation flux and optical properties. An empirical representation of the solar radiation pressure is thought to absorb the residuals of analytical modelling approaches. The largest radiation force effect is the solar radiation pressure. Thus, this chapter will discuss the empirical representation of solar radiation pressure.

In this chapter, an empirical solar radiation pressure model named DREMT (Direct Radiation pressure Empirical Model with Thermal effects) is developed based on the physics of radiation pressure. The DREMT contains direct solar radiation pressure and thermal re-radiation pressure for a box-wing satellite model. The development process of the DREMT is purely analytical but it appears in an empirical looking.

6.1 Assumptions in the satellite's geometry and attitude

The development of the DREMT is based on several assumptions. They are listed as follows:

- **Box-wing geometry**

The satellite's shape is assumed to have a pair of solar panels and a box. This is a reasonable assumption for the Galileo satellites. The box-wing geometry makes feasible writing out the analytical formula of solar radiation pressure.

- **Nominal attitude**

The satellite is assumed to be in nominal attitude. For the Galileo satellites, the BFS z-axis is always pointing to the centre of Earth. The solar panels are always perpendicular to the Sun-satellite vector. This makes the Sun moves in the xz plane of the BFS. Under the nominal attitude, the position of the Sun in BFS can only be represented by the latitude of the Sun φ (the longitude of the Sun is always 180).

6. EMPIRICAL REPRESENTATION OF SOLAR RADIATION PRESSURE

6.1.1 Box-wing geometry and radiation pressure computation

The satellite is assumed to have a pair of solar panels and a box as the satellite bus for the box-wing satellite model. The Sun-facing side of the solar panel has only one material. The rear side of the solar panels is not illuminated by the solar radiation, thus, it is not considered.

As for the satellite bus of Galileo satellites, an assumption is made that all the absorbed radiation is diffusely emitted instantaneously as thermal energy. This process generates thermal re-radiation pressure on the surfaces of the satellite bus that are illuminated by the solar radiation. Therefore, the direct solar radiation pressure and the thermal re-radiation pressure can be computed for the satellite bus.

According to Eq. 5.12, the direct solar radiation pressure is computed:

$$\mathbf{F}_{\text{srp}} = \frac{WA}{c} \left[-\nu\mu\mathbf{e}_n + \left((1-\nu\mu)\mathbf{e}_s - \frac{2}{3}\nu(1-\mu)\mathbf{e}_n \right) \cos(\theta) - \mu\nu \cos(2\theta)\mathbf{e}_n \right] \quad (6.1)$$

where

A : area of the surface

W : solar radiation flux

ν : reflectivity of the material

μ : specularity of the material

c : light speed

\mathbf{e}_n : surface normal

\mathbf{e}_s : the direction of incident solar radiation flux

θ : the angle between anti-incident and the surface normal; $\cos(\theta) = -\mathbf{e}_n \cdot \mathbf{e}_s$

On the satellite bus, because all the absorbed radiation are emitted instantaneously in a diffuse way, the thermal re-radiation pressure is computed using Eq. 3.16 and Eq. 5.5:

$$\mathbf{F}_{\text{trr}} = -\frac{2}{3} \frac{WA}{c} \cos(\theta) (1-\nu) \mathbf{e}_n \quad (6.2)$$

For the solar panels, Eq. 6.1 is applied to get the direct solar radiation pressure. For the surfaces of satellite bus that are illuminated by the solar radiation, Eq. 6.1 and Eq. 6.2 have to be added up and this generates the following equation:

$$\mathbf{F}_{\text{srp+trr}} = \frac{WA}{c} \left[-\nu\mu\mathbf{e}_n + \left((1-\nu\mu)\mathbf{e}_s - \frac{2}{3}(1-\nu\mu)\mathbf{e}_n \right) \cos(\theta) - \mu\nu \cos(2\theta)\mathbf{e}_n \right] \quad (6.3)$$

Equation 6.3 and Eq. 6.1 are the basis of the development of DERTM.

6.1.2 Nominal attitude and angular parameters

An attitude describes the pointing of satellite body fixed frame in space. Different satellites may have different definitions of body fixed frame when they are manufactured [Montenbruck et al., 2015a]. GNSS satellites are operated with yaw-steering attitude (nominal attitude) during non-eclipse seasons. In this mode, the satellite is continuously

6. EMPIRICAL REPRESENTATION OF SOLAR RADIATION PRESSURE

rotating around the Earth-pointing navigation antenna boresight such that the solar panels can be adjusted perpendicular to the Sun to maximize the energy collection.

In the definition of body fixed frame of Galileo satellites, positive z-axis is along the navigation antenna boresight and pointing to the centre of Earth, y axis is along the solar panel rotation axis which means y axis is perpendicular to the Sun–satellite direction. For the Galileo satellites, the atomic clocks are set at +x panel of the satellite bus and should avoid being illuminated by the Sun for stability of the clocks [European Global Navigation Satellite Systems Agency, 2017a; Montenbruck et al., 2015a]. Take all these conditions into consideration, the orientation of Galileo satellites is described by three unit vectors along the axes of body fixed frame:

$$\begin{cases} \mathbf{e}_z = -\frac{\mathbf{r}}{\|\mathbf{r}\|} \\ \mathbf{e}_y = \frac{\mathbf{e}_s \times \mathbf{e}_z}{\|\mathbf{e}_s \times \mathbf{e}_z\|} \\ \mathbf{e}_x = \mathbf{e}_y \times \mathbf{e}_z \end{cases} \quad (6.4)$$

where \mathbf{e}_s is a unit vector pointing from the satellite to the Sun, \mathbf{r} is the satellite's position.

Under the definition of body fixed frame of Galileo satellites, the satellite-Sun vector is confined to the xz plane of the body fixed frame (see chapter 1.2.1). The Sun sweeps around negative x-axis in the body fixed frame. The -z panel, +z panel and -x panel of the satellite bus can be illuminated, with -z and +z panel illuminated alternately, -x is always under the solar radiation. Based on the illumination of the Sun on the satellite bus, the angle φ (i.e. the latitude) between the Sun vector and the xy plane of the BFS is chosen to describe the position of the Sun. Figure 6.1 shows the illumination of box-wing geometry with respect to angular parameter φ .

Angle φ determines which panel of the satellite bus is illuminated (-z panel or the +z panel). If $\varphi \geq 0$, the +z panel is illuminated. If $\varphi \leq 0$, the -z panel is illuminated. Under nominal attitude, the position of the Sun in BFS can be fully expressed using angle φ . The incident solar radiation direction \mathbf{e}_s is given as follows:

$$\mathbf{e}_s = (\cos \varphi, 0, -\sin \varphi)^T \quad (6.5)$$

Apart from the satellite body fixed frame, the DYB system is also used to empirically describe solar radiation pressure. The D direction is pointing from the satellite to the Sun. Y direction is opposite to the satellite body fixed y-axis and B direction completes the right hand system [Arnold et al., 2015; Springer et al., 1999b]. Thus the transformation between the DYB system and the BFS is given

$$\mathbf{x}_{\text{bfs}} = \begin{pmatrix} -\cos \varphi & 0 & \sin \varphi \\ 0 & -1 & 0 \\ \sin \varphi & 0 & \cos \varphi \end{pmatrix} \mathbf{x}_{\text{dyb}} \quad (6.6)$$

6. EMPIRICAL REPRESENTATION OF SOLAR RADIATION PRESSURE

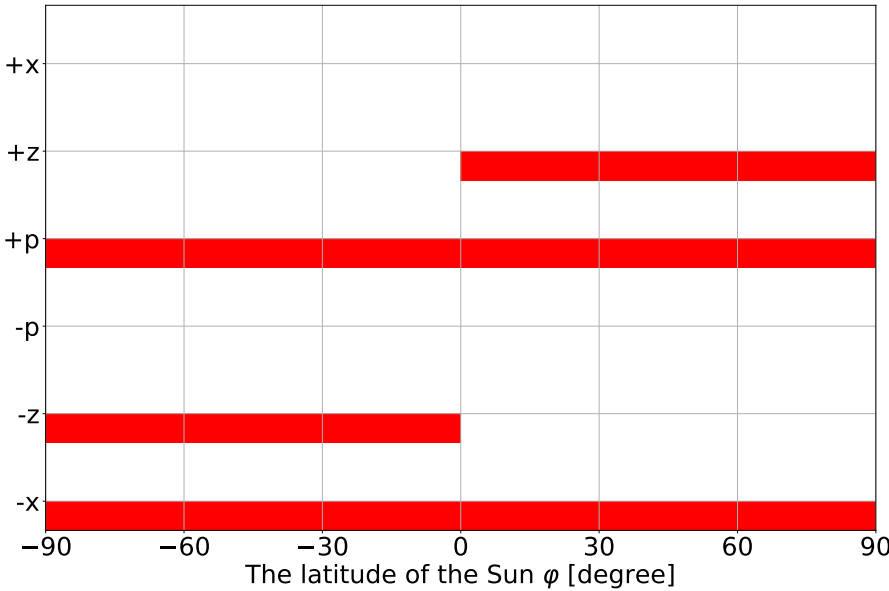


Figure 6.1: The solar radiation illumination of the box-wing geometry with respect to φ . “+p” represents the sun-facing side of solar panels, “-p” represents the rear side of solar panels.

In the ECOM (Extended CODE Orbit Model) that is expressed in the DVB system, it uses the orbital angle Δu as the only angular parameter [Arnold et al., 2015; Springer et al., 1999b]. Orbital angle Δu is the angle difference between the argument of latitude of the satellite (u) and the argument of latitude of the Sun (u_s) in the orbital plane. i.e.

$$\Delta u = u - u_s \quad (6.7)$$

Figure 6.2 shows the geometrical relations among the Sun elevation over orbital plane (β), orbital angle (Δu) and the Earth-Probe-Sun angle (ε). The Sun is very far from the Earth, an approximation is made that the distance from the Sun to the Earth is equal to the distance from the Sun to the satellite. Under this approximation, the relation between them is given [Bar-Sever, 1996; Bar-Sever and Russ, 1997]

$$\cos \varepsilon \doteq \cos \beta \cos \Delta u \quad (6.8)$$

There are also models such as the GSPM using the angle ε which is the Earth-Probe-Sun angle as the angular parameters to empirically represent the direct solar radiation pressure [Bar-Sever and Kuang, 2004; 2005; Bar-Sever and Russ, 1997; Ziebart, 2004]. As shown in Fig. 6.3, the relation between ε and φ is given by

$$\varepsilon = \frac{\pi}{2} - \varphi \quad (6.9)$$

Angle ε varies between β and $\pi - \beta$ and angle φ varies between $|\beta| - \frac{\pi}{2}$ and $\frac{\pi}{2} - |\beta|$. Equation 6.8 also shows that solar radiation pressure can not be represented by only the angular parameter Δu , it also relates to the Sun elevation β . In the orbit determination practice with ECOM like empirical models, the observation data are processed daily,

6. EMPIRICAL REPRESENTATION OF SOLAR RADIATION PRESSURE

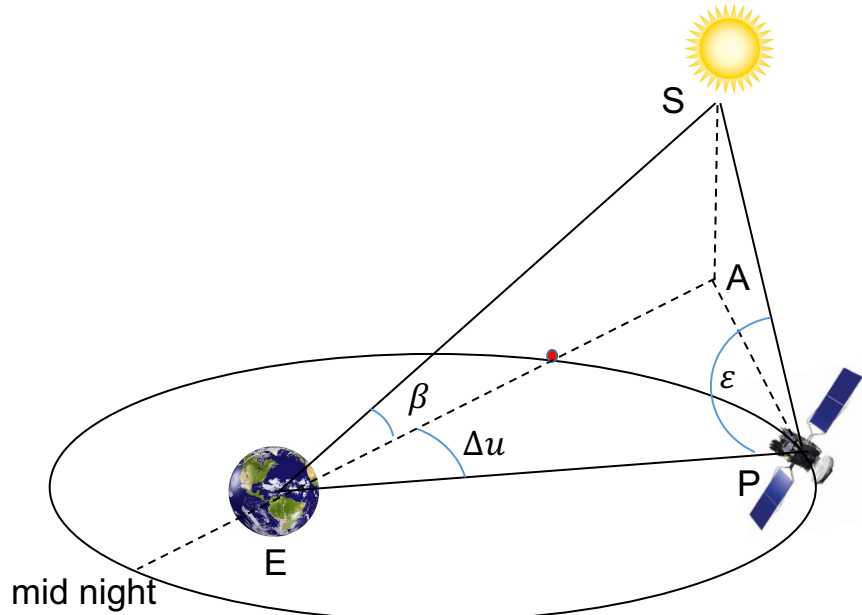


Figure 6.2: The geometry among angle β , Δu and ϵ . ‘E’ represents the Earth, ‘P’ represents the satellite and ‘S’ stands for the Sun.

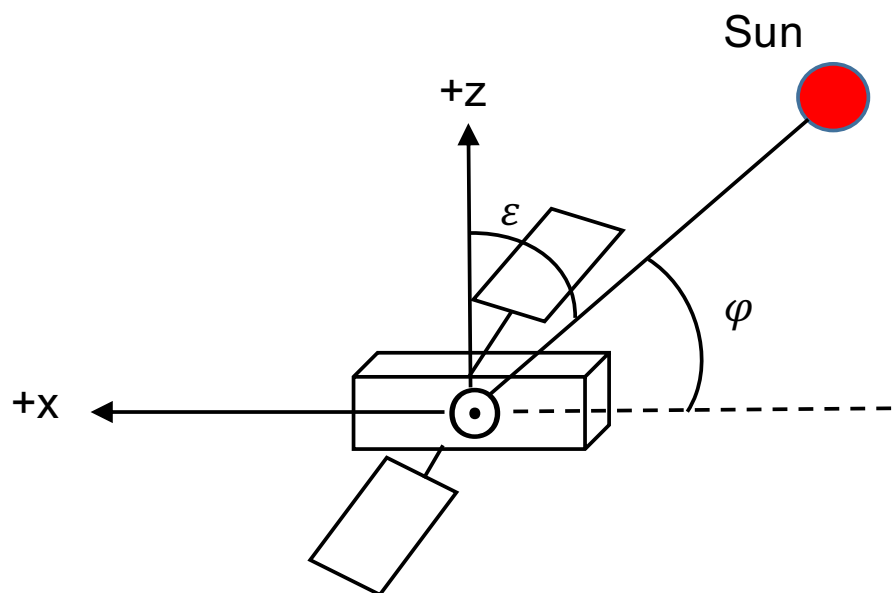


Figure 6.3: This shows the relation between ϵ and φ is $\epsilon = \frac{\pi}{2} - \varphi$

6. EMPIRICAL REPRESENTATION OF SOLAR RADIATION PRESSURE

the Sun elevation β is assumed to be a constant during 24 hours. The Galileo satellite orbits derived from GNSS measurements can be validated independently by the Satellite Laser Ranging (SLR). The SLR residuals show a correlation with β angle (especially at a lower β). It is believed that this is caused by the deficiency of the solar radiation pressure model.

6.2 Modelling method of the DREMT

6.2.1 Apply the Box-wing geometry

Although the real-world satellites are in very complex geometry, GNSS satellites are all very like a box plus a pair of wings. The box-wing geometry can capture the main signal of solar radiation pressure. The solar radiation pressure for the box-wing model is computed by applying Eq. 6.1 to the solar panels and Eq. 6.3 to the satellite bus. The parameters used in the modelling are shown in Table 6.1. The steps of modelling solar radiation pressure for the box-wing geometry are described in the following sections.

Table 6.1: The parameters used for the box-wing model

surface	area	reflectivity (ν)	specularity (μ)
solar panels	A_p	ν_p	μ_p
-x panel	A_{-x}	ν_{-x}	μ_{-x}
-z panel	A_{-z}	ν_{-z}	μ_{-z}
+z panel	A_{+z}	ν_{+z}	μ_{+z}

6.2.1.1 Solar panels

The solar panels are always tracking the Sun and they are perpendicular to the Sun-satellite vector. Thus, the angle $\theta = 0$ and the surface normal to the solar panel is $\mathbf{e}_n = -\mathbf{e}_s$. Therefore the force in BFS x and z components on the solar panels are given according to Eq. 6.1

$$\begin{cases} F_x^p = \frac{WA_p}{c}(1 + \frac{2}{3}\nu_p + \frac{1}{3}\nu_p\mu_p) \cos \varphi \\ F_z^p = -\frac{WA_p}{c}(1 + \frac{2}{3}\nu_p + \frac{1}{3}\nu_p\mu_p) \sin \varphi \end{cases} \quad (6.10)$$

6. EMPIRICAL REPRESENTATION OF SOLAR RADIATION PRESSURE

6.2.1.2 -x panel

When the solar radiation illuminates on the -x panel, the angle $\theta = |\varphi|$ and the surface normal is $\mathbf{e}_n = (-1, 0, 0)^T$. Therefore, the forces on the -x panel are given by

$$\begin{cases} F_x^{-x} = \frac{WA_{-x}}{c} \left[\frac{1}{2}(1 + \nu_{-x}\mu_{-x}) + \frac{2}{3}(1 - \nu_{-x}\mu_{-x}) \cos \varphi + \frac{1}{2}(1 + \nu_{-x}\mu_{-x}) \cos 2\varphi \right] \\ F_z^{-x} = \frac{WA_{-x}}{c} \frac{\mu_{-x}\nu_{-x}-1}{2} \sin 2\varphi \end{cases} \quad (6.11)$$

6.2.1.3 -z panel

When the solar radiation illuminates on the -z panel, angular parameter $\varphi \leq 0$. The angle $\theta = \frac{\pi}{2} + \varphi$. The surface normal to -z panel is $\mathbf{e}_n = (0, 0, -1)^T$. Thus, the forces on the -z panel are

$$\begin{cases} F_x^{-z} = \frac{WA_{-z}}{c} \frac{\mu_{-z}\nu_{-z}-1}{2} \sin 2\varphi \\ F_z^{-z} = \frac{WA_{-z}}{c} \left[\frac{1}{2}(1 + \nu_{-z}\mu_{-z}) - \frac{2}{3}(1 - \nu_{-z}\mu_{-z}) \sin \varphi - \frac{1}{2}(1 + \nu_{-z}\mu_{-z}) \cos 2\varphi \right] \end{cases} \quad (6.12)$$

6.2.1.4 +z panel

If the solar radiation illuminates on the +z panel, angular parameter $\varphi > 0$. The angle $\theta = \frac{\pi}{2} - \varphi$. The surface normal to +z panel is $\mathbf{e}_n = (0, 0, 1)^T$. Thus, the forces on +z panel are

$$\begin{cases} F_z^{+z} = \frac{WA_{+z}}{c} \left[-\frac{1}{2}(1 + \nu_{+z}\mu_{+z}) - \frac{2}{3}(1 - \nu_{+z}\mu_{+z}) \sin \varphi + \frac{1}{2}(1 + \nu_{+z}\mu_{+z}) \cos 2\varphi \right] \\ F_x^{+z} = \frac{WA_{+z}}{c} \frac{1-\mu_{+z}\nu_{+z}}{2} \sin 2\varphi \end{cases} \quad (6.13)$$

Two variables δ_1 and δ_2 are introduced because the solar radiation illuminates on -z and +z panel alternately.

$$\begin{cases} \delta_1 = 1, \delta_2 = 0, \varphi \geq 0 & +z \text{ panel} \\ \delta_1 = 0, \delta_2 = 1, \varphi < 0 & -z \text{ panel} \end{cases} \quad (6.14)$$

Therefore, the resultant force is given by

$$\begin{cases} F_x = F_x^p + F_x^{-x} + \delta_1 F_x^{+z} + \delta_2 F_x^{-z} \\ F_z = F_z^p + F_z^{-x} + \delta_1 F_z^{+z} + \delta_2 F_z^{-z} \end{cases} \quad (6.15)$$

Note that solar radiation pressure computed in the box-wing model has no y component since y panel is never illuminated under the nominal yaw-steering attitude.

6. EMPIRICAL REPRESENTATION OF SOLAR RADIATION PRESSURE

Equation 6.15 is the solar radiation pressure for the box-wing model.

6.2.2 Parameterization of the box-wing model

The box-wing model (Eq. 6.15) has 12 parameters which are shown in Tab. 6.1. However, some of the parameters can be expressed as one, such as the three parameters for the solar panels. Table 6.2 shows the first try of parameterization. By combining the parameters for the solar panels (i.e. A_p , ν_p , μ_p), the total number of parameters has reduced from 12 to 10.

Table 6.2: The parameters for the first try of parameterization of the box-wing model

surface	parameters
solar panels	$C_1 = A_p(1 + \frac{2}{3}\nu_p + \frac{1}{3}\nu_p\mu_p)$
-x panel	$C_2 = A_{-x}; C_3 = A_{-x}\nu_{-x}; C_4 = A_{-x}\nu_{-x}\mu_{-x}$
-z panel	$C_5 = A_{-z}; C_6 = A_{-z}\nu_{-z}; C_7 = A_{-z}\nu_{-z}\mu_{-z}$
+z panel	$C_8 = A_{+z}; C_9 = A_{+z}\nu_{+z}; C_{10} = A_{+z}\nu_{+z}\mu_{+z}$

After the first try of parameterization, the box-wing model becomes

$$\left\{ \begin{array}{l} F_x = \frac{W}{c} \left[C_1 \cos \varphi + \frac{(C_2+C_4)}{2} + \frac{2}{3}(C_2 - C_4) \cos \varphi + \frac{1}{2}(C_2 + C_4) \cos 2\varphi \right. \\ \quad \left. + \frac{1}{2}\delta_1(C_8 - C_{10}) \sin 2\varphi \right. \\ \quad \left. + \frac{1}{2}\delta_2(C_7 - C_5) \sin 2\varphi \right] \\ \\ F_z = \frac{W}{c} \left[-C_1 \sin \varphi - \frac{1}{2}(C_2 - C_4) \sin 2\varphi \right. \\ \quad \left. + \delta_1 \left(-\frac{1}{2}(C_8 + C_{10}) - \frac{2}{3}(C_8 - C_{10}) \sin \varphi + \frac{1}{2}(C_8 + C_{10}) \cos 2\varphi \right) \right. \\ \quad \left. + \delta_2 \left(\frac{1}{2}(C_5 + C_7) - \frac{2}{3}(C_5 - C_7) \sin \varphi - \frac{1}{2}(C_5 + C_7) \cos 2\varphi \right) \right] \end{array} \right. \quad (6.16)$$

Some parameters in Eq. 6.16 are strongly correlated. Reorganising the coefficients in Eq. 6.16 and some new parameters are defined in Tab. 6.3.

Table 6.3: The parameters for the second try of parameterization of the box-wing model

parameters	definition
P_1	C_1
P_2	$C_2 + C_4$
P_3	$C_2 - C_4$
P_4	$C_5 + C_7$
P_5	$C_5 - C_7$
P_6	$C_8 + C_{10}$
P_7	$C_8 - C_{10}$

After the second try of parameterization, the box-wing model becomes

6. EMPIRICAL REPRESENTATION OF SOLAR RADIATION PRESSURE

$$\begin{cases} F_x = \frac{W}{c} \left[(P_1 + \frac{2}{3}P_3) \cos \varphi + P_2 \cos^2 \varphi - \frac{1}{2}\delta_2 P_5 \sin 2\varphi + \frac{1}{2}\delta_1 P_7 \sin 2\varphi \right] \\ F_z = \frac{W}{c} \left[(-P_1 - \frac{2}{3}(\delta_1 P_7 + \delta_2 P_5)) \sin \varphi - \frac{1}{2}P_3 \sin 2\varphi + (\delta_2 P_4 - \delta_1 P_6) \sin^2 \varphi \right] \end{cases} \quad (6.17)$$

Although Eq. 6.17 is already in a relatively simple form, it can be further simplified by assuming that the $-z$ and $+z$ panel have the same area and optical properties. This assumption was used in the enhanced solar radiation pressure modelling in [Montenbruck et al. \[2015b\]](#). That is,

$$\begin{cases} P_4 = P_6 \\ P_5 = P_7 \end{cases} \quad (6.18)$$

After the simplification, only one variable δ is needed to identify which side of the z panels ($+z$ or $-z$) is illuminated.

$$\begin{cases} \delta = 1, \varphi \geq 0 & +z \text{ panel} \\ \delta = -1, \varphi < 0 & -z \text{ panel} \end{cases} \quad (6.19)$$

Equation 6.17 becomes

$$\begin{cases} F_x = \frac{W}{c} \left[Q_1 \cos \varphi + Q_2 \cos^2 \varphi + Q_3 |\sin 2\varphi| \right] \\ F_z = \frac{W}{c} \left[\left(\frac{4}{3}(Q_4 - Q_3) - Q_1 \right) \sin \varphi - Q_4 \sin 2\varphi - \delta Q_5 \sin^2 \varphi \right] \end{cases} \quad (6.20)$$

where the parameters “Q” are defined in the following Tab. 6.4.

Table 6.4: This definitions of parameters “Q”

parameters	definition
Q_1	$P_1 + \frac{2}{3}P_3$
Q_2	P_2
Q_3	$\frac{1}{2}P_5$
Q_4	$\frac{1}{2}P_3$
Q_5	P_4

Equation 6.20 can also be converted into the DSB system. It becomes:

$$\begin{cases} F_D = \frac{W}{c} \left[-Q_1 + \frac{2}{3}(Q_4 - Q_3) - \frac{2}{3}(Q_4 - Q_3) \cos 2\varphi - Q_2 \cos \varphi - Q_5 |\sin \varphi| \right. \\ \quad \left. + (Q_2 - 2Q_4) \cos \varphi \sin^2 \varphi + (Q_5 - 2Q_3) \cos^2 \varphi |\sin \varphi| \right] \\ F_B = \frac{W}{c} \left[\frac{2}{3}(Q_4 - Q_3) \sin 2\varphi + (Q_2 - 2Q_4) \sin \varphi \cos^2 \varphi \right. \\ \quad \left. - \delta(Q_5 - 2Q_3) \cos \varphi \sin^2 \varphi \right] \end{cases} \quad (6.21)$$

6. EMPIRICAL REPRESENTATION OF SOLAR RADIATION PRESSURE

6.2.3 Empirical representation of box-wing model

Equation 6.21 is the foundation for the representation of box-wing based solar radiation pressure expressed in the DYB system. The purpose of the empirical representation of the box-wing model in orbit modelling is to find a formula which contains several parameters to be estimated together with the orbital parameters (the satellite's position and velocity). One problem of directly using Eq. 6.21 in orbit estimation is that some terms are correlated with each other. This will weak the structure of the model which causes a bad accuracy in estimation. Thus, the main work is how to choose the parameters to be estimated.

Table 6.5: The values of “Q” parameters in Eq. 6.21 for Galileo satellites. unit: [m²]

parameters	value (IOV)	value (FOC)	related surfaces
$\frac{2}{3}(Q_4 - Q_3) - Q_1$	-14.4817	-14.3969	solar panels, -x, z
$-\frac{2}{3}(Q_4 - Q_3)$	0.5600	0.4752	-x, z
$-Q_2$	-1.32	-1.32	-x
$-Q_5$	-3.0	-3.2545	z
$Q_2 - 2Q_4$	0.0	0	-x
$Q_5 - 2Q_3$	0.0	0.5090	z

In the first place, the contribution (the magnitude) of each term in Eq. 6.21 is computed based on an *a priori* box-wing model (both IOV and FOC satellites) described in Tab. 5.1 and Tab. 5.2. This helps to analyse which terms have larger contribution and should not be ignored. The “Q” parameters are computed (the optical properties of satellite components that have multiple materials are averaged) and shown in Tab 6.5. The characteristics of Eq. 6.21 are as follows:

- In D component, the largest contribution comes from $\frac{2}{3}(Q_4 - Q_3) - Q_1$. This is mainly due to the solar panels and the difference between -x panel and the z panel. The second largest term is $-Q_5$ which is a parameter for the z panel. Then comes the parameter for the -x panel $-Q_2$. Term $-\frac{2}{3}(Q_4 - Q_3)$ represents the difference between -x panel and z panel. For satellite bus that has a cuboid shape (Galileo satellites), this parameter is important in estimation. Parameter $Q_2 - 2Q_4$ is related to the specular reflection on the -x panel and $Q_5 - 2Q_3$ is related to the specular reflection on the z panel. The D component is dominated by terms with coefficients $\frac{2}{3}(Q_4 - Q_3) - Q_1$, $-Q_5$, $-Q_2$ and $\frac{2}{3}(Q_4 - Q_3)$.
- In B component, three parameters $\frac{2}{3}(Q_4 - Q_3)$, $Q_2 - 2Q_4$, and $Q_5 - 2Q_3$ have contribution. Less than 5% of the total solar radiation force is in B component. As shown in Tab. 6.5, the B component is dominated by the term with coefficient $\frac{2}{3}(Q_4 - Q_3)$ for IOV satellites. However, the term with coefficient $Q_5 - 2Q_3$ is also important for the FOC satellites due to the specular radiators on the +z panel.

The more correlated the parameters, the more difficult to separate them in estimation. Thus, the task of correlation analysis is to choose the parameters that are less

6. EMPIRICAL REPRESENTATION OF SOLAR RADIATION PRESSURE

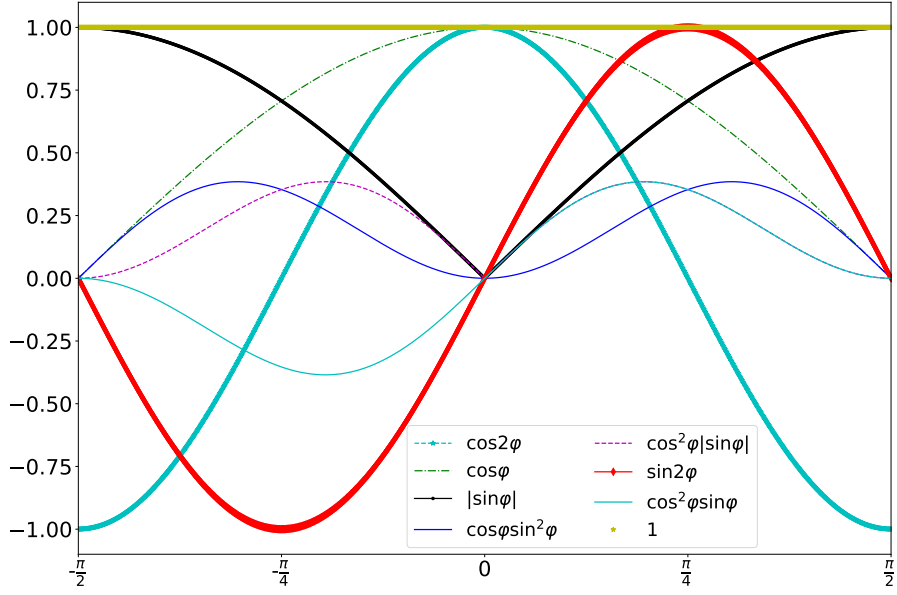


Figure 6.4: The variation of the function for each term in Eq. 6.21

correlated with each other. The functions of each term in Eq. 6.21 are shown in Fig. 6.4. Terms $\cos \varphi$ and $\cos 2\varphi$ have similar trend, thus, it is better not to estimate parameters for these two terms at the same time. The terms $\cos \varphi \sin^2 \varphi$, $\cos^2 \varphi \sin \varphi$, and $\cos^2 \varphi |\sin \varphi|$ are also very similar. The magnitude of these three functions are almost half of the other functions. This means these three terms have less contributions.

Based on above analysis on the magnitude of each term and the correlations between the parameters, the terms estimated in both D and B are determined. In D component, constant $\frac{2}{3}(Q_4 - Q_3) - Q_1$ and Q_5 can be estimated at the same time; either Q_2 or $\frac{2}{3}(Q_4 - Q_3)$ is estimated. That means the estimated parameters in D component are either $\frac{2}{3}(Q_4 - Q_3) - Q_1, Q_5, Q_2$ or $\frac{2}{3}(Q_4 - Q_3) - Q_1, Q_5, \frac{2}{3}(Q_4 - Q_3)$. The rest terms in D component are represented by $\sin 2\Delta u$ (Δu is the difference between the latitude of the satellite and the latitude of the Sun in orbital plane). In B component, the parameter $\frac{2}{3}(Q_4 - Q_3)$ is estimated. It appears in the D component as well. To estimate a same parameter in both the D and B component can strengthen the estimation. In this way, the parameters estimated in D component are confirmed: $\frac{2}{3}(Q_4 - Q_3) - Q_1, Q_5, \frac{2}{3}(Q_4 - Q_3)$. The rest terms in B component are represented by $\cos \Delta u$. There are two reasons to introduce the terms with Δu in the D and B components. One is that angular parameter Δu is less likely to be correlated with the terms expressed in angular parameter φ . The other is that it is reported in the development of ECOM-2 that there should be twice-per-revolution term in D and one-per-revolution term in B [Arnold et al., 2015].

The above box-wing model does not include force in BFS y-axis, a y-bias parameter is used to deal with the force due to the imbalanced heat dump of radiators on the +y and -y panels. Therefore, the empirical looking DREMT (in the unit of $\text{nm} \cdot \text{s}^{-2}$) is expressed:

6. EMPIRICAL REPRESENTATION OF SOLAR RADIATION PRESSURE

$$\mathbf{a}_{\text{DREMT}} = F_s \cdot \frac{\text{AU}^2}{\|\mathbf{r}_\odot\|^2} \cdot (D(\varphi, \Delta u) \cdot \mathbf{e}_D + Y \cdot \mathbf{e}_Y + B(\varphi, \Delta u) \cdot \mathbf{e}_B) \quad (6.22)$$

where F_s is the shadow function, \mathbf{r}_\odot is the vector from the satellite to the Sun. AU is the astronomical unit.

The three components $D(\varphi, \Delta u)$, Y_0 and $B(\varphi, \Delta u)$ are expressed

$$\begin{cases} D(\varphi, \Delta u) = X_1 - X_2 \cos 2\varphi - X_3 |\sin \varphi| + X_4 \sin 2\Delta u \\ Y = X_6 \\ B(\varphi, \Delta u) = X_2 \sin 2\varphi + X_5 \cos \Delta u \end{cases} \quad (6.23)$$

where

$$X_1 = \frac{E_s}{mc} \left[\frac{2}{3} (Q_4 - Q_3) - Q_1 \right];$$

$$X_2 = \frac{E_s}{mc} \left[\frac{2}{3} (Q_4 - Q_3) \right];$$

$$X_3 = \frac{E_s}{mc} Q_5;$$

X_4 : they are used to absorb the residuals in D;

X_5 : they are used to absorb the residuals in B;

X_6 : the y-bias parameter;

c is the light speed, E_s is the TSI and m is the mass of the satellite.

6.3 Accuracy loss of the DREMT

The DREMT is developed based on a box-wing model with some approximations. One questions that how accurate is the DREMT comparing with the box-wing model is produced. In this study, the DREMT is fitted to the accelerations computed from the box-wing geometry using Eq. 6.15. This is different from the box-wing model described by Eq. 6.21 or Eq. 6.20 because Eq. 6.15 does not assume the -z and +z panel are the same. The optical properties of the box-wing model used in the calculation of Eq. 6.15 are shown in Tab. 5.1 and Tab. 5.2. In order to make comparisons between different empirical models, the 5-parameter ECOM-1 (see Eq. 6.24), 7-parameter ECOM-2 (see Eq. 6.25), box-wing model (Eq. 6.20) and the DREMT (Eq. 6.23) are tested. If the accelerations computed from Eq. 6.15 are taken as the “truth”, the fitting residuals of different empirical models are used to assess their accuracy loss.

$$\mathbf{a}_{DYB} = \begin{pmatrix} 1 & 0 & 0 & 0 & 0 \\ 0 & 1 & 0 & 0 & 0 \\ 0 & 0 & 1 & \cos \Delta u & \sin \Delta u \end{pmatrix} \begin{pmatrix} D_0 \\ Y_0 \\ B_0 \\ B_c \\ B_s \end{pmatrix} \quad (6.24)$$

6. EMPIRICAL REPRESENTATION OF SOLAR RADIATION PRESSURE

$$\mathbf{a}_{DYZB} = \begin{pmatrix} 1 & \cos 2\Delta u & \sin 2\Delta u & 0 & 0 & 0 & 0 \\ 0 & 1 & 0 & 0 & 0 & 0 & 0 \\ 0 & 0 & 0 & 0 & 1 & \cos \Delta u & \sin \Delta u \end{pmatrix} \begin{pmatrix} D_0 \\ D_{2,c} \\ D_{2,s} \\ Y_0 \\ B_0 \\ B_{1,c} \\ B_{1,s} \end{pmatrix} \quad (6.25)$$

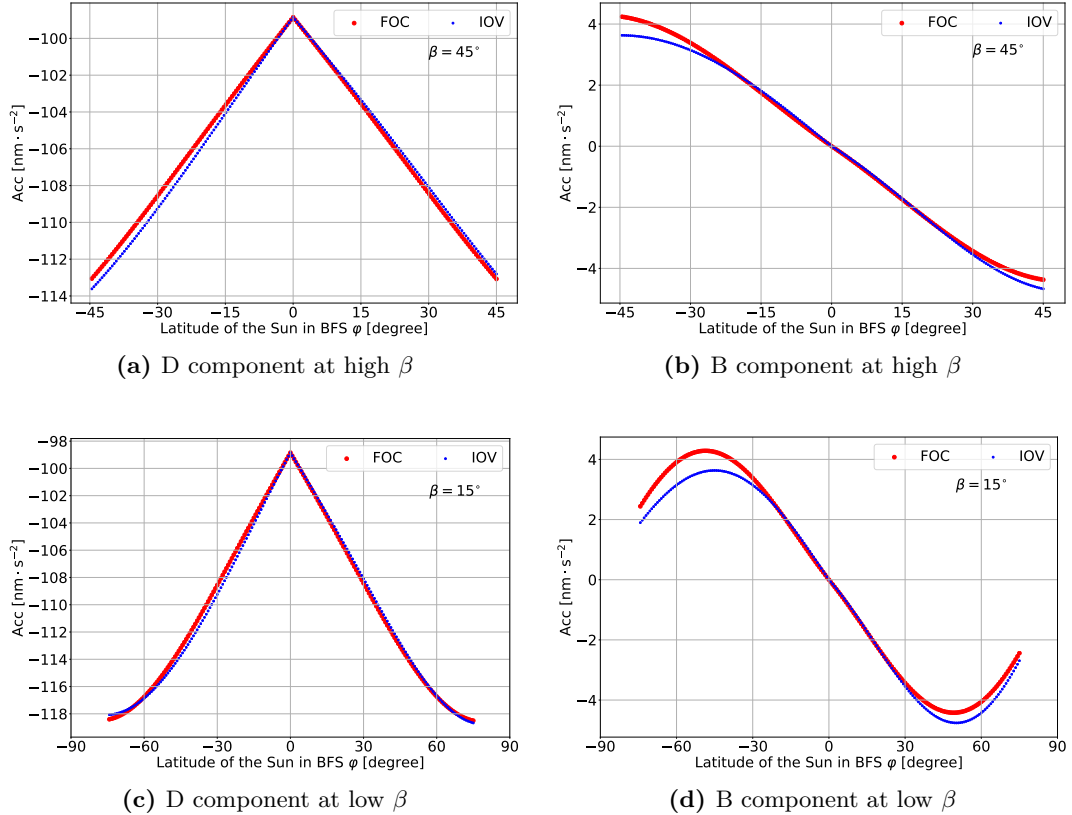


Figure 6.5: The box-wing accelerations in the D and B components for the IOV and FOC satellites.

The variations of the acceleration computed from Eq. 6.15 for both the Galileo IOV and FOC satellites are shown in Fig. 6.5. In the calculation, a low ($\beta = 15^\circ$) and a high ($\beta = 45^\circ$) Sun elevation are chosen. As the range of β varies, the range of the latitude of Sun (φ) in body fixed frame is varying. In terms of the magnitude of acceleration in D and B component, over 95% of the total solar radiation pressure is in the D component. The fitting RMS in D and B components for the ECOM-1, ECOM-2 and the DREMT over all the Sun elevation are shown in Fig. 6.6. The average fitting RMS for the IOV and FOC satellites are shown in Tab. 6.6.

As Fig. 6.6 shows, the fitting RMS in both D and B components grow as the decreasing of Sun elevation β . In the D component, the 5-parameter ECOM-1 has the largest fitting RMS among the 3 empirical models, the 7-parameter ECOM-2 is better

6. EMPIRICAL REPRESENTATION OF SOLAR RADIATION PRESSURE

Table 6.6: The statistics of the fitting RMS of ECOM-1, ECOM-2 and DREMT for IOV and FOC satellites over all the Sun elevations. unit: $[\text{nm} \cdot \text{s}^{-2}]$

model components	IOV mean	FOC mean	IOV std.	FOC std.
ECOM-1 D	2.270	2.252	1.152	1.164
ECOM-1 B	0.217	0.206	0.256	0.254
ECOM-2 D	0.500	0.474	0.249	0.235
ECOM-2 B	0.217	0.206	0.255	0.255
DREMT D	0.157	0.121	0.128	0.118
DREMT B	0.138	0.096	0.092	0.061

than ECOM-1 but worse than the DREMT. At a lower β , the fitting RMS can reach 3.5, 1.0 and 0.5 $\text{nm} \cdot \text{s}^{-2}$ for ECOM-1, ECOM-2 and DREMT separately. The average fitting RMS in D component for the 3 models are 2.252, 0.474, and 0.121 $\text{nm} \cdot \text{s}^{-2}$ separately as shown in Tab. 6.6. In the B component, the ECOM-1 and ECOM-2 have the same expression which makes their fitting RMS the same. One interesting point is that the B component RMS of DREMT is smaller than that of the ECOM-1 and ECOM-2 when the Sun elevation β is smaller than 30°, but larger than that of the ECOM-1 and ECOM-2 at a relatively higher β (higher than 40°). The average fitting RMS of DREMT is 0.096 $\text{nm} \cdot \text{s}^{-2}$ while 0.206 $\text{nm} \cdot \text{s}^{-2}$ for the ECOM-1 and ECOM-2.

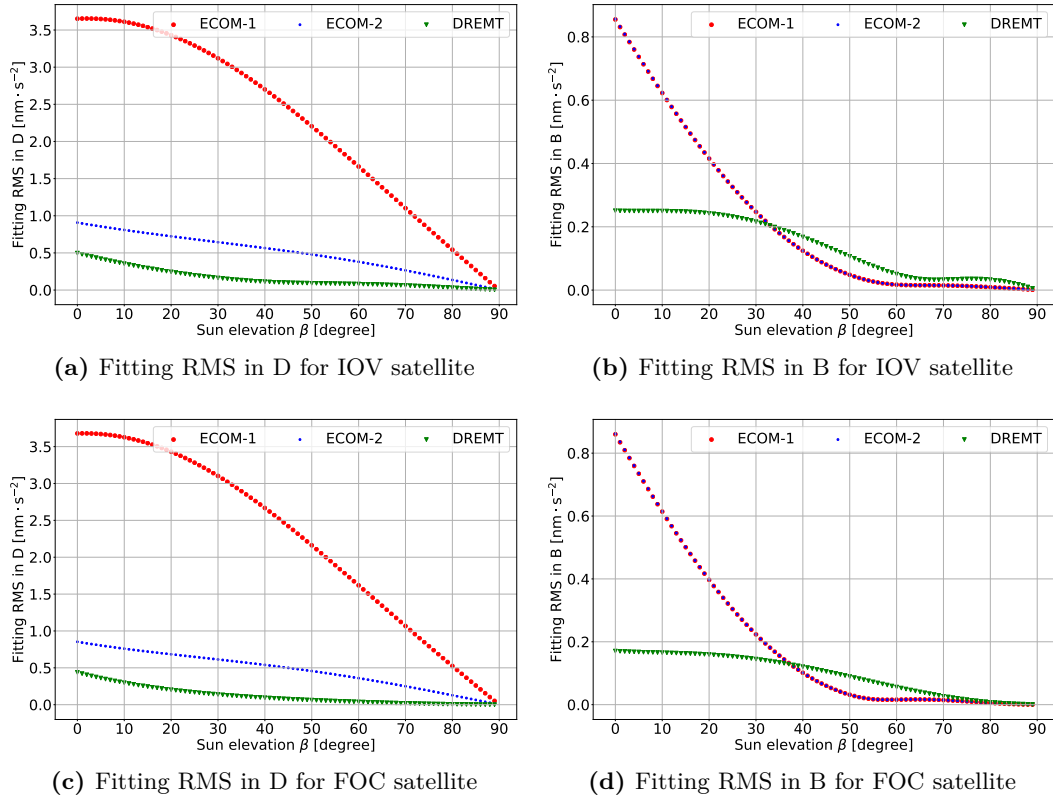


Figure 6.6: The fitting RMS in D and B components for the 3 empirical models: ECOM-1, ECOM-2 and the DREMT.

Based on the above calculation results, we can conclude that the DREMT is the

6. EMPIRICAL REPRESENTATION OF SOLAR RADIATION PRESSURE

most accurate among the 3 empirical models (ECOM-1, ECOM-2 and DREMT) for both IOV and FOC satellites. The average of the fitting RMS are 0.157 and 0.121 $\text{nm} \cdot \text{s}^{-2}$ in the D component for IOV and FOC satellites. The B component average fitting RMS are 0.138 and 0.096 $\text{nm} \cdot \text{s}^{-2}$ for IOV and FOC satellites.

6.4 Can the DREMT absorb other forces on the satellite bus?

As described in section 5.2 of chapter 5, there are radiators on the +x, +y and -y panels of the IOV and FOC satellite bus. There are even radiator on the +z panel of the satellite bus for FOC satellites. The heat dump of these radiators causes corresponding thermal radiation forces. In addition, the antenna thrust and the direct Earth radiation pressure are in negative z-axis of the body fixed frame. The y-bias parameter in the DREMT is thought to deal with the force effects on the +y and -y panels. The antenna thrust, direct Earth radiation pressure and thermal radiation forces on the +x and +z radiators lead to resultant force in the x-axis and z-axis of the body fixed frame.

In this research, we assume the accelerations in the x-axis and z-axis are a_x and a_z separately. They are converted into the DYB system using Eq. 6.6.

$$\begin{cases} a_D = & a_z \sin \varphi - a_x \cos \varphi \\ a_B = & a_z \cos \varphi + a_x \sin \varphi \end{cases} \quad (6.26)$$

The term $\|\sin \varphi\|$ in D component of the DREMT can absorb part of a_z . The absorption of the DREMT to a_x is not obvious. In order to test how much of the a_x and a_z can be absorbed by the DREMT, an experiment similar to the fitting test in section 6.3 is performed. The only difference is that a value of $a_x = a_z = 10 \text{ nm} \cdot \text{s}^{-2}$ is added to the “truth” acceleration computed from Eq. 6.15. Table 6.7 shows the statistics of the fitting RMS for the 3 models. Figure 6.7 shows the variations of fitting RMS for IOV and FOC satellites over all the β .

Table 6.7: The statistics of the fitting RMS of ECOM-1, ECOM-2 and DREMT for IOV and FOC satellites over all the Sun elevations with additional acceleration in x and z axes. unit: [$\text{nm} \cdot \text{s}^{-2}$]

model components	IOV mean	FOC mean	IOV std.	FOC std.
ECOM-1 D	3.008	2.883	1.403	1.394
ECOM-1 B	0.241	0.228	0.256	0.251
ECOM-2 D	1.131	1.127	0.613	0.654
ECOM-2 B	0.241	0.228	0.256	0.252
DREMT D	0.974	0.981	0.528	0.582
DREMT B	4.479	4.559	0.434	0.359

It shows that the ECOM-1 and ECOM-2 can greatly absorb the constant accelerations in x-axis and z-axis. There is no significant growth in the fitting RMS for

6. EMPIRICAL REPRESENTATION OF SOLAR RADIATION PRESSURE

these two models (see Fig. 6.7 and 6.6). It seems that the DREMT cannot deal with the constant accelerations in x-axis and z-axis, especially in B component. With the added a_x and a_z , the fitting RMS of DREMT in B component can reach to over 4 $\text{nm} \cdot \text{s}^{-2}$ for both the IOV and FOC satellites. Although the fitting RMS of DREMT in D component also shows a significant increase compared with the case that a_x and a_z are not added in, the average of the fitting RMS in D are less than 1 $\text{nm} \cdot \text{s}^{-2}$ for both the IOV and FOC satellites.

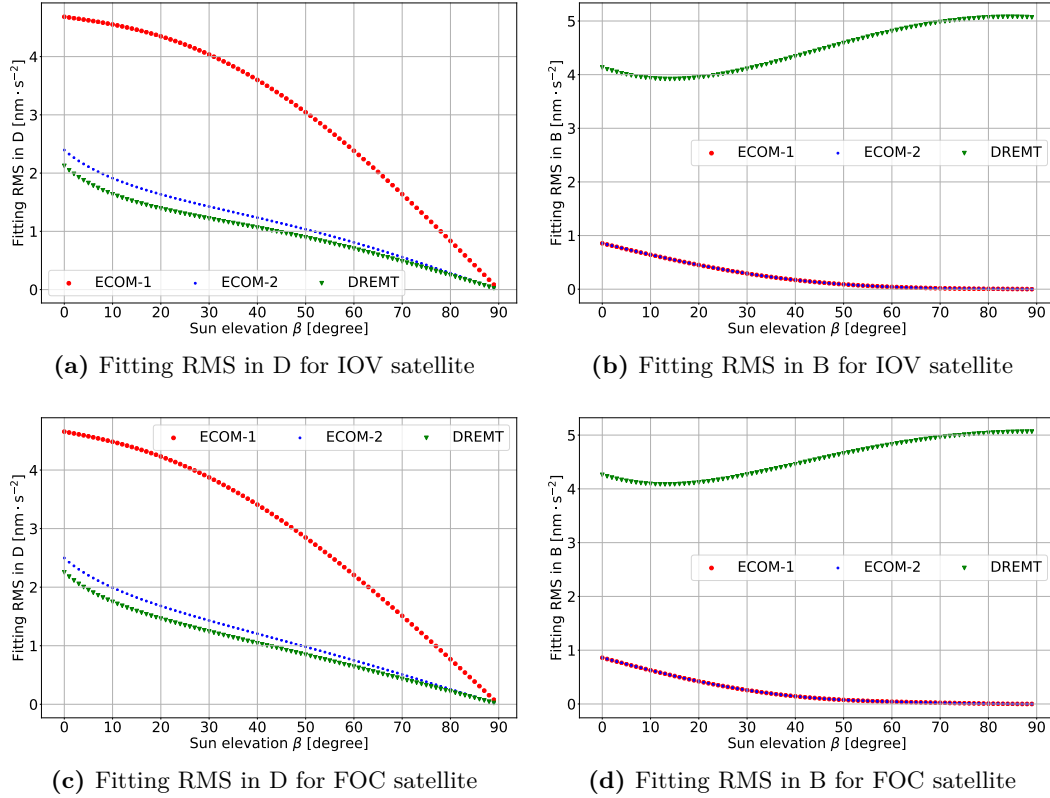


Figure 6.7: The fitting RMS in D and B components with constant accelerations a_x and a_z for the 3 empirical models: ECOM-1, ECOM-2 and the DREMT.

Based on the above analysis, we can conclude that the newly developed DREMT cannot effectively absorb other forces such as the antenna thrust, direct Earth radiation pressure and thermal radiation forces on radiators. These forces cause significant growth in the fitting RMS of B component of the DREMT. Thus, it is recommended that these forces have to be physically modelled when using the DREMT.

6.5 Consistency with the ray tracing solar radiation pressure model

Solar radiation pressure model (the grid files) derived using ray tracing approach has the ability to capture more details than the box-wing model. This model includes direct solar radiation pressure and thermal re-radiation pressure for the satellite bus.

6. EMPIRICAL REPRESENTATION OF SOLAR RADIATION PRESSURE

The details on the geometry of satellite bus have some influences on the solar radiation pressure modelling. Thus, a question is generated:

How good does the DREMT deal with the complex shape of the satellite bus in radiation pressure modelling?

This question can be answered by fitting the DREMT to the ray tracing derived solar radiation pressure acceleration. The fitting RMS shows the consistency between the DREMT and solar radiation pressure model derived using ray tracing approach. Still, the ECOM-1 and ECOM-2 are used as comparisons in this test. The statistics of the fitting experiment are shown in Tab. 6.8. The variations of the fitting RMS in D and B components are shown in Fig. 6.8.

Table 6.8: The statistics of the fitting RMS of ECOM-1, ECOM-2 and DREMT with the ray tracing model for Galileo satellites over all the Sun elevations. unit: [$\text{nm} \cdot \text{s}^{-2}$]

model components	IOV mean	FOC mean	IOV std.	FOC std.
ECOM-1 D	1.895	1.874	1.011	0.934
ECOM-1 B	0.205	0.167	0.122	0.100
ECOM-2 D	0.452	0.426	0.249	0.166
ECOM-2 B	0.205	0.168	0.122	0.100
DREMT D	0.258	0.172	0.161	0.066
DREMT B	0.507	0.345	0.152	0.081

As shown in Fig. 6.8, the DREMT has a better performance fitting the ray tracing derived accelerations in the D component than the ECOM-1 and ECOM-2. Compared with the fitting experiment using the box-wing model, the fitting RMS of the DREMT in D component is slightly larger. However, in the B component, the DREMT is worse than the ECOM-1 and ECOM2. As shown in Tab. 6.8, the B component fitting RMS of the DREMT are 0.507 (IOV) and 0.345 (FOC) $\text{nm} \cdot \text{s}^{-2}$ and the D component fitting RMS are 0.258 (IOV) and 0.172 (FOC) $\text{nm} \cdot \text{s}^{-2}$.

The differences between the Box-wing model and the ray tracing derived model are shown in Fig. 6.9. It shows that the differences in acceleration between the ray tracing derived model and the box-wing model can reach over $3 \text{ nm} \cdot \text{s}^{-2}$. The computation results in the fitting experiment show that most of these differences can be absorbed by the DREMT.

Based on above computation, we can conclude that the DREMT is consistent with the ray tracing derived solar radiation model to around $0.5 \text{ nm} \cdot \text{s}^{-2}$. This also indicates that most of the force effects caused by the complex shape of the satellite bus can be absorbed by the DREMT. In addition, the test results on ECOM-1 and ECOM-2 show that ECOM-2 can absorb those force effects better than the ECOM-1.

6.6 Summary

In this chapter, a new empirical solar radiation pressure model DREMT is put forward. This model considers the direct solar radiation and thermal re-radiation pressure for a

6. EMPIRICAL REPRESENTATION OF SOLAR RADIATION PRESSURE

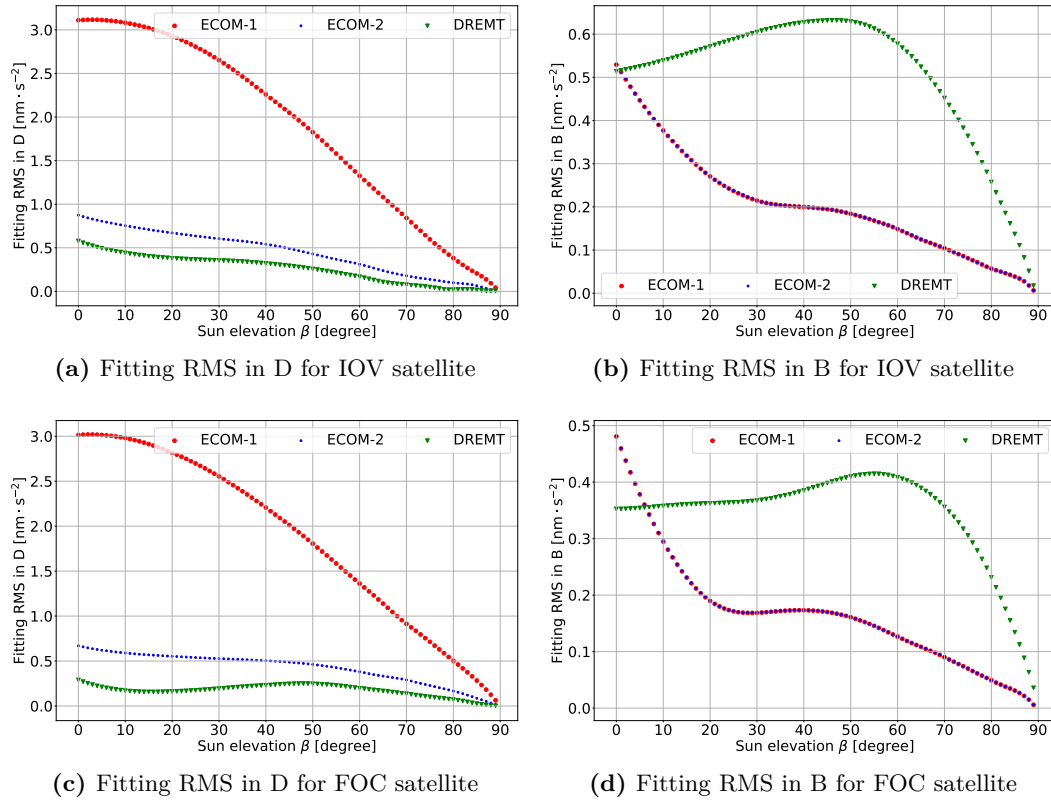


Figure 6.8: The RMS in D and B components of fitting the 3 empirical models to the ray tracing model.

simple box-wing satellite geometry. Its characteristics are as follows:

- Box-wing geometry and nominal attitude

The DREMT is built based on box-wing geometry and the nominal attitude of the Galileo satellites. The approach of building the DREMT can be extended to be suitable for other GNSS satellites.

- Direct solar radiation pressure and the thermal re-radiation pressure

The DREMT considered the direct solar radiation pressure on the solar panels. For the satellite bus, it is assumed to be covered with black MLI. All the absorbed solar radiation is emitted instantaneously as thermal energy.

- Assume -z and +z panels are the same

The -z panel and +z panel of the satellite bus are assumed to have the same optical properties. This is useful for simplification of the model.

- Correlation between parameters are considered

The correlation between parameters in the model does harm to estimation. A compromise has been made to balance the accuracy and the correlation. This is done by ignoring some terms which have less contributions and adding terms with respect to angular argument Δu .

6. EMPIRICAL REPRESENTATION OF SOLAR RADIATION PRESSURE

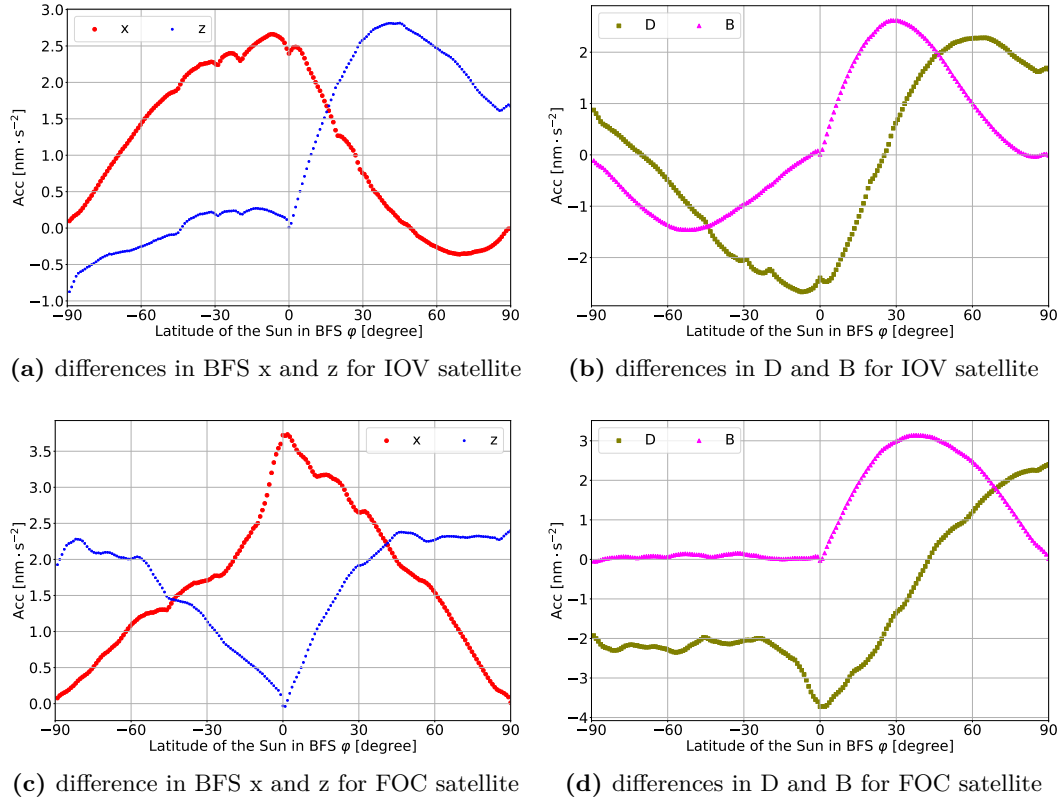


Figure 6.9: The acceleration differences between the ray tracing derived model and the box-wing model for IOV and FOC satellites.

The DREMT is developed based on the box-wing model and contains errors due to approximations. Its accuracy loss has been evaluated by fitting DREMT to the accelerations generated from the box-wing model. It turns out that the DREMT can fit the box-wing model to 0.157 (IOV) and 0.121 (FOC) $\text{nm} \cdot \text{s}^{-2}$ in D component, 0.138 (IOV) and 0.096 (FOC) $\text{nm} \cdot \text{s}^{-2}$ in B component.

The ability of dealing with direct Earth radiation pressure, antenna thrust, and thermal radiation forces on the radiators are also tested for the DREMT. Adding $a_x = a_z = 10 \text{ nm} \cdot \text{s}^{-2}$ in the box-wing model to simulate those force effects. The fitting experiment results show that the DREMT **cannot effectively** absorb those forces in the B component. However, it outperforms the ECOM-1 and ECOM-2 in the D component. This also indicates that modelling those forces is important when using ECOM-1, ECOM-2 or the DREMT in orbit estimations.

The consistency between the DREMT and the ray tracing derived solar radiation pressure model is checked by fitting DREMT to the accelerations generated from the ray tracing. This is to test if the DREMT has the ability to deal with the complex shape of the satellite bus. The fitting results show that most of the force effects caused by the complex shape of the satellite bus can be absorbed by the DREMT. The fitting RMS are 0.258 (IOV) and 0.172 (FOC) $\text{nm} \cdot \text{s}^{-2}$ in D component, 0.507 (IOV) and 0.345 (FOC) $\text{nm} \cdot \text{s}^{-2}$ in B component.

6. EMPIRICAL REPRESENTATION OF SOLAR RADIATION PRESSURE

Chapter 7

Validation of force models in orbit prediction

GNSS broadcast ephemeris are actually predicted positions of the satellites. The improvements in the orbit prediction can lead to improvements in the broadcast ephemeris. A satellite's trajectory in space is affected by the forces acting on it. Better force models make the prediction of a satellite's trajectory closer to the "truth". A comparison between the published precise orbit and the predicted orbit is used to validate the force models developed in the previous chapters.

In this chapter, the precise orbit data and the orbit prediction are introduced. Then, the impacts of individual force effects on the orbit of Galileo satellites are presented. The individual force effects studied are direct solar radiation pressure (SRP), direct Earth radiation pressure (ERP), Thermal Re-radiation pressure (TRR), antenna thrust (AT), the shadow function, and multiple reflections in SRP modelling. However, these physical models contain un-modelled force effects and the accuracy in orbit prediction is shown. The empirical models include ECOM-1, ECOM-2 and DREMT are used to absorb the un-modelled force effects. The orbit prediction accuracy of these empirical models and the combination of physical force models and the empirical models in orbit prediction performance are assessed.

7.1 Precise orbit data and orbit prediction

7.1.1 Precise orbit data

The precise orbit data used in this study is provided by the Centre for Orbit Determination in Europe (CODE) of the IGS Multi-GNSS Experiment and Pilot Project (MGEX) in the form of positions (x , y , and z coordinates in ECEF) with an interval of 15 minutes. There are 237 stations in the IGS MGEX network, among which 231 stations can track Galileo satellites (see Fig. 7.1). The wide distribution of observation stations does good to the precise orbit determination of Galileo satellites.

The positions of Galileo satellites are solved using carrier phase observations with

7. VALIDATION OF FORCE MODELS IN ORBIT PREDICTION

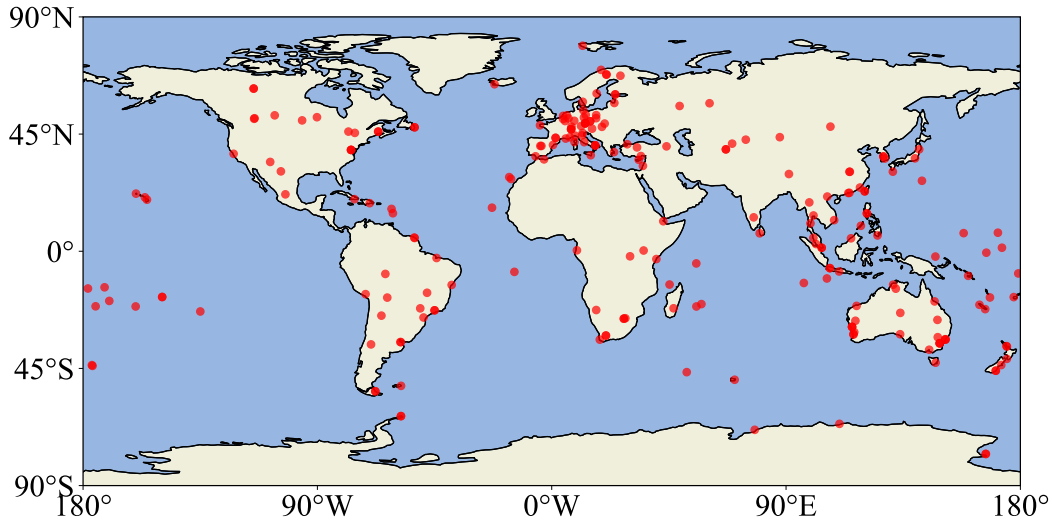


Figure 7.1: The distribution of the MGEX stations that track Galileo satellites.

3-day arcs as a batch. The data processing strategy of CODE is shown in Tab. 7.1. A key in the precise orbit determination is the radiation pressure model. The SRP model used has been changed from the 5-parameter ECOM-1 to ECOM-2 since 2015 [Prange et al., 2016]. A Satellite Laser Ranging check on the Galileo precise orbit quality showed that the mean SLR offsets are -44.9, and -35.0 mm for the IOV and FOC satellites. This indicate that the CODE precise orbit is a good source for validating the accuracy of the predicted orbit using the force models developed in this study.

Table 7.1: The strategy of CODE MGEX orbit solution

Terms	explanation
satellites	GPS + GLONASS + Galileo + BeiDou + QZSS
Stations NO.	130 (GPS), 110 (GLONASS), 85 (Galileo), 55 (BeiDou), 20 (QZSS)
processing scheme	phase double difference network processing
SRP model	ECOM-2 (since 2015)
IERS conventions	IERS2010 (since 2012)

In this study, we use the CODE daily orbit solutions in the whole 2016 as a baseline. These orbit solutions are treated as the “truth” in the validation of predicted orbit. In the orbit fitting experiment, these precise orbits are also used as observations to get the initial orbital parameters (position and velocity) and the parameters in the empirical radiation pressure models. In 2016, there are 3 Galileo IOV satellites ¹ and 5 Galileo FOC satellites that are available. They are listed in the following Tab. 7.2.

¹One Galileo IOV satellite E20 was unavailable since 2014.

7. VALIDATION OF FORCE MODELS IN ORBIT PREDICTION

Table 7.2: The list of the IOV and FOC satellites available in 2016

satellite type	PRN
IOV	E11, E12, E19
FOC	E14, E22, E24, E26, E30

7.1.2 Orbit prediction

A satellite's position in space at any time is determined by the initial position, velocity and the forces acting on the satellite. The process of determining the position of a satellite at a future time is called orbit prediction. In the orbit prediction tests of the Galileo satellites, the initial position and velocity are obtained from the precise orbit products. The largest force acting on a satellite is the Earth's gravitational force [Montenbruck and Gill, 2005]. The computation of the Earth's gravitational force is in the Earth Centred Earth Fixed (ECEF) frame which is defined to be rotating with the Earth. Generally, the satellite's position is expressed in the Earth Centred Initial (ECI) frame which can simplify the equations of motion [Montenbruck and Gill, 2005]. The connection between the ECI and ECEF is the Earth Orientation Parameters (EOP) which are varying with time. In this study, the purpose is to test the force models, thus, the satellite's orbit from a past time is simulated. There are two reasons: firstly, there is no need to worry about the EOPs because they have been determined and published by the International Earth Rotation and Reference System Service (IERS) [Luzum, 2009; Vondrak and Richter, 2004]. This makes our predicted orbit only relate to the non-gravitational forces which are modelled in this study; secondly, the satellite's positions at a past time have already been precisely (cm level) determined by CODE which can provide a baseline to validate the predicted orbit.

In mathematics, the orbit prediction problem can be described as follows. Given a state vector at time t which includes the satellite's position $\mathbf{r}(t)$ and velocity $\mathbf{v}(t)$

$$\mathbf{y}(t) = \begin{pmatrix} \mathbf{r}(t) \\ \mathbf{v}(t) \end{pmatrix} \quad (7.1)$$

The first-order differential equation of state vector $\mathbf{y}(t)$ with respect to time is

$$\frac{d}{dt} \mathbf{y}(t) = \mathbf{f}(t, \mathbf{y}) = \begin{pmatrix} \mathbf{v}(t) \\ \mathbf{a}(t, \mathbf{r}, \mathbf{v}) \end{pmatrix} \quad (7.2)$$

where $\mathbf{a}(t, \mathbf{r}, \mathbf{v})$ is the acceleration acting on the satellite at time t . Usually, $\mathbf{a}(t, \mathbf{r}, \mathbf{v})$ is complex and difficult to be written explicitly in an analytical way. The most widely used approach is the numerical integration. Given the initial state vector $\mathbf{y}_0 = \mathbf{y}(t_0)$ at t_0 and the force models which can provide the acceleration at any time, the state vector at time t is given by the first-order Taylor expansion

$$\mathbf{y}(t) = \mathbf{y}(t_0) + (t - t_0)\mathbf{f}(t_0, \mathbf{y}_0) \quad (7.3)$$

7. VALIDATION OF FORCE MODELS IN ORBIT PREDICTION

Equation 7.3 is the basis for all the numerical integrators. There are many numerical integration approaches that can solve the problem. In this study, a degree 7 Runge-Kutta method is utilised to do the calculation [Butcher, 1996].

7.1.3 Orbit dynamic fitting

The precise orbit used in this study only includes the positions of the Galileo satellites. However, in the orbit prediction, the initial velocity is also needed. The initial velocity of a satellite can be computed by fitting the initial position and velocity to precise orbit data. In this way, the velocity is accurately determined and also the positions from the precise orbit data get adjusted. In the orbit fitting process, except for the initial positions and velocity, the parameters in the force models can also be adjusted. The process of adjusting the initial state vector and the force model parameters based the precise orbit products is called orbit dynamic fitting.

The orbit dynamic fitting involves several iterations. For an orbital arc from t_0 to t (as shown in Fig. 7.2), the initial position and velocity at t_0 is obtained from the CODE precise orbit data by interpolation, which can give out a coarse value (due to errors in interpolation) of the position and velocity at t_0 . A predicted orbit can be generated using this coarse position and velocity. Then, the predicted orbit is compared with the reference orbit (precise orbit from the CODE). The corrections to the position and velocity at t_0 is calculated according to the difference between the predicted orbit and the reference orbit using least square. After applying the corrections, a fitted orbit is generated. After several iterations, the fitted orbit will be close to the reference orbit. Any point in the fitted orbit arc can be taken as the start of the following orbit prediction test. The mathematics of orbit fitting can be found in appendix B.

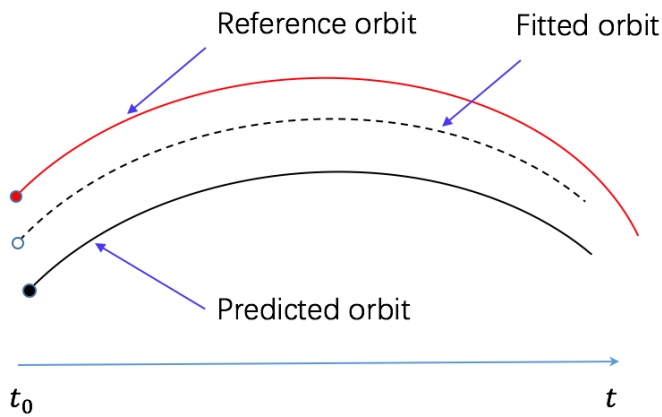


Figure 7.2: The relations amongst reference orbit, fitted orbit and predicted orbit.

7.1.4 Indicators to assess the accuracy of predicted orbit

In this study, there are several indicators to assess the quality of predicted orbit. One is the RMS of predicted orbit. This is to calculate the root mean square of the position differences between the predicted orbit and precise orbit data. The RMS is computed in 3 components (radial, along and cross).

$$\left\{ \begin{array}{l} RMS_R = \sqrt{\frac{1}{n} \sum_{i=1}^n \Delta r_{R,i}^2} \\ RMS_A = \sqrt{\frac{1}{n} \sum_{i=1}^n \Delta r_{A,i}^2} \\ RMS_C = \sqrt{\frac{1}{n} \sum_{i=1}^n \Delta r_{C,i}^2} \\ RMS_{3D} = \sqrt{\frac{1}{n} \sum_{i=1}^n (\Delta r_{R,i}^2 + \Delta r_{A,i}^2 + \Delta r_{C,i}^2)} \end{array} \right. \quad (7.4)$$

where n is the total number of epochs, $\Delta r_{R,i}$, $\Delta r_{A,i}$, and $\Delta r_{C,i}$ are the radial, along and cross track orbit differences at epoch i which are converted from the ECI position differences.

Another indicator is orbit contribution of the Signal In Space Ranging Error (SISRE). SISRE is a key indicator for GNSS performance monitoring. It includes the contributions of the orbits and clocks [Montenbruck et al., 2018]. In this study, only the contribution of orbit is discussed. The orbit contribution ($SISRE_{orb}$) mainly depends on the predictability of orbital motion. The instantaneous $SISRE_{orb,i}$ at epoch i is computed as follows [Montenbruck et al., 2018]:

$$SISRE_{orb,i} = \sqrt{w_R^2 \Delta r_{R,i}^2 + w_{A,C}^2 (\Delta r_{A,i}^2 + \Delta r_{C,i}^2)} \quad (7.5)$$

At an altitude of Galileo satellites, the weight factors $w_R^2 = 0.984$, $w_{A,C}^2 = 0.128$. The RMS of the instantaneous $SISRE_{orb,i}$ is computed

$$RMS_{SISRE,orb} = \sqrt{\frac{1}{n} \sum_{i=1}^n SISRE_{orb,i}^2} \quad (7.6)$$

7.2 The impacts on the Galileo satellites' orbit

In this study, a set of force models include direct solar radiation pressure, direct Earth radiation pressure, thermal re-radiation pressure and the antenna thrust are developed. The impacts of these individual force model on the Galileo satellites' orbit are investigated by a 24-hour orbit prediction. In addition, in the ray tracing approach, the magnitude of acceleration due to multiple reflections and its impact on the satellite's orbit are analysed. When a satellite goes into eclipse, a shadow function PPM_atm is developed to describe the scaling of solar flux at a satellite's location. Compared with

7. VALIDATION OF FORCE MODELS IN ORBIT PREDICTION

the widely used SECM, the improvements in the orbit are revealed in 1 to 7 days orbit predictions.

In the figures showing variations of accelerations for the individual effect, the variable Δu is chosen as the angular parameter. The reason is that Δu is more visually understandable in describing the relative positions of the Sun, the Earth and the satellite, which makes it easier to see some physical changes (such as the switch in radiation flux illumination between the sun-facing side and the rear side of the solar panels) that cause the variations in acceleration.

Figure 7.3 show the illumination of both the solar radiation and Earth radiation on the satellite (including the satellite bus and the solar panel) under the nominal attitude assumption. The $+z$ panel is always illuminated by the Earth radiation flux, sun-facing side of the solar panels and $-x$ panel are always illuminated by the solar flux. The solar flux illuminates on $+z$ when $90 < \Delta u < 270$, it shines on $-z$ panel for the rest time. The Earth radiation flux shines on the sun-facing side of solar panels when $90 < \Delta u < 270$, it illuminates on the rear side of solar panels for the rest time.

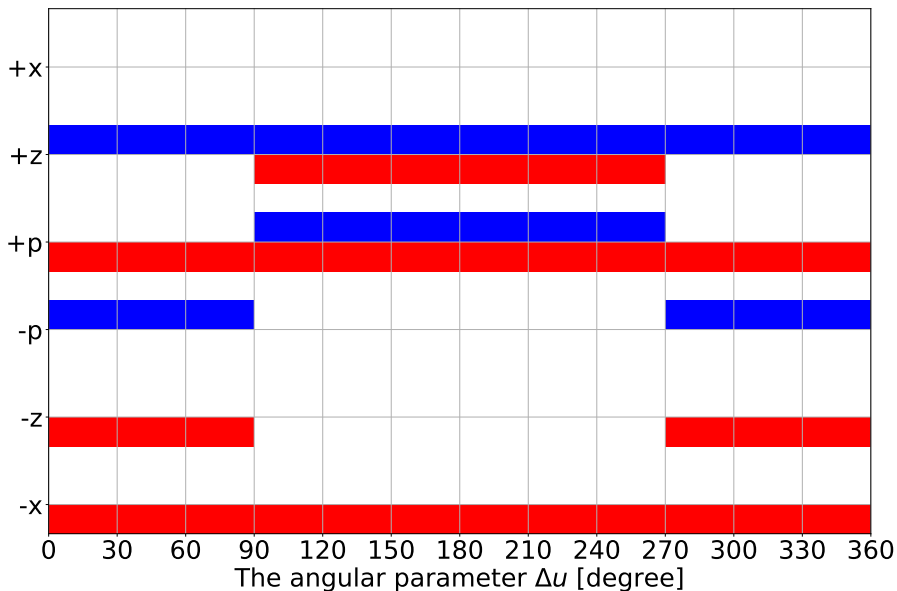


Figure 7.3: The illumination of the solar radiation and Earth radiation on the solar panels and the satellite bus. The red bar and blue bar represent solar radiation and Earth radiation separately. “ $+p$ ” and “ $-p$ ” stands for the sun-facing side and rear side of solar panels.

7.2.1 The direct solar radiation pressure

The direct solar radiation pressure (SRP) is the largest among all the non-gravitational forces acting on Galileo satellites. The magnitude of the direct SRP is about $107 \text{ nm} \cdot \text{m}^{-2}$ ($85 \text{ nm} \cdot \text{m}^{-2}$ from the solar panels and $22 \text{ nm} \cdot \text{m}^{-2}$ from the satellite bus) for the Galileo satellites. Figure 7.4 shows the variation of the direct SRP of one Galileo IOV satellite over one orbit. In the radial and along track, the SRP has a large variation. In the cross track, the variation is relatively smaller. From the cross track component, the switch between $-z$ and $+z$ panel of the satellite bus can be seen

7. VALIDATION OF FORCE MODELS IN ORBIT PREDICTION

at $\Delta u = 90$ and 270 degrees. The switch causes a discontinuity in the cross-sectional area between the solar radiation flux and the satellite surfaces and the direct SRP has a discontinuity accordingly.

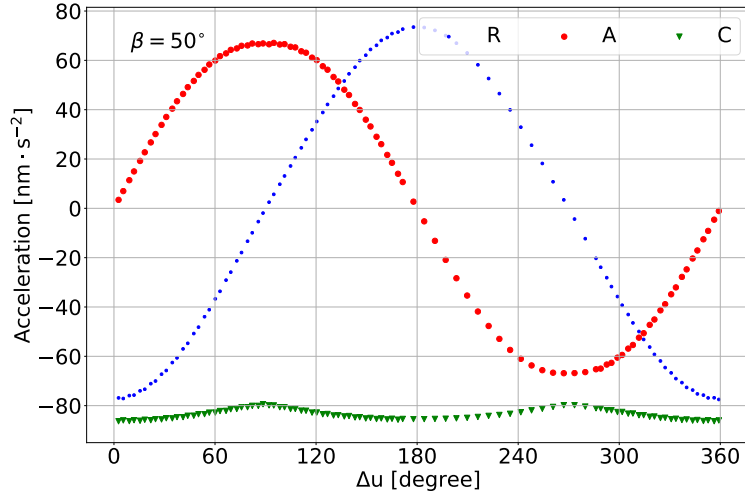


Figure 7.4: The variation of direct solar radiation pressure with respect to the orbital angle Δu for one Galileo IOV satellite.

The impact of SRP on the orbit is revealed by the RMS of orbit differences between orbit prediction results with and without the SRP model. What shows in Fig. 7.5 is the orbit error RMS within 24 hours caused by the direct SRP. In 24 hours, the orbit error RMS can reach about 30m, 70m and 9m in orbit radial, along track and cross track separately.

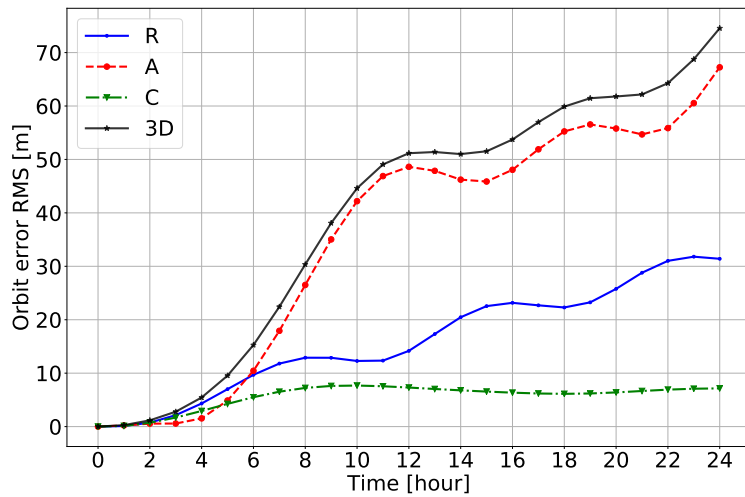


Figure 7.5: The RMS of orbit errors in radial, along, cross and 3D caused by the direct solar radiation pressure in 24 hours

7.2.2 The thermal re-radiation pressure

The thermal re-radiation pressure (TRR) modelled in this study mainly includes forces caused by the re-radiation of absorbed solar and Earth radiation on the satellite bus.

7. VALIDATION OF FORCE MODELS IN ORBIT PREDICTION

This force is modelled with the ray tracing approach and is provided to the users together with the direct solar radiation pressure of the satellite bus in the grid files.

The magnitude of TRR acceleration is around $10 \text{ nm} \cdot \text{m}^{-2}$ as shown in Fig. 7.6. The radial component of the TRR acceleration shows clearly the switch of the Sun illumination between $-z$ and $+z$ panel of the satellite bus when $\Delta u = 90^\circ$ or 270° . Figure 7.7 shows that the TRR acceleration can cause about 1.5 m, 3.7 m and 0.4 m in the orbit error RMS in radial, along and cross track within 24 hours separately.

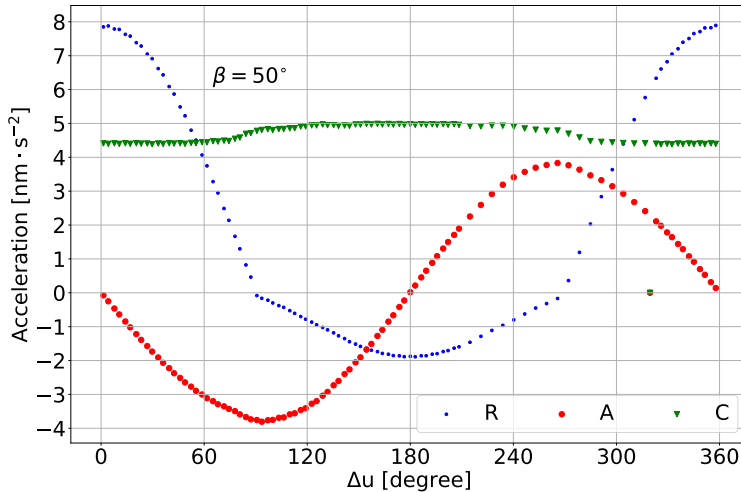


Figure 7.6: The variation of TRR acceleration with respect to the orbital angle Δu for one Galileo IOV satellite.

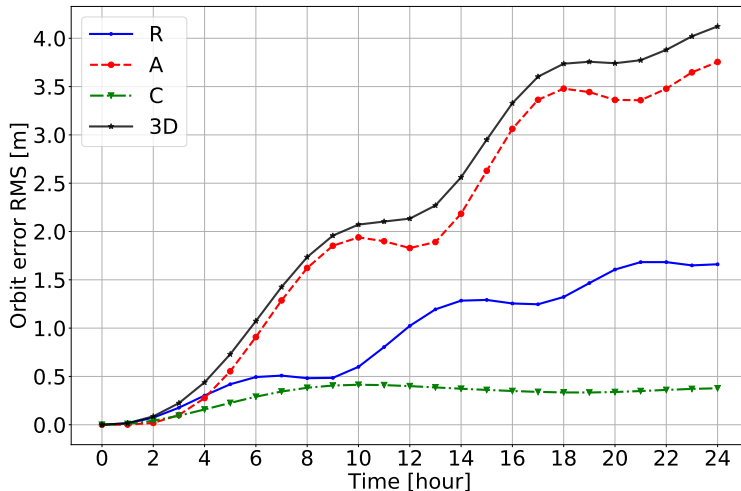


Figure 7.7: The RMS of orbit errors in radial, along, cross and 3D caused by the TRR within 24 hours

7.2.3 The direct Earth radiation pressure

The direct Earth radiation pressure is caused by the illumination of Earth radiation on the satellite. At the altitude of the Galileo satellites, the shortwave and longwave Earth radiation fluxes are shown in Fig. 7.8a and Fig. 7.8b separately. Both the

7. VALIDATION OF FORCE MODELS IN ORBIT PREDICTION

shortwave and longwave radiation have the largest component in radial direction. For the longwave Earth radiation flux, the radial component is about $8 \text{ W} \cdot \text{m}^{-2}$, the along and cross track are less than $2 \text{ W} \cdot \text{m}^{-2}$. The variation of longwave Earth radiation flux is mainly driven by the spatial distribution of the Earth radiation flux and the satellite's altitude.

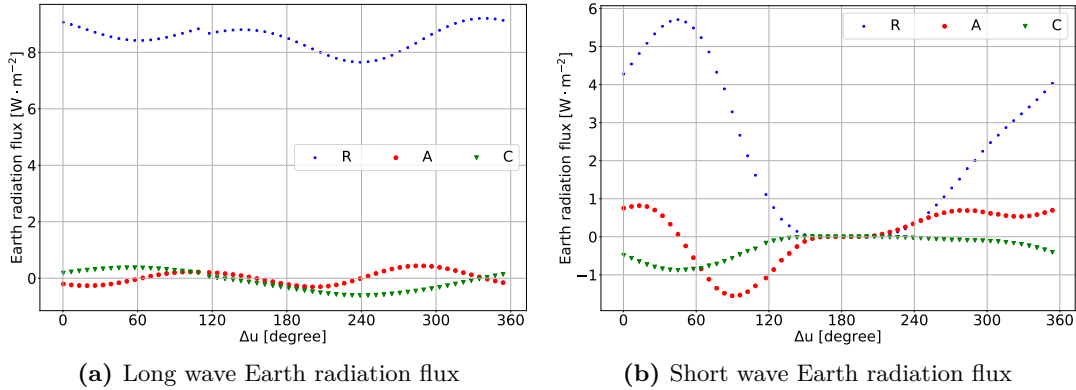


Figure 7.8: The variations of shortwave and longwave Earth radiation flux at a IOV satellite's position.

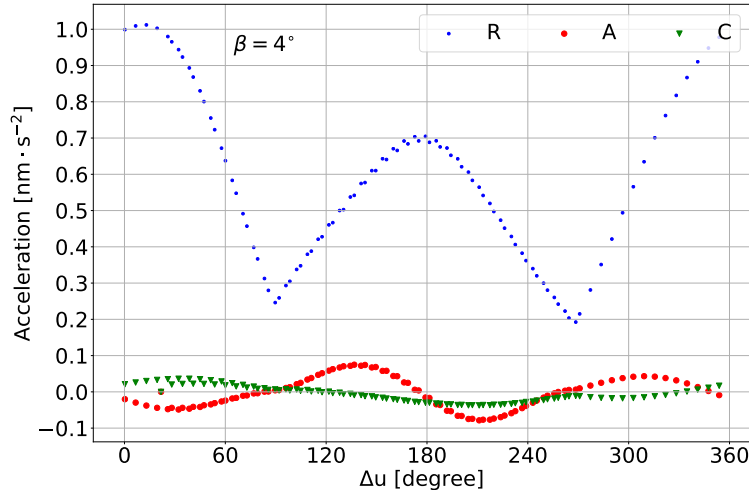


Figure 7.9: The variation of direct Earth radiation pressure with respect to the orbital angle Δu for one Galileo IOV satellite.

For the shortwave Earth radiation flux, the radial component is the largest and varying between 0 to $6 \text{ W} \cdot \text{m}^{-2}$. The along and cross track are less $1 \text{ W} \cdot \text{m}^{-2}$. The shortwave Earth radiation is caused by the reflection of solar radiation on the Earth's surface, the clouds and the atmosphere, the shortwave Earth radiation flux that reaches the satellite becomes 0 if the satellite is not on the sun-facing side of the Earth (as shown in Fig. 7.8a when $150^\circ \leq \Delta u \leq 210^\circ$). The average of the total of shortwave and longwave Earth radiation flux at the Galileo satellites' location is about $11 \text{ W} \cdot \text{m}^{-2}$. This value is about $15 \text{ W} \cdot \text{m}^{-2}$ for the GPS satellites [Grey and Ziebart, 2014] and is about $10 \text{ W} \cdot \text{m}^{-2}$ for the Beidou IGSO satellites [Li et al., 2017]. The higher the

7. VALIDATION OF FORCE MODELS IN ORBIT PREDICTION

altitude of the satellites, the lower the Earth radiation flux at the satellite's location.

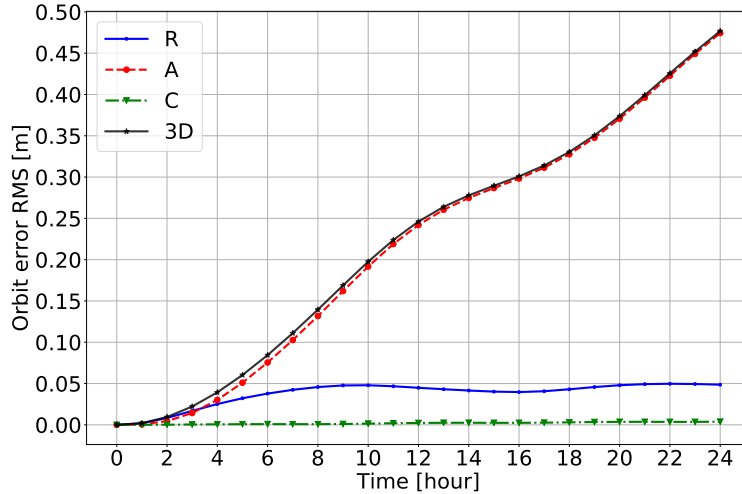


Figure 7.10: The RMS of orbit errors in radial, along, cross and 3D caused by the direct Earth radiation pressure within 24 hours.

Figure 7.9 shows the ERP acceleration during one orbit for a Galileo IOV satellite. Both the along and cross track are less than $0.1 \text{ nm} \cdot \text{s}^{-2}$. The largest lies in the radial and it is 3-10 times larger than the acceleration in the along and cross track. Under the nominal attitude, the Earth radiation can illuminate on both the sun-facing and the rear side of the solar panels. The Earth radiation illumination switches between the sun-facing side and rear side of solar panels when $\Delta u = 90$ or 270 degrees. The rear side and sun-facing side of the solar panels have different optical properties and the switch causes a discontinuity in the radial component of the ERP acceleration as shown in Fig. 7.9. The impacts of ERP on the satellite's orbit are shown in Fig. 7.10. It shows that the orbit error RMS can reach 0.05 m , 0.48 m , and 0.01 m within 24 hours in radial, along and cross track if ERP is ignored.

7.2.4 The multiple reflections in ray tracing

The multiple reflections in the ray tracing approach should be considered in the solar radiation pressure (SRP) modelling. In the SRP modelling of the Galileo satellites, the maximum number of reflections should be no less than 3 [Li et al., 2018]. If the modelling with 3 reflections is taken as the “truth”, the differences in acceleration between the “truth” and the modelling results of only 1 reflection are shown in Fig. 7.11a (IOV) and Fig. 7.11b (FOC). The IOV and FOC satellites show different patterns in the multiple reflection accelerations because of the different structures of the satellite bus. The magnitude of the acceleration due to multiple reflections can reach over $0.15 \text{ nm} \cdot \text{s}^{-2}$ for the IOV satellites and $0.3 \text{ nm} \cdot \text{s}^{-2}$ for the FOC satellites. When Δu is 90 or 270 degrees, there exist a discontinuity in the acceleration. It has a physical explanation that the sun illumination switches between $-z$ and $+z$ panel.

Figure 7.12a and Fig. 7.12b show the RMS in orbit errors due to the multiple reflection accelerations for the IOV and FOC satellite separately. If the multiple reflec-

7. VALIDATION OF FORCE MODELS IN ORBIT PREDICTION

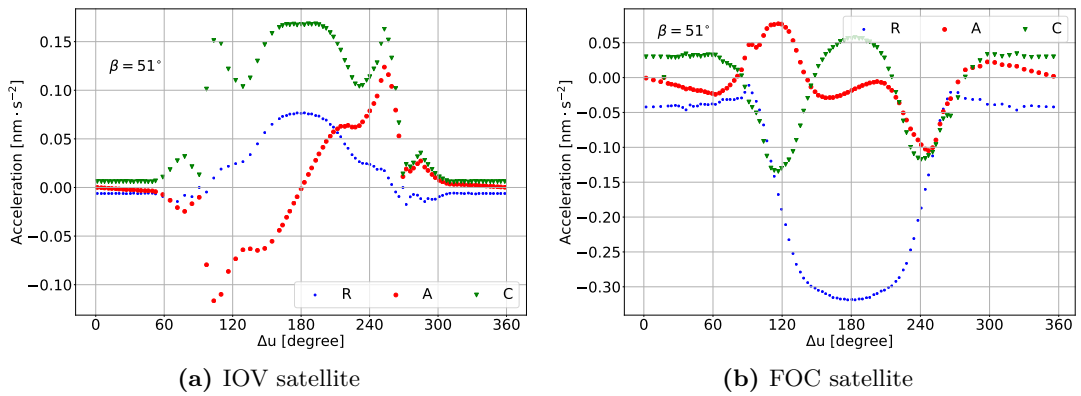


Figure 7.11: The difference in accelerations caused by the 3 reflections and 1 reflection models in the ray tracing for IOV and FOC satellites.

tion effect is ignored, in the radial, the orbit error RMS can reach 1 cm and 2 cm after 24 hours for the IOV and FOC satellites separately, the along track orbit error RMS can reach over 5 cm and 10 cm for the IOV and FOC satellites, in the cross track, the orbit error RMS reach over 1 cm for the IOV satellite but less than 5 mm for the FOC satellite.

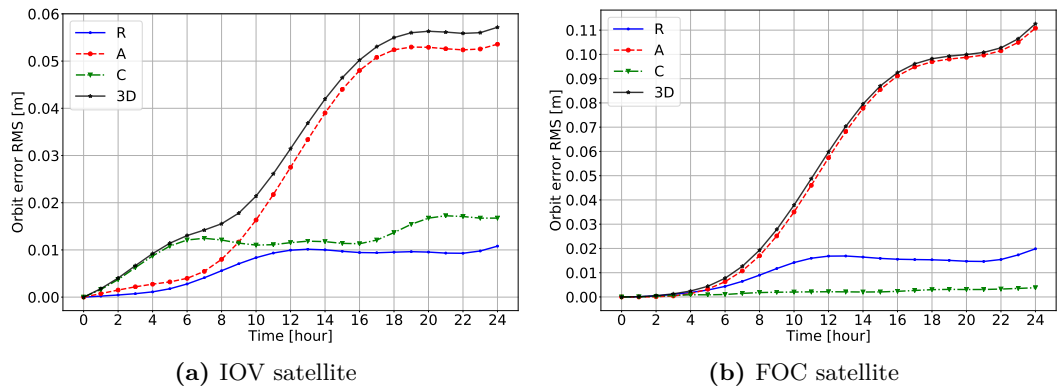


Figure 7.12: The RMS of orbit errors of IOV and FOC satellites in radial, along, cross and 3D within 24 hours caused by the 3rd reflections in the ray tracing derived model.

7.2.5 The antenna thrust

Navigation antenna thrust (AT) is in the radial direction under the nominal attitude. The magnitude of AT depends on the antenna transmit power. The details of navigation antenna transmit power for Galileo satellites can be found in Tab. 3.8. The typical transmit power for IOV and FOC satellites are 160 and 265 W separately. The magnitude of AT are 0.76 and $1.26 \text{ nm} \cdot \text{s}^{-2}$ calculated using the transmit power. Fig. 7.13 shows the RMS in orbit errors due to neglect of antenna thrust for the IOV and FOC satellites separately. If the antenna thrust is ignored, within 24 hours, the orbit error RMS can reach 0.08 m, 0.6 m, and 0.01 m in radial, along and cross for IOV satellites, the orbit error RMS reach 0.1 m, 1.1 m, and 0.01 m in radial, along and cross

7. VALIDATION OF FORCE MODELS IN ORBIT PREDICTION

track for FOC satellites.

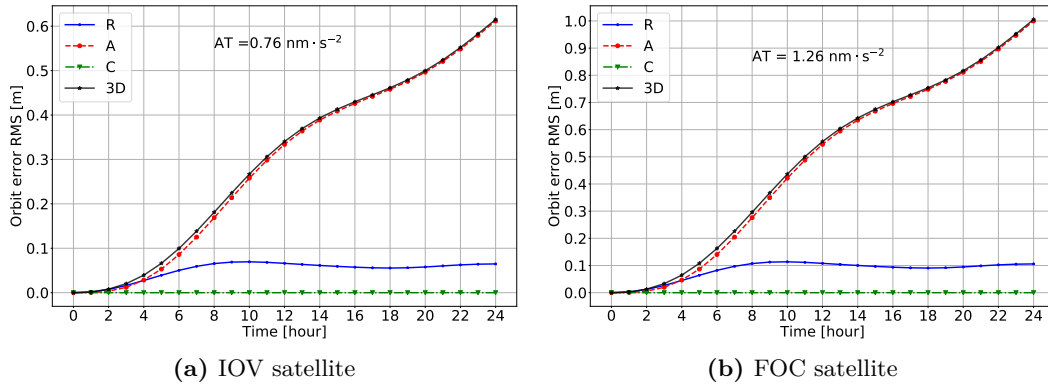


Figure 7.13: The RMS of orbit errors of IOV and FOC satellites in radial, along, cross and 3D within 24 hours caused by antenna thrust.

7.2.6 The impacts of shadow function on the orbit

The shadow function is a scalar for the solar radiation flux when satellites are in penumbrae. The errors in the shadow function directly cause errors in the solar radiation flux at a satellite's location. In chapter 4, the values of the shadow function PPM_{atm} are compared with several previous shadow function models and showed improvements in modelling using the GRACE accelerometer observations as a validation.

The shadow function modelling is affected by both the geometry of the solid Earth (ellipsoidal Earth) and the Earth's atmosphere. In order to analyse the impacts of these two effects on the orbit, the PPM_{atm} , PPM and $SECM$ are used in the tests. The PPM_{atm} includes both the Earth's oblateness and the atmospheric effects while PPM only considers the Earth's oblateness and totally ignores the atmospheric effects. The $SECM$ uses a spherical Earth model in modelling and also does not consider the atmospheric effects. The differences between the PPM_{atm} and the PPM is caused by the atmospheric effects and the differences between the PPM and the $SECM$ is mainly caused by the Earth's oblateness.

We choose 6 Galileo satellites that are in 3 different orbital planes during their eclipse seasons in 2016 to show the impacts of different shadow function models on the orbit. In the orbit prediction tests, the force models used include direct solar radiation pressure [Li et al., 2018], thermal re-radiation pressure, direct Earth radiation pressure) [Li et al., 2017] and Antenna thrust. The nominal attitude is applied during eclipses. All the tests use the same attitude law during eclipses. The only variable is the shadow function model. Thus, the use of nominal attitude during eclipses won't affect the comparison results between different shadow function models. The precise orbit data are used as a baseline in orbit comparison. The initial state (position and velocity) is obtained by orbit fitting using the first 2 hours' precise orbit. No empirical parameters are used in the orbit fitting. After obtaining the initial position and velocity in the orbit fitting, the orbit prediction is performed for the next 1 day, 3 days, 5 days, and

7. VALIDATION OF FORCE MODELS IN ORBIT PREDICTION

7 days. These “orbit fitting and prediction” processes are performed over the eclipse seasons during 2016. Table 7.3 shows the satellites information and time span used in the data processing.

Table 7.3: The satellite information in shadow function tests

Type	PRN	Orbital plane	time span (DOY)
IOV	E11	B	1-20, 162-200, 330-360
FOC	E22	B	1-20, 162-200, 330-360
FOC	E08	C	85-115, 270-300
IOV	E19	C	85-115, 270-300
FOC	E24	A	10-40, 195-225
FOC	E30	A	10-40, 195-225

Table 7.4: The average RMS in radial orbit error over 7 days’ orbit prediction with the SECM, the PPM and the PPM_atm [m]

Satellites	SECM	PPM	PPM_atm
E11	1.984	1.991	1.931
E22	2.196	2.206	2.144
E08	1.396	1.407	1.320
E19	3.731	3.742	3.665
E24	1.212	1.217	1.182
E30	2.342	2.351	2.286
average	2.144	2.152	2.088

Table 7.4 shows the RMS in radial orbit error after 7 days’ prediction with the shadow function models SECM, PPM, and the PPM_atm. On average, the SECM is better than PPM by 8 mm while PPM_atm is better than PPM by 64.3 mm.

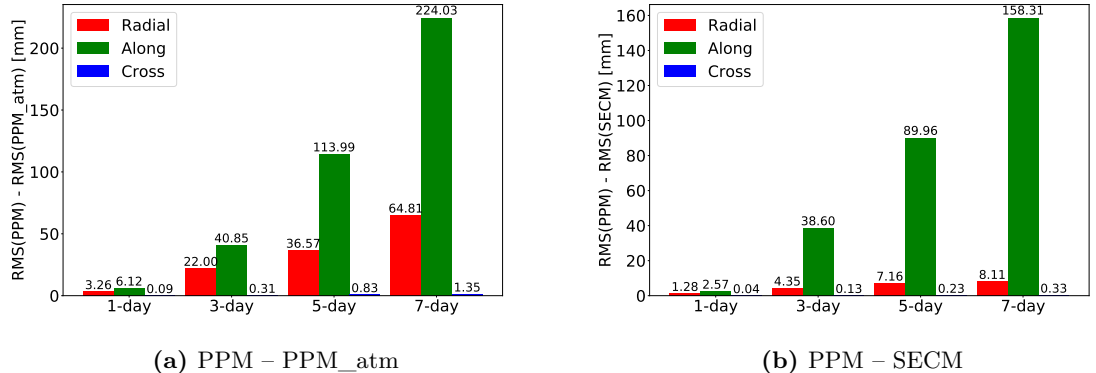


Figure 7.14: The difference in orbit error RMS amongst shadow function models PPM, SECM and PPM_atm.

Figure 7.14a shows the difference in the RMS of orbit prediction errors between the PPM and the PPM_atm. A positive value in Fig. 7.14a means the RMS of the PPM is larger than that of PPM_atm. The difference in the RMS of 1-day, 3-day,

7. VALIDATION OF FORCE MODELS IN ORBIT PREDICTION

5-day and 7-day's orbit prediction error between PPM and PPM_atm are 3.26 mm, 22.0 mm, 36.57 mm, 64.81 mm in the radial direction, 6.12 mm, 40.85 mm, 113.99 mm and 224.03 mm in the along track separately.

Figure 7.14b shows the difference in the RMS of orbit prediction error between the SECM and the PPM. The positive value in Fig. 7.14b shows the RMS of the PPM is larger than that of the SECM. The difference in the RMS of 1-day, 3-day, 5-day and 7-day's orbit prediction error between PPM and SECM are 1.28 mm, 4.35 mm, 7.16 mm, 8.11 mm in the radial direction, 2.57 mm, 38.60 mm, 89.96 mm and 158.31 mm in the along track separately.

Both Fig. 7.14a and Fig. 7.14b show that the orbital errors in the cross track due to the mismodelling of the shadow function are negligibly small, even the 7-day's orbit prediction RMS in the cross track is less than 1 mm. This is due to the fact that the Sun elevation over orbital plane is low during eclipse seasons, which makes the SRP mainly in the radial and along track directions.

7.2.7 Orbit prediction with the physical models

Applying all the physical force models (including SRP, TRR, ERP and the ANT) developed in this study to a 24-hour orbit prediction of the Galileo satellites, the performance of the physical force models are shown by comparing the predicted orbit with the reference orbit from the CODE. The RMS in 3D orbit error and the orbit contribution of the SISRE are chosen as measures to evaluate the quality of the force models.

The SRP, ERP, and TRR are computed from the grid files generated using the ray tracing approach. The box-wing model is less accurate in modelling the interactions between radiation flux and the satellite surfaces, so, it is not tested in the orbit prediction tests. The data processing strategy includes two part: the first part is a 2-hour orbit fitting, the second part is a 24-hour orbit prediction. In terms of the orbit fitting, the parameters that are fitted to the reference orbit are the initial position and velocity. There are no empirical parameters involved in the data processing. This can avoid the impacts of empirical parameters on the evaluation. The orbit fitting time span is from 6 o'clock to 8 o'clock each day. Then, the position and velocity at 8 o'clock are used as the initial state in the next 24-hour orbit prediction. This data processing strategy has been applied to the chosen Galileo satellites over 2016.

What shown in Tab. 7.5 is the orbit error RMS of 24-hour prediction with the force models SRP, TRR, ERP and ANT. The 3 IOV satellites can achieve about 0.2 to 0.3 m in the SISRE_orb, and the 5 FOC satellites around 0.5 m. This also indicates that the force models developed for the IOV satellites are better than that for the FOC satellites. One hypothesis is that there exists a radiator on the -z panel of the Galileo FOC satellite bus, the thermal radiation force is not modelled due to lack of heat dumping power. The thermal radiation force due to radiators on the -z panel produce accelerations in radial direction. The clue that all the tested FOC satellites have larger radial orbit error compared with the IOV satellites may support this hypothesis.

7. VALIDATION OF FORCE MODELS IN ORBIT PREDICTION

Table 7.5: The average RMS of 24-hour orbit prediction with the force models (SRP+TRR+ERP+ANT) for the year 2016 [m]

Type	PRN	Radial	Along	Cross	3D	SISRE_orb
IOV	E11	0.194	0.619	0.076	0.657	0.206
IOV	E12	0.303	0.779	0.120	0.848	0.314
FOC	E14	0.462	2.455	0.095	2.502	0.551
IOV	E19	0.191	0.707	0.110	0.749	0.208
FOC	E22	0.522	3.096	0.072	3.141	0.647
FOC	E24	0.436	2.263	0.098	2.308	0.516
FOC	E26	0.531	2.947	0.078	2.996	0.643
FOC	E30	0.462	2.292	0.104	2.341	0.540

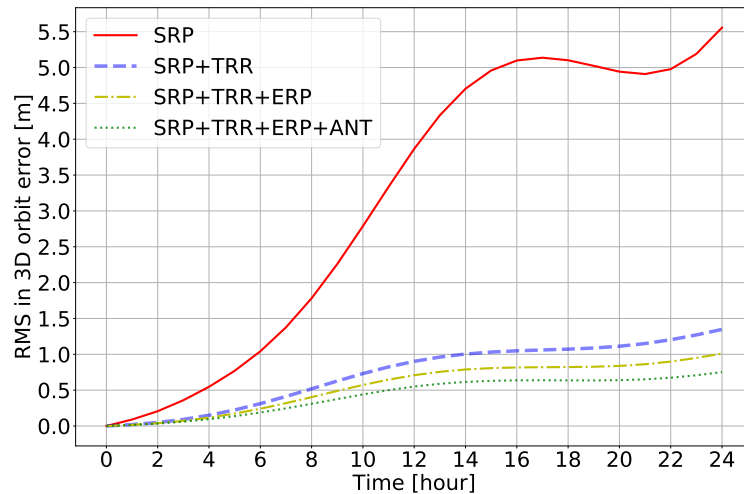


Figure 7.15: The RMS of 3D orbit errors in 24 hours for the various combinations of non-gravitational force models for the Galileo IOV satellites (average of E11, E12 and E19).

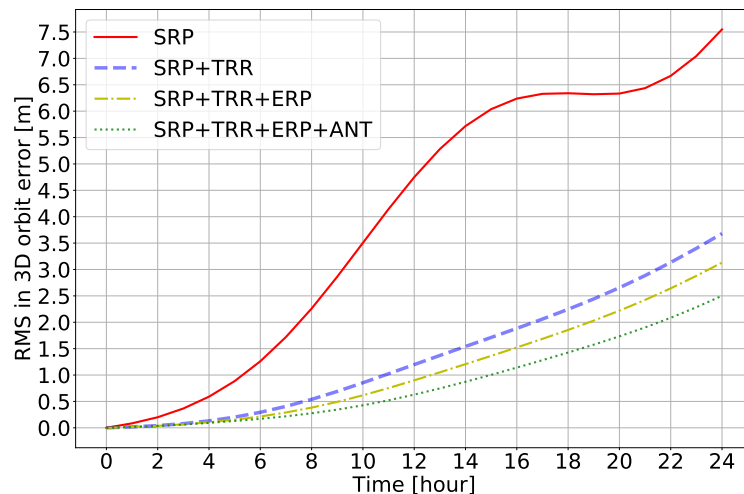


Figure 7.16: The RMS of 3D orbit errors in 24 hours for the various combinations of non-gravitational force models for the Galileo FOC satellites (average of E14, E22, E24, E26 and E30).

7. VALIDATION OF FORCE MODELS IN ORBIT PREDICTION

Figure 7.15 and Fig. 7.16 show the RMS in 3D orbit error of different combination of force models within 24 hours for the IOV and FOC satellites separately. Using the SRP model can make the orbit errors reduce from 80 m to several meters (5.5 m for IOV satellites and 7.5 m for FOC satellites). The TRR makes another big contribution to improve the orbit modelling accuracy. It gives a reduction of about 4 m in the 3D orbit error RMS. Applying the ERP and ANT makes the 3D orbit error RMS reduce by 0.5 m respectively. The results give a clear conclusion that accurate force models can improve the orbit quality. However, the results also show that there are errors in the current physical force models.

7.2.8 Why the along track orbit error is larger than that in radial

In the above data analysis, we observed that the along track orbital error is always the largest. This phenomenon has also been observed in the results of precise orbit determination of GNSS satellites. There might be two reasons for this phenomenon: one is the residual force in along track, the other is the correlation between the radial orbit error and along track orbit error. The radial orbit error is tightly related to the computation of Earth's gravitational acceleration. The errors in Earth's gravitational force (the largest force acting on GNSS satellites) changes the velocity of the satellites and thus generates errors in along track. The orbit error analysis of ERP is a typical example. The ERP acceleration is the largest in the radial direction but causes the largest orbit error in the along track. This section gives out an explanation from the view of orbital mechanics.

In a situation that one satellite is in circular orbit and the Earth gravitational force is considered under a spherically symmetric Earth model, the relation between the error (Δr) in orbit radial and the error in the mean anomaly ΔM is given [Adhya, 2005]:

$$\Delta M = -\frac{3\pi\Delta r}{a} \frac{t}{T} \quad (7.7)$$

where t is the time duration from the reference time, T is the orbit period. a is the radius of the circular orbit. The error in the along track ΔL is calculated

$$\Delta L = a \cdot \Delta M = -\frac{3\pi t}{T} \Delta r \quad (7.8)$$

Equation (7.8) shows the relations between the along track orbit error and the radial orbit error for a circular orbit in a two-body problem. The along track orbit error is 3π times larger than that in the radial over one orbit. It also shows that when $\Delta r > 0$ (i.e. the radius of the orbit is increased by Δr), the satellite falls behind by ΔL . This is because that satellites in higher altitude have slower velocity.

7.3 Long-term orbit prediction with empirical models

The physical models developed in this study can not cover all the force effects acting on the satellites, empirical models are used to absorb the un-modelled effects in the long-term (7 days) orbit prediction. The two widely used empirical models ECOM-1 and ECOM-2 are used as a baseline to compare with the newly developed DREMT. The benefits of using physical models in the orbit fitting and prediction are revealed using the RMS in the SISRE_{orb} and the orbital radial, along track and cross track as indicators in a 1-7 day orbit prediction.

The data processing strategy is similar as that in the tests of purely physical models. There are two parts in the data processing strategy: one is a 2-day orbit fitting, the other is the following 7 days orbit prediction. The reason why a longer arc (2 hours in the purely physical models test) is used in the orbit fitting is that there are more parameters (position, velocity and the empirical parameters) to estimate comparing with the tests in section 7.2.7. Longer arc allows more data to be used in the estimation which makes the solutions more stable. There are literature showing that the best arc length in orbit fitting is 42-48 hours for a better performance in orbit prediction [Geng et al., 2018]. In the 2-day orbit fitting process, the parameters in empirical models are assumed to be constant. The last epoch in the 2-day orbit fitting process is used as the start of the next 7-day orbit prediction, which means the position and velocity of the last epoch is used as an initial state for the prediction. The estimated empirical parameters are assumed to be constant over the 7 days prediction period. This data processing strategy is used for the chosen Galileo satellites over 2016.

For the Galileo satellites, the eclipse seasons usually come when the Sun elevation β is less than 14° . During eclipse seasons, the satellite attitude is not known and it is assumed to be nominal attitude in this study. The errors in the satellite attitude cause errors in radiation pressure modelling. Thus, the performance of the developed force models are evaluated in both the eclipse and non-eclipse periods for the chosen Galileo satellites.

7.3.1 Empirical models only

The empirical models used in this study include the ECOM-1 (see Eq. 6.24), ECOM-2 (see Eq. 6.25) and the DREMT (see Eq. 6.22 and Eq. 6.23). There are 5, 7, and 6 parameters to estimate in the ECOM-1, the ECOM-2, and the DREMT separately. The performance of the 3 different empirical models are evaluated using the orbit fitting RMS and the orbit prediction error RMS and RMS in SISRE_{orb} as the indicators.

Figure 7.17a and Fig. 7.17b show the average RMS of 2-day orbit fitting for the models ECOM-1, ECOM-2 and the DREMT. When the satellites are not in eclipses, the 2-day orbit fit RMS (average of the 8 satellites) is about 4.8, 2.0 and 2.4 cm for the ECOM-1, ECOM-2 and DREMT separately. The DREMT is slightly larger than ECOM-2 in the 2-day fit RMS. When the satellites are in eclipses, all the 3 models get larger fit RMS than the non-eclipse periods. The 2-day fit RMS are 7.3, 5.7 and 6.0

7. VALIDATION OF FORCE MODELS IN ORBIT PREDICTION

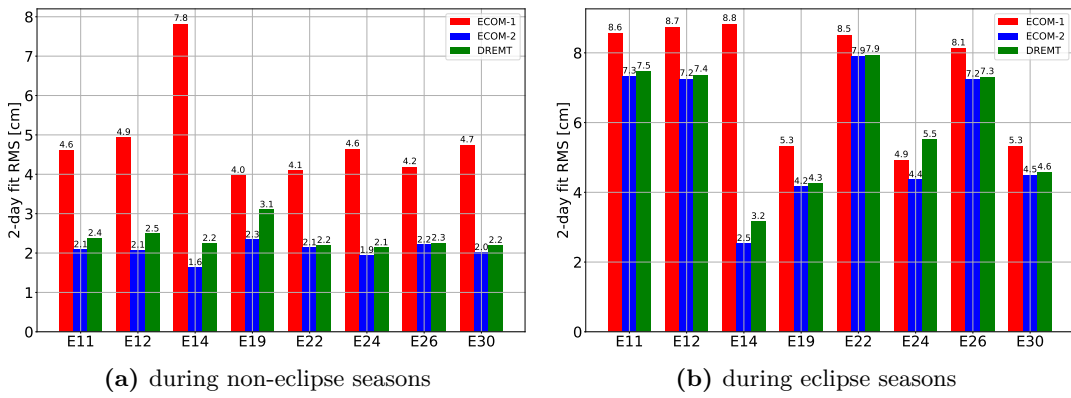


Figure 7.17: The average RMS of 2-day orbit fitting for IOV and FOC satellites using ECOM-1, ECOM-2 and the DREMT.

cm for ECOM-1, ECOM-2 and DREMT. This is likely due to the fact that a nominal attitude is applied in this research. ECOM-1 model has a larger fit RMS for E14 than the other satellites. But, ECOM-2 and DREMT do not show this phenomenon. This is like due to E14 was launched into a wrong orbit (highly eccentric). The changes in its operating status causes changes in radiation pressure acting on the satellite. The ECOM-1 can not capture these changes and leads to a larger fit RMS.

Figure 7.18 (during non-eclipse seasons) shows RMS in orbit errors (radial, along and cross track) and the RMS in SISRE_{orb} for 7-day orbit prediction. During non-eclipse seasons, DREMT is better than ECOM-1 and ECOM-2 for all these 4 indicators (RMS in radial, along, cross and SISRE_{orb}) as shown in Tab. 7.6. In the radial direction, the error RMS in predicted orbit is around 0.11 m for DREMT, which is much smaller than that for ECOM-1 (0.50 m) and ECOM-2 (0.55 m). In the along track, the error RMS are 2.39, 2.41 and 1.34 m for the ECOM-1, ECOM-2 and DREMT separately. In the cross track, the orbit error RMS are 0.22, 0.15 and 0.14 m for ECOM-1, ECOM-2 and DREMT. The DREMT achieves similar performance as the ECOM-2 and they are both better than ECOM-1. Due to great improvements in the radial and along track for the DREMT, it has the lowest SISRE_{orb} among these 3 models. The RMS values of SISRE_{orb} are 1.03, 1.06, and 0.50 m for these 3 models.

Table 7.6: The average RMS (non-eclipse) in radial, along, cross track and the SISRE_{orb} of all the chosen satellites for a 7-day orbit prediction. unit: [m]

Model	Radial	Along	Cross	SISRE _{orb}
ECOM-1	0.501	2.387	0.224	1.026
ECOM-2	0.547	2.413	0.145	1.058
DREMT	0.111	1.338	0.142	0.504

When the satellites are in eclipse, the 7-day orbit prediction error RMS in radial, along, cross track and the RMS in SISRE_{orb} are shown in Fig. 7.19. Table 7.7 shows the average RMS of all the chosen Galileo satellites for the 3 models. For the ECOM-1 and ECOM-2, the orbit error RMS in radial get decreased compared with that in

7. VALIDATION OF FORCE MODELS IN ORBIT PREDICTION

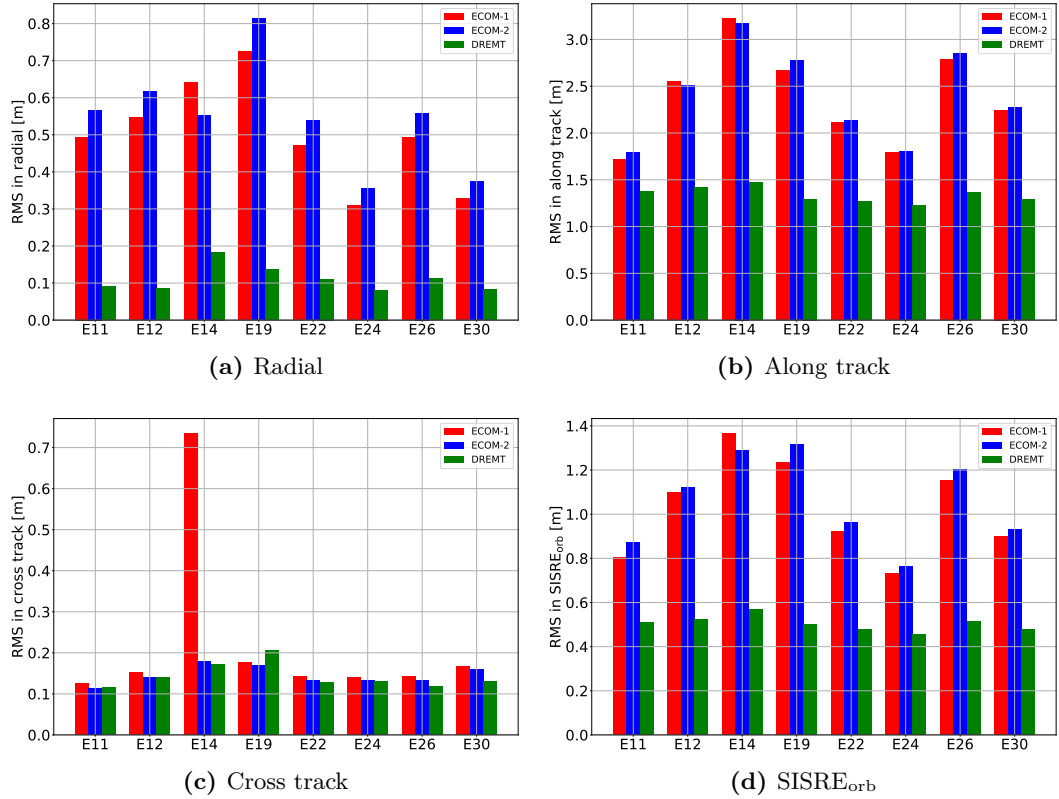


Figure 7.18: The average RMS in radial, along track, cross track and the SISRE_{orb} of a 7-day orbit prediction without *a priori* models during non-eclipse seasons.

non-eclipse periods, but, the along and cross track orbit errors get increased. ECOM-1 and ECOM-2 get 0.39 and 0.29 m separately in radial orbit error RMS. In the cross track, ECOM-1 and ECOM-2 get 0.40 and 0.33 m separately. In the along track, the orbit error RMS are 5.28 and 5.13 m for ECOM-1 and ECOM-2. The along track orbit error RMS gets almost doubled for ECOM-1 and ECOM-2 compared with that in non-eclipse time. Consequently, the RMS in SISRE_{orb} gets almost doubled for ECOM-1 and ECOM-2 due to the large errors in along track. The DREMT shows a different trend compared with ECOM-1 and ECOM-2. It gets larger orbit error RMS in all the 4 indicators compared with that in non-eclipse time. The RMS values are 0.31, 5.08, 0.32, and 1.87 in radial, along track, cross track and SISRE_{orb}.

Table 7.7: The average RMS (during eclipses) in radial, along, cross track and the SISRE_{orb} of all the chosen satellites for a 7-day orbit prediction. unit: [m]

Model	Radial	Along	Cross	SISRE _{orb}
ECOM-1	0.387	5.278	0.398	1.962
ECOM-2	0.293	5.134	0.331	1.885
DREMT	0.308	5.077	0.318	1.865

Figure 7.20 presents the average RMS in SISRE_{orb} of the orbit prediction within 7 days. During non-eclipse seasons (as shown in Fig. 7.20a), the ECOM-1 is slightly

7. VALIDATION OF FORCE MODELS IN ORBIT PREDICTION

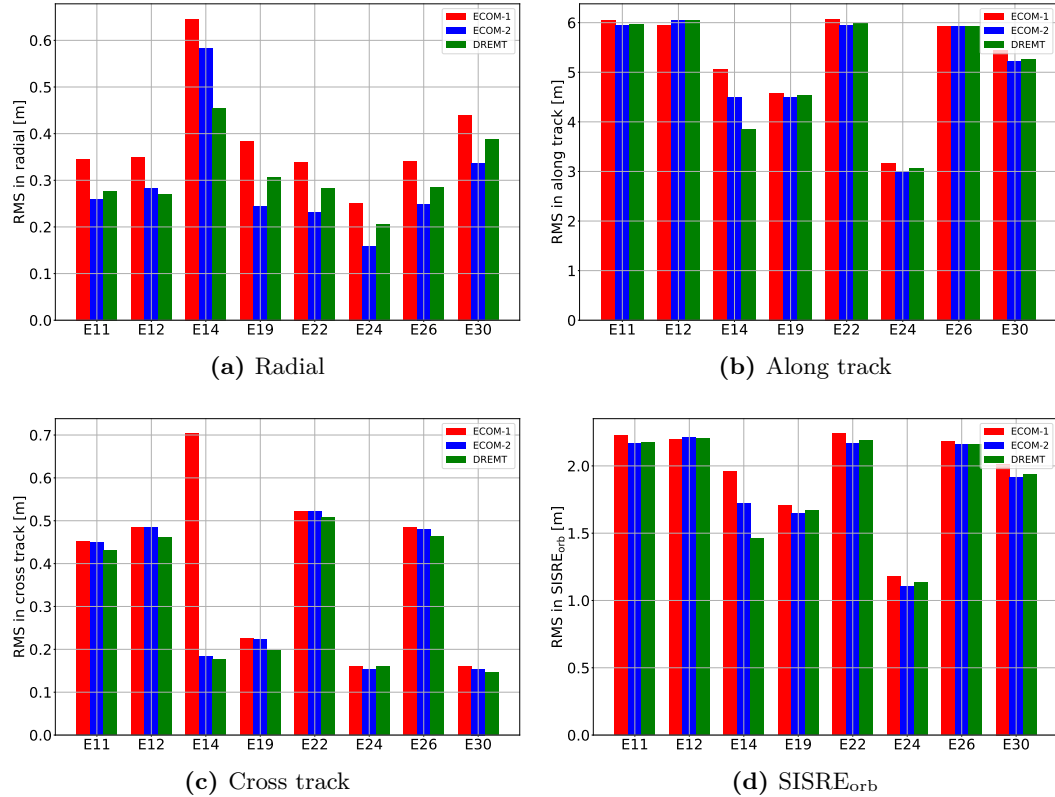


Figure 7.19: The average RMS in radial, along track, cross track and the SISRE_{orb} of 7 days orbit prediction without *a priori* models during eclipse seasons.

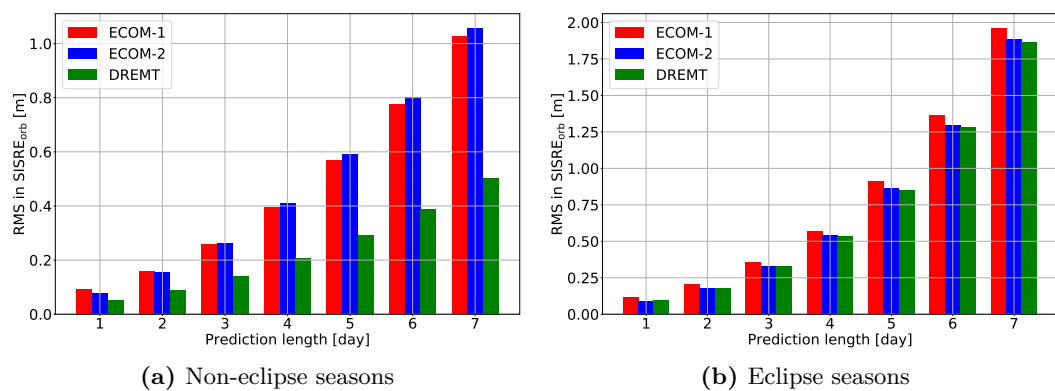


Figure 7.20: This figure shows the SISRE of 1 to 7 day's orbit prediction for IOV satellites using ECOM-1, ECOM-2 and the DREMT.

better than ECOM-2. The DREMT improved the RMS of SISRE_orb in orbit prediction by a factor of 2 compared with ECOM-1 and ECOM-2. However, during eclipse seasons, these 3 models almost have similar performance which is worse than that in non-eclipse seasons.

7.3.2 Empirical models + *a priori* force models

Section 7.3.1 discussed the performance of 3 empirical models (ECOM-1, ECOM-2 and DREMT) in orbit prediction aided by the *a priori* force models. The empirical models ECOM-1 and ECOM-2 do not consider any physical information about the satellite while the DREMT is developed based on a box-wing satellite model. Therefore, the performance of ECOM-1 and ECOM-2 should be improved by introducing *a priori* models. For the newly developed empirical model DREMT, because it already has the box-wing geometry constraint implicitly, the improvements in the orbit fit and orbit prediction depend on the accuracy of the *a priori* models.

In this section, the experiment is exactly the same as that in section 7.3.1 except the use of *a priori* force models developed in this study. These *a priori* force models include direct solar radiation pressure, direct Earth radiation pressure, thermal re-radiation pressure and antenna thrust. The information on the *a priori* physical models are listed in Tab. 7.8.

Table 7.8: The information on *a priori* models used in this section

Model name	Configuration
Direct solar radiation pressure	solar panel computation (see 5.4.1), grid files from ray tracing (see 5.5.1), PPM_atm shadow function (see 4)
Direct Earth radiation pressure	solar panel computation (see 5.4.2), Earth radiation flux model (see 3.2), grid files from ray tracing (see 5.5.1)
Thermal re-radiation pressure	grid files from ray tracing (see 5.5.1), thermal radiation flux (see 3.3)
Antenna thrust	Antenna transmit power (see 3.4), Antenna thrust computation (see 5.6.1)

Figure 7.21 presents the 2-day orbit fit RMS for the satellites in non-eclipse (7.21a) and eclipse seasons (7.21b) separately. After applying a set of physical models, the fitting RMS of ECOM-1 in non-eclipse seasons is greatly reduced to around 2.4 cm. The fitting RMS of ECOM-2 and DREMT are 2.2 cm and 2.4 cm. Compared with the results not using any *a priori* models (see section 7.3.1), the ECOM-2 gets slightly larger (4 mm) RMS while the DREMT almost stays the same. The abnormal fitting RMS for E14 with ECOM-1 disappeared after using these *a priori* models. This proved that the abnormal fitting RMS in section 7.3.1 is caused by the deficiency of the ECOM-1. During the eclipse seasons, the 2-day fitting RMS is larger than that in non-eclipse seasons. The ECOM-1, ECOM-2 and DREMT get 6.2 cm, 5.8 cm and 5.9 cm separately

7. VALIDATION OF FORCE MODELS IN ORBIT PREDICTION

in the 2-day fitting RMS.

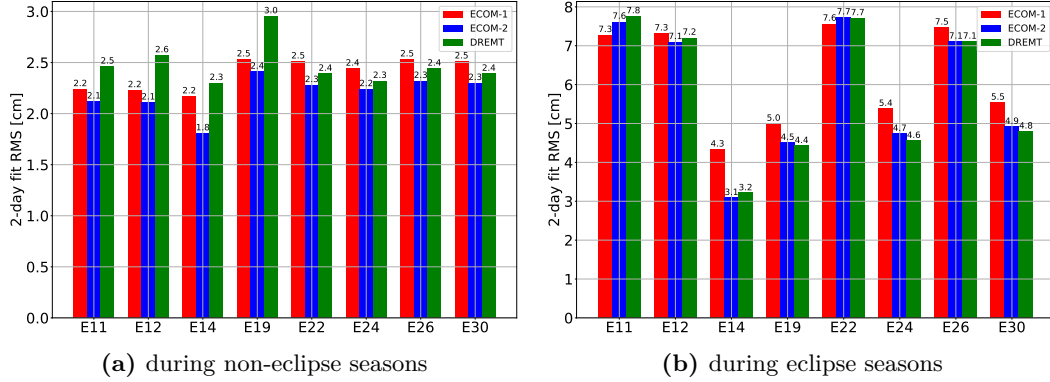


Figure 7.21: The average RMS of 2-day orbit fitting for the Galileo satellites using ECOM-1, ECOM-2 and the DREMT with the augmentation of the *a priori* force models.

Table 7.9: The average RMS (during non-eclipses) in radial, along, cross track and the SISRE_{orb} of all the chosen satellites for a 7-day orbit prediction with *a priori* models. unit: [m]

Model	Radial	Along	Cross	SISRE _{orb}
ECOM-1	0.101	1.324	0.131	0.495
ECOM-2	0.101	1.324	0.132	0.500
DREMT	0.108	1.323	0.134	0.494

Figure 7.22 shows the mean of orbit error RMS (radial, along and cross) and the mean RMS in SISRE_{orb} for a 7-day orbit prediction with *a priori* force models during non-eclipse seasons. Due to the constraint of *a priori* force models, the average RMS in all the 4 indicators show identical results for the 3 different empirical models (see Tab. 7.9). For this 7-day orbit prediction with *a priori* models, the mean RMS in radial, along track and cross track are about 0.1 m, 1.3 m and 0.5 m separately for all the 3 empirical models. In addition, an abnormal RMS (around 0.17 m) in radial direction is seen in Figure 7.22a for E14 satellite. But, this abnormal radial RMS value is greatly reduced compared with that without *a priori* models (around 0.72 m). This shows that applying *a priori* models improved the orbit prediction results.

When the satellites are in eclipse, the average RMS of orbit errors and SISRE_{orb} for each satellite over a 7-day orbit prediction are presented in Fig. 7.23. Table 7.10 shows the average RMS of the 4 indicators over all the chosen Galileo satellites. The average RMS in radial are 0.267 m, 0.315 m, and 0.276 m for ECOM-1, ECOM-2 and DREMT. In the along track, the orbit error RMS for these 3 empirical models are 5.111 m, 5.200 m, and 5.056 m separately. In the cross track, ECOM-1, ECOM-2 and DREMT get RMS of 0.325 m, 0.330 m, and 0.317 m separately. In the RMS of SISRE_{orb}, ECOM-1, ECOM-2 and DREMT achieve 1.867 m, 1.911 m, and 1.846 m separately. Compared with the RMS of these 4 indicators in non-eclipses seasons, the results in eclipse are significantly larger.

7. VALIDATION OF FORCE MODELS IN ORBIT PREDICTION

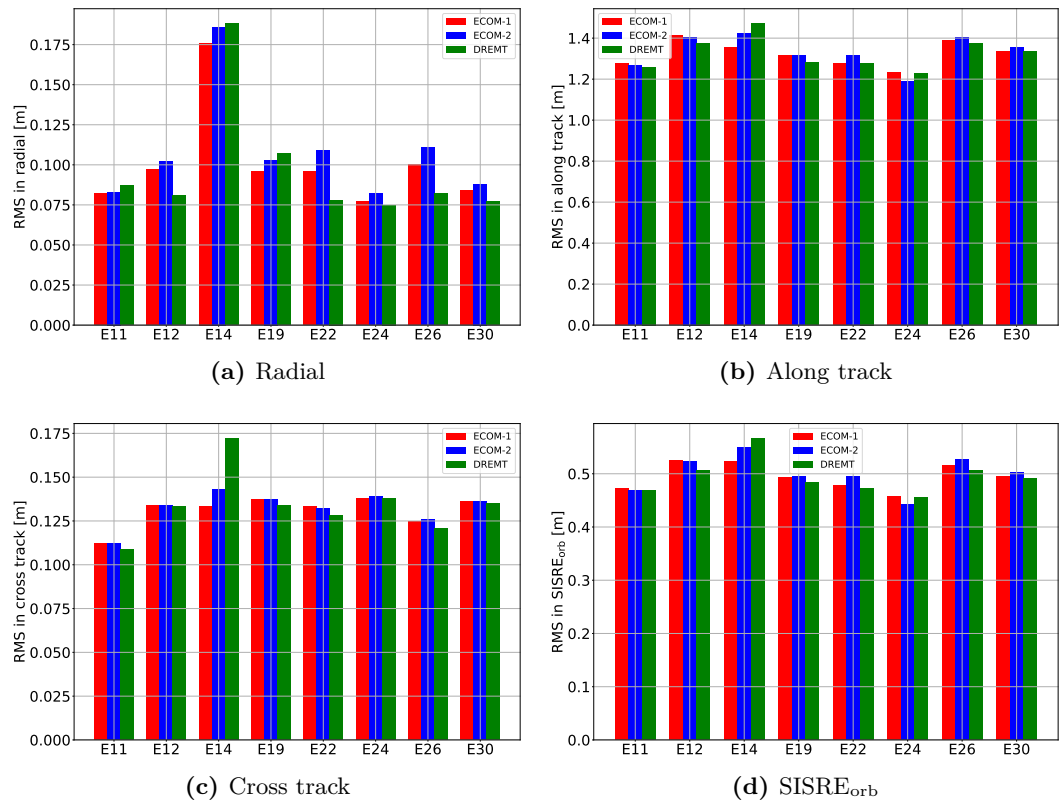


Figure 7.22: The average RMS in radial, along track, cross track and the SISRE_{orb} of 7 days orbit prediction with *a priori* models during non-eclipse seasons.

Figure 7.24 presents the average RMS in SISRE_{orb} of the orbit prediction within 7 days. With the use of the *a priori* force models developed in this study, the results in Figure 7.24 are identical for different empirical models. During non-eclipse seasons (as shown in Fig. 7.24a), the RMS of SISRE_{orb} is less than 10 cm within a 2-day prediction, it increases to about 0.5 m within a 7-day prediction. During eclipse seasons, the RMS of SISRE_{orb} is less than 0.3 m within a 3-day prediction and it increases to about 2 m within a 7-day prediction. On the whole, the performance of these 3 empirical models with *a priori* force models in non-eclipse time is better than that in eclipse by a factor of 4.

Table 7.10: The average RMS (during eclipses) in radial, along, cross track and the SISRE_{orb} of all the chosen satellites for a 7-day orbit prediction with *a priori* models. unit: [m]

Model	Radial	Along	Cross	SISRE _{orb}
ECOM-1	0.267	5.111	0.325	1.867
ECOM-2	0.315	5.200	0.330	1.911
DREMT	0.276	5.056	0.317	1.849

7. VALIDATION OF FORCE MODELS IN ORBIT PREDICTION

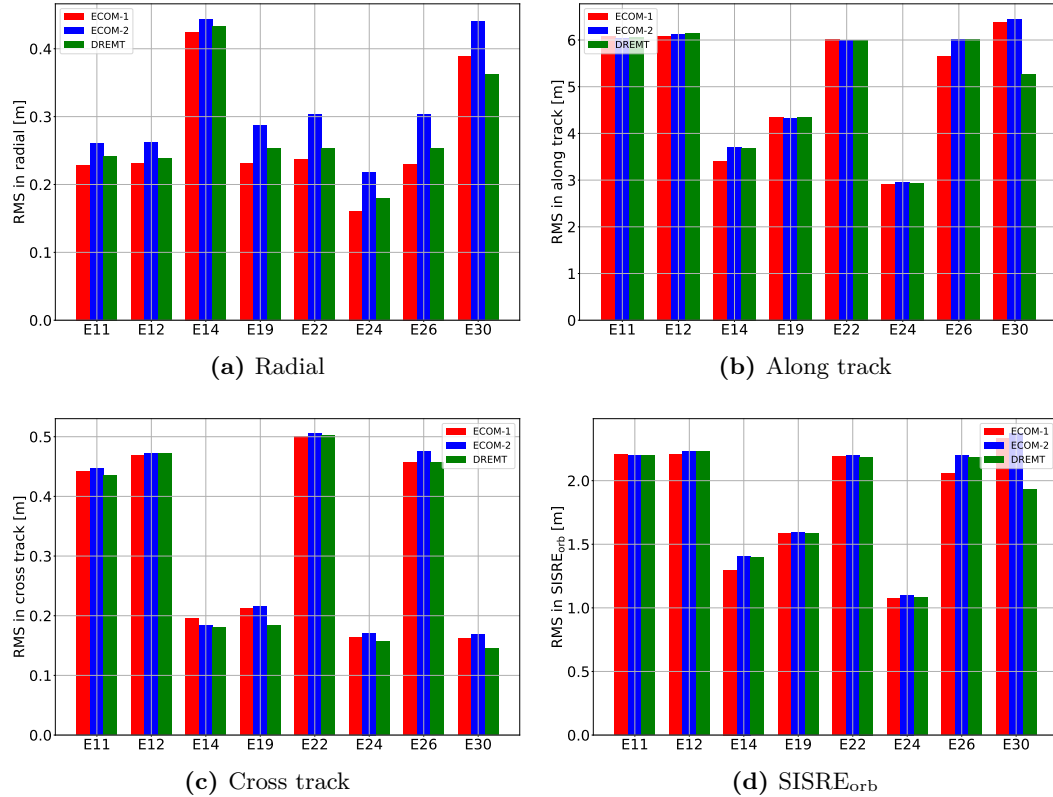


Figure 7.23: The average RMS in radial, along track, cross track and the SISRE_{orb} of 7 days orbit prediction with *a priori* models during eclipse seasons.

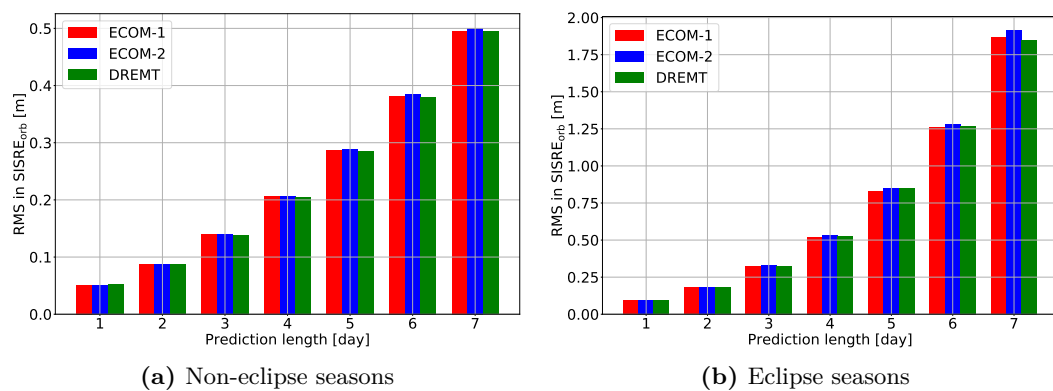


Figure 7.24: This figure shows the SISRE of 1 to 7 day's orbit prediction for IOV satellites using ECOM-1, ECOM-2 and the DREMT.

7.3.3 Findings

In this section, a long-term orbit prediction test is performed on 3 different empirical models (ECOM-1, ECOM-2 and DREMT). The benefits from using *a priori* models are also revealed. The principal findings are listed as follows:

- The newly developed DREMT has a performance (around 2 cm) similar to the ECOM-2 and they are both better than the ECOM-1 (around 5 cm) in terms of 2-day orbit fitting without any *a priori* models for satellites in non-eclipse seasons. For the satellites in eclipse, the fitting RMS of all the 3 empirical models get increased, which are around 7.3 cm, 5.7 cm, and 6.0 cm for ECOM-1, ECOM-2 and DREMT separately. The fitting RMS for ECOM-1 reduced greatly if a set of *a priori* force models are introduced. There is no significant decrease in the fitting RMS for ECOM-2 and DREMT with *a priori* force models.
- In terms of 7-day orbit prediction test, the use of *a priori* force models can reduce the orbit prediction errors for both the ECOM-1 and ECOM-2. During non-eclipse seasons, when *a priori* force models are used, for the ECOM-1, the orbit error RMS in radial, along track, cross track and RMS in SISRE_orb of a 7-day orbit prediction has reduced from 0.501 m, 2.387 m, 0.224 m, 1.026 m to 0.101 m, 1.324 m, 0.131 m, 0.495 m, for the ECOM-2, the RMS in these 4 indicators are reduced from 0.547 m, 2.413 m, 0.145 m, 1.058 m to 0.101 m, 1.324 m, 0.132 m, 0.500 m.
- Both the 2-day orbit fitting and the 7-day orbit prediction tests show that the empirical models (ECOM-1, ECOM-2 and DREMT) get identical results if the *a priori* force models are applied during non-eclipse seasons.
- Both the orbit fitting and the 7-day orbit prediction tests show that the performance of ECOM-1, ECOM-2 and the DREMT in eclipse seasons are worse than that in non-eclipse seasons.

7.4 Reconstruction of acceleration from empirical models

Section 7.3 validates the force models in a 7-day orbit prediction. It shows that the performance of ECOM-1 and ECOM-2 is greatly improved by introducing a set of *a priori* force models. The improvement of the newly developed DREMT does not get improved significantly. The reason maybe that the ECOM-1 and ECOM-2 model do not contain any *a priori* information while the DREMT is developed based on a box-wing satellite model. In order to further validate this hypothesis, the radiation pressure accelerations for one IOV (E11) and FOC (E22) satellites are reconstructed from the estimated empirical parameters in orbit fitting tests. Then, a comparison in the reconstructed accelerations among ECOM-1, ECOM-2, DREMT and the physical *a priori* models are performed.

7. VALIDATION OF FORCE MODELS IN ORBIT PREDICTION

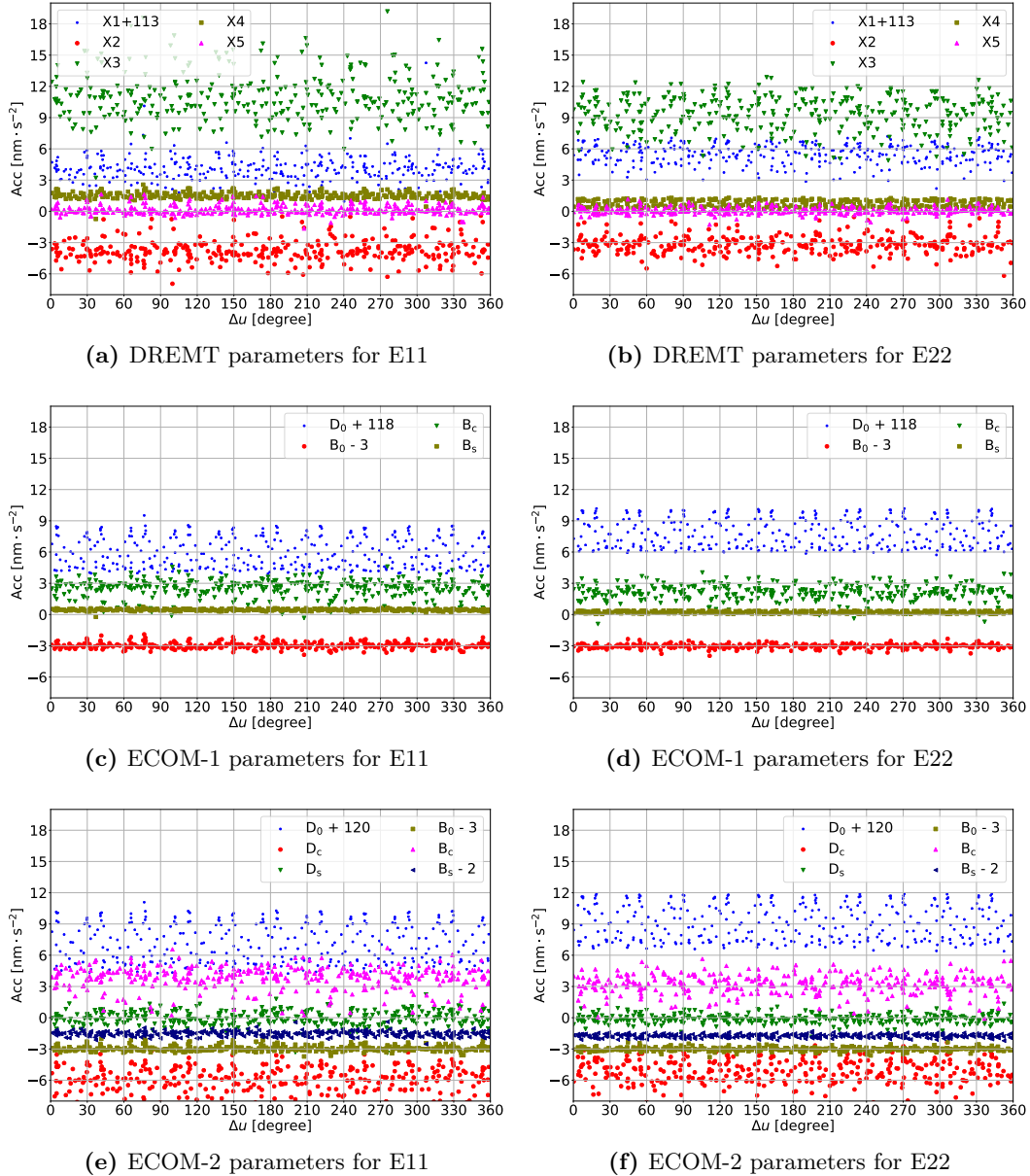


Figure 7.25: The empirical parameters of ECOM-1, ECOM-2, DREMT for E11 and E22 over non-eclipse seasons.

Table 7.11: The average and standard deviation of each parameter in ECOM-1, ECOM-2 and DREMT. unit: $[\text{nm} \cdot \text{s}^{-2}]$

sat	Model	$X_1 (D_0)$	$X_2 (D_c)$	$X_3 (D_s)$	$X_4 (B_0)$	$X_5 (B_c)$	B_s
E11	ECOM-1	-112.1 ± 1.5			0.04 ± 0.3	2.5 ± 0.9	0.5 ± 0.1
E22	ECOM-1	-110.2 ± 1.4			-0.04 ± 0.2	2.1 ± 0.8	0.2 ± 0.1
E11	ECOM-2	-112.9 ± 1.9	-6.0 ± 1.4	-0.02 ± 0.7	0.07 ± 0.3	3.8 ± 1.1	0.5 ± 0.2
E22	ECOM-2	-110.9 ± 1.7	-5.1 ± 1.2	-0.1 ± 0.4	-0.02 ± 0.2	3.2 ± 1.0	0.3 ± 0.2
E11	DREMT	-108.9 ± 1.3	-3.7 ± 1.1	11.1 ± 2.7	1.5 ± 0.3	0.17 ± 0.4	
E22	DREMT	-107.5 ± 1.0	-3.1 ± 0.9	9.4 ± 1.7	0.8 ± 0.3	0.06 ± 0.3	

7. VALIDATION OF FORCE MODELS IN ORBIT PREDICTION

The orbit fitting results during non-eclipse seasons for these two satellites are chosen to obtain the empirical parameters of each model (the results during eclipse seasons may not be reliable). The average values of each parameter over the non-eclipse seasons are used as the final parameters to construct the accelerations. The ‘y bias’ parameter (Y_0) is thought to be caused by the power imbalance between radiators mounted on the -y and +y panels and it is not reconstructed in this study. The variations of empirical parameters for ECOM-1, ECOM-2, and DREMT are shown in Fig. 7.25. The average values of each parameter are shown in Tab. 7.11. The accelerations of these 3 empirical models can be reconstructed using the values of these parameters. Figure 7.26 and Fig. 7.27 show the reconstructed accelerations in D and B components for E11 and E22 separately. The result from *a priori* models is tagged as “Physical”, which are the same as that used in section 7.3.2. The comparisons between these 4 models are performed with a relatively high β and low β (a value $\beta = 15.4^\circ$ is used to make sure the satellite is not in eclipse).

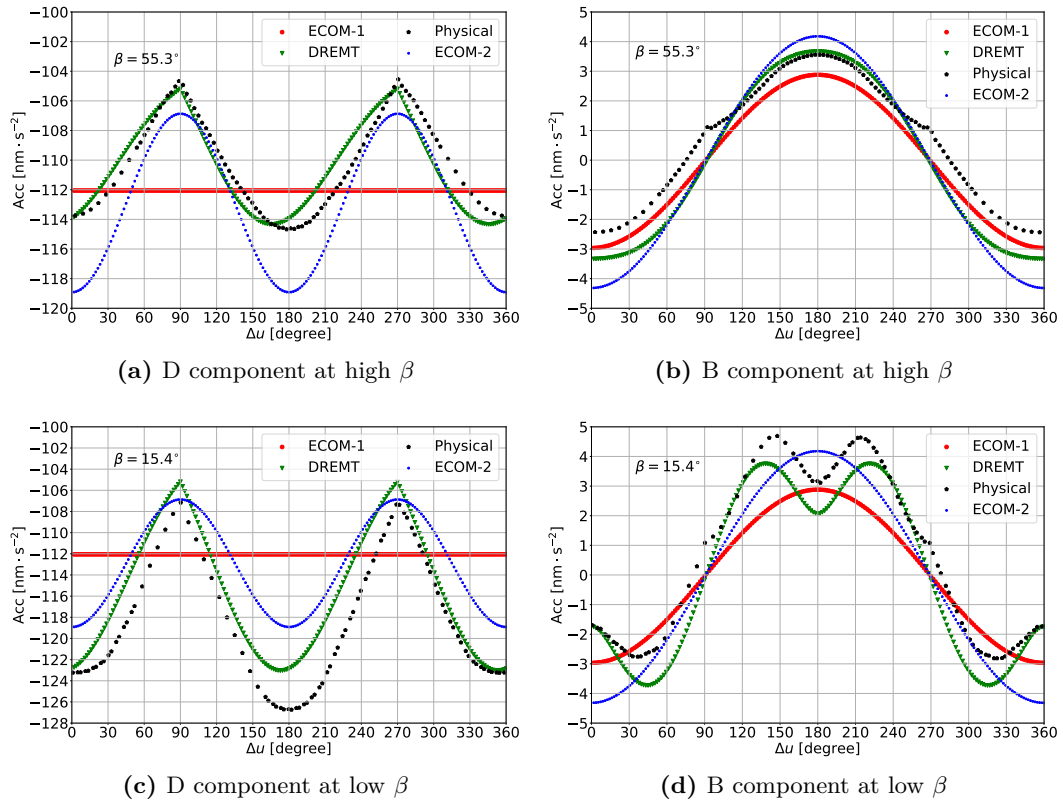


Figure 7.26: The reconstructed accelerations in the D and B components of E11 (IOV) for the ECOM-1, ECOM-2, DREMT, and the physical models.

Over 95% of the radiation force lies in D component (with a magnitude of about $110 \text{ nm} \cdot \text{m}^{-2}$). The 5-parameter ECOM-1 assumes that the acceleration in D component is constant. This assumption limits the accuracy of the ECOM-1. For the Galileo satellites, the variation of acceleration in D component is mainly driven by the varying cross-sectional area between the solar flux and the satellite bus. Both the ECOM-2 and the DREMT can deal with this variation. For both the low β and high β cases,

7. VALIDATION OF FORCE MODELS IN ORBIT PREDICTION

the variations of the D component are similar. There exist a discontinuity when $\Delta u = 90$ and 270 degrees (due to the switch of sun illumination between $-z$ and $+z$ panel). Both the DREMT and the physical models can capture this characteristic, however, the ECOM-2 shows a smooth curve around the switch which makes the model less realistic in physics.

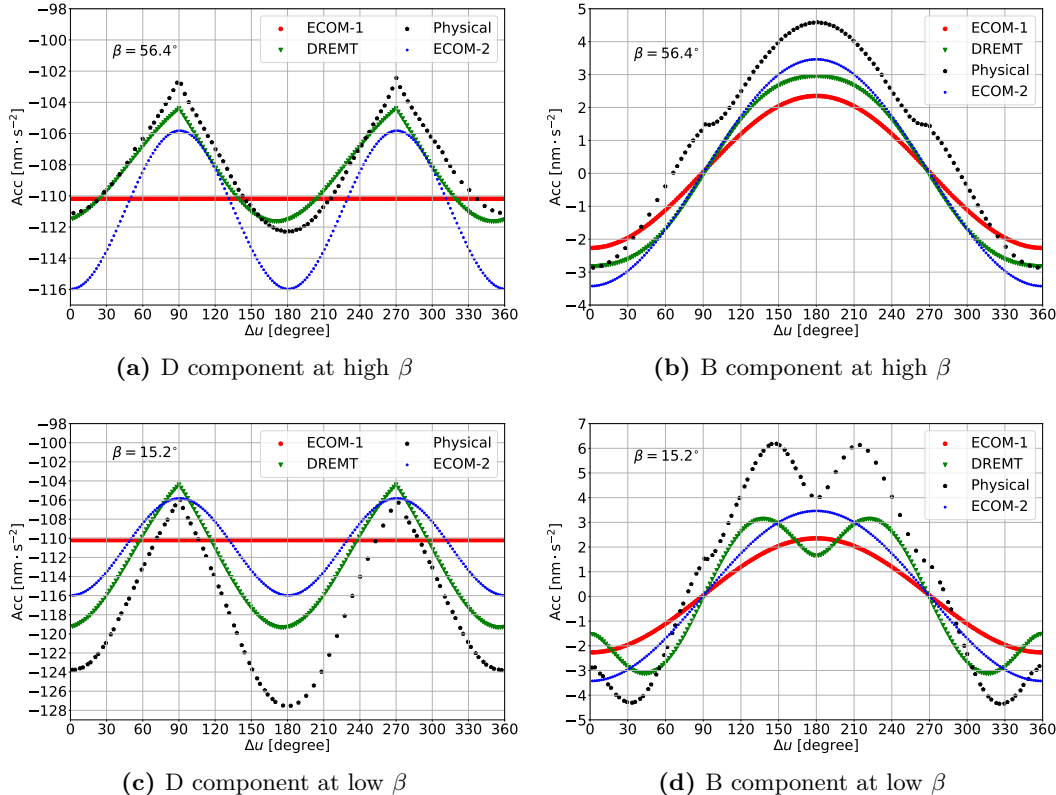


Figure 7.27: The reconstructed accelerations in the D and B components of E22 (FOC) for ECOM-1, ECOM-2, DREMT, and the physical models.

The magnitude of acceleration in B component is around $5 \text{ nm} \cdot \text{m}^{-2}$. The acceleration in B component varies differently from a high β to a low β . In the high β case, ECOM-1, ECOM-2, and the DREMT have similar trend as the physical model. However, in the low β case, both the ECOM-1 and ECOM-2 can not capture more signals than the DREMT and the physical models. It shows that the DREMT has a good consistency with the physical models.

One deficiency of ECOM-1 and ECOM-2 is that they do not represent the realistic physical effects in the acceleration derived from radiation pressure. As Fig. 7.26 and 7.27 show, the variation trend of the ECOM-1 and ECOM-2 are different from the physical model at a low β . By introducing *a priori* physical models in orbit prediction, this deficiency can be overcome to some extent and improved the orbit prediction results.

The DREMT is built based on the box-wing assumption of the satellites. It implicitly contains the constraint of box-wing model. From the reconstruction of accelerations, we can see that the DREMT has similar variation trend as the physical models

both in high and low β cases. This implies that the DREMT has more physical information than the ECOM-1 and ECOM-2. In addition, the DREMT allows the parameters be adjusted according to the tracking data. The DREMT has an advantage over the purely empirical models (the ECOM-1 and ECOM-2) in terms of physical information. Meanwhile, the DREMT is also superior to the physical models due to the fact that its parameters can be adjusted according to the actual tracking data. These two characteristics make DREMT the best among ECOM-1, ECOM-2 in the 7-day orbit prediction tests. The above analysis also confirmed the reason put forward at the beginning of this section.

7.5 Summary

This section gives validation results of the force models (both the physical models and empirical model DREMT) developed in this study. Firstly, the impacts of each physical effect on the Galileo satellites orbit have been calculated in a 24-hour orbit prediction. These physical effects include SRP, ERP, TRR, ANT, Multi-reflection, shadow function. Tab. 7.12 shows the average RMS of orbit errors caused by each physical effect in 24-hour orbit prediction.

Table 7.12: The magnitude of each physical effect and their RMS in 24-hour orbit prediction.

Effect	Radial (m)	Along (m)	Cross (m)	3D (m)	mag. ($\text{nm} \cdot \text{s}^{-2}$)
SRP	30	65	8	70	110.0
TRR	1.6	3.8	0.4	4.2	8.0
ERP	0.05	0.45	0.01	0.48	1.0
ANT	0.08	0.7	0.001	0.8	1.26
Multi-reflection	0.015	0.07	0.018	0.08	0.2

When all the developed physical models (SRP+TRR+ERP+ANT) are applied to a 24-hour orbit prediction test, the RMS in 3D orbit error are 0.7 m for IOV satellites and 2.5 m for the FOC satellites. This result shows that the physical models for IOV satellite are better than that of FOC satellites. The shadow function is a relatively weak effect for the Galileo orbit. The radial RMS of 7-day orbit prediction can be improved by 5.6 cm using newly developed PPM_atm compared with the widely used SECM.

In the long-term (7 days) orbit prediction test, the first 2 days are used to obtain the initial position and velocity for the next 7 days prediction. The tests are done in the eclipse and non-eclipse seasons for the chosen Galileo satellites in 2016.

During non-eclipse seasons, the 2-day orbit fit RMS are improved greatly (60%) for the ECOM-1 by introducing *a priori* physical force models. The improvements for ECOM-2 and DREMT in orbit fitting are not significant. In the orbit prediction test, the orbit errors (assessed by orbit errors in radial, along, cross and the SISRE_{orb}) using both ECOM-1 and ECOM-2 are reduced significantly by using *a priori* force models. Similarly, the improvement for DREMT is not significant. In addition, all

7. VALIDATION OF FORCE MODELS IN ORBIT PREDICTION

the 3 empirical models (ECOM-1, ECOM-2 and DREMT) get identical results after applying *a priori* models. The reason for this is that the ECOM-1 and ECOM-2 are purely empirical and do not contain any *a priori* information while the DREMT is developed based on a box-wing satellite model. Therefore, the *a priori* models can compensate the un-modelled force for ECOM-1 and ECOM-2. However, the DREMT already contains *a priori* information implicitly and can absorb the un-modelled force better than ECOM-1 and ECOM-2, thus, the application of *a priori* models to DREMT does not achieve significant performance. The reconstructed acceleration for one IOV (E11) and FOC (E22) satellites show clearly the variation trend of ECOM-1, ECOM-2, DREMT and the physical model. The DREMT and physical model have the same variation trend (the shape of the curve) for both high and low Sun elevation β . This further confirms the reason of why DREMT does not get significantly improved by using *a priori* models while the ECOM-1 and ECOM-2 do.

When satellites are in eclipse seasons, the performance of ECOM-1, ECOM-2 and the DREMT are worse than that in non-eclipse seasons. One possible reason may be the attitude of satellites in eclipse. The DREMT is developed under nominal attitude assumption and it should not apply to non-nominal attitude cases. Even when *a priori* models are used, the performance does not improve significantly.

Chapter 8

Conclusions and discussion

A overview of this thesis is given in the first section, and then the second section summarises this project in relation to the general objectives that was given in section 1.3.1. Then the conclusions are presented to address the detailed objectives in section 1.3.2. This is followed by the research contributions of this thesis in the view of the author. In the end, section 8.5 closes this thesis by presenting some ideas for the future work.

8.1 Overview of the thesis

This thesis is organised by the technical elements of radiation pressure modelling in relation to the general objective.

Chapter 1 is the introduction of this thesis giving the context, motivation and objectives of the research. In chapter 2, the published literature on the topic of radiation pressure modelling is reviewed. In chapter 3, the modelling methods of radiation flux (including solar radiation flux, Earth radiation flux, thermal radiation flux and navigation antenna transmit power) are presented. As a complementary part to the solar radiation flux modelling, a shadow function modelling method was put forward to scale the solar radiation flux when satellites are in eclipses in chapter 4. In chapter 5, the interactions between radiation flux and satellite surfaces are modelled using a ray tracing technique of high efficiency in computation. In chapter 6, an empirical solar radiation pressure model (DREMT) was developed based on a box-wing satellite model. In chapter 7, both the physical models and the empirical models are tested in orbit prediction. The benefits of using *a priori* information in radiation pressure modelling are revealed.

8.2 Summary in relation to the general objective

The ultimate aim of this research is to develop a set of radiation pressure models to improve the orbit prediction results for Galileo satellites. This aim is principally motivated by the link between force models and the quality of Galileo orbit. The

8. CONCLUSIONS AND DISCUSSION

research aim is implemented with 4 components: radiation flux modelling (including shadow function modelling during eclipse), interactions between radiation flux and satellite surfaces, empirical representation of solar radiation pressure and the validation of force models in orbit prediction. The first two components are about the physics of radiation pressure and help to build the physical models using *a priori* information about the satellites. Based on the physics, an empirical model is developed with some approximations to compensate the effects caused by limitations of physical models. In the end, both the physical models and the empirical models are validated in orbit prediction by comparing the predicted orbit with the precise orbit provided by CODE.

In the 24-hour orbit prediction test, the precise orbit data in the first 2-hours of each day during 2016 are used to obtain the initial state for the next 24 hours prediction. The impacts of each physical effect including SRP, TRR, ERP, AT, multiple reflection effects in ray tracing and shadow function on both the Galileo IOV and FOC satellites orbit in 24 hours are shown. The magnitude of SRP, TRR, ERP, AT and multiple reflections are 110, 8, 1.0, 0.8 and $0.2 \text{ nm} \cdot \text{s}^{-2}$. The RMS of 3D orbit errors caused by ignoring these effects are 70.0, 4.2, 0.48, 0.8, and 0.08 m in 24 hours.

In the 7-day orbit prediction, due to more parameters (6 initial state parameter + parameters in empirical models) to estimate, precise orbit data in 2-day arc length is used to obtain the initial state for the next 7-day orbit prediction. Three empirical models (ECOM-1, ECOM-2 and DREMT) are tested. In the analysis of force models, the orbit prediction tests are carried out in two schemes: purely empirical models and empirical models + physical models (SRP, TRR, ERP, ANT). In the time domain, the orbit prediction was done in non-eclipse seasons and eclipse seasons for the chosen 8 Galileo satellites. All the models perform better in non-eclipse seasons than that in eclipse seasons. For the orbit prediction without *a priori* models during non-eclipse seasons, DREMT is better than ECOM-1 and ECOM-2. After applying *a priori* models, all the 3 models get similar performance, the performance of ECOM-1 and ECOM-2 get significant improved but DREMT does not. The reason is that ECOM-1 and ECOM-2 do not contain any *a priori* information while the DREMT is developed based on a box-wing satellite model. This reason is further confirmed by the reconstructed accelerations of these 3 models. It shows that the DREMT is the closest to the physical models in the variation trend which means the major contribution of the physical models can be absorbed by the DREMT. The unabsorbed parts of physical models provide constraints to the ECOM-1 and ECOM-2 and contribute to the improvements in orbit prediction performance.

8.3 Conclusions and achievement of detailed objectives

In this section, the outcomes of the research in relation to each of the detailed objectives are described, and the findings are summarised.

8. CONCLUSIONS AND DISCUSSION

8.3.1 Modelling Earth radiation pressure

Before 2012, earth radiation pressure had been ignored in GNSS orbit modelling community for a long time. With the improvements in orbit accuracy, the modelling of Earth radiation pressure becomes more in demand. In the case of Earth radiation pressure modelling for Galileo satellites, the following questions need to be answered.

What is the magnitude of Earth radiation flux and Earth radiation pressure for Galileo satellites? How does it affect the orbit prediction? In the modelling, can we reach a balance between accuracy and computation time?

In this research, we used CERES Earth radiation flux observations in Earth radiation flux modelling. It contains shortwave (SW) and longwave (LW) Earth radiation flux. The global mean Earth radiation flux (SW + LW) on the TOA is around 337 $\text{W} \cdot \text{m}^{-2}$; 100 $\text{W} \cdot \text{m}^{-2}$ for SW and 237 $\text{W} \cdot \text{m}^{-2}$ for LW (see Fig. 3.12). At an altitude (around 230,00 km) of Galileo satellites, the Earth radiation flux is around 12 $\text{W} \cdot \text{m}^{-2}$ (see Fig. 3.13). The Earth radiation flux is mainly in the radial direction as shown in Fig. 7.8. This also makes the Earth radiation pressure mainly in the radial direction as shown in Fig. 7.9. The magnitude of ERP acceleration can reach to $1 \text{ nm} \cdot \text{s}^{-2}$. Under the nominal attitude, the variation of ERP in the radial force is driven by the orientation of solar panels. As shown in Fig. 7.9, the illumination of Earth radiation flux on the solar panels switches between sun-facing side and rear side when $\Delta u = 90$ or 270 degrees. The RMS of orbit errors in 3D caused by omission of ERP in 24 hours can reach to 0.48 m. This makes it an important force in precise orbit prediction.

In the calculation of the Earth radiation flux reaching a satellite's location, the slowest part is to find the visible area on the Earth's surface to the satellite. Based on the CERES grid dataset, the computer has to check the visibility of every cell (total number is 64800) one by one. In order to speed up this process, the raw CERES grid is reorganised into a triangular mesh with different levels (see Chapter 3.2). The more the subdivision, the more accurate, but conversely this increases the runtime. In the accuracy (see 3.2.5.2) and runtime (see 3.2.5.3) tests, I find that level 3 division can meet the accuracy requirement in Earth radiation flux for the Galileo satellites. This indicates that the computation efficiency can be improved by over 100 times (see Tab. 3.7) comparing with the raw CERES grid. Therefore, a balance between the runtime and accuracy can be achieved in Earth radiation flux modelling.

8.3.2 Development of shadow function during eclipse

When satellites are in eclipse, the solar radiation flux reaching the satellites is reduced due to the occlusion of the solar radiation by the Earth. This process is described by a shadow function. The most widely used shadow function in GNSS field is the SECM. The research questions related to this topic are as follows:

What is the accuracy of the SECM? The shadow function problem contains the effects due to Earth's oblateness (a geometrical problem) and atmospheric effect (a physical problem). Can we build a more accurate shadow function model considering

8. CONCLUSIONS AND DISCUSSION

the above two processes? Which is more important among the two effects (Earth's oblateness and atmospheric effects) for the Galileo satellites?

A new shadow function called PPM_atm (see Chapter 4) is developed in this study considering both the Earth's oblateness and atmospheric effects. In the accuracy test of the model, GRACE accelerometer observations are used to generate a shadow function (see Eq. 4.47). Taking the accelerometer observation derived shadow function as the truth, the errors of SECM has a mean of 0.1107 and a standard deviation of 0.1741, the errors of the PPM_atm has a mean of -0.0079 and a standard deviation of 0.0220 as shown in Tab. 4.4. This shows that the PPM_atm is better than the SECM by a factor of 10. There are no accelerometers installed on Galileo satellites, thus, the absolute accuracy of the models can not be assessed by direct measurements.

The atmospheric effects are more important than the Earth's oblateness in modelling the shadow function. This conclusion can be proved by the comparisons between PPM and the SECM_atm in the values of shadow functions. The PPM only consider the Earth's oblateness and totally ignore the atmospheric effects. The SECM_atm consider the atmospheric effects but uses a spherical Earth (the Earth's oblateness is ignored). The SECM ignore both the atmospheric effects and Earth's oblateness in modelling. In terms of the values of shadow function, the SECM_atm is better than the PPM (see Tab. 4.5 and Tab. 4.4). This means the errors caused by the Earth's oblateness is smaller than that caused by the atmospheric effects.

In terms of the orbit prediction test, 6 Galileo satellites in 3 different orbital planes are chosen. A 7-day orbit prediction shows that the PPM_atm can improve the radial RMS by 5.6 cm compared with the SECM (see Tab. 7.4). Fig. 7.14a and Fig. 7.14b show that PPM_atm is better than PPM and SECM in prediction, and SECM is better than PPM. This is probably due to that the errors in Earth's oblateness and the errors in atmospheric effects can be cancelled to some extent.

8.3.3 Fast ray tracing approach to model flux–surface interactions

In modelling the interactions between the radiation flux and complex satellite surfaces, a ray tracing technique is used. However, the standard ray tracing is slow to deal with satellite models of several hundred components with a small pixel spacing. In this study, a BVH data structure is used to reorganise satellite components and speeds up the computation by a factor of 30–50 (see Tab. 5.6). This technique is used to compute the SRP, ERP, and the TRR on the satellite bus. Related to the ray tracing, several research questions need to be answered.

What pixel spacing and number of reflections should be used in the ray tracing? What is the magnitude of accelerations caused by multiple reflections and its impacts on the Galileo orbit? Radiation pressure derived accelerations are sensitive to the input optical properties, what is the uncertainty in the resultant acceleration derived from ray tracing if the uncertainty of the optical properties are known?

In order to explore optimized pixel spacing in the ray tracing, a pixel spacing of

8. CONCLUSIONS AND DISCUSSION

0.1 mm is used as the truth, a series of pixel spacings from 1 m to 1 mm are tested. It shows that 1 mm pixel spacing in the ray tracing is good in modelling SRP for both the IOV and FOC satellites. The errors caused by the pixel spacing are less than $0.01 \text{ nm} \cdot \text{s}^{-2}$ for both the IOV and FOC satellites when 1 mm pixel spacing is used (see Fig. 5.6). Compared with the results of 1 reflection, the magnitude of acceleration caused by 3 reflections in ray tracing is in the range of 0.1 to $0.3 \text{ nm} \cdot \text{s}^{-2}$ for both IOV and FOC satellites (see Fig. 7.11). In a 24-hour orbit prediction test, the RMS in 3D orbit errors are 5 cm and 10 cm for the IOV and FOC satellites separately (see Fig. 7.12).

In terms of the optimized number of reflections, the results from 10 reflections are used as the truth, reflection number ranges from 1 to 10 are tested. It shows that the maximum error in acceleration is less than $0.01 \text{ nm} \cdot \text{s}^{-2}$ if the number of reflection is set to be 3 (see Fig. 5.8 and 5.7). In the uncertainty analysis of the ray tracing derived acceleration, if the standard deviations of the reflectivity and specular are 0.0001, the standard deviation in the acceleration is less than $1 \text{ nm} \cdot \text{s}^{-2}$. In addition, the uncertainty of the resultant acceleration is not to do with the pixel spacing as shown in Tab. 5.7.

8.3.4 Development of an empirical solar radiation pressure model

The current widely used empirical models are ECOM-1 and ECOM-2. They are developed in a purely empirical way. A new way of developing empirical models is put forward in Chapter 6 and a new empirical model (DREMT) is produced. This method starts from the physics of radiation pressure and makes reasonable assumptions. The parameters of the DREMT have specific physical meanings. Several research questions need to be answered related to this topic.

Can we develop an empirical solar radiation pressure model considering the physics of radiation pressure? What is the accuracy of the DREMT? Can the DREMT absorb other radiation forces in the BFS x and z direction? How good can the DREMT fit the solar radiation pressure model derived from the ray tracing?

A new empirical model (DREMT) considering the physics of radiation pressure has been developed in Chapter 6. In DREMT, it includes the direct solar radiation pressure and thermal re-radiation pressure under a nominal attitude. The DREMT is developed based on a box-wing model, the “truth” can be calculated in a analytical way. The approximations in the development of DREMT cause inaccuracy. The accuracy loss is evaluated by fitting DREMT to the analytical box-wing model. It shows that the fitting RMS is in the level of $0.2 \text{ nm} \cdot \text{s}^{-2}$ for both IOV and FOC satellites (see Tab. 6.6), which is better than both the ECOM-1 and ECOM-2. When a $10 \text{ nm} \cdot \text{s}^{-2}$ acceleration is added manually on the x and z components of the BFS to the analytical box-wing model, it shows that the DREMT can not fully absorb these accelerations (especially in the B component of the DREMT). The ECOM-1 and ECOM-2 perform better than DREMT as shown in Tab. 6.7. When we fit the empirical models (ECOM-1, ECOM-2 and DREMT) to the ray tracing model, it shows that DREMT performs better than

8. CONCLUSIONS AND DISCUSSION

ECOM-1 and ECOM-1 in D component but worse than ECOM-1 and ECOM-2 in the B component (see Tab. 6.8 and Fig. 6.8).

8.3.5 Performance assessment of force models in orbit prediction

The performance of the physical models and the empirical models are evaluated using orbit prediction for 8 Galileo satellites in 2016. In terms of the physical models, their impacts on the Galileo orbit are evaluated in a 24-hour prediction. The performance of the empirical models are evaluated in a 7-day orbit prediction. The research questions related to this topic are as follows:

*What are the impacts of individual force models on Galileo satellite orbit? How is the performance of newly developed DREMT compared with the ECOM-1 and ECOM-2? What is the improvement in orbit prediction when *a priori* force models are applied?*

The impacts of individual force models on the Galileo orbit are shown in a 24-hour orbit prediction (see Tab. 7.12). The magnitude of SRP, TRR, ERP, ANT and multiple reflections are in the level of 110, 8, 1, 0.8, and $0.2 \text{ nm} \cdot \text{s}^{-2}$ separately. The RMS of 3D orbit errors caused by omitting these effects are 70.0, 4.2, 0.48, and 0.08 m in 24 hours.

The performance of the empirical models (without *a priori* models) are tested in a 2-day orbit fit and 7-day orbit prediction. When satellites are not in eclipse, the DREMT is superior to ECOM-1 and similar to ECOM-2 in the performance of orbit fitting (see Fig. 7.17a). The DREMT is also better (improved by around 50%) than ECOM-1 and ECOM-2 in 7-day orbit prediction (see Fig. 7.18 and Tab. 7.6). When satellites are in eclipse, the performance of the 3 empirical models is generally worse than that in non-eclipse in orbit fitting (see Fig. 7.17b) and orbit prediction (see Fig. 7.19 and Tab. 7.7).

When *a priori* models are applied, all the ECOM-1, ECOM-2, and the DREMT have similar performance in both orbit fitting (see Fig. 7.21a) and orbit prediction (see Fig. 7.22 and Tab. 7.9) for satellites in non-eclipse. They are as good as the DREMT without *a priori* models. There is a significant improvement for ECOM-1 and ECOM-2 with *a priori* models. The DREMT does not get significant improvements because it already implicitly contains a box-wing model. This can be proved from the reconstructed accelerations for these 3 models (see Fig. 7.27 and Fig. 7.26). It is still the case that these 3 models get reduced performance in eclipse seasons in orbit fitting (see 7.17b) and prediction (see Fig. 7.20b). This shows that the application of *a priori* models does not help much in improving the orbit prediction during eclipses.

8.4 Research contributions

The contributions to knowledge of the research conducted for this thesis can be summarized as follows:

- Developed a runtime and accuracy configurable Earth radiation flux model. This

8. CONCLUSIONS AND DISCUSSION

Earth flux model allows the application of CERES observations to be practical in Earth radiation pressure modelling. The newly developed Earth flux model can run 100 times faster and has an accuracy loss of only 0.36% for Galileo satellites.

- Develop a shadow function (PPM_atm) to describe the solar radiation flux reduction in eclipse. The validation using GRACE accelerometer observations showed that it is 10 times more accurate than the widely used SECM.
- The SRP model computation efficiency has been improved by a factor of 30–50 using BVH in the ray tracing. The improvements in computation efficiency allows the method be used more widely (spacecraft with more complex shape). Based on this ray tracing algorithm, the acceleration due to multiple reflections are explored. In addition, the uncertainty in the resultant force can be computed from the uncertainty of the input optical properties.
- Developed an empirical model (DREMT) that implicitly contains the box-wing model. The development of DREMT shows a novel approach to build empirical solar radiation pressure models. The validation in orbit fitting and orbit prediction show the impact of DREMT.
- Further proved that the performance of ECOM-1 and ECOM-2 in orbit prediction for Galileo satellites can be improved by 50% aiding by *a priori* models in non-eclipse seasons. This shows the importance of considering physics when building solar radiation pressure models.

8.5 Future work

Though a lot of work has been undertaken in this thesis, more work is required in the future. The “to-do list” is as follows:

- The inputs of the ray tracing approach need to be more accurate (primarily the input material properties of the satellite surfaces). It is the main error source in solar radiation pressure modelling. These data could be obtained from satellite manufacturers, but not necessarily to the required accuracy. Thus, one possibility to get optical properties with the required accuracy is to measure them in a laboratory. The preliminary calculation in section 5.3.7 shows that the standard deviation of the optical properties should reach 0.01 if the standard deviation of the resultant force is required to be $0.1 \text{ nm} \cdot \text{s}^{-2}$.
- Computation efficiency of direct solar radiation pressure modelling can be further improved by using GPU (Graphics Processing Unit). The ray tracing algorithm is very suitable in “parallel computation”. However, this require rewriting the ray tracing software. In addition, more components could be included in the ray tracing software if the computation efficiency is improved, one of which is the Laser Retroreflect Array (LRA). The solar radiation on the LRA is reflected back

8. CONCLUSIONS AND DISCUSSION

directly towards the source. Another effect is the thermal gradient force on the solar panels, it can be modelled based on the necessary satellite information. To include these effects in modelling can further improve the physics-based model.

- In terms of shadow function modelling, the atmospheric effect is modelled using a linear function in this study. In the future study, an atmospheric air density model should be introduced. This should further improve the performance of the PPM_atm.
- The philosophy of empirical solar radiation force modelling can be extended and applied to other GNSS satellites. The thermal radiation force due to radiators on the -z and +x panel and antenna thrust should be considered in the next version of the empirical solar radiation pressure model. In addition, the empirical model should be extended to work for GNSS satellites under non-nominal attitude. This requires more analysis and the regeneration of the empirical representation. Also, the DREMT should be tested in precise orbit determination. In the process of precise orbit determination, the impact of the DREMT on the geodetic parameters should be assessed. Another check should be carried out is that if the dependency between SLR residuals and Sun elevation over orbital plane reduced using the DREMT.

Appendix A

Calculation on spherical surface

A.1 The Great-circle distance

The great-circle distance or orthodromic distance is the shortest distance between two points on the surface of a sphere, measured along the surface of the sphere. Let the geographical latitude and longitude of two points on the Great-circle be (φ_1, λ_1) and (φ_2, λ_2) . According to the spherical law of cosine, the central angle $\Delta\sigma$ between these two points is:

$$\Delta\sigma = \arccos(\sin \varphi_1 \sin \varphi_2 + \cos \varphi_1 \cos \varphi_2 \cos(\lambda_1 - \lambda_2)) \quad (\text{A.1})$$

The arc length between these two points is given

$$d = R\Delta\sigma \quad (\text{A.2})$$

where R is the radius of the sphere.

A.2 Intersection between great circle arcs

As shown in Fig. A.1, the vertices P_1 and P_2 form an arc while P_3 and P_4 form another arc. The great circles of P_1P_2 and P_3P_4 have two intersections S_1 and S_2 . But only S_1 should be chosen as the solution. The calculation process is described as follows.

The inputs of this algorithm are the latitude and longitude in radians of the vertices $P_1(\varphi_{P_1}, \lambda_{P_1})$, $P_2(\varphi_{P_2}, \lambda_{P_2})$, $P_3(\varphi_{P_3}, \lambda_{P_3})$, and $P_4(\varphi_{P_4}, \lambda_{P_4})$. The output is the latitude and longitude of the solution $S_1(\varphi_{S_1}, \lambda_{S_1})$.

- **Convert latitude and longitude into Cartesian coordinates**

The conversion is done with the following formula (assume the radius of the sphere is 1):

$$\begin{aligned} x &= \cos \varphi \cos \lambda \\ y &= \cos \varphi \sin \lambda \\ z &= \sin \varphi \end{aligned} \quad (\text{A.3})$$

A. CALCULATION ON SPHERICAL SURFACE

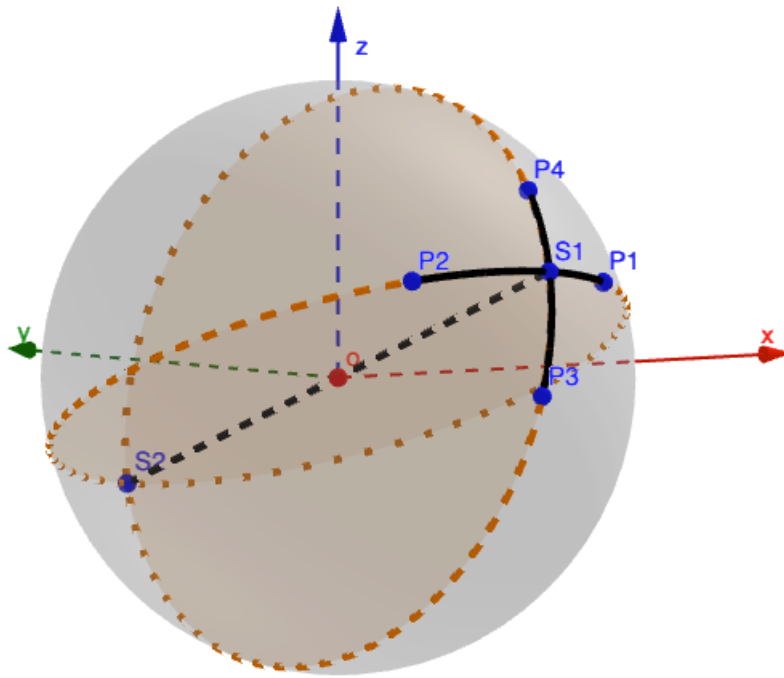


Figure A.1: The intersection between two great circle arcs.

where x , y , and z are the Cartesian coordinates while φ and λ are the latitude and longitude. Apply the above formula to P_1 , P_2 , P_3 , and P_4 . The Cartesian coordinates are calculated: $P_1(X_{P_1}, Y_{P_1}, Z_{P_1})$, $P_2(X_{P_2}, Y_{P_2}, Z_{P_2})$, $P_3(X_{P_3}, Y_{P_3}, Z_{P_3})$, and $P_4(X_{P_4}, Y_{P_4}, Z_{P_4})$.

- **Calculate the normals to planes intercepted by the great circles**

All the great circles contain the centre of the sphere, thus, any two vertices on the arc of great circles and the centre of the sphere can form a plane. The normals to planes can be calculated by a cross product between the vector from the centre of the sphere to the first point and the vector from the centre of the sphere to the second point. The two normals $\mathbf{V}_1 = (X_{V_1}, Y_{V_1}, Z_{V_1})^T$ and $\mathbf{V}_2 = (X_{V_2}, Y_{V_2}, Z_{V_2})^T$ are computed by

$$\begin{aligned} X_{V_1} &= Y_{P_1}Z_{P_2} - Z_{P_1}Y_{P_2} \\ Y_{V_1} &= Z_{P_1}X_{P_2} - X_{P_1}Z_{P_2} \\ Z_{V_1} &= X_{P_1}Y_{P_2} - Y_{P_1}X_{P_2} \end{aligned} \tag{A.4}$$

$$\begin{aligned} X_{V_2} &= Y_{P_3}Z_{P_4} - Z_{P_3}Y_{P_4} \\ Y_{V_2} &= Z_{P_3}X_{P_4} - X_{P_3}Z_{P_4} \\ Z_{V_2} &= X_{P_3}Y_{P_4} - Y_{P_3}X_{P_4} \end{aligned} \tag{A.5}$$

- **Calculate the direction of the intersection line between the two planes**

Because the intersection line between the two planes is perpendicular to both the normals to the planes, the direction of the intersection line $\mathbf{D} = (X_D, Y_D, Z_D)^T$

A. CALCULATION ON SPHERICAL SURFACE

is computed by the cross product of the two normals and then is normalised, i.e.

$$\mathbf{D} = \frac{\mathbf{V}_1 \times \mathbf{V}_2}{\|\mathbf{V}_1 \times \mathbf{V}_2\|} \quad (\text{A.6})$$

- **Choose the right solution**

Two great circle have two intersections $S_1(X_{S_1}, Y_{S_1}, Z_{S_1})$ and $S_2(X_{S_2}, Y_{S_2}, Z_{S_2})$. Within an unit sphere, the coordinates of the two intersections are given by

$$\begin{aligned} X_{S_1} &= X_D \\ Y_{S_1} &= Y_D \\ Z_{S_1} &= Z_D \end{aligned} \quad (\text{A.7})$$

$$\begin{aligned} X_{S_2} &= -X_D \\ Y_{S_2} &= -Y_D \\ Z_{S_2} &= -Z_D \end{aligned} \quad (\text{A.8})$$

Usually, the solutions to the intersections of two arcs have two situations (no intersection or only 1 intersection). The intersection separates the two arcs into two separately, the test condition is that the arc lengths of the two separated parts ($d_{P_1 S_1}$, $d_{S_1 P_2}$, $d_{P_3 S_1}$, $d_{S_1 P_4}$) should add up to the arc lengths of the origin arcs ($d_{P_1 P_2}$, $d_{P_3 P_4}$).

Condition for S_1

$$\begin{aligned} d_{P_1 P_2} &= d_{P_1 S_1} + d_{S_1 P_2} \\ d_{P_3 P_4} &= d_{P_3 S_1} + d_{S_1 P_4} \end{aligned} \quad (\text{A.9})$$

and condition for S_2

$$\begin{aligned} d_{P_1 P_2} &= d_{P_1 S_2} + d_{S_2 P_2} \\ d_{P_3 P_4} &= d_{P_3 S_2} + d_{S_2 P_4} \end{aligned} \quad (\text{A.10})$$

The solution who passes through the above test will be the intersection, otherwise, the two arcs do not intersect. Once the solution is fixed, the Cartesian coordinates of S_1 or S_2 are converted into longitude and latitude as the output.

A.3 The area of polygon on spherical surface

A spherical polygon has n vertices and sides (Fig. A.2 shows the case where $n = 4$). The sum of the polygon's interior angles must equal the sum of all the internal angles associated with $n - 2$ triangles whose combined area equals that of the polygon. Thus the area of a spherical polygon is given by

$$A_p = \left(\sum_{i=1}^n \alpha_i - (n - 2)\pi \right) R^2 \quad (\text{A.11})$$

A. CALCULATION ON SPHERICAL SURFACE

where R is the radius of the sphere, α_i is the interior angle at i^{th} vertex.

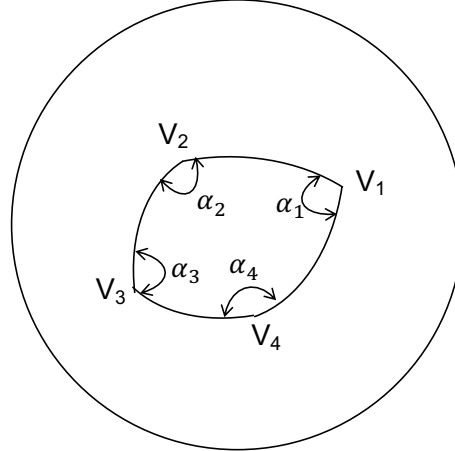


Figure A.2: A spherical polygon with 4 vertices (sides are Great-circle arcs). The interior angle are α_1 , α_2 , α_3 , and α_4 .

The inputs of the algorithm are the latitude and longitude of the vertices in counter clockwise order and the output is the area of the spherical polygon. The main problem is how to calculate the interior angle at each vertex according to equation A.11. As shown in Fig. A.3, the interior angle α_P at vertex P is formed by arc AP and PB . The latitude and longitude at the three vertices are $A(\varphi_A, \lambda_A)$, $P(\varphi_P, \lambda_P)$, and $B(\varphi_B, \lambda_B)$. A coordinate transformation is applied in order to calculate α_P easily.

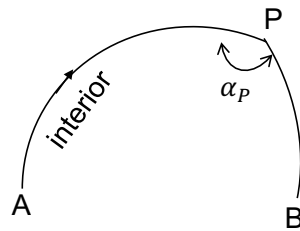


Figure A.3: The interior angle and path from A to B

The original latitude and longitude are based on the north pole, the transformation here is to use vertex P as the “north pole”. After the transformation, the latitude and longitude of all the vertex at the new coordinate system become $A(\varphi'_A, \lambda'_A)$, $P(\varphi'_P, \lambda'_P)$, and $B(\varphi'_B, \lambda'_B)$. The longitudes for vertex A and B after the transformation are calculated using the following formulae [Bevis and Cambareri, 1987]

$$\begin{aligned}\lambda'_A &= \arctan \frac{\sin(\lambda_A - \lambda_P) \cos \varphi_A}{\sin \varphi_A \cos \varphi_P - \cos \varphi_A \sin \varphi_P \cos(\lambda_A - \lambda_P)} \\ \lambda'_B &= \arctan \frac{\sin(\lambda_B - \lambda_P) \cos \varphi_B}{\sin \varphi_B \cos \varphi_P - \cos \varphi_B \sin \varphi_P \cos(\lambda_B - \lambda_P)}\end{aligned}\quad (\text{A.12})$$

The interior angle α_P is calculated by

$$\alpha_P = \lambda'_B - \lambda'_A \quad (\text{A.13})$$

A. CALCULATION ON SPHERICAL SURFACE

Once the interior angle for each vertex is calculated, equation A.11 is used to calculate the area of the spherical polygon.

A. CALCULATION ON SPHERICAL SURFACE

Appendix B

The mathematics of orbit fitting

In mathematics, the satellite's position at time t is a function of the initial state vector \mathbf{y}_0 and the dynamic parameters \mathbf{p} .

$$\mathbf{y}(t) = \mathbf{F}(t, \mathbf{y}_0, \mathbf{p}) \quad (\text{B.1})$$

The linearisation of Eq. B.1 with respect to \mathbf{y}_0 and \mathbf{p} is given

$$\mathbf{y}(t) = \mathbf{F}_0(t, \mathbf{y}_0, \mathbf{p}) + \frac{\partial \mathbf{y}(t)}{\partial \mathbf{y}_0} \delta \mathbf{y}_0 + \frac{\partial \mathbf{y}(t)}{\partial \mathbf{p}} \delta \mathbf{p} \quad (\text{B.2})$$

where $\mathbf{F}_0(t, \mathbf{y}_0, \mathbf{p})$ is the initial value of $\mathbf{y}(t)$ (i.e. the predicted satellite's position from t_0 to t with the initial state vector \mathbf{y}_0 and force model parameters \mathbf{p}), $\delta \mathbf{y}_0$ is the correction to the initial state vector, $\delta \mathbf{p}$ is the correction to the initial force model parameters.

The partial derivatives of the state vector at time t with respect to the initial state vector is called state transition matrix $\Phi(t, t_0)$. The partial derivatives of the state vector over the force model parameters is called sensitivity matrix $\mathbf{S}(t)$. i.e.

$$\Phi(t, t_0) = \frac{\partial \mathbf{y}(t)}{\partial \mathbf{y}_0} \quad (\text{B.3})$$

$$\mathbf{S}(t) = \frac{\partial \mathbf{y}(t)}{\partial \mathbf{p}} \quad (\text{B.4})$$

$$\frac{d\Phi}{dt} = \frac{d}{dt} \frac{\partial \mathbf{y}(t)}{\partial \mathbf{y}_0} = \frac{\partial}{\partial \mathbf{y}_0} \frac{d}{dt} \mathbf{y}(t) = \frac{\partial \mathbf{f}(t)}{\partial \mathbf{y}_0} = \frac{\partial \mathbf{f}(t)}{\partial \mathbf{y}(t)} \frac{\partial \mathbf{y}(t)}{\partial \mathbf{y}_0} = \frac{\partial \mathbf{f}(t)}{\partial \mathbf{y}(t)} \Phi(t, t_0) \quad (\text{B.5})$$

where $\mathbf{f}(t) = \frac{d}{dt} \mathbf{y}(t)$ is the first derivatives of state vector with respect to time.

$$\frac{\partial \mathbf{f}(t)}{\partial \mathbf{y}(t)} = \begin{pmatrix} \mathbf{0}_{3 \times 3} & \mathbf{I}_{3 \times 3} \\ \frac{\partial \mathbf{a}(t, \mathbf{r}, \mathbf{v})}{\partial \mathbf{r}(t)} & \frac{\partial \mathbf{a}(t, \mathbf{r}, \mathbf{v})}{\partial \mathbf{v}(t)} \end{pmatrix}_{6 \times 6} \quad (\text{B.6})$$

Generally speaking, the force models are related to satellite position, satellite velocity and time, thus matrix $\frac{\partial \mathbf{f}(t)}{\partial \mathbf{y}(t)}$ can be calculated which means an differential equation

B. THE MATHEMATICS OF ORBIT FITTING

of the state transition matrix is obtained. This is also called the variation equation of the transition matrix and it is used to get the state transition matrix with numerical integration. According to the definition of the state transition matrix, the initial value for the numerical integration is $\Phi(t_0, t_0) = \mathbf{I}_{6 \times 6}$.

As for the sensitivity matrix $\mathbf{S}(t)$, we have following chain rule:

$$\frac{d\mathbf{S}(t)}{dt} = \frac{d}{dt} \frac{\partial \mathbf{y}(t)}{\partial \mathbf{p}} = \frac{\partial}{\partial \mathbf{p}} \frac{dy(t)}{dt} = \frac{\partial \mathbf{f}(t, \mathbf{y}, \mathbf{p})}{\partial \mathbf{p}} = \frac{\partial \mathbf{f}}{\partial \mathbf{p}} + \frac{\partial \mathbf{f}}{\partial \mathbf{y}} \frac{\partial \mathbf{y}}{\partial \mathbf{p}} = \frac{\partial \mathbf{f}}{\partial \mathbf{p}} + \frac{\partial \mathbf{f}}{\partial \mathbf{y}} \mathbf{S}(t) \quad (\text{B.7})$$

where

$$\frac{\partial \mathbf{f}(t)}{\partial \mathbf{p}(t)} = \left(\begin{array}{c} \mathbf{0}_{3 \times n_p} \\ \frac{\partial \mathbf{a}(t, \mathbf{r}, \mathbf{v}, \mathbf{p})}{\partial \mathbf{p}(t)} \end{array} \right)_{6 \times n_p} \quad (\text{B.8})$$

where n_p is the number of dynamic parameters. Equation (B.7) is also called the variation equation of the sensitivity matrix. In the same way as the state transition matrix, this can also be solved by the numerical integrator with initial value $\mathbf{S}(t_0) = \mathbf{0}_{6 \times n_p}$.

After obtaining the state transition matrix $\Phi(t, t_0)$ and the sensitivity matrix $\mathbf{S}(t)$, Equation (B.2) is written as

$$\mathbf{y}(t) - \mathbf{F}_0(t, \mathbf{y}_0, \mathbf{p}) = (\Phi(t, t_0) \quad \mathbf{S}(t)) \begin{pmatrix} \delta \mathbf{y}_0 \\ \delta \mathbf{p} \end{pmatrix} \quad (\text{B.9})$$

If we have got many epochs of observations (epoch time t varies from t_0 to t_e) and the initial values of \mathbf{y}_0 and \mathbf{P} , the above Eq. B.9 can be solved using a least square approach with the unknowns $\delta \mathbf{y}_0$ and $\delta \mathbf{p}$.

$$\begin{pmatrix} \delta \mathbf{y}_0 \\ \delta \mathbf{p} \end{pmatrix} = \begin{pmatrix} \sum_{t_0}^{t_e} \Phi^T(t, t_0) \Phi(t, t_0) & \sum_{t_0}^{t_e} \Phi^T(t, t_0) \mathbf{S}(t) \\ \sum_{t_0}^{t_e} \mathbf{S}^T(t) \Phi(t, t_0) & \sum_{t_0}^{t_e} \mathbf{S}^T(t) \mathbf{S}(t) \end{pmatrix}^{-1} \begin{pmatrix} \sum_{t_0}^{t_e} \Phi^T(t, t_0) (\mathbf{y}(t) - \mathbf{F}_0(t, \mathbf{y}_0, \mathbf{p})) \\ \sum_{t_0}^{t_e} \mathbf{S}^T(t) (\mathbf{y}(t) - \mathbf{F}_0(t, \mathbf{y}_0, \mathbf{p})) \end{pmatrix} \quad (\text{B.10})$$

Once the corrections $\delta \mathbf{y}_0$ and $\delta \mathbf{p}$ are solved, the fitted orbit can be generated. It may need several iterations to get convergent because Eq. B.9 is highly non-linear.

References

- Abdel-Aziz, Y. A. Lorentz force effects on the orbit of a charged artificial satellite: A new approach. *Applied Mathematical Sciences*, 1(31):1511–1518, 2007. ISSN 0094243X. doi: 10.1063/1.2711134.
- Abdel-Aziz, Y. A. and Khalil, K. I. Electromagnetic effects on the orbital motion of a charged spacecraft. *Research in Astronomy and Astrophysics*, 14(5):589–600, 2014. ISSN 16744527. doi: 10.1088/1674-4527/15/4/009.
- Adhya, S. *Thermal Re-Radiation Modelling for the Precise Prediction and Determination of Spacecraft Orbits*. PhD thesis, University College London, 2005.
- Adhya, S., Sibthorpe, A., Ziebart, M., and Cross, P. Oblate Earth Eclipse State Algorithm for Low-Earth-Orbiting Satellites. *Journal of Spacecraft and Rockets*, 41(1):157–159, 2004. ISSN 0022-4650. doi: 10.2514/1.1485.
- Aksnes, K. Short-period and long-period perturbations of a spherical satellite due to direct solar radiation. *Celestial Mechanics*, 13(1):89–104, 1976. ISSN 00088714. doi: 10.1007/BF01228536.
- Altamimi, Z., Angermann, D., Argus, D., Blewitt, G., Boucher, C., Chao, B., Drewes, H., Eanes, R., Feissel, M., Ferland, R., Herring, T., Holt, B., Johannson, J., Larson, K., Ma, C., Manning, J., Meertens, C., Nothnagel, A., Pavlis, E., Petit, G., Ray, J., Ries, J., Scherneck, H.-G., Sillard, P., and Watkins, M. The Terrestrial Reference frame and the Dynamic Earth. *EOS, Transactions, American Geophysical Union*, 82(25):273–284, 2001.
- Andrés, J. I., Noomen, R., and None, S. V. Numerical simulation of the LAGEOS thermal behavior and thermal accelerations. *Journal of Geophysical Research: Solid Earth*, 111(9): 1–14, 2006. ISSN 21699356. doi: 10.1029/2005JB003928.
- Anselmo, L., Farinella, P., Milani, A., and Nobili, A. M. Effects of the Earth-reflected Sunlight on the Orbit of the LAGEOS Satellite. *Astronomy and Astrophysics*, 8(1):3–8, 1983.
- Arnold, D., Meindl, M., Beutler, G., Dach, R., Schaer, S., Lutz, S., Prange, L., Sośnica, K., Mervart, L., and Jäggi, A. CODE's new solar radiation pressure model for GNSS orbit determination. *Journal of Geodesy*, 89(8):775–791, 2015. ISSN 14321394. doi: 10.1007/s00190-015-0814-4.
- Ashkin, A. Applications of laser radiation pressure. *Science (New York, N.Y.)*, 210(4474): 1081–1088, 1980. ISSN 0036-8075. doi: 10.1126/science.210.4474.1081.
- Bar-Sever, Y. E. A new model for GPS yaw attitude. *Journal of Geodesy*, 70(11):714–723, 1996. ISSN 0949-7714. doi: 10.1007/BF00867149.
- Bar-Sever, Y. E. and Kuang, D. New empirically derived solar radiation pressure model for global positioning system satellites. Technical report, The Interplanetary Network Progress Report 42-160, 2004.
- Bar-Sever, Y. E. and Kuang, D. New empirically derived solar radiation pressure model for global positioning system satellites during eclipse seasons. *IPN Progress Report*, pages 1–4, 2005.
- Bar-Sever, Y. E. and Russ, K. M. New and Improved Solar Radiation Models for GPS Satellites Based on Flight Data. Technical report, Jet Propulsion Laboratory, California, 1997.
- Beekman, G. I.O.Yarkovsky and the discovery of 'his' effect. *Journal for the History of Astron-*

REFERENCES

- omy, 37(126):71–86, 2006.
- Bertels, D. Intersections of great circles on a sphere, 2005.
- Bettadpur, S. Recommendation for a-priori Bias&Scale Parameters for Level-1B ACC Data (Version2), 2009.
- Bettadpur, S. GRACE-Product specification document. Technical report, Center for Space Research, The university of Texas at Austin, 2012.
- Beutler, G., Brockmann, E., Gurtner, W., Hugentobler, U., Mervart, L., Rothacher, M., and Verdun, A. Extended orbit modeling techniques at the CODE processing center of the international GPS service for geodynamics (IGS): theory and initial results. *Manuscr. Geod.*, 19(6):367–386, 1994.
- Beutler, G. Modeling and estimating the orbits of GNSS: Key principles in history and future. Technical report, IGS workshop 2014, California, 2014.
- Bevis, M. and Cambareri, G. Computing the area of a spherical polygon of arbitrary shape. *Mathematical Geology*, 19(4):335–346, may 1987. ISSN 0882-8121. doi: 10.1007/BF00897843.
- Boulton, W. J. The effect of solar radiation pressure on the orbit of a cylindrical satellite. *Planetary and Space Science*, 32(3):287–296, 1984. doi: [https://doi.org/10.1016/0032-0633\(84\)90164-8](https://doi.org/10.1016/0032-0633(84)90164-8).
- Butcher, J. A history of Runge-Kutta methods. *Applied Numerical Mathematics*, 20(3):247–260, mar 1996. ISSN 01689274. doi: 10.1016/0168-9274(95)00108-5.
- Case, K., Kruizinga, G., and Wu, S.-C. GRACE Level 1B Data Product User Handbook, 2010. URL ftp://podaac.jpl.nasa.gov/allData/grace/docs/Handbook_1B_v1.3.pdf.
- CERES. CERES_SYN1deg_Ed4A Data Quality Summary (10/3/2017). Technical report, NASA, 2017.
- Cerri, L., Berthias, J. P., Bertiger, W. I., Haines, B. J., Lemoine, F. G., Mercier, F., Ries, J. C., Willis, P., Zelensky, N. P., and Ziebart, M. Precision orbit determination standards for the JASON series of altimeter missions. *Marine Geodesy*, 33(SUPPL. 1):379–418, 2010. ISSN 01490419. doi: 10.1080/01490419.2010.488966.
- Chan, F. A general method for computing the total solar radiation force on complex space-craft structures. Technical report, NASA,Goddard Space Flight Centre, Rockville, Maryland,United States, 1981. URL <https://ntrs.nasa.gov/archive/nasa/casi.ntrs.nasa.gov/19820002193.pdf>.
- Chen, J., Tan, W., Li, C., Zeng, G., and Yang, J. History, Present and Future of Solar Radiation Pressure Theory. In *China Satellite Navigation Conference*, volume 304, pages 41–53, 2014. ISBN 978-3-642-54742-3. doi: 10.1007/978-3-642-54743-0.
- Chesley, S. R., Ostro, S. J., Vokrouhlický, D., Čapek, D., Giorgini, J. D., Nolan, M. C., Margot, J. L., Hine, A. A., Benner, L. A., and Chamberlin, A. B. Direct Detection of the Yarkovsky Effect by Radar Ranging to Asteroid 6489 Golevka. *Science*, 302(5651):1739–1742, 2003. ISSN 00368075. doi: 10.1126/science.1091452.
- China Satellite Navigation Office. BeiDou constellation, 2018. URL <http://www.beidou.gov.cn/xt/xtjs/>.
- Dach, R., Arnold, D., Prange, L., Beutler, G., Schaer, S., and Jaggi, A. Updating the CODE GNSS Orbit Model. Technical report, EUREF 2015 Symposium, Leipzig,Germany, 2015. URL <http://www.euref.eu/symposia/2015Leipzig/03-04-Dach.pdf>.
- De Moraes, R. V. Combined solar radiation pressure and drag effects on the orbits of artificial satellites. *Celestial Mechanics*, 25(3):281–292, 1981. ISSN 00088714. doi: 10.1007/BF01228965.
- Delva, P. and Puchades, N. Galileo gravitational redshift test with Eccentric satellites. Technical report, PSL Research University, 2017.
- Doornbos, E., Scharroo, R., Klinkrad, H., Zandbergen, R., and Fritsche, B. Improved modelling of surface forces in the orbit determination of ERS and ENVISAT. *Canadian Journal of*

REFERENCES

- Remote Sensing*, 28(4):535–543, 2002. ISSN 17127971. doi: 10.5589/m02-055.
- Eberly, D. Perspective projection of an ellipsoid. *Geometric Tools, LLC*, pages 1–4, 1999. URL <http://www.geometrictools.com/Documentation/PerspectiveProjectionEllipsoid.pdf>.
- ESA. Space in Images, 2015. URL <http://www.esa.int/spaceinimages/Images>.
- ESA. The overview of ESABASE, 2018. URL <http://esabase2.net/esabase2-overview/>.
- Eugster, H. *Real-time georegistration of video data using low-quality navigation sensors and 3D digital landscape models*, volume 85. Swiss Geodetic Commission, 2012. ISBN 9783908440291. URL <https://www.sgc.ethz.ch/sgc-volumes/sgk-85.pdf>.
- European Global Navigation Satellite Systems Agency. Galileo Satellite Metadata, 2017a. URL <https://www.gsc-europa.eu/galileo-gsc-overview/system>.
- European Global Navigation Satellite Systems Agency. GNSS market report, 2017b. URL <https://www.gsa.europa.eu/system/files/reports/gnss{ }mr{ }2017.pdf>.
- European Global Navigation Satellite Systems Agency. Galileo system status, 2018. URL <https://www.gsc-europa.eu/system-status/Constellation-Information>.
- Falcone, M. Galileo system status. In *ION GNSS+ 2016*, pages 2410–2430, Portland, 2016.
- Farinella, P. and Vokrouhlický, D. Thermal force effects on slowly rotating, spherical artificial satellites-I. Soalr heating. *Planetary and Space Science*, 44(12):1551–1561, 1996. ISSN 00320633. doi: 10.1016/S0032-0633(96)00073-6.
- Fliegel, H. F., Gallini, T. E., and Swift, E. R. Global Positioning System Radiation Force Model for geodetic applications. *Journal of Geophysical Research*, 97(B1):559, 1992. ISSN 0148-0227. doi: 10.1029/91JB02564.
- Fliegel, H. F. and Gallini, T. E. Solar force modeling of block IIR Global Positioning System satellites. *Journal of Spacecraft and Rockets*, 33(6):863–866, 1996. ISSN 0022-4650. doi: 10.2514/3.26851.
- Fliegel, H. F., Warner, L. F., and Vrba, F. J. Photometry of Global Positioning System Block II and IIA Satellites. *Journal of Spacecraft and Rockets*, 38(4):609–616, 2001. ISSN 00224650. doi: 10.2514/2.3725.
- Forrest, A. R. Future trends in computer graphics: How much is enough? *Journal of Computer Science and Technology*, 18(5):531–537, 2003.
- Fritzsche, B., Ivanov, M., Kashkovsky, A., Koppenwallner, G., Kudryavtsev, A., Voskoboinikov, U., and Zhukova, G. Radiation pressure forces on complex spacecraft. Technical report, HTG,Germany and ITAM,Russian,ESOC contract 11908/96/D/IM, 1998.
- García, A., Luque, D., Navarro, P., and Tobías, G. Galileo simple box-wing model plus ECOM for improving orbit and clock prediction performances. In *29th International Technical Meeting of the Satellite Division of the Institute of Navigation, ION GNSS 2016*, volume 4, pages 2849–2863, Portland,Oregon, 2016. ISBN 9781510834101.
- Geng, T., Zhang, P., Wang, W., and Xie, X. Comparison of Ultra-Rapid Orbit Prediction Strategies for GPS, GLONASS, Galileo and BeiDou. *Sensors*, 18(2):477, feb 2018. ISSN 1424-8220. doi: 10.3390/s18020477.
- Grey, S. and Ziebart, M. Developments in High Fidelity Surface Force Models and their Relative Effects on Orbit Prediction. *AIAA/AAS Astrodynamics Specialist Conference*, 1(August):1–8, 2014. doi: 10.2514/6.2014-4135.
- Grey, S., Marchand, R., Ziebart, M., and Omar, R. Sunlight Illumination Models for Spacecraft Surface Charging. *IEEE Transactions on Plasma Science*, 45(8):1898–1905, 2017. ISSN 00933813. doi: 10.1109/TPS.2017.2703984.
- Guo, J. *The Impacts of Attitude, Solar Radiation and Function Model on Precise Orbit Determination for GNSS Satellites*. PhD thesis, Wuhan University, 2014.
- Guo, J., Xu, X., Zhao, Q., and Liu, J. Precise orbit determination for quad-constellation satel-

REFERENCES

- lites at Wuhan University: strategy, result validation, and comparison. *Journal of Geodesy*, 90(2):143–159, 2016. ISSN 14321394. doi: 10.1007/s00190-015-0862-9.
- Hofmann-Wellenhof, B., Lichtenegger, H., and Collins, J. *Global Positioning System: Theory And Practice*. Springer-Verlag Wien, 1993. ISBN 978-3-7091-6199-9.
- Hormann, K. and Agathos, A. The point in polygon problem for arbitrary polygons. *Computational Geometry: Theory and Applications*, 20(3):131–144, 2001. ISSN 09257721. doi: 10.1016/S0925-7721(01)00012-8.
- Hubaux, C., Lemaître, A., Delsate, N., and Carletti, T. Symplectic integration of space debris motion considering several Earth's shadowing models. *Advances in Space Research*, 49(10): 1472–1486, 2012. ISSN 02731177. doi: 10.1016/j.asr.2012.02.009.
- Hughes, G. B. and Chraibi, M. Calculating ellipse overlap areas. *Computing and Visualization in Science*, 15(5):291–301, 2012. ISSN 14329360. doi: 10.1007/s00791-013-0214-3.
- Information and Analysis Center for Positioning Navigation and Timing. GLONASS constellation status, 2018. URL <https://www.glonass-iac.ru/en/GLONASS/>.
- Jaeggi, A., Bock, H., Thaller, D., Dach, R., Beutler, G., Prange, L., and Meyer, U. Precise Orbit Determination of Low Earth Satellites At AIUB. *ESA Living Planet Symposium*, 2010 (July), 2010.
- Kang, Z., Tapley, B., Bettadpur, S., Ries, J., Nagel, P., and Pastor, R. Precise orbit determination for the GRACE mission using only GPS data. *Journal of Geodesy*, 80(6):322–331, 2006. ISSN 09497714. doi: 10.1007/s00190-006-0073-5.
- Khalil, I. K. and Abd, M. A. The effects of the Moon's shadow and pre-shadow on the artificial satellites motion. *Astronomy Studies Development*, 1, 2011.
- Klinger, B. and Mayer-Gürr, T. The role of accelerometer data calibration within GRACE gravity field recovery: Results from ITSG-Grace2016. *Advances in Space Research*, 58(9): 1597–1609, 2016. ISSN 18791948. doi: 10.1016/j.asr.2016.08.007.
- Klinkrad, H. and Fritzsche, B. Orbit and attitude perturbations due to aerodynamics and radiation pressure. Technical Report December, ESTEC, 1998.
- Klinkrad, H., Koeck, C., and Renard, P. Precise satellite skin-force modelling by means of Monte-Carlo ray-tracing. *ESA Journal*, 14(4):409–430, 1990.
- Klinkrad, H., Koeck, C., and Renard, P. Key features of a satellite skin force modelling technique by means of Monte-Carlo ray tracing. *Advances in Space Research*, 11(6):147–150, 1991. ISSN 02731177. doi: 10.1016/0273-1177(91)90244-E.
- Knocke, P. C. and Ries, J. Earth radiation pressure effects on satellites. Technical report, CSR-TM-87-01,Center for Space Research, the University of Texax at Austin,USA, 1987.
- Knocke, P. C., Ries, J., and Tapley, B. Earth radiation pressure effects on satellites. In *AIAA/AAS Astrodynamics Specialist Conference*, Minneapolis,United States, 1988.
- Knocke, P. C. *Earth radiation pressure effects on satellites*. PhD thesis, The University of Texas at Austin, 1989.
- Kopp, G. Earth's Incoming Energy: The Total Solar Irradiance. *Comprehensive Remote Sensing*, 5:32–66, 2018. doi: 10.1016/B978-0-12-409548-9.10366-5.
- Kopp, G. and Lean, J. L. A new, lower value of total solar irradiance: Evidence and climate significance. *Geophysical Research Letters*, 38(1):L01706, jan 2011. ISSN 00948276. doi: 10.1029/2010GL045777.
- Kozai, Y. Effects of the Solar-Radiaiton Pressure on the motion of an artificial satellite. *Smithsonian Contributions to Astrophysics*, 6(2):109–112, 1961. ISSN 00088714.
- Kubo-oka, T. and Sengoku, A. Solar radiation pressure model for the relay satellite of SELENE. *Earth, Planets and Space*, 51(9):979–986, 1999. ISSN 18805981. doi: 10.1186/BF03351568.
- Kucharski, D., Kirchner, G., Bennett, J. C., Lachut, M., Sośnica, K., Koshkin, N., Shakun, L., Koidl, F., Steindorfer, M., Wang, P., Fan, C., Han, X., Grunwaldt, L., Wilkinson, M.,

REFERENCES

- Rodríguez, J., Bianco, G., Vespe, F., Catalán, M., Salmins, K., del Pino, J. R., Lim, H.-C., Park, E., Moore, C., Lejba, P., and Suchodolski, T. Photon pressure force on space debris TOPEX/Poseidon measured by Satellite Laser Ranging. *Earth and Space Science*, 4(10), 2017. ISSN 23335084. doi: 10.1002/2017EA000329.
- Laboratory for Atmospheric and Space Physics at the University of Colorado. The SORCE spacecraft description, 2018. URL <http://lasp.colorado.edu/home/sorce/spacraft/>.
- Lála, P. Earth albedo effects in the motion of artificial earth satellites. *Advances in Space Research*, 10(3-4):317–320, 1990. ISSN 02731177. doi: 10.1016/0273-1177(90)90362-4.
- Lautman, D. Perturbations of a close-Earth satellite due to sunlight diffusely reflected from the Earth. *Celestial Mechanics*, 15(4):387–420, 1977.
- Lebedev, P. N. Experimental Examination of Light Pressure. *Annalen der Physik*, 6(433):1–26, 1901. ISSN 00033804. doi: 10.1002/andp.19013111102.
- Li, Z., Ziebart, M., Grey, S., and Bhattacharai, S. Earth Radiation Pressure Modelling for Beidou IGSO Satellites. In *China Satellite Navigation Conference*, pages 63–67, Shanghai, 2017.
- Li, Z., Ziebart, M., Bhattacharai, S., Harrison, D., and Grey, S. Fast solar radiation pressure modelling with ray tracing and multiple reflections. *Advances in Space Research*, 61(9): 2352–2365, 2018. ISSN 18791948. doi: 10.1016/j.asr.2018.02.019.
- Li, Z., Ziebart, M., Bhattacharai, S., and Harrison, D. A shadow function model based on perspective projection and atmospheric effect for satellites in eclipse. *Advances in Space Research*, 63(3):1347–1359, oct 2019. doi: 10.1016/j.asr.2018.10.027.
- List, M., Bremer, S., Rievers, B., and Selig, H. Modelling of Solar Radiation Pressure Effects: Parameter Analysis for the MICROSCOPE Mission. *International Journal of Aerospace Engineering*, 2015:1–14, 2015. ISSN 1687-5966. doi: 10.1155/2015/928206.
- Liu, J., Gu, D., Ju, B., Shen, Z., Lai, Y., and Yi, D. A new empirical solar radiation pressure model for BeiDou GEO satellites. *Advances in Space Research*, 57(1):234–244, 2016. ISSN 18791948. doi: 10.1016/j.asr.2015.10.043.
- Lochry, R. R. *The perturbative effects of diffuse radiations from the Earth and Moon on Close Satellites*. PhD thesis, UCLA, 1966.
- Longo, C. and Rickman, S. Method for the Calculation of Spacecraft Umbra and Penumbra Shadow Terminator Points. *NASA Technical Paper*, 1(April):41, 1995.
- Luzum, B. Recent and Anticipated Changes to the International Earth Rotation and Reference Systems Service (IERS) Conventions. In *Proceedings of the 2009 International Technical Meeting of The Institute of Navigation*, pages 706–710, Anaheim, CA, USA, 2009.
- Maxwell, J. C. *A Treatise on Electricity and Magnetism*, volume I. Dover Publication Inc, 3rd editio edition, 1891. ISBN 486-60636-8. doi: 10.1016/0003-6870(73)90259-7.
- McMahon, J. W. and Scheeres, D. J. Improving orbit determination with low-order fourier solar radiation pressure models. *Advances in the Astronautical Sciences*, 150:1093–1112, 2014. ISSN 00653438.
- Mendoza, B. Total solar irradiance and climate. *Fundamentals of Space Environment Science*, 35(5):882–890, 2005. doi: DOI10.1016/j.asr.2004.10.011.
- Miller, J. R., Bhandari, P., Novak, K., and Lyra, J. MLI Blanket Effective Emittance Variance and its Effect on Spacecraft Propellant Line Thermal Control. In *46th International Conference on Environment Systems*, Vienna, Austria, 2016.
- Moffitt, J. R., Chemla, Y. R., Smith, S. B., and Bustamante, C. Recent advances in optical tweezers. *Annu. Rev. Biochem.*, 77:205–28, 2008. ISSN 0066-4154. doi: 10.1146/annurev.biochem.77.043007.090225. URL <http://www.ncbi.nlm.nih.gov/pubmed/18307407>.
- Montenbruck, O., Schmid, R., Mercier, F., Steigenberger, P., Noll, C., Fatkulin, R., Kogure, S., and Ganeshan, A. S. GNSS satellite geometry and attitude models. *Advances in Space Research*, 56(6):1015–1029, 2015a. ISSN 18791948. doi: 10.1016/j.asr.2015.06.019.
- Montenbruck, O., Steigenberger, P., and Hugentobler, U. Enhanced solar radiation pressure

REFERENCES

- modeling for Galileo satellites. *Journal of Geodesy*, 89(3):283–297, 2015b. ISSN 14321394. doi: 10.1007/s00190-014-0774-0.
- Montenbruck, O. and Gill, E. *Satellite Orbits Models, Methods and Applications*. Springer Berlin Heidelberg, Berlin, Heidelberg, corrected edition, 2005. ISBN 978-3-540-67280-7. doi: 10.1007/978-3-642-58351-3.
- Montenbruck, O., Hauschild, A., Steigenberger, P., Hugentobler, U., Teunissen, P., and Nakamura, S. Initial assessment of the COMPASS/BeiDou-2 regional navigation satellite system. *GPS Solutions*, 17(2):211–222, apr 2013. ISSN 1080-5370. doi: 10.1007/s10291-012-0272-x.
- Montenbruck, O., Steigenberger, P., and Hauschild, A. Multi-GNSS Signal-in-Space Range Error Assessment - Methodology and Results. *Advances in Space Research*, 61(12):3020–3038, jun 2018. doi: 10.1016/j.asr.2018.03.041. URL <http://linkinghub.elsevier.com/retrieve/pii/S0273117718302813>.
- Muhleman, D., Hudson, R., Holdridge, D., Carpenter, R., and Oslund, K. Observed Solar Pressure Perturbations of Echo I. *American Association for the Advancement of Science*, 132 (3438):1487–1487, 1960.
- NASA. LAGEOS: LAser GEodynamic Satellite, 1976. URL <https://lageos.cddis.eosdis.nasa.gov>.
- National Coordination Office for Space-Based Positioning Navigation And Timing. GPS constellation status, 2018. URL <https://www.gps.gov/governance/excom/nco/>.
- Neta, B. and Vallado, D. On Satellite Umbra / Penumbra Entry and Exit Positions. *Journal of the Astronautical Sciences*, 95 PART 2(August 2017):1–29, 1997. ISSN 00653438.
- Nichols, E. F. and Hull, G. F. The Pressure Due to Radiation. *Proceedings of the American Academy of Arts and Sciences*, 38(20):559, 1903. ISSN 01999818. doi: 10.2307/20021808.
- Nichols, E. and Hull, G. Pressure due to light and heat radiation. *The Astrophysical Journal*, 15:62, 1902.
- Nick. Spectrum of solar radiation, 2008. URL https://commons.wikimedia.org/wiki/File:Solar_spectrum.svg#filehistory.
- Nonweiler, T. R. F. Algorithms: Algorithm 326: Roots Of Low-order Polynomial Equations. *Communications of the ACM*, 11(4):269–270, 1968.
- Parkinson, R. W., Jones, H. M., and Shapiro, I. I. Effects of Solar Radiation Pressure on Earth Satellite Orbits. *Science*, 131(3404):920–921, 1960. ISSN 0036-8075. doi: 10.1126/science.131.3404.920.
- Peter, H., Jäggi, A., Fernández, J., Escobar, D., Ayuga, F., Arnold, D., Wermuth, M., Hackel, S., Otten, M., Simons, W., Visser, P., Hugentobler, U., and Féménias, P. Sentinel-1A First precise orbit determination results. *Advances in Space Research*, 60(5):879–892, 2017. ISSN 18791948. doi: 10.1016/j.asr.2017.05.034.
- Poliakhova, E. Solar radiation pressure and the motion of earth satellites. *AIAA Journal*, 1 (12):2893–2909, 1963.
- Prange, L., Dach, R., Lutz, S., Schaer, S., and Jäggi, A. The CODE MGEX orbit and clock solution. Technical report, AIUB, 2016.
- Ren, X., Zhang, X., Xie, W., Zhang, K., Yuan, Y., and Li, X. Global Ionospheric Modelling using Multi-GNSS: BeiDou, Galileo, GLONASS and GPS. *Scientific Reports*, 6, 2016. ISSN 20452322. doi: 10.1038/srep33499.
- Robertson, R. V. *Highly Physical Solar Radiation Pressure Modeling During Penumbra Transitions*. PhD thesis, Faculty of the Virginia Polytechnic Institute and State University, 2015.
- Rodriguez-Solano, C. J. *Impact of non-conservative force modeling on GNSS satellite orbits and global solutions*. PhD thesis, Technische Universität München, 2014.
- Rodriguez-Solano, C. J., Hugentobler, U., and Steigenberger, P. Earth radiation pressure model for GNSS satellite. Technical report, EGU 2011, 2011.

REFERENCES

- Rodriguez-Solano, C. J., Hugentobler, U., and Steigenberger, P. Impact of albedo radiation on GPS satellites. *International Association of Geodesy Symposia*, 136:113–119, 2012a. ISSN 09399585. doi: 10.1007/978-3-642-20338-1_14.
- Rodriguez-Solano, C. J., Hugentobler, U., and Steigenberger, P. Adjustable box-wing model for solar radiation pressure impacting GPS satellites. *Advances in Space Research*, 49(7): 1113–1128, 2012b. ISSN 02731177. doi: 10.1016/j.asr.2012.01.016.
- Rodriguez-Solano, C. J., Hugentobler, U., Steigenberger, P., and Lutz, S. Impact of Earth radiation pressure on GPS position estimates. *Journal of Geodesy*, 86(5):309–317, 2012c. ISSN 09497714. doi: 10.1007/s00190-011-0517-4.
- Rothacher, M., Beutler, G., and Springer, T. The impact of the Extended CODE Orbit Model on the Estimation of Earth Rotation Parameters. Technical report, IGS workshop, Silver Spring, 1996.
- Rubincam, D. P. Yarkovsky Thermal Drag on LAGEOS. *Journal of Geophysical Research: Solid Earth*, 93(B11):13805–13810, 1988. ISSN 01480227. doi: 10.1029/JB093iB11p13805.
- Schaer, S. How to use CODE’s Global Ionosphere Maps. Technical report, Astronomical Institute, University of Berne, 1996.
- Sehnal, L. Radiation pressure effect on the motion of artificial Earth satellites. *Dynamics of Satellites*, pages 262–272, 1969.
- Sehnal, L. The motion of an artificial satellite under the terrestrial radiation pressure. *Advances in Space Research*, 1(6):37–41, 1981. ISSN 02731177. doi: 10.1016/0273-1177(81)90005-3.
- Shapiro, I. I. and Jones, H. M. Perturbations of the Orbit of the Echo Balloon. *Science*, 132 (3438):1484–1486, 1960. ISSN 0036-8075 (Print). doi: 10.1126/science.132.3438.1484.
- Sibois, A., Selle, C., Desai, S., Sibthorpe, A., and Weiss, J. GSPM13: An updated Empirical Model for Solar Radiation Pressure Forces Acting on GPS Satellites. Technical report, IGS workshop 2014, 2014.
- Sibthorpe, A., Weiss, J., Harvey, N., Kuang, D., and Bar-Sever, Y. Empirical Modelling of Solar Radiation Pressure Forces Affecting GPS Satellites. Technical report, AGU Fall Meting, San Francisco, 2010. URL http://acc.igs.org/orbits/srp-models{_}JPL{_}agu10.pdf.
- Sibthorpe, A., Bertiger, W., Desai, S. D., Haines, B., Harvey, N., and Weiss, J. P. An evaluation of solar radiation pressure strategies for the GPS constellation. *Journal of Geodesy*, 85(8): 505–517, 2011. ISSN 09497714. doi: 10.1007/s00190-011-0450-6.
- Sibthorpe, A. *Precision Non-Conservative Force Modelling For Low Earth Orbiting Spacecraft*. PhD thesis, University College London, 2006.
- Smith, D. E. and Dunn, P. J. Long term evolution of the Lageos Orbit. *Geophysical Research Letters*, 7(6):437–440, 1980. ISSN 19448007. doi: 10.1029/GL007i006p00437.
- Song, Y. J. and Kim, B. Y. The effect of the Earth’s oblateness on predicting the shadow conditions of a distant spacecraft: Application to a fictitious lunar explorer. *Advances in Space Research*, 57(1):355–366, 2016. ISSN 18791948. doi: 10.1016/j.asr.2015.09.028.
- Sopin, D., Bogolepov, D., and Ulyanov, D. Real-time SAH BVH construction for ray tracing dynamic scenes. *Proceedings of the 21th International Conference on Computer Graphics and Vision (GraphiCon)*, pages 74–77, 2011.
- Sosnica, K., Rodriguez-Solano, C. J., Thaller, D., Dach, R., Jaggi, A., Baumann, C., and Beutler, G. Impact of Earth Radiation Pressure on LAGEOS Orbits and on the Global Scale. Technical report, 18th International Workshop on Laser Ranging, Fujiyoshida, Japan, 2013. URL <https://cddis.nasa.gov/lw18/docs/posters/13-Po22-Sosnica.pdf>.
- Springer, T. A., Beutler, G., and Rothacher, M. Improving the orbit estimates of GPS satellites. *Journal of Geodesy*, 73(3):147–157, 1999a. ISSN 09497714. doi: 10.1007/s001900050230.
- Springer, T. A., Beutler, G., and Rothacher, M. A New Solar Radiation Pressure Model for GPS Satellites. *GPS Solutions*, 2(3):50–62, 1999b. ISSN 1080-5370. doi: 10.1007/PL00012757.
- Srivastava, V. K., Yadav, S. M., Ashutosh, Kumar, J., Kushvah, B. S., Ramakrishna, B. N.,

REFERENCES

- and Ekambram, P. Earth conical shadow modeling for LEO satellite using reference frame transformation technique: A comparative study with existing earth conical shadow models. *Astronomy and Computing*, 9:34–39, 2015. ISSN 22131337. doi: 10.1016/j.ascom.2014.10.001.
- Steigenberger, P., Thoelert, S., and Montenbruck, O. GNSS satellite transmit power and its impact on orbit determination. *Journal of Geodesy*, 92(6):609–624, jun 2018. ISSN 0949-7714. doi: 10.1007/s00190-017-1082-2.
- Tan, L., Wang, Z., and Gu, H. Radiation pressure and laser cooling of a three-level atom in a ladder configuration. *Chinese Physics*, 13(7):1005, 2004.
- Tapley, B. D., Bettadpur, S., Watkins, M., and Reigber, C. The gravity recovery and climate experiment: Mission overview and early results. *Geophysical Research Letters*, 31(9), 2004. ISSN 00948276. doi: 10.1029/2004GL019920.
- Teunissen, P. J. and Montenbruck, O. *Springer Handbook of Global Navigation Satellite Systems*. Springer International Publishing, Cham, 2017. ISBN 978-3-319-42926-7. doi: 10.1007/978-3-319-42928-1.
- Tobias, G. and Garcia, A. J. Box-wing model approach for solar radiation pressure modelling in a multi-GNSS scenario. Technical report, EGU General Assembly 2016, Spain, 2016.
- Touboul, P., Willemenot, E., Foulon, B., and Josselin, V. Accelerometers for CHAMP, GRACE and GOCE space missions: Synergy and evolution. *Bollettino di Geofisica Teorica ed Applicata*, 40(3-4):321–327, 1999. ISSN 00066729.
- Tuer, T. W. and Springer, G. S. A Test Particle Monte Carlo method. *Computers & Fluids*, 1 (4):399–417, 1973. ISSN 0045-7930. doi: 16/0045-7930(73)90006-6.
- Vallado, D. A. *Fundamentals of Astrodynamics and Applications*. Microcosm Press/Springer, 3rd editio edition, 2007. ISBN 978-11881883180. doi: 10.2514/2.4291.
- Vetter, J. R. Fifty years of orbit determination: Development of modern astrodynamics methods. *Johns Hopkins APL Technical Digest (Applied Physics Laboratory)*, 27(3):239–252, 2007. ISSN 02705214.
- Virdee, H. S. *Radiation Pressure Torque and Computational Attitude Modelling of Space Debris*. Phd thesis, University College London, 2016.
- Vokrouhlický, D. and Farinella, P. Radiative forces and LAGEOS' orbit. *Advances in Space Research*, 16(12):15–19, 1995a. ISSN 02731177. doi: 10.1016/0273-1177(95)91013-1.
- Vokrouhlický, D. and Farinella, P. Specular reflection of sunlight from wavy ocean surfaces and the albedo effect on satellite orbits. I. A statistical model. *Astronomy and Astrophysics*, 298: 307–322, 1995b.
- Vokrouhlický, D., Farinella, P., and Mignard, F. Solar radiation pressure perturbations for Earth satellites. I: A complete theory including penumbra transitions. *Astronomy and Astrophysics*, 280:295–312, 1993.
- Vokrouhlický, D., Farinella, P., and Mignard, F. Solar radiation pressure perturbations for Earth satellites. II: An approximate method to model penumbra transitions and their long-term orbital effects on LAGEOS. *Astronomy and Astrophysics*, 285:333–343, 1994a.
- Vokrouhlický, D., Farinella, P., and Mignard, F. Solar radiation pressure perturbations for Earth satellites III. Global atmospheric phenomena and the albedo effect. *Astronomy and Astrophysics*, 290:324–334, 1994b.
- Vokrouhlický, D. The geomagnetic effects on the motion of an electrically charged artificial satellite. *Celestial Mechanics & Dynamical Astronomy*, 46(1):85–104, 1989. ISSN 09232958. doi: 10.1007/BF02426715.
- Vondrák, J. and Richter, B. International Earth Rotation and Reference Systems Service (IERS) web: www.iers.org. *Journal of Geodesy*, 77(10-11):585–678, 2004. ISSN 0949-7714. doi: 10.1007/s00190-003-0370-1.
- Wald, I., Mark, W. R., Günther, J., Boulos, S., Ize, T., Hunt, W., Parker, S. G., and Shirley, P. State of the Art in Ray Tracing Animated Scenes. In Dieter, S. and Bittner, J., editors,

REFERENCES

- Eurographics 2007 - State of the Art Reports.* The Eurographics Association, 2007. doi: 10.2312/egst.20071056.
- Wielicki, B. A., Barkstrom, B. R., Harrison, E. F., Lee, R. B., Smith, G. L., and Cooper, J. E. Clouds and the Earth's Radiant Energy System (CERES): An Earth Observing System Experiment, 1996. ISSN 00030007.
- Williams, P. A., Hadler, J. A., Lee, R., Maring, F. C., and Lehman, J. H. Use of radiation pressure for measurement of high-power laser emission. *Opt. Lett.*, 38(20):4248–4251, 2013. ISSN 1539-4794. doi: 10.1364/OL.38.004248.
- Wineland, D., Drullinger, R. E., and Walls, F. Radiation-pressure cooling of bound resonant absorbers. *Physical review letters*, 40(1639), 1978.
- Yarkovsky, I. O. The density of luminiferous ether and the resistance it offers to motion, 1901.
- Zhang, R., Tu, R., Zhang, P., Liu, J., and Lu, X. Study of satellite shadow function model considering the overlapping parts of Earth shadow and Moon shadow and its application to GPS satellite orbit determination. *Advances in Space Research*, feb 2018. ISSN 02731177. doi: 10.1016/j.asr.2018.02.002.
- Ziebart, M. and Dare, P. Analytical solar radiation pressure modelling for GLONASS using a pixel array. *Journal of Geodesy*, 75(11):587–599, 2001. ISSN 09497714. doi: 10.1007/s001900000136.
- Ziebart, M., Adhya, S., Sibthorpe, A., Edwards, S., and Cross, P. Combined radiation pressure and thermal modelling of complex satellites: Algorithms and on-orbit tests. *Advances in Space Research*, 36(3):424–430, 2005. ISSN 02731177. doi: 10.1016/j.asr.2005.01.014.
- Ziebart, M. Analytical SRP Model for GLONASS: Initial Results. Technical report, Applied Geodesy Research Unit, School of Surveying, University of East London, 1998. URL <http://www2.unb.ca/gge/Personnel/Dare/IGEX1999.pdf>.
- Ziebart, M. *High Precision Analytical Solar Radiation Pressure Modelling for GNSS Spacecraft*. PhD thesis, The University of East London, 2001.
- Ziebart, M. Generalised Analytical Solar Radiation Pressure Modelling Algorithm for Spacecraft of Complex Shape. *Journal of Spacecraft and Rockets*, 41(5):840–848, 2004. ISSN 00224650.